Understanding the Structure of Silver Nanoparticles and Its Influence on Surface Reactivity

by

Joseph Daniel Padmos

Submitted in partial fulfilment of the requirements
for the degree of Doctor of Philosophy

at

Dalhousie University
Halifax, Nova Scotia
December 2015

Table of Contents

List of Tables

List of Figures

Abstract

Silver nanoparticles (Ag NPs) have proven to be useful for biomedical applications, as the ability to fine-tune properties such as size, shape, composition, and surface structure is a distinct advantage for their associated antibacterial properties. Their surface structure is especially important, as it can influence NP stabilization as well as govern any further surface reactivity. Despite the huge amount of research being performed on metal NPs in general, their surface structure is a much less studied parameter, partly because the averaging effect from the non-surface atoms of NPs makes it difficult to isolate. However, with the employment of element-specific techniques such as X-ray absorption spectroscopy (XAS), the surface structure of metal NPs can be more easily investigated. The research presented in this thesis explored the surface structures of Ag-based NPs using XAS, in order to gain fundamental and practical insight to their physicochemical properties and surface reactivity. In particular, the structures of thiolate-protected Ag NPs in both organic and aqueous solutions were investigated, and were found to be highly sulfidized at their surfaces. The sulfidized surface structures also caused reduced antibacterial activity in comparison to more metallic surface structures. In addition to monometallic Ag NPs, a series of bimetallic AgAu NPs was also examined. The atomic structure within the cores of each type of AgAu NP was dependent on the molar ratios of the metals, yet each type had a similar surface structure that was predominantly composed of Ag. The AgAu NPs exhibited lower antibacterial activity compared to pure Ag NPs, but also showed significantly reduced cytotoxicity, thereby demonstrating their potential for therapeutic applications. Furthermore, the surface structures of chloride-adsorbed, Ag-coated anisotropic Au NPs were examined to understand ligand and alloy effects on NP stabilization. The surface structures were found to be sensitive to their formation mechanism and facet type, which sheds light on the mechanism of Ag- and chloride-induced NP growth. Overall, this thesis contributes to a better understanding of how ligands and alloying can control the surface properties and reactivity of Ag-based NPs.

List of Abbreviations and Symbols Used

NP	Nanoparticle
E_o	Absorption Edge Energy
APS	Advanced Photon Source
S_o^2	Amplitude Reduction Factor
Å	Ångstrom
J	Atomic Structure Parameter
SXRMB	Beamline 06B1-1 at CLS (Soft X-Ray Microcharacterization Beamline)
HXMA	Beamline 06ID-1 at CLS (Hard X-ray Microstructure Analysis)
R	Bond length
CLS	Canadian Light Source
CTAC	Cetyltrimethylammonium Chloride
CN	Coordination Number
α	Cowley Parameter
Cys	Cysteine
σ^2	Debye-Waller Factor
°C	Degrees Celsius
DFT	Density Functional Theory
DDT	Dodecanethiol
Z_{eff}	Effective Nuclear Charge
ΔE_o	Energy Shift Parameter
$\mu(E)$	Experimental X-ray Absorption Coefficient
EXAFS	Extended X-Ray Absorption Fine Structure
FCC	Face-centered Cubic
I_f	Fluorescence Intensity
FLY	Fluorescence Yield
FT	Fourier-transform
Au NPs	Gold Nanoparticles
HRTEM	High Resolution Transmission Electron Microscopy
$\mu_o(E)$	Intrinsic X-ray Absorption Coefficient

K	Kelvin
MIC	Minimum Inhibitory Concentration
NMR	Nuclear Magnetic Resonance Spectroscopy
1D	One-dimensional
$\lambda(k)$	Photoelectron Mean Free Path
PVP	Polyvinylpyrrolidone
$\hbar$	Reduced Planck's Constant
g	Relative Centrifugal Force
$f(k)$	Scattering Amplitude of a Neighbouring Atom
$\delta(k)$	Scattering Phase Shift of a Neighbouring Atom
Ag NPs	Silver Nanoparticles
SPR	Surface Plasmon Resonance
TOAB	Tetraoctylammonium Bromide
RSH	Thiol
RS-	Thiolate
TEY	Total Electron Yield
TEM	Transmission Electron Microscopy
2D	Two-dimensional
UV-vis	Ultraviolet-visible Spectroscopy
UPD	Underpotential Deposition
WT	Wavelet-transform
k	Wavenumber
$\chi(E)$	X-ray Absorption Fine Structure
XANES	X-ray Absorption Near Edge Structure
XAS	X-Ray Absorption Spectroscopy
I_t	X-ray Intensity After Transmission
I_o	X-ray Intensity Before Transmission
XRD	X-ray Diffraction
XPS	X-ray Photoelectron Spectroscopy

Acknowledgements

I would like to first thank my supervisor, Peng Zhang. Peng started me out on this journey and has been extremely supportive of my scientific and academic endeavors, always pushing me to achieve my best. I am so grateful for all that he has taught me and will cherish his scientific advice, as well as his wisdom during particularly hard times. I would also like to thank the rest of my supervisory committee: Heather Andreas, Jan Rainey, and Donald Weaver. Their attention to my research, encouragement, and constructive criticism have been much appreciated.

I would like to thank all previous and current Zhang group members, especially Stephen Christensen, Mark MacDonald, Zac Cormier, Paul Duchesne, Daniel Chevrier, Peter Cho, and Arti Dhoot. I benefitted immensely from their friendship, intelligence, and enthusiasm for research.

I also would like to acknowledge all of the beamline scientists and collaborators, of which there are many. Thanks to Yongfeng Hu, Ning Chen, and Robert Gordon, for their support at the CLS and APS. Donald Weaver, Mark Filiaggi, Chad Mirkin, De-en Jiang, Maxine Langman, Zhan Yang, Robert Boudreau, Michelle Personick, and Paul Duchesne also deserve my upmost praise, as they were amazing collaborators to work with.

I would like to thank my parents Andrew and Patricia, and my older brothers Jeremy and Alastair, for their constant support and encouragement throughout my life. I would also like sincerely thank my extended family: Anju, Chander, Vivek, Monika, and Arveen, for their encouragement and patience, especially in the final stages of this work.

Finally, my own family, Karmina, Oscar, Annika, and even our two cats Louie and Bizzy, deserve the most recognition for helping me through this PhD. I am so fortunate to have such a wonderful family and they make my life so much better in every way. Their constant love and support have made this PhD possible, and therefore I dedicate this work to them.

Chapter 1 - Introduction

1.1 Overview

The study of nanomaterials, generally defined as materials that have at least one physical dimension between 1-100 nm, has led to impressive scientific developments in the past few decades. In particular, noble metal nanoparticles (NPs) have been at the forefront of these developments, with numerous methodologies established to synthesize NPs with different sizes, shapes, compositions, and surface structures. As a result, they have been applied to a broad range of fields, such as catalysis,[1–3] biochemical sensing,[1,4] and particularly medicine, where their potential in antibacterial and drug delivery applications have also been demonstrated.[5–7] The innovative uses of NPs arise as a result of their fascinating physicochemical properties which differ from that of their bulk counterparts.

In general, the unique properties of NPs are a result of their high surface-to-volume ratio (*i.e.,* large number of surface atoms) compared to bulk materials. For example, in catalytically active bulk materials (Pt, Pd, *etc.*), the number of catalytic sites are based on the available atoms on the surface, and thus most of the atoms in metal bulk are inactive. For NPs where the number of surface atoms are much greater, their catalytic activity is correspondingly greater than the bulk per mass.[8] In addition to a greater number of surface atoms, the smaller size of NPs can also cause unique effects on electronic related properties. This is because as a metal particle becomes nanometer-sized, the metal orbital bands become semi-quantized.[9,10] The more separated orbitals change the energy required for electronic transitions, and therefore, change the electronic

properties of the metal. Another typical example of the size effect is demonstrated by the optical properties of Ag and Au NPs. In this way, Ag and Au NPs exhibit yellow or red colours in solution due to a collective oscillation of their surface electrons, also known as surface plasmon resonance (SPR, discussed further in section 1.4.2).[11,12] Furthermore, NPs with sizes below the classic nanomaterial size regime experience further quantization in their orbitals, which can influence their electronic properties even more.[10,13] In fact, the discovery of these much different properties from NPs has led to the distinction of nanoclusters (NCs), which are NPs typically less than 2 nm in diameter.[14]

The shape of NPs also plays a large role in their physicochemical properties and as a result considerable interest has been given to the concept of NP shape control. Besides spherical NPs, more complex NP shapes have been prepared such as discs, cubes, rods, wires, and prisms, to name a few.[9,15–19] Shape can have a dramatic effect on the physicochemical properties of NPs,[9,15–19] most notably their optical properties. This is because the number of dimensional characteristics correlates to the number of SPR features observed. In metal nanorods for example, two SPR features are observed because of the multiple absorptions in each dimension of the rods (*i.e.,* longitudinal and transversal).[17] Shape effects have also been correlated to catalytic activity,[18] as well as antibacterial activity of various NPs.[19]

Compositional changes from alloying two or more metals together can also have a drastic effect on NP properties, which can be different from the individual NPs. This is often demonstrated by the optical properties of bimetallic Ag/Au NPs, where Ag and Au NPs usually have individual SPR bands at around 400-420 nm and 520-550 nm, respectively, but Ag/Au NPs can have SPR bands in between those values based on their composition.[11,12,20,21] Further to this effect, the way in which they are alloyed together

(*i.e.,* atomic arrangement) can also have an effect on their properties and makes the morphology of bimetallic NPs an important factor to consider as well.[11,12,20,21]

Finally, the arrangement, composition, and ligation of atoms at the NP surface, defined together as surface structure, are also heavily correlated with NP properties. Despite the enormous developments in NP characterization, surface structure and its influence on other NP properties is much less understood. In part this is because isolating surface atoms with traditional analytical techniques is difficult as, depending on NP size, the averaging effect from the bulk of the NPs is sometimes large enough to effectively mask them. As such, surface structural characterization of NPs represents one of the largest challenges in modern materials science. However, element-specific techniques, such as X-ray absorption spectroscopy (XAS), can more comprehensively investigate the surface structure of metal NPs. The study of Ag NP surface structure and its effect on surface-related reactions is the central idea of this thesis.

1.2 Silver Nanoparticles (Ag NPs)

Among the vast assortment of nanomaterials currently being studied, Ag NPs are some of the most extensively investigated because of their practical use in many modern applications. Their unique and fascinating physicochemical properties have initiated this modern use, but in fact, Ag NPs also have a long history. For example, one of the earliest known applications of Ag NPs was as a colour additive in the Lycurgus cup (*c.a.,* 400 C.E.), which yields the unique green-to-red colour changes when light is shone through it. Later examinations of the glass composition revealed embedded Ag and Au NPs with relative concentrations of 68 % and 32 % respectively.[22] Ag NPs have since been

exploited for their unique optical properties in bio- and chemical-sensing technologies, but perhaps their most well-known characteristic is their antibacterial activity.

1.2.1 Antibacterial Activity of Ag and Ag NPs

Bulk Ag and Ag^+ compounds are generally recognized to possess antibacterial properties and have actually been used in this capacity for centuries. One of the earliest uses of Ag for this purpose was by ancient civilizations who used Ag containers to preserve water for long periods of time.[23] Similarly, early pioneers in North America dropped Ag coins into water and milk to prevent spoilage.[23] This observed preservation ability also inspired the concept of using Ag culinary utensils and cups (hence the term "silverware"), although their use eventually became more of a socioeconomic descriptor despite being practical.[23] Ag also saw many historical applications in medicine, one famous example being the use of Ag sutures to close surgical wounds in order to decrease the chance of systemic infection.[24] Another medical use of Ag was the direct application of Ag foil into open wounds to prevent local infection.[25,26] This application actually inspired the use of Ag^+-containing compounds such as silver nitrate and silver sulfadiazine for the prevention of wound infections, a practice which is still employed today for burn treatments.[25,26] In these cases, Ag^+ ions are released gradually from wound dressings or topical creams, and have shown to decrease the chance of bacterial infections, thus improving the healing process and/or reducing healing time.[25,26]

More recently, Ag NPs have gained wider attention for their remarkable antibacterial activities and have even been incorporated into commercial products in which antibacterial properties are required, such as textiles,[27] catheters,[28] burn wound dressings,[29] medical instruments,[30] and orthopedic implant materials.[31,32] Their enhanced

antibacterial activity stems in part from their increased number of reactive Ag surface sites, as compared to bulk Ag. Ag NPs also undergo partial dissolution in most aqueous solutions, thereby releasing Ag^+ ions from their surfaces which also exhibit antibacterial activity.[33–35] However, their surface protection by ligands also prevents the immediate sequestering and inactivation of Ag and Ag^+ by biological molecules that contain elements such as Cl and S; these molecules react readily with Ag and Ag^+ thereby enabling the Ag or Ag^+ to interact with the intended bacterial target. In a sense, Ag NPs are much like a drug delivery system, as they provide a reservoir of Ag and Ag^+ which can be delivered to the target site.

Ag NPs have been observed to have a broad spectrum of antibacterial activity against both Gram-positive and Gram-negative bacteria.[6] In general, most studies have observed a greater effectiveness against Gram-negative bacteria, which is thought to be related to their cell wall structure. Gram-negative bacteria are distinguished by a thin layer of peptidoglycan (~ 2 nm), an outer membrane composed of lipopolysaccharides, phospholipids, and proteins, and an inner membrane composed of just phospholipids and proteins.[36] In contrast, Gram-positive bacteria contain a thicker, more rigid peptidoglycan layer (~ 30 nm) with embedded proteins, and an inner membrane of phospholipids and proteins.[36] Some studies have observed that Ag NPs can permeate into the less rigid cell wall structure of Gram-negative bacteria, leading to greater effectiveness; this permeation is prevented in Gram-positive bacteria by their thicker peptidoglycan layers.[37] It has also been hypothesized that the negatively charged lipopolysaccharides in Gram-negative bacteria can attract positively charged Ag^+ ions, thereby contributing to a greater effect on Gram-negative bacteria.[38,39]

Although the effect of various Ag NPs on bacteria has been well reported, the extent to which bacteria are affected by the Ag NP surface (the particle-specific effect) or by Ag^+ ions (the ion-specific effect) remains somewhat of an open debate. For example, several studies have suggested that the attachment of Ag NPs to the cell walls of bacteria and subsequent interaction with surface proteins causes bacteria to be ruptured leading to cell death.[39–43] Other studies have shown that Ag NPs can permeate through bacteria cell walls and interfere with cytoplasm proteins[40] or DNA,[42] causing inhibition of their replication and proliferation. However, these particular mechanisms were generally more observed for Gram-negative bacteria, wherein the less rigid cell wall is more susceptible to this type of mechanism.

On the other hand, other studies have demonstrated that the antibacterial mechanism of Ag NPs is primarily related to Ag^+ ions, which can affect both types of bacteria.[44–47] Ag^+ ions can undergo many of the same reactions as Ag, where they react with membrane or cytoplasm proteins, or interfere with DNA replication; all which can lead to cell death.[44,48] Recently, it has also been observed that the dissolution of Ag^+ ions from Ag NPs was prevented under anaerobic conditions, and as a result, they had zero antibacterial activity against Gram-negative bacteria.[45] When the same Ag NPs were examined under aerobic conditions, the dissolution of Ag^+ occurred and the antibacterial activity was observed to correlate with that of a similar concentration of Ag^+. The authors concluded from this study that Ag NPs likely rely on the ion-specific effect for their antibacterial activity. In general, the consensus in the literature is that Ag^+ ions are most likely the major contributor to the antibacterial activity of Ag NPs, while the particle-specific effect is minor.

Another indirect mechanism of antibacterial activity broadly observed in the literature is based on the generation of reactive oxygen species (ROS) from either the Ag NPs themselves or released Ag^+ ions.[41,44,49–54] ROS are essentially free radicals, such as peroxides and hydroxyl radicals, and can be generated from reactions outside or inside bacteria or as a consequence of cell damage/disruption. ROS subsequently catalyze the oxidation of other cellular components (*i.e.,* "oxidative stress") and their intracellular concentration in bacteria has been shown to correlate with growth inhibition.[54]

Overall, there are multiple mechanisms that can be attributed to Ag NP antibacterial activity, and it is likely that a general antibacterial mechanism cannot be easily determined. However, these multiple mechanisms are actually an advantage when it comes to applications, as they can inhibit the development of bacterial resistance. This is especially important in modern times, as bacterial resistance against current antibiotics is a common problem, and has even led to the classification of multi-drug resistant bacteria. The fact that Ag NPs can have multiple mechanisms of antibacterial activity is therefore considered a genuine advantage despite increasing their complexity.

In addition to their relatively lower tendency toward the development of bacterial resistance, the major advantage of using Ag NPs for antibacterial applications is that their size, shape, composition, and surface structure can all be tailored, thereby providing more controlled delivery of the Ag or Ag^+ from the Ag NPs. For example, the size of Ag NPs has demonstrated an influence on antibacterial activity, where the increase in surface area as a result of the reduced size can simply increase the number of surface reactions possible.[5,40,55] The size of the Ag NPs can also control the permeation of the Ag NPs into the bacteria, as Ag NPs under 10 nm have been shown to penetrate Gram-negative bacteria more effectively than larger Ag NPs.[40] In addition, smaller size and higher

surface area can result in a more rapid Ag^+ dissolution from the Ag NP, which can also result in higher antibacterial activity.[40] The shape of Ag NPs has also been shown to affect antibacterial activity, with some studies reporting that truncated Ag nanoprisms had higher antibacterial activity than nanorods or spheres as a result of their higher surface energy facets.[19] Compositional changes from alloying other metals to Ag NPs (either at their surface or in the core) can also modify antibacterial activity. For example, the antibacterial activity of AgAu NPs has recently demonstrated a dependence on the atomic arrangement of the Ag and Au at their surfaces.[56] Finally, the surface structure of Ag NPs can also have an effect on the antibacterial activity by impacting either the direct surface interactions with bacteria, or by changing the rate of dissolution from the Ag NPs. For example, various surface-protecting ligands on Ag NPs demonstrated different Ag^+ dissolution rates, and have led to different antibacterial activities.[57,58] The effect of surface structure on Ag NP antibacterial activity is a central theme of this thesis, and will be discussed further in later chapters.

1.2.2 Cytotoxicity of Ag and Ag NPs

One of the most commonly observed adverse effects of exposure to Ag and Ag^+ compounds is argyria, which is characterized by a bluish discolouration of the skin and other tissues in the body.[59] Although generally considered to be non-life-threatening, this effect illustrates the potential for adverse effects following exposure to Ag. For Ag NPs, additional health concerns exist, despite their current use in commercial products. One of the major concerns for Ag NPs is that they may interact with many different parts of the body via systemic circulation. Exposure of Ag NPs through dermal absorption, oral administration, inhalation, or intravenous injection can lead to broad and extended

circulation throughout the main organs of the body, including the kidney, skin, liver, lungs, spleen, and brain.[60–62] Ag NPs have also been observed to be internalized by cell types including human mesenchymal cells, fibroblasts, and more.[60–65] In some cases, their size and surface-protecting ligands have been shown to be contributing factors to their internalization. For example, 5 nm Ag NPs demonstrated greater uptake into various human cell lines versus 20 and 50 nm Ag NPs.[66] The surface protecting ligands of Ag NPs can also control cell uptake, as polymer protected Ag NPs had reduced fibroblast cell uptake than that of thiolate-protected Ag NPs.[64]

The consequence of broad and extended circulation is the potentially deleterious effects of Ag NPs on the organs, tissues, and cells of the body. For example, damage to various cell types has been reported, such as the aforementioned human mesenchymal cells and fibroblasts.[60–65] The effects on mammalian cells largely occur through similar mechanisms as seen in bacteria, including interaction with cellular thiols and DNA, and generation of ROS and subsequent oxidative stress.[48,61] The same debate surrounds the effect of Ag NPs on cells as to whether particle- or ion-specific effects are the predominant cause of cytotoxicity, as both have been observed. In this case however, the multiple mechanisms of Ag NP effects on cells are an obvious disadvantage to their application, and makes the study of their overall health impact more crucial. Indeed, although the potential negative impact of Ag NPs on the human body has been demonstrated in recent years, it seems that the commercialization of Ag-compounds or Ag NPs has sometimes preceded their overall risk assessment. For instance, some commercially available products that contain Ag-compounds or Ag NPs have demonstrated significant toxic effects toward both bacteria and certain mammalian cells.[29] Therefore, it is now even more important that a balance is struck between the

toxicity of Ag NPs to normal cells and bacteria, in order to achieve the best performance and safety. For this reason, it is crucial to formulate Ag NPs with controlled size, composition, and surface structure in order to control the interplay between their antibacterial activity and cytotoxicity.

1.3 Synthesis of Metal NPs

While early examples of metal NP preparation have been reported in history, such as the previously described Lycurgus cup, one of the most famous systematically controlled chemical methods was reported by Faraday in 1857.[67] Faraday first reduced Au salts with phosphorus to produce thin films of reddish colour, and used this technique to control their colour. Much later, in 1951, Turkevich reported a similar chemical reduction technique that used heat and citrate anions to reduce and stabilize Au NPs in water.[68] This particular technique was revisited by Frens in 1973, who reported a mechanism of NP size control by modifying citrate:Au ratios.[69] Further modifications of the Turkevich and Frens methods have also led to the preparation of other metal NPs, such as Ag NPs.[70] The next major preparation breakthrough occurred in 1994, when Brust and Schiffrin reported a two-phase method to prepare Au NPs by reducing metal ions stabilized by tetraoctylammonium bromide (TOAB) in the presence of alkylthiols in toluene.[71] Water-soluble sodium borohydride ($NaBH_4$) was used as the reducing agent, which resulted in NPs forming at the solvent interface more slowly than a one-phase synthesis, and overall produced more uniformly sized NPs than previous methods. The original Brust-Schiffrin method also demonstrated the ability to modify the size of NPs based on the ratios of ligand to metal, but has since been expanded to utilize different organosulfur ligands, metals, and reducing agents.[72–75]

Since these important examples in history, the synthesis of metal NPs has become a vast area of research with many different methodologies being developed to produce specific NP structures. In general, NP syntheses can be divided into two general approaches of top-down and bottom-up. In top-down syntheses, a larger material is taken and reduced to a smaller size by a physical procedure. This can be carried out mechanically, such as with ball-milling, or by physical deposition or elimination of elements, such as nanolithography.[76–79] The major drawbacks of top-down approaches are that the resulting NPs often include a large number of defects and impurities, and are less uniform in general.[80,81]

The bottom-up approach usually takes place in solution, and relies on chemical reactions that assemble NPs on an atomic scale. This is initiated by the reduction of metal precursor compounds in aqueous or organic solution which can occur by chemical, electrochemical, or photoreductive means.[9,10] However, the most common approach to preparing NPs is by chemical reduction, whereby a reducing agent is used to reduce the precursor compounds to zero-valent metal atoms. The metal atoms then self-assemble into NPs with the assistance of a surface protecting molecule (described as a ligand once bound to the NP). This technique is often used to create Au and Ag NPs (and many others) from precursor metal compounds such as gold tetrachloroaurate ($HAuCl_4$) or silver nitrate ($AgNO_3$).

Chemical reduction can be carried out with a variety of reducing agents such as ethylene glycol, sodium citrate, and N-dimethylformamide, but most the most common for preparing metal NPs is sodium borohydride ($NaBH_4$).[9,10] $NaBH_4$ has a high reducing power and can reduce a number of different types of metals, including Ag, where it undergoes the following partial reactions in aqueous solution:[82,83]

$$Ag^{+}_{(aq)} + BH_4^{-}{}_{(aq)} + 4\ H_2O_{(l)} \rightarrow Ag_{(s)} + B(OH)_4^{-}{}_{(aq)} + 3.5\ H_{2(g)} + H^{+}_{(aq)} \quad (1.1)$$

$$BH_4^{-}{}_{(aq)} + 4\ H_2O_{(l)} \rightarrow B(OH)_4^{-}{}_{(aq)} + 4\ H_{2(g)} \quad (1.2)$$

After the metal ions are reduced, the metal atoms have a strong tendency to form clusters in order to reduce their high surface energies. In Ag NP synthesis, excess BH_4^- has been shown to protect the surface of the nascent clusters via electrostatic interactions with the surface.[83] However, this stabilization mechanism is only temporary, as the BH_4^- decomposes spontaneously in water (Eqn. 1.2). Thus, protecting ligands are most often employed to prevent the aggregation and excessive growth of the clusters by interacting with the NP surfaces. The interaction between the ligand and surface can be strong chemical bonding or weaker electrostatic bonding, and typically defines strong ligands or weak ligands, respectively. Some examples of strong and weak protecting ligands used in this work will be further discussed in the following section.

1.3.1 NP Surface Protection

NPs have high surface energies as a result of their small size and have a tendency to aggregate while in solution in order to reduce those energies. To address this, protecting ligands are introduced to the solution to self-assemble onto the NP surface and prevent further growth. Protecting ligands are an extremely important part of metal NP synthesis as they determine their morphological features such as size and shape, which in turn have an effect on their physicochemical properties.

Some of the most common ligands used to protect metal NPs are thiolates (RS-, where R denotes an alkyl group), because strong bonding between S and metal can yield highly stable and uniformly sized NPs.[84–88] It is widely accepted that thiolate ligands are

generated from the spontaneous reaction of thiols (RSH) with metals to form a thiolate-metal bond following dissociation of H:[88,89]

$$R\text{-}S\text{-}H + M^0 \rightarrow R\text{-}S^-\text{-}M^+\text{-}M^0 + \tfrac{1}{2}\, H_{2(g)} \quad (1.3)$$

In particular for Ag NPs, thiolate ligand formation has also been demonstrated to involve oxygen, leading to the reaction:[90]

$$2\ R\text{-}S\text{-}H_{(aq)} + 2\ Ag_{(s)} + O_{2(g)} \rightarrow 2\ R\text{-}S\text{-}Ag_{(aq)} + 2\ H_2O_{(l)} \quad (1.4)$$

The general affinity of S toward noble metals also means that a variety of organosulfur molecules can be used to stabilize NPs.[10,71,88] For example, dialkyl sulfides (RSR), proteins, amino acids, and some thiol substituted polymers have also been used to protect noble metal NPs.[4,10,37,58,71,88,91–95] The various organosulfur molecules used as protecting ligands in this thesis are shown in Figure 1.1.

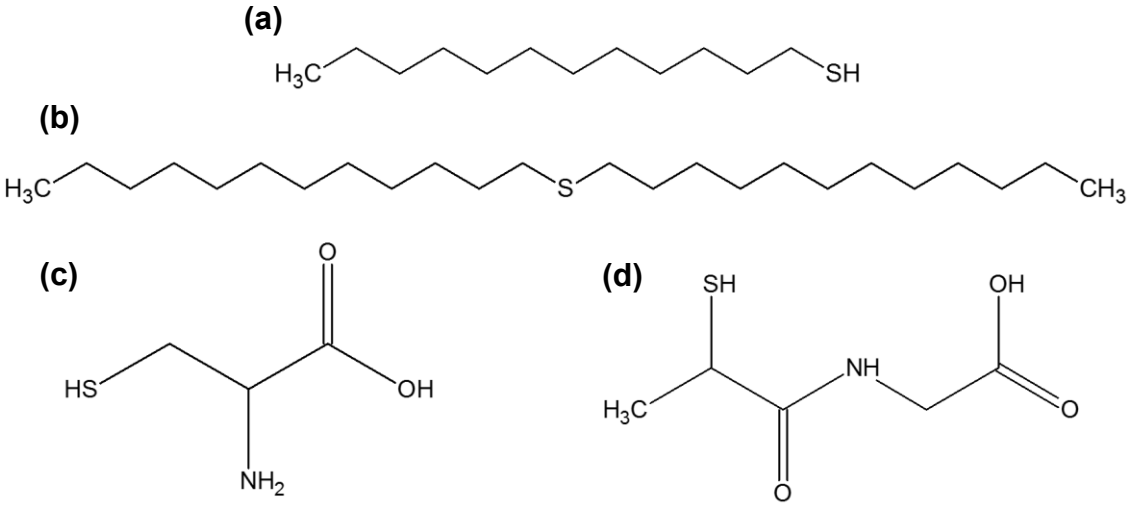

Figure 1.1. Organosulfur molecules used in the preparation of metal NPs (a) 1-dodecanethiol (b) didodecyl sulfide (c) cysteine (d) 2-mercaptopropionylglycine (tiopronin).

The nature of the thiolate-metal bonding in metal NPs has been the subject of intense study in recent years, particularly for Au and Ag. In general, thiolate adsorption

onto metal NP surfaces has shown to result in significant charge transfer between metal and S.[96,97] For Au-thiolate bonding, S donates lone pair electrons to Au s-orbitals, followed by back-donation of electrons from Au d-orbitals to S d-orbitals.[98,99] This donation/back-donation mechanism leads to the strong bonding of the Au-S, and is thought to contribute, along with aurophilic bonding, to the generation of unique "staple" surface structures (-RS-Au-SR-) observed for some Au NCs.[98,100] The discovery of the "staple" structures of Au NCs has led to an improved understanding of the nature of their Au-S bonding and, by extension, their unique physicochemical properties.

On the other hand, the nature of Ag-S bonding in thiolate-protected NCs/NPs seems to be slightly different from that of Au-S. For example, the net charge transfer between Ag and S has been predicted to be greater than Au and S,[101,102] which may alter the above-described donation/back-donation mechanism and lead to different surface bonding in Ag NCs (or NPs). Indeed, reports of thiolate-protected Ag NCs/NPs generally reveal very different surface structures compared to thiolate-protected Au NPs/NCs. In some cases, thiolate-protected Ag NCs/NPs have exhibited reconstructed surfaces consisting of more sulfidized Ag components, such as Ag_2S_5 structures on top of metal Ag cores,[84,103] or even more heavily sulfidized NC/NP surfaces.[58,75,104–106]

The surface sulfidation of Ag NCs/NPs compared to those of Au appears to be similar to the case of their bulk forms. That is, unlike Au, Ag has a higher propensity to become more sulfidized, and can readily undergo various sulfidation reactions (*e.g.,* Ag jewelry "tarnishing"), including the following: [107]

$$4\ Ag_{(s)} + 2\ S^{2-}_{(aq)} + O_{2(g)} + 2\ H_2O_{(l)} \rightarrow 2\ Ag_2S_{(s)} + 4\ OH^-_{(aq)} \qquad (1.5)$$

Sulfidation of Ag can result in a thermodynamically stable structure of Ag sulfide (Ag_2S, typically the acanthite form) which can grow into the bulk until all the Ag is converted

into Ag_2S.[108] This mechanism has been observed in Ag NP systems with external sources of inorganic sulfide (*e.g.,* sodium sulfide, hydrogen sulfide, *etc.*) which provide the S^{2-} required for the reaction in Equation 1.4.[109–111] Furthermore, the ability of organosulfur molecules (*e.g.,* thiols) to induce sulfidation at Ag NP surfaces has also been demonstrated.[58,75,104–106] In these cases, the S^{2-} is most likely provided after the cleavage of S-C bonds as a result of S-Ag bonding and subsequent electron displacement.[112–114] This sulfidation effect is further discussed in Chapters 2, 3, and 4 which examine the effect of various organosulfur ligands on the surface structure of Ag NPs/NCs.

As previously discussed, the S of thiolates bond strongly with metal NP surfaces to prevent aggregation. However, there are many other ligand types which depend on weaker interactions to the surface of the metal NPs. For example, NPs prepared with the common Turkevich method depend on weak stabilization through the carboxylate anions of citrate molecules.[68,115] Compared to thiolates, it is generally accepted that citrate is considered to be weak ligand, by virtue of its lower binding strength to NPs. These weaker interactions typically result in larger sizes of NPs, however, it should be noted that this general technique can provide NPs with a range of sizes and shapes by modifying the reaction conditions such as ligand:metal ratios, temperature, and pH.[70,116] Therefore, although these types of ligands weakly interact with the NP surface, they can provide the necessary stability to prevent aggregation, even for smaller NPs (*e.g.,* < 5 nm).[117]

Surfactants are another class of weak protecting ligand that can form micelle structures in solution to subsequently control size and shape.[118] Common examples are tetraoctylammonium bromide (TOAB), tetraoctylphosphonium bromide (TOPB), and cetyltrimethylammonium bromide/chloride (CTAB/CTAC)[119] (Figure 1.2). These types

of ligands usually rely on halides (*e.g.,* Br^- or Cl^-) to both protect the NP surface and interact with their respective cationic group (*e.g.,* ammonium or phosphonium). Some surfactants have been demonstrated to be highly influential on the shape of NPs, as they show preferential binding to certain facets, which in turn causes growth on other facets, leading to specific shapes.[120]

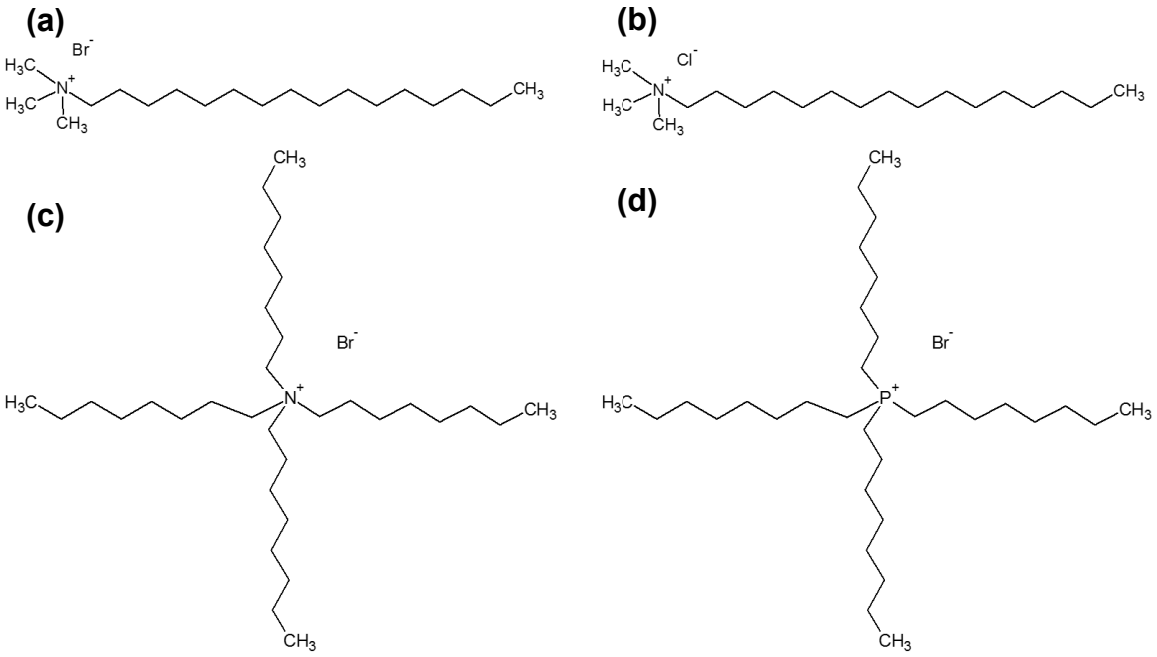

Figure 1.2. Surfactant molecules used in the preparation of metal NPs. (a) cetyltrimethylammonium bromide (CTAB) (b) cetyltrimethylammonium chloride (CTAC) (c) tetraoctylammonium bromide (TOAB) (d) (tetraoctylphosphonium bromide (TOPB).

Polymers are another class of ligand that provide significant stabilization largely by their steric bulk, preventing agglomeration by multiple interactions from polymer side groups. Polymers can also be tailored to have different molecular weights and side groups in order to provide control over the NPs. For instance, polyethylene glycol (Figure 1.3a) has been used to make various metal NPs, and can be modified to provide various substituent groups. Polyvinylpyrrolidone (PVP, Figure 1.3b) is another example of a

common polymer used for metal NP stabilization, and provides stability through coordination of amido groups to the metal surface.[121,122] In addition to providing facile synthetic routes to monometallic Ag NPs, various methods utilizing PVP have also resulted in uniquely shaped Ag NPs, such as nanoprisms, nanocubes, and nanorods, as well as bimetallic NPs.[123–125]

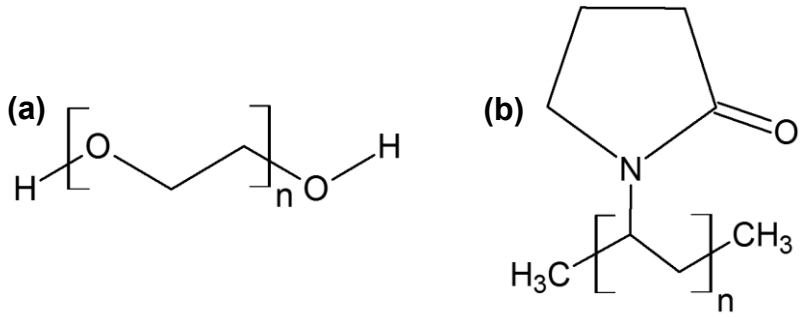

Figure 1.3. Polymers used in the preparation of metal NPs. (a) Polyethylene glycol (PEG) (b) Polyvinylpyrrolidone (PVP).

1.3.2 Bimetallic NPs

The synthesis of bimetallic NPs can be accomplished using many of the methods used to produce monometallic NPs; the main difference is that the methods include the use of two metals. Bimetallic NPs are especially interesting in that they can potentially provide physicochemical properties of each metal within the NP. For example, the optical properties of bimetallic AgAu NPs can change depending on the concentration of their constituent metals.[123] The catalytic properties of bimetallic NPs can also be enhanced; for example, Au-core/Ag-shell NPs have demonstrated a higher catalytic activity than their monometallic counterparts.[126] Antibacterial properties of AgAu NPs have also been shown to be controlled by alloying, and in some cases were reported to be more effective than pure Ag NPs.[127] Common to bimetallic particles is that their properties are largely dependent on the atomic arrangement, or morphology, of the metals within the NPs.

There are many different types of morphologies that bimetallic NPs can adopt, but the most common are random alloy, core-shell, and cluster-on-cluster (Figure 1.4).[128] The random alloy morphology describes NPs that have metals randomly distributed throughout the NP. The core-shell morphology describes NPs that have one type of metal in the core and one type of metal in the shell. The cluster-on-cluster morphology describes NPs that have small groups (or "islands") of a second atom type that are clustered together. All of these morphologies have the potential to change the physicochemical properties of the NPs and their morphologies depend on the synthetic conditions used. Like monometallic NPs, the most common synthetic techniques for bimetallic NPs are based on chemical reduction in solution where the metals are either co-reduced,[21,128,129] or sequentially reduced.[56,128–130]

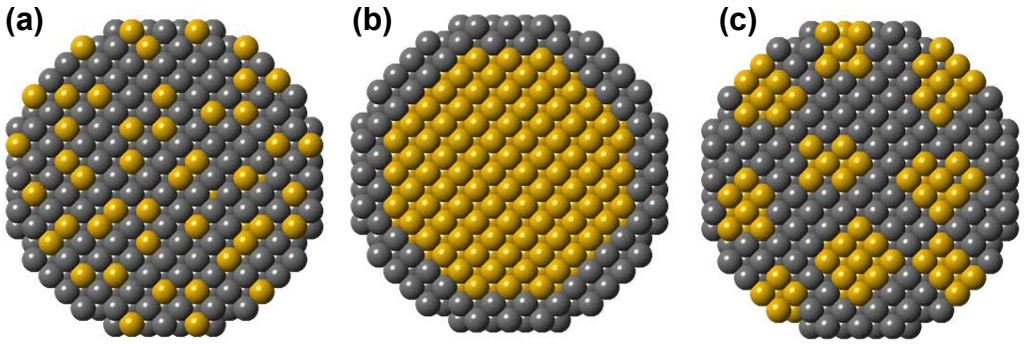

Figure 1.4. Common bimetallic NP morphologies. (a) random alloy, (b) core-shell, and (c) cluster-on-cluster.

The co-reduction of bimetallic NPs describes the simultaneous reduction of the metal ions in solution. Using this technique, the molar ratio of the metal precursor ions are controlled, which typically leads to final metal concentrations of the same ratio. The co-reduction method has been shown to lead to random alloy[21] and core-shell

morphologies.[129] The most commonly controlled experimental factors in the preparation of bimetallic NPs using the co-reduction method are the metals and protective ligands. Depending on the type of metals used, the resulting atomic structure of the NPs can vary dramatically. For example, if the reduction rate of one metal is greater than the other, that metal will typically form the core of an NP, to which the other metal will reduce onto, thus leading to a core-shell type morphology.[128,129] Conversely, if they have similar reduction rates, then the metal ions will most likely be reduced simultaneously, leading to random-alloyed NPs.[128,129] Furthermore, the protecting ligand can have an effect on the co-reduction process by altering the availability of one metal if that ligand has a greater affinity for that metal over the other. Typically, the metal to which the ligand prefers to bind with will end up on the outside of the NPs, while the other metal will end up in the core of the NP.[128,129] However, the initial interaction of the metal ions and the ligands can also affect the reduction potentials of the metals, leading to a variation in their reduction rates, and thus potentially changing their atomic structure.

Sequential reduction begins with the formation of NPs of one type of metal, commonly referred to as "seeds". The NP seeds are used to provide a surface onto which the second metal is reduced, typically resulting in core-shell morphologies.[128,129] This technique has been used to prepare a variety of bimetallic NPs containing metals such as Pt, Cu, Ag, Au, Fe, among others.[128,129] After the initial seed NPs are formed, the reduction of the second metal is commonly carried out by either a galvanic reaction between the two metals, or by a secondary reducing agent.[128,129] In the case of galvanic reduction, a second metal with a higher reduction potential is added; therefore, in theory many different combinations of bimetallic NPs can be created by this technique. For example, since the reduction potential of $AuCl^{4-}$/Au (0.99 V) is higher than that of

Ag^{+}/Ag (0.80), Au^{3+} can be reduced to Au in the presence of Ag according to the following reaction:

$$3\ Ag_{(s)} + AuCl_4^-{}_{(aq)} \rightarrow Au_{(s)} + 3\ Ag^+_{(aq)} + 4\ Cl^-_{(aq)} \quad (1.6)$$

This leads to the replacement of Ag atoms from the seed NPs with Au atoms, and this technique has been employed to produce bimetallic AgAu NPs with random alloy[130] and core-shell type structures.[56]

The second sequential reduction is also commonly carried with another reducing agent. Usually, a weaker reducing agent is used for the second reduction in order to promote the deposition of the second metal onto the seed NPs, and avoid the formation of two sets of monometallic NPs. The driving force for the deposition of the second metal can be attributed to its preferential reduction by the weaker reducing agent and the higher surface energy of the NPs, where the energy required for reduction is reduced.[128,129] Furthermore, this type of synthesis is versatile, and can be used to deposit metals which have higher reduction potentials than the seed NPs (including Au on Ag),[131] as well as the reverse deposition of metals with higher oxidation potentials such as Ag onto Au seed NPs.[126,132,133] This is possible because of the process of underpotential deposition (UPD) occurs, which has been typically defined as the deposition of one metal onto another metal substrate at potentials less negative than for bulk deposition.[134–136]

The UPD process has been well-studied for bulk surfaces and, more recently, has been shown to be a critical process in the preparation of metal monolayers on metal NPs.[120,136,137] The UPD process results in monolayer deposition because the binding energy of the substrate-metal is larger than that of the metal-metal.[135] During UPD, the deposited metal forms epitaxially and adopts the ordering of the underlying surface. Theoretical modelling of Ag adsorption on Au NPs shows that preferential deposition

occurs on the {111} or {100} surfaces of Au,[138] but this can also be controlled by experimental conditions. For example, UPD has been exploited in the growth of various anisotropic Au NPs, where small amounts of Ag were added to growth solutions of $HAuCl_4$, resulting in the deposition of Ag monolayers onto the Au NPs which controlled further growth.[120] It was found that by varying the amount of Ag in the growth solution, specific deposition was promoted by facet-specific stabilization and, as a result the shape of the NPs was modified.[120] Halogen-based surfactants play an important role in the surface protection and UPD process, and work synergistically with Ag to stabilize the specific facets on the Au NPs.[139] These types of NPs were the subject of a surface structural characterization study and will be discussed further in Chapter 6.

1.4 Characterization Techniques

The physicochemical properties of NPs are largely dictated by their size, shape, composition, and surface structure. Therefore, in principle, the specific tailoring or rational design of their properties is achievable through modification of these aspects. Designing tailored NPs, however, is predicated on the ability of those aspects to be characterized. This has presented many challenges, and often major developments in the study of metal NPs are correlated with the invention or refinement of characterization technologies. For example, electron microscopy techniques, such as transmission electron microscopy (TEM), scanning electron microscopy (SEM), and high resolution-TEM (HRTEM) allowed many of the first characterizations of metal NPs, such as size distributions, morphologies, and crystalline structures.[140] UV-visible spectroscopy (UV-vis) is another useful technique that can be used to gain supporting information on NP size, composition, and structure.[11,17,20,21] Electron diffraction (ED), X-ray diffraction

(XRD), and X-ray photoelectron spectroscopy (XPS) are techniques that can all yield information about NP composition and oxidation state.[141] In addition, ^{1}H and ^{13}C nuclear magnetic resonance (NMR) spectroscopy, Fourier-transformed infrared (FTIR) spectroscopy, and Raman spectroscopy are all techniques that can be used to study the NPs from the perspective of the ligands bound to NPs.[141] Most recently, extended X-ray absorption fine structure (EXAFS) and X-ray absorption near edge structure (XANES) spectroscopy are techniques that have become very popular in the characterization of metal NPs;[141] this is due to their ability to probe the oxidation state and chemical environment of each constituent element, thus providing a comprehensive understanding of NP structure and composition from both the metal and ligand perspectives. Overall, there are a multitude of characterization techniques available to study metal NPs but the main tools chosen for use in the work of this thesis were UV-vis, TEM, EXAFS, and XANES. Thus, the following sections provide background information regarding those techniques.

1.4.1 Electron Microscopy

Electron microscopy techniques are useful in the study of nanomaterials as they allow direct visualization, thereby providing information regarding size, shape, and morphology. The most common type used is TEM because it can study many different types of samples, including cells, microorganisms, and inorganic materials (*e.g.,* nanomaterials).[140,142] When TEM is performed, high-energy electrons are passed through the sample material, and the absorption or scattering of those electrons is detected to produce an image on a camera.[142] Dark-field TEM produces images that show the sample as a bright spot, which is a function of greater scattering of electrons by the sample, while

the background appears dark. On the other hand, bright-field TEM produces images that show the sample as a dark spot due to absorbance of the electrons from the interaction with the sample, while the background is lighter. Furthermore, the atomic number of the sample being observed is correlated to the darkness of the resulting spot.[142] In this way, heavier elements like metals are detected as darker spots, while the lighter elements like carbon are usually not observed. To view metal NPs by TEM, the sample must be thin enough for electrons to pass through. Therefore, NPs are usually dispersed onto a semi-transparent grid and allowed to dry. This allows the NPs to spread out along the grids, which enables more electrons to pass through resulting in greater image quality. After the images are recorded, computer software such as ImageJ can be used to measure the size distribution and shape of the NPs.[143] Figure 1.5 shows a TEM image of Ag NPs, which appear dark due to their higher atomic number than the carbon-coated grid.

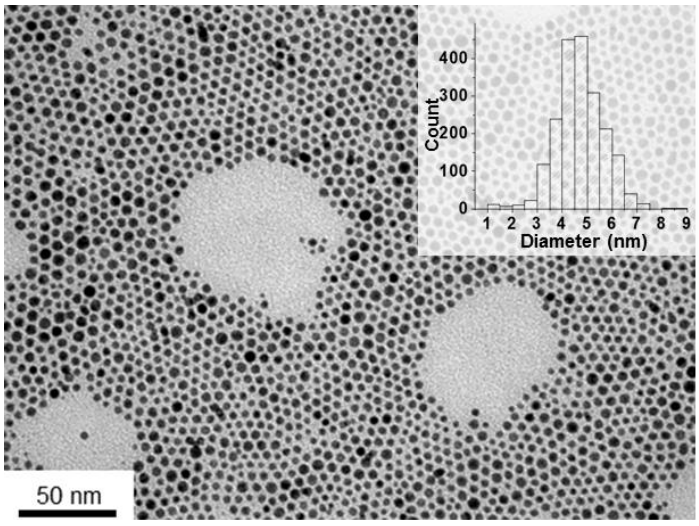

Figure 1.5. TEM of metal NPs. The image shows the dark contrast of Ag NPs which allows their morphology and size distribution (inset figure) to be assessed. Reprinted with permission from Padmos et al.[75]

Although TEM is commonly used to characterize nanomaterials, there are still inherent limitations to the technique. The samples must be dried and then examined under high vacuum; therefore, information regarding their solvated state cannot be obtained. Most importantly, TEM images are localized to the region of view currently being analyzed; that is, the images do not characterize the entire sample, but reveal only one particular region. Although the images captured by TEM are usually representative of the entire sample, it is important to use other complementary techniques. For example, UV-vis and XAS allow for a more global perspective, since a larger portion of the sample may be examined simultaneously.

1.4.2 UV-visible Spectroscopy (UV-vis)

UV-vis is a useful tool in the characterization of noble metal NPs because some metals at the nanoscale, such as Au and Ag, exhibit characteristic surface plasmon resonance (SPR) bands in the visible light region of the electromagnetic spectrum. SPR is an effect derived from a collective oscillation of electrons near the surface of nanomaterials, as a result of induced dipoles from incoming electromagnetic waves.[11,12] Figure 1.6 schematically illustrates how a surface plasmon oscillation is generated in a spherical metal NP, as well as the resulting SPR peak of Ag NPs. When a NP interacts with a wavelength of light longer than its diameter, its free electrons are polarized and a relative charge difference is created at the NP surface.[11,12] Coulombic forces then compensate for this difference and induce electron oscillations that resonate with the frequency of the incoming light.[11,12] This resonance occurs at the surface of the metal and is dependent on its size, shape, composition, and surface structure, as well as the dielectric properties of the surrounding medium.[11,12]

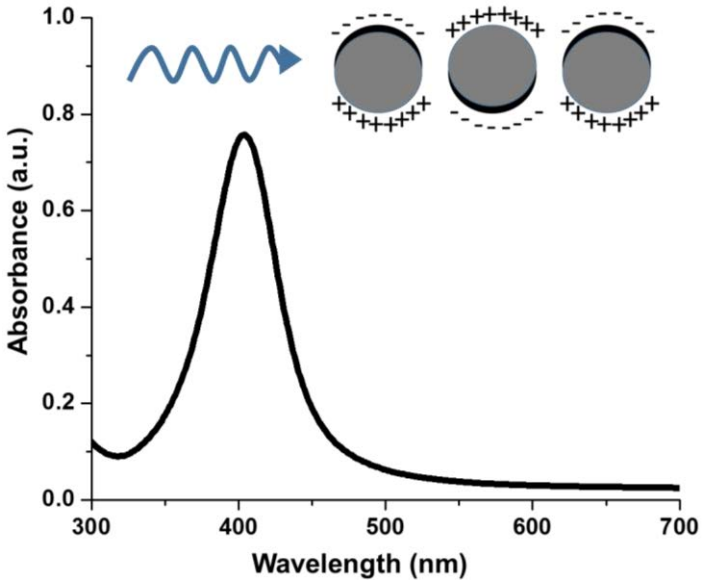

Figure 1.6. Surface plasmon resonance (SPR) of metal NPs generated from electron oscillations at the surface of the NPs.

Most importantly, the profile of the SPR peaks of NPs can be used to help deduce corresponding morphological features. For example, spherical Ag and Au NPs show a distinct SPR peak at around 400-450 and 520-550 nm, respectively.[11,12,20,21] Those SPR peaks are dependent on the size of the NPs, and generally show a blue-shift in peak position with decreasing size.[144] In addition, the width of the SPR band is also indicative of the size distribution of NPs within a sample, with a sharp peak denoting that the NPs have a narrow size distribution (*i.e.,* they are monodisperse), while a broad peak denotes a sample with a broad size distribution of NPs (*i.e.,* they are polydisperse).[145] The profile of the SPR peak can also partly describe both the shape and atomic structure of the NPs. For spherical NPs, there will be only one direction of polarization, resulting in one SPR peak. However, if the particle is multi-dimensional, such as in a nanorod, there will be both longitudinal and transverse polarizations, and thus two SPR peaks will be present in its spectrum.[17]

UV-vis can also be especially useful when studying bimetallic systems such as AgAu NPs, as both metals have distinct SPR features. Taking the case of sequential reduction of Au onto Ag NPs (Figure 1.7),[123] the analysis of the resulting SPR bands can be used to help deduce the atomic structure of the NPs. In this way, as Au is added to the Ag NPs, the SPR band of the resulting particles will generally shift to increasing wavelengths and approach the typical SPR of Au NPs around 520 nm.[12,21] The profile of the SPR band can also be used to indicate the morphology of bimetallic NPs (*e.g.*, random alloy or core-shell structures).[11,12,20,21] If the NPs formed have an alloy-type structure, then only one SPR band will occur, with the peak position showing a linear dependence on the concentration of Au.[12,21] On the other hand, if there are two SPR peaks, then there exists the possibility of either individual monometallic NPs of each metal, or of core-shell NPs.[11,12,20,21]

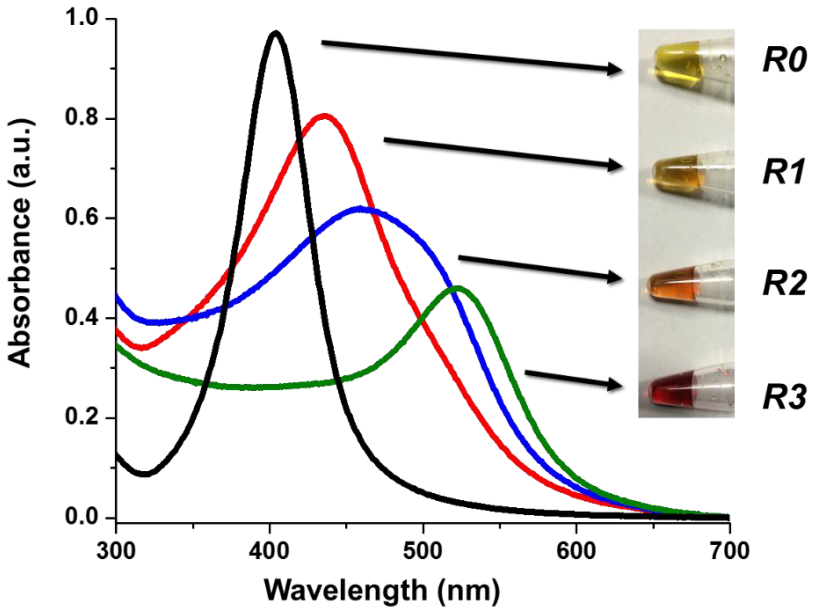

Figure 1.7. UV-vis spectra of bimetallic AgAu NPs. The spectra show the change in SPR peak position with increasing Au additions (R0-R3), along with the corresponding change in solution colour (inset). Reproduced with permission from Padmos et al.[56]

Since SPR effects are usually localized to the NP surface, they can be significantly affected by surface chemistry. For example, changing the dielectric constant of the surrounding material will affect the SPR oscillation frequency, due to the changed ability of the surface to accommodate electron charge density from the NPs.[12] The type of protecting ligand will have an even more significant effect on the SPR of metal NPs, as strong ligands such as thiolates can alter the electron density of the NP surface, and cause the SPR peak position to shift compared to NPs with weaker ligands.[12,146,147] Further to the effect of surface structure, the generation of sulfide on the surface of Ag NPs has been recognized to dampen and shift SPR peaks to longer wavelengths.[148]

Based on the dependence of SPR on size, shape, composition, and surface chemistry, UV-vis is certainly a useful tool for characterizing metal NPs. However, the SPR profiles of NPs cannot always be unequivocally correlated to their structure. For example, in bimetallic AgAu NPs, the SPR of both metals can be visible if they are in a core-shell arrangement, although depending on the concentration of each in the NPs (or thickness of the core/shell), the two SPR peaks can appear as one broad peak, which is similar to what is observed for a random-alloy structure.[123] In addition, while the SPR wavelength generally correlates with the size of NPs, thiolate ligands can cause SPR shifts toward longer wavelengths and can therefore convolute size characterization.[12,75,146,147] It is for these reasons that UV-vis is rarely the sole characterization tool used to study NP systems, but is primarily used to complement other techniques and provide more comprehensive information.

1.5 X-Ray Absorption Spectroscopy (XAS)

Characterization techniques such as UV-vis and TEM are important in studying nanomaterials, but cannot be used to obtain detailed information about local atomic structure or electronic properties. This depth of characterization is an ongoing challenge in the study of nanomaterials, as the long range order required for traditional structural characterization methods (*e.g.*, X-ray crystallography) is often limited in these materials. Towards addressing this challenge, XAS is a tool that can be used to study nanomaterial systems in either solid or amorphous phases (including liquids) and can provide rich information about their local environments.[149–152] XAS is now being routinely used throughout a wide range of scientific fields, including chemistry, biology, environmental science, and materials science.

XAS measures X-ray absorption by core-level electrons in atoms of the material being examined.[149–152] In this manner, X-rays are transmitted through a material and if they possess energy equal to the binding energy of a core-electron they will be absorbed, resulting in the promotion of core-electrons to unoccupied or continuum states.[149–152] At energies greater than the binding energy, core-electrons are emitted as photoelectrons with kinetic energies dependent on the difference in energy between the incident X-ray and core-electron.[149–152] As a consequence of the absorption, the amount of X-rays transmitted through a material will be subsequently decreased; this decrease can be quantified by measuring the intensity of the X-rays transmitted (I_t) relative to their initial intensity (I_o). The degree to which a material absorbs X-rays is called the absorption coefficient, $\mu(E)$, and can be derived from X-ray transmission using the equation:

$$\mu(E) = \log (I_o/I_t) \tag{1.7}$$

In addition, $\mu(E)$ can also be derived from the X-ray fluorescence following the generation of a core-hole by the excitation of a core-electron. This core-hole is then filled by another electron in the atom and the decay of the excited state releases an X-ray with energy characteristic of the initially excited core-electron. Therefore, $\mu(E)$ can also be obtained from X-ray florescence by the relationship:

$$\mu(E) \propto (I_f/I_o) \tag{1.8}$$

where I_f is the fluorescence intensity resulting from the X-ray absorption at that specific energy.

Regardless of local environment, all atoms have an intrinsic absorption coefficient ($\mu_o(E)$), which is dependent on atomic number, atomic mass, and the incident X-ray energy.[151] When plotted against energy, a smooth function with a stepped increase at a specific energy is observed. The specific energy at which this step occurs is often referred to as the absorption edge (or "white line" for historical reasons), and coincides with the binding energy of the core-electron being excited.[149–152] Because electron binding energies for each element are unique, absorption edges are also unique to each element.[149–152] Therefore, XAS is an element-specific technique as the X-rays can be tuned to the different energies required for promoting core-electrons within different elements. This is especially useful for studying metal-ligand systems in metal NPs, as both metal and ligand perspectives can be used acquire information about the NPs. In addition, the energy of the X-rays can also be tuned to excite specific core-electrons (*e.g.,* K, L_1, L_2, L_3, M_1, *etc.*) within the element of interest. For example, the two most studied absorption edges for the NPs described herein are the K- and the L_3-edges, corresponding to core-electron transitions from 1s to valence p-orbitals and 2p to valence d-orbitals, respectively.

The general goal of XAS is to measure the effective absorption coefficient ($\mu(E)$) of the element being probed as a function of the X-ray energy. This value changes as the absorption behaviour of the element is influenced by the interaction with its local environment. In this sense, $\mu(E)$ is measured near and above the absorption edge of the element under study and results in a spectrum similar that shown in Figure 1.8. A complete XAS spectrum can be described by two main regions, the first being X-ray absorption near-edge structure (XANES) and the second being extended X-ray absorption fine structure (EXAFS). The XANES and EXAFS regions can yield specific information relative to the absorbing atom and will be described in the following sections.

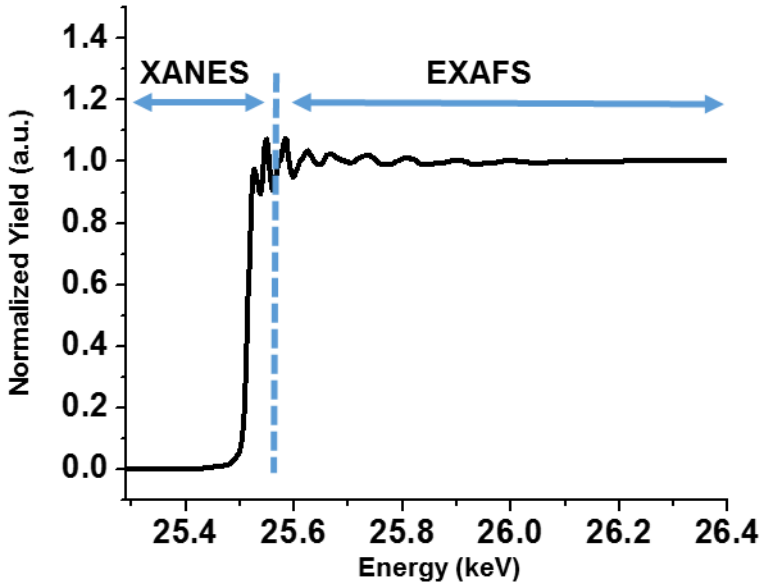

Figure 1.8. Ag K-edge XAS spectrum showing XANES and EXAFS regions.

1.5.1 X-ray Absorption Near-Edge Structure (XANES)

The XANES region of an XAS spectrum typically ranges from ± 30 eV from the absorption edge and can be subdivided into the pre-edge, absorption edge, and post-edge (Figure 1.9a). The most intense region of a XANES spectrum is the absorption edge, which arises as a result of electronic transitions from occupied to unoccupied states.

However, electronic transitions can also occur at energies lower than the absorption edge due to orbital hybridization induced by coordinating species, resulting in their appearance in the pre-edge region.[153] These pre-edge features are not typically seen in the metal K-edge and L_3-edge XANES spectra of Ag and Au NPs; however, some ligand K-edge XANES spectra have demonstrated this type of feature. For example, S K-edge XANES of thiolate-protected metal NPs can exhibit a small pre-edge feature that occurs as a result of coordination between S and metal (shown in Figure 1.9b).[75,154]

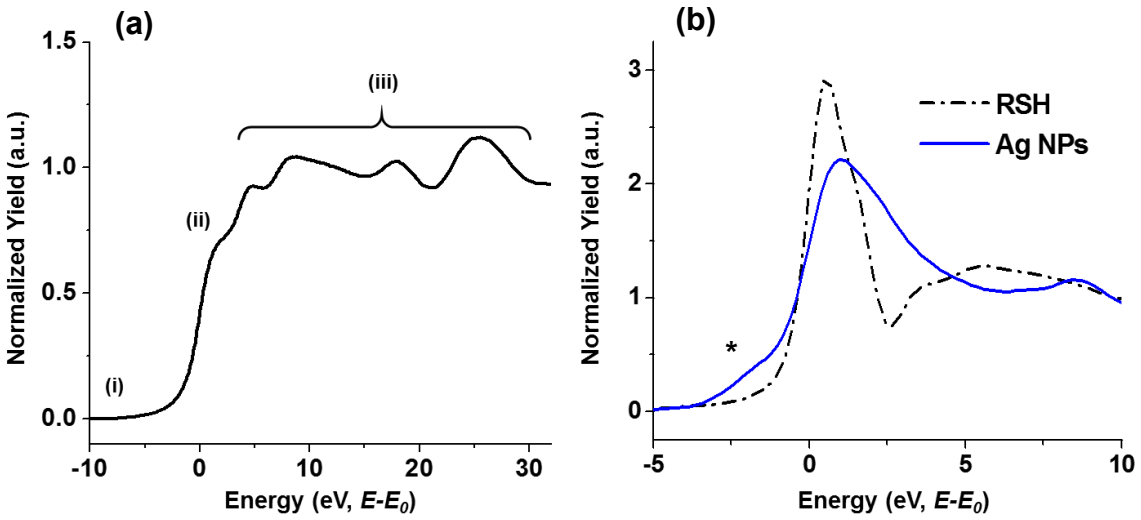

Figure 1.9. XANES spectra (a) Ag L_3-edge XANES spectrum of Ag foil showing the (i) pre-edge (ii) absorption edge and (iii) multiple scattering features. (b) S K-edge XANES spectrum showing the pre-edge feature (*) cause by a metal-thiolate interaction. Reproduced with permission from Padmos et al.[75]

The most identifiable and thus far quantifiable feature of XANES is the absorption edge, which is due to the initial intense decrease of transmitted X-rays as a result of their absorption by the element being examined. This region of XANES can reveal many different aspects of the absorbing atom's local environment, such as oxidation state and ligand interactions.[149–152] This is because the absorption edge correlates to element- and edge-specific electronic transitions, which are sensitive to the atom's effective nuclear

charge (Z_{eff}). Because oxidation state and ligand interaction can change the Z_{eff} of an atom, these properties can be characterized using the XANES absorption edge.[153] For example, the energy required to promote K- and L_3-edge transitions is higher in an oxidized metal because of larger Z_{eff}; therefore, these absorption edges occur at higher energies than the non-oxidized metal. Due to their proximity to the positively charged nucleus, 1s electrons more strongly experience the change in Z_{eff}; therefore, the K-edge XANES absorption peak position has been widely used to determine the oxidation states of various metals.[152,153] Although a similar peak shift can potentially be observed in metal L_3-edge XANES spectra, it is more common to relate the intensity of the L_3-absorption edge to oxidation state, as there is a more direct correlation of its intensity to empty d-orbitals.[96,155,156] Taking Ag as an example, the d-orbitals of Ag bulk metal are completely full (d^{10}) whereas the number of d-electrons in a Ag^+ compound will be less (from s-p-d hybridization); hence, the intensity of the L_3-absorption edge of the Ag^+ compounds will be greater. In reality, the d-electrons in bulk Ag metal and oxidized bulk Ag are slightly less than their nominal configurations (also due to s-p-d hybridization),[96,97,157] but the trend in L_3-edge XANES intensity is observed nonetheless.

The chemical species attached to the absorbing atom can also have an effect on both K- and L_3-edge XANES. For metal-ligand systems that contain electronegative atoms such as S and Cl, a greater metal-ligand covalency occurs; this can result in a lower Z_{eff} and lead to a shift in metal K-edge absorption edge position to lower energies.[153] Since the L_3-absorption edge intensity is related to empty d-orbitals, significant changes in the L_3-absorption edge intensity can be correlated to the chemical species attached to the absorbing atom.[96,155,156] For example, thiolates adsorbed onto transition metals remove electron density from metal d-orbitals, resulting in more electron transitions to empty d-

orbitals and thus a more intense L_3-absorption edge.[97,155] In bimetallic systems such as AgAu alloys, a decrease in the Ag L_3-absorption edge has been attributed to Au d-electron redistribution to Ag orbitals.[156,158]

Furthermore, as a result of their smaller size relative to bulk materials, metal NPs exhibit interesting electronic effects at the absorption edge.[96,97,155,157] For example, as the orbital bands of metal NPs become slightly more quantized because of their smaller size, there is less s-p-d hybridization and less transfer of d-electrons to s- and p-orbitals. Therefore, the intensity of the L_3-absorption edges of metal NPs are slightly increased relative to those of their bulk counterparts.[96,97,155,157]

Finally, the post-edge region of XANES is largely attributed to scattering of photoelectrons between multiple neighbours (*i.e.,* multiple scattering). In this energy region, the kinetic energies of the absorption-induced photoelectrons are low and their mean free paths are large.[159] As a result, the emitted photoelectrons can scatter from multiple atoms and return to the original absorbing atom. These returning photoelectrons then modulate $\mu(E)$ and create the spectral oscillations immediately following the absorption edge. These oscillations provide qualitative information regarding the structure around the absorbing atom, including metal lattice type. For example, the first few oscillations of the Au L_3-edge, as well as the Ag K- and L_3-edges (*e.g.,* feature (iii) in Figure 1.9a), are distinctive of the face-centered cubic (FCC) lattice type of the two metals. The multiple scattering oscillations can also potentially provide quantitative information, although current methods do not offer a comprehensive refinement strategy for multiple scattering within nanomaterials, as the many different scattering paths are hard to accommodate theoretically.[150] Moreover, these multiple scattering features can also be dramatically minimized by the nanosize effect, which makes them harder to

refine. For this reason, the absorption edge remains the most commonly characterized region of the XANES spectra of nanomaterials.

1.5.2 XANES Analysis

Analysis of XANES spectra is most often carried out by qualitative comparison with reference materials. XANES spectra are first calibrated to the absorption edge of the absorbing atom using the inflection point of the absorption edge. The pre-edge and the post-edge regions are then normalized via polynomial fitting and division by the absorption edge intensity.[160,161] By normalizing the spectra in this way, the oxidation states of samples can be compared by examining the intensity of the absorption edge relative to reference materials. Another common method of XANES analysis is to carry out linear combination refinements of the XANES spectrum using appropriate reference spectra.[160,161] This analysis can yield the percentage of each component in the unknown, as well as the overall quality of the refinement. Most often, the references used are spectra from physical samples, however, structural references can potentially be produced using *ab initio* calculations, such as those performed by the FEFF code (further discussed in section 1.5.5).

1.5.3 Extended X-ray Absorption Fine Structure (EXAFS)

The oscillations that begin approximately 30 eV after the absorption represent the EXAFS region. These oscillations are a result of a similar process as the multiple scattering in XANES; however, at higher energies, the mean free path of the emitted photoelectron is limited, and so single scattering is the dominant process. When the emitted photoelectron travels outward, it interacts with the electron density of neighbouring atoms to produce a backscattered photoelectron that travels towards the

original absorbing atom with phase and amplitude that depend on both the incident energy of the X-ray and the atomic number of the neighbouring atoms (Figure 1.10).[151] The oscillations which occur in the EXAFS region are a result of constructive or destructive interference between the original and backscattered photoelectrons. For example, when the backscattered photoelectron is in phase with the original photoelectron, absorption will increase, and thus $\mu(E)$ is increased.[150] Conversely, if the backscattered photoelectron is out of phase with the original photoelectron, absorption (and $\mu(E)$) will decrease. The modulation of $\mu(E)$ as a result of this scattering process is the basis of EXAFS and provides quantitative local structural information regarding the absorbing atom.

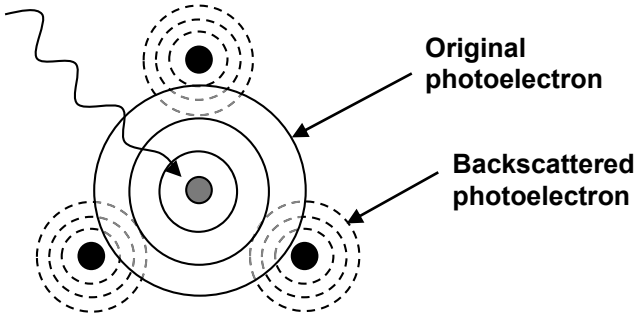

Figure 1.10. X-rays produce photoelectron waves between the neighbouring atoms resulting in oscillations of the EXAFS spectra.

1.5.4 EXAFS Analysis

The analysis of EXAFS can be conducted using many different computer programs, including WinXAS[162] and the IFEFFIT package.[160,161] These programs contain functions that are useful for processing EXAFS spectra, as well as the required functions to refine the EXAFS data to obtain structural information. In order to extract this information from an EXAFS spectrum, it must first be processed to isolate the fine structure, $\chi(E)$, described by the following equation:

$$\chi(E) = \frac{\mu(E) - \mu_O(E)}{\Delta\mu_O(E)} \quad (1.9)$$

where the intrinsic absorption coefficient, $\mu_o(E)$, is represented by a background function and subtracted from the actual absorption coefficient, $\mu(E)$, and then divided by the difference in intensity before and after the edge ($\Delta\mu_o(E)$).[149–152] Isolating $\chi(E)$ is achieved by first fitting pre-edge and post-edge lines to the spectrum (Figure 1.11a), and then normalizing their difference ($\Delta\mu_o(E)$), to be one (Fig 1.11b). The absorption edge energy (E_o) is then identified by finding the inflection point of the spectrum using its first or second derivative. A smooth background curve is then fit to the post-edge to account for the background absorption ($\mu_o(E)$), which is subsequently subtracted from the real absorption ($\mu(E)$), resulting in $\chi(E)$. The EXAFS oscillations in $\chi(E)$ are derived from an interference effect between photoelectron waves, therefore it is often described in terms of the photoelectron wavenumber, k :

$$k = \sqrt{\frac{2m(E-E_0)}{\hbar^2}} \quad (1.10)$$

where E_o is the absorption edge energy, E is the incident photon energy, m is the electron mass of an electron, and $\hbar$ is the reduced Planck's constant.[149–152] The resulting $\chi(k)$ is commonly referred to as the k-space (Figure 1.11c) and is often weighted by multiplying $\chi(k)$ by k^2 or k^3 to account for the natural decay of oscillations with increasing energy or k.[152] The choice of k-weighting depends on the system being examined, as the EXAFS scattering amplitudes are dependent on the X-ray energy and atomic numbers of both the absorbing atoms and neighbouring atoms.[149–152] Furthermore, the frequencies of the oscillations in $\chi(k)$ correlate to neighbouring coordination paths around the absorbing atom which can be isolated via Fourier-transformation. The Fourier-transformed EXAFS

spectrum is commonly referred to as *R*-space (Figure 1.11d), and describes the radial bond distribution around the absorbing atom, where the peaks represent backscattering of identical atoms at approximately the same distance from the absorbing atoms. Compared to *k*-space, the *R*-space is more directly illustrative of the local environment, wherein the intensity and position of the peaks correspond to coordination number and bond lengths, respectively. However, it should be noted that the radial distance is slightly shifted from the actual bond length because of phase shifting.[149] In addition, the choice of *k*-weighting is also reflected in the overall intensity of *R*-space spectra, but the same coordination number and bond length should still be attained from each scattering path.

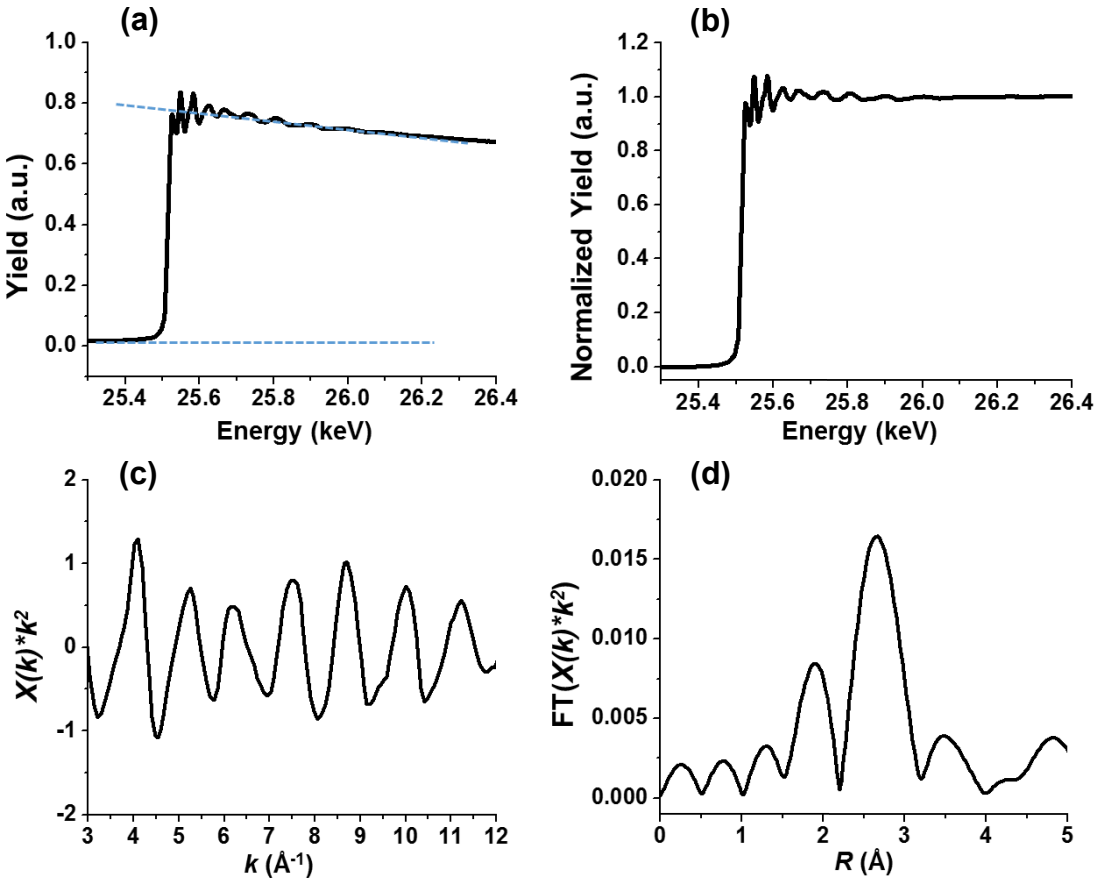

Figure 1.11. EXAFS data refinement. (a)-(b) The pre-edge and post-edge are normalized to a difference of one. (c) The EXAFS is then transformed into *k*-space and weighted appropriately. (d) The *k*-space is then Fourier-transformed to *R*-space.

Local information about the absorbing atom can be extracted by refining the *k*- or *R*-space with the EXAFS equation:

$$\chi(k) = \sum_j \frac{S_0^2 N_j e^{-2k^2\sigma_j^2} e^{\frac{-2R_j}{\lambda(k)}} f_j(k)}{kR_j^2} \sin(2kR_j + \delta(k)) \qquad (1.11)$$

where N is coordination number, R is the bond length, σ^2 is the Debye-Waller coefficient proportional to the root-mean-squared displacement of the scattering atom (which accounts for thermal and vibrational disorder), $\lambda(k)$ is the mean free path of the photoelectron, $f(k)$ is the scattering amplitude of the neighbouring atom, $\delta(k)$ is the scattering phase shift of the neighbouring atom, and j is the coordination shell (also known as path or sphere) of identical atoms at approximately the same distance from the absorbing atom.[149–152] Finally, S_o^2 is the amplitude reduction factor which accounts for intrinsic loss of intensity in the X-ray absorption spectrum.[149–152]

The structural parameters N, R, and σ^2 can be obtained by refining the R-space with the EXAFS equation using a least-squares refinement method. WinXAS[162] or IFEFFIT[160,161] allow the user to fix, constrain, or vary any of the N, R, σ^2, or S_o^2 variables of each scattering path in the system being studied. In addition, the energy-shift parameter, ΔE_o, is included in the refinement to account for phase differences between experimental and theoretical backscattering paths.[163] In order to carry out the refinements, the $f(k)$ and $\delta(k)$ for the neighbouring atoms must be known. These values can be derived from experimental EXAFS spectra of reference materials such as metal foils, but are more commonly generated by *ab initio* simulations of appropriate structural models using the FEFF code,[164,165] described in more detail in section 1.5.5.

Another more recently defined approach to EXAFS analysis is conducted by wavelet-transforming *k*-space data,[166,167] which offers the possibility of obtaining structural information from the absorbing atoms without refinement of the EXAFS using a numerical approach, as described above. While Fourier-transformation of *k*-space leads to radial-space plot of the individual frequencies and intensities of backscattering neighbouring atoms, wavelet-transformation of EXAFS signal yields a plot which shows where the individual frequencies (and their corresponding intensities) originate from in the *k*-space (Figure 1.12).[166] As the region of *k*-space can be correlated with the type of backscattering atom, lighter elements correspond to the low energy *k*-space region, while heavier elements correspond to higher *k*-space region.[166]

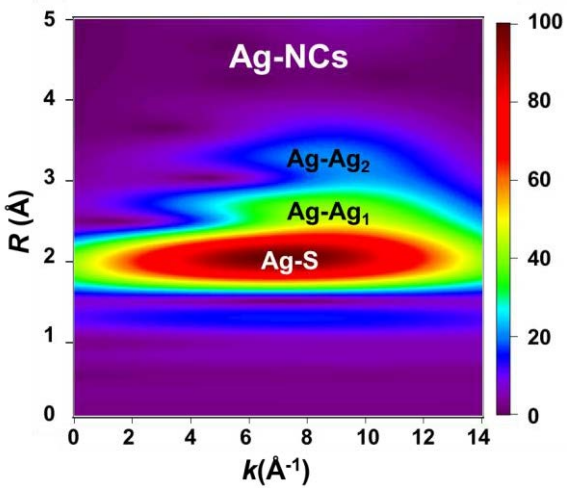

Figure 1.12. Wavelet-transformed EXAFS of Ag NCs showing the bonding paths within the EXAFS. Reproduced with permission from Padmos et al.[105]

1.5.5 *Ab-initio* Calculations Using FEFF

FEFF is an *ab-initio* self-consistent multiple scattering code that uses a Green's function to calculate the backscattering phase amplitudes and phase shifts required for EXAFS *R*-space refinements.[164,165] In order to carry out these calculations, the atomic coordinates of structural models are first obtained from known crystal structures or

generated by programs such as Crystal Maker. Crystal structures can be constructed by using the respective space-groups and symmetry of the material, and by defining the number of atoms in a cluster. Moreover, atomic coordinates can also be provided by other computational methods, such as density functional theory (DFT) structural optimization calculations. The FEFF code then calculates the electronic structure of atoms around the absorbing atom in a specific radius using a relativistic atomic potential approach.[164,165] To reduce computational cost, a muffin-tin approximation is used, wherein the atomic potentials are estimated around an atom to a specific radius, and the potentials between the atoms (interstitial region) are held constant.[164,165] The effective mean-free path, amplitude, and phase for each scattering path are generated from the calculations and used to refine the experimental *R*-space spectra. Within the same calculations, FEFF can also generate simulated EXAFS spectra that can be used for qualitative comparison to experimental spectra. In addition, the FEFF code is able to simulate XANES spectra by calculating the electronic transition energies of an absorbing atom as they change due to interactions with neighbouring atoms.

1.5.6 Synchrotron X-rays

A synchrotron facility can provide high energy X-rays along a continuous energy spectrum, and is therefore often used for XAS experiments (Figure 1.13). Synchrotron radiation is electromagnetic radiation that is emitted by electrons as they are accelerated around a curved path.[168] To achieve this radiation, electrons produced by a linear accelerator are injected into a booster ring where they are further accelerated to near-relativistic speeds.[168] The electrons are then injected into a storage ring where they are propelled by a series of bending magnets, generating the electromagnetic radiation that is

finally delivered to the various beamline stations for use in XAS experiments.[168] Some synchrotrons also have insertion devices, such as wigglers or undulators, placed at various straight parts of the synchrotron to induce acceleration of the electron beam. Wigglers produce a broader electron beam with increased intensity and higher range of X-ray energies than bending magnets.[168] On the other hand, undulators produce a narrower electron beam with a much higher X-ray intensity but with a lower range of energy.[168]

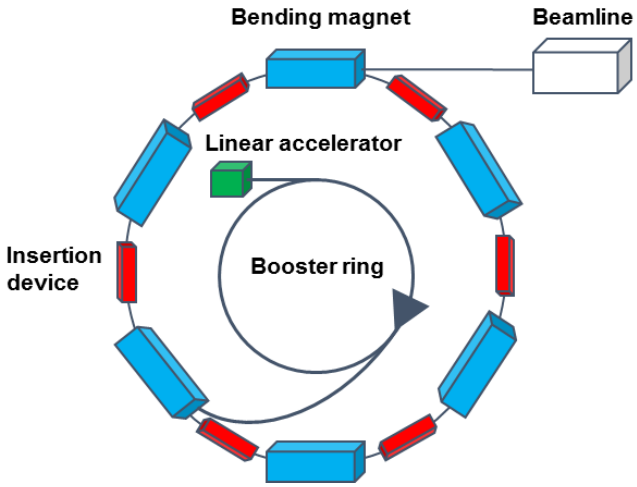

Figure 1.13. A general schematic of a synchrotron facility.

The following synchrotron facilities were used in this work:

1. Canadian Light Source (CLS) Soft X-Ray Microcharacterization (SXRMB/06B1-1) bending-magnet beamline for Ag L_3-edge XANES and S K-edge XANES/EXAFS experiments.[169]
2. CLS Hard X-ray Micro Analysis (HXMA/06ID-1) wiggler beamline for Ag K-edge XANES/EXAFS experiments.[170]
3. Advanced Photon Source (APS) Pacific-Northwest Consortium/X-ray Science Division (PNC/XSD/Sector 20) bending-magnet beamline for Ag K-edge XANES/EXAFS and Au L_3-edge XANES/EXAFS experiments.[171]

1.5.7 Synchrotron XAS Experimental Setup

Various beamlines have different experimental setups, but in most cases, X-ray absorption is measured either directly by transmission or indirectly by fluorescence or electron yield, shown schematically in Figure 1.14.[152] In transmission mode, the incoming intensity (I_o) and transmitted intensity (I_t) are measured by ion chambers and then are used to directly calculate $\mu(E)$ according to Eqn. 1.7.[150,152] In fluorescence mode, the intensity of the characteristic fluorescence of the sample (I_f) is measured, usually by a solid state detector.[150,152] I_o and I_f are then used to calculate $\mu(E)$ according to Eqn. 1.8. For wet-chemically prepared metal NPs, the solvent is often completely removed to yield more concentrated samples (powders), which are easily packed in kapton film and then measured. In these cases, where the element of interest is high in concentration, transmission mode is typically used as it generally leads to a direct measurement of $\mu(E)$.[150,152] On the other hand, fluorescence mode is seldom used in cases where the sample concentration is high, as self-absorption effects can severely reduce fluorescence (and thereby $\mu(E)$).[150,152] Lastly, electron yield mode measures the number of electrons that are lost to the continuum as a result of the absorption process.[150,152] In this technique, either a liquid or powdered sample is placed onto the sample holder. Since the emitted electrons are being measured, both the sample and the sample holder must be sufficiently conductive. In addition, due to the relatively short mean free path of the electrons, electron yield mode is more surface-sensitive and does not suffer from the same self-absorption effects as fluorescence mode.[150,172]

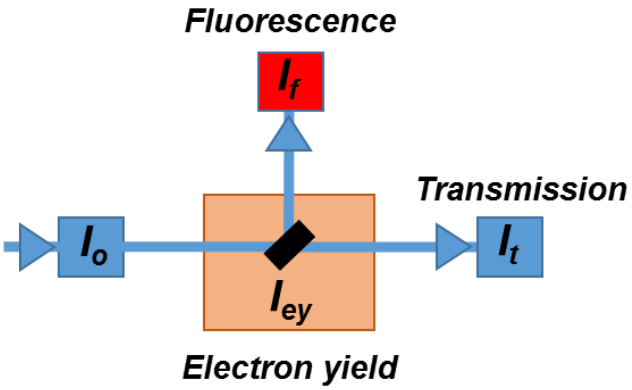

Figure 1.14. A schematic illustrating the various modes of XAS collection.

1.6 Thesis Motivation and Objectives

The rational design of nanomaterials is predicated on the ability to understand the relationships between their structure and properties. Despite the rapid development of Ag NPs and their subsequent implementation in various antibacterial applications, their structure-property relationships are less understood. In fact, there is relatively little information in the literature regarding the surface structure of commonly prepared Ag NPs. This thesis was motivated by the need for a deeper understanding of the structure and surface reactivity of Ag NPs, and thus the following objectives were established:

1. Determine the effects of organic and aqueous organosulfur ligands on the surface structure and antibacterial activities of Ag NPs.

2. Determine the effects of Au alloying on the atomic arrangement, antibacterial activity, and cytotoxic activity in bimetallic AgAu NPs.

3. Determine the surface structure of Ag monolayers on anisotropic Au NPs and understand the influence of structure on shape control.

1.7 Structure of Thesis

Following the introduction, Chapter 2 consists of a study that examined organic-soluble Ag NPs that were stabilized by various organosulfur ligands. The Ag NPs were studied with UV-vis, TEM, and XAS, in order to explore the effect of ligand type and concentration on the resulting surface structures.

Chapter 3 consists of a study that examined water-soluble Ag NPs prepared with thiolate and non-organosulfur based ligands. The Ag NPs were studied with UV-vis, TEM, and XAS in order to assess the differences in their surface structures. The impact of those surface structures on their antibacterial activity against a variety of bacteria was also discussed.

Chapter 4 includes a similar study to Chapter 3, but focussed on thiolate-protected Ag NCs with a unique one-dimensional chain-like assembly. The Ag NCs were characterized with UV-vis, TEM, and XAS. The surface structure of the Ag NCs was determined through wavelet-transformed EXAFS analysis and multi-path Ag K-edge EXAFS refinements. The antibacterial activity of the Ag NCs against various bacteria was also determined.

In Chapter 5, the effect of Au incorporation to Ag NPs was studied in order to characterize the alloying effect of Au on the structure of the resulting AgAu NPs. The NPs were prepared with varying concentrations of Au and Ag and then characterized by UV-vis, TEM, and XAS. Their overall atomic structures were determined and this information was then used to rationalize the bioactivity of the NPs against both bacteria and mammalian cells.

Chapter 6 describes a collaborative study on the surface structures of Ag-coated anisotropic Au NPs with different shapes. A series of Ag-coated Au NPs was examined with XAS in order to deduce their respective surface structures, including the bonding of Cl^- on the Ag monolayers. DFT calculations performed by collaborators were used to support the XAS findings, as well as to examine Cl^- concentration effects on surface structure from a theoretical perspective.

Chapter 7 describes the overall conclusions and potential future work.

Chapter 2 - The Surface Structure of Organosulfur Stabilized Silver Nanoparticles

2.1 Contributions

J.D.P. synthesized the NPs, carried out the general characterization, conducted the XAS experiments, and wrote the manuscript. P.Z. supervised J.D.P. and helped revise the manuscript.

2.2 Foreword

The discovery of the special "staple" bonding interaction between thiolates and Au NPs has enabled the understanding of many of the unique properties of Au NPs. This has generated interest in similar systems, such as thiolate-protected Ag NPs. This chapter focuses on the effect of concentration and type of organosulfur ligand on the surface structure of Ag NPs. In addition, this chapter also develops the fundamental methodology for the analysis of Ag NP surface structure from both ligand and metal perspectives using X-ray absorption spectroscopy.

2.3 Introduction

One of the most common types of metal nanoparticles (NPs) studied are alkylthiolate (in the general form, RS-) protected metal NPs because of their generally high stability and modifiable end groups.[71] Thiolate ligands are also common to studies of self-assembled monolayers (SAMs) and the information gathered from these studies is very analogous to SAMs. Such frequent use of thiolate ligands in the preparation of metal NPs has led to closer investigations of the surface bonding structure between metal and ligand. For example, it was recently determined that surface bonding on thiolate-protected gold nanoclusters (Au NCs) exhibited a "staple" bonding motif (-RS-M-SR-),[100] as opposed to the traditional metal-thiolate bonding (*e.g.*, thiolate on three-fold hollow site of metal surface). This important finding has understandably induced much interest in studying similar systems to determine whether or not they exhibit compositions and other properties that are similar to, or differ from, those of thiolate-protected Au NPs/NCs. For example, Ag NPs can be synthesized in the same way using thiolate ligands, and similar surface structure and composition studies on Ag NPs are a natural progression to understand how thiolate ligands may change the properties of these systems.

Metal NPs have also been prepared using a variety of organosulfur containing protecting ligands other than thiolates, such as dialkyl sulfides (in the general form, RSR).[95,173] Dialkyl sulfides have commonly been used in the preparation of self-assembled monolayers (SAMs)[174–176] and are shown to generally adopt a much weaker bond to the surface of bulk metals. On bulk Au, dialkyl sulfides usually physisorb (~60 kJ/mol), and have about half the bond strength to Au compared to thiolate ligands, which chemisorb (~120 kJ/mol).[176] A similar physisorption bonding of dialkyl sulfides to Au NP

systems has also been demonstrated.[95,173] However, to the best of our knowledge there are limited studies, if any, on dialkyl sulfide-protected Ag NPs. Given the high sensitivity of the NP surface structure to the protecting ligands, this work also examines Ag NPs prepared with didodecyl sulfide (DDS) to ascertain the difference in surface structure and composition of dialkyl sulfide- and thiolate-protected Ag NPs.

Atomic structure determination of these samples with X-ray crystallography is difficult because of the inability to achieve single crystals and therefore, alternative methods of structural determination must be used. X-ray absorption spectroscopy (XAS) is a powerful tool that can provide valuable information about the local structure and electronic properties of MNPs with different morphologies, surface chemistries, and composition.[149–152] For example, extended X-ray absorption fine structure (EXAFS) spectroscopy can provide quantitative information on the distance of neighbouring atoms and coordination number and type of neighbouring atoms.[149–152] In addition, L_3-edge X-ray absorption near edge structure (XANES) spectroscopy of noble metals, including Ag, can provide a wealth of information on the average oxidation state, local coordination environment, and electronic structure.[149–152] Furthermore, since XAS is element-specific, the combination of studying MNPs from both the metal and ligand perspective can allow an even more comprehensive determination of composition and bonding structure. There have been many XAS studies on Au NPs protected by thiolate ligands, however, there appears to be a lack of XAS studies on Ag-based thiolate- and dialkyl sulfide-protected NPs, particularly from a multi-core (Ag K- and L_3-edge), multi-element (Ag and S) perspective. Therefore, we comprehensively study thiolate- and dialkyl sulfide-protected Ag NPs with XAS in order to elucidate information regarding the composition and surface structure of the Ag NPs.

2.4 Experimental

2.4.1 Synthesis of Ag NPs

Ag NPs in this study were synthesized using a slightly modified two-phased, Brust-Schiffrin approach.[71] First, 0.05 mmoles of Ag acetate (Aldrich, 98 %) was added to 0.15 mmoles of tetraoctylammonium bromide (TOAB) (Aldrich, 98 %) and then 1-dodecanethiol (DDT) (Aldrich, 98.8 %) or didodecyl sulfide (DDS) (Aldrich, 98.8 %) corresponding to ratios of 6Ag:1DDT, 3Ag:1DDT, 1Ag:1DDT, 1Ag:1DDS or 1Ag:3DDS was added. Then, 25 mL of toluene was added to the mixture and sonicated briefly until the solids were dissolved. The solution was then mixed with a magnetic stirrer and added to 0.5 mmoles of sodium borohydride ($NaBH_4$) (Aldrich, 99 %) in 5 mL of toluene. Finally, 20 μL of ultrapure water (18.2 MΩcm) was added to initiate the reaction between $NaBH_4$ and the Ag acetate. The mixture was allowed to stir for 2 hours and then transferred into a separatory funnel and shaken. The aqueous phase containing various impurities was discarded and the remaining organic phase was purified further by successive ethanol addition and centrifugation.[177] In this way, the solvent was first removed completely with a Rotovap at a temperature of 30 °C. 20 mL of anhydrous ethanol was then added to the dried samples and then centrifuged at 10,000 *g* to collect the Ag NPs at the bottom of the centrifuge tubes. The remaining ethanol with the excess reagents and impurities was discarded and the sample was dispersed in another 20 mL of ethanol. This process was repeated a total of 3 times and then finally dispersed in toluene as the final product. The purified samples were then stored as solutions in sample vials, sealed by parafilm with argon and refrigerated at 4 °C.

2.4.2 General Characterization

UV-visible spectroscopy was carried out using a Varian Cary 100 Bio UV-visible spectrophotometer. 0.25 mL of each sample was added to 2.75 mL of toluene in a quartz cuvette. Spectra were recorded with the Varian software from 300-700 nm. The solutions were characterized with Transmission Electron Microscopy (TEM) using a Philips Technai-12 TEM operated at 80 kV. Samples were prepared by placing a drop of Ag NP solutions on carbon-coated TEM grids. The films on the TEM grids were allowed to dry at room temperature before analysis. Images were taken with the TEM and later analyzed with the java based program ImageJ.[143] At least 300 particles were counted per image and their size distribution (average diameter) was measured.

2.4.3 X-ray Absorption Spectroscopy (XAS)

XAS experiments at hard X-ray energies were conducted at the Canadian Light Source (HXMA beamline) and the Advanced Photon Source (PNC/XSD beamline). Soft X-ray energy XAS were performed at the Canadian Light Source (SXRMB beamline). Room-temperature Ag K-edge EXAFS experiments were performed at HXMA in transmission mode where the Ag NP solutions were placed in front of the X-ray beam in Teflon sample vials. An XAS spectrum of a reference Ag foil was collected simultaneously for each measurement. Room-temperature Ag L_3-edge XANES and S K-edge EXAFS experiments were carried out at SXRMB in total electron yield mode (TEY). The Ag NP solutions were dropped onto an aluminum plate, allowed to dry, and then attached to a sample holder which sat in the chamber of the SXRMB.

All of the XAS spectra were processed with WinXAS[162] or IFEFFIT[160,161] software packages. Raw Ag K-edge EXAFS data was converted to *k*-space and then

Fourier-transformed to *R*-space using a Hanning function (*k*-range 2.5-12 $Å^{-1}$). *R*-space spectra were refined with the IFEFFIT package[160,161] (*R*-range of 1.5-3.3 Å) with one Ag-Ag path and one Ag-S path, correlated ΔE_o values, and an amplitude reduction factor (S_o^2) of 0.9, determined by the bulk Ag *R*-space refinement. For the S K-edge EXAFS, the *k*-space spectra were Fourier-transformed with a Hanning function (*k*-range 2.5-9 $Å^{-1}$) and refined (*R*-range of 1.3-3.0 Å) with one S-C path and one S-Ag path, correlated ΔE_o values, and an amplitude reduction factor (S_o^2) of 0.65, determined by the bulk Ag_2S *R*-space refinement. *Ab initio* simulations of structural models were generated using the FEFF 8.2 code[164,165] in order to refine the experimental spectra in the *R*-space. The Ag L_3-edge and S K-edge XANES spectra were normalized so that the difference between the pre-edge and post-edge was equal to one, and then normalized to their absorption edge energy (E_o = 0 eV at the absorption edge).

2.5 Results and Discussion

2.5.1 General Characterization

After the addition of the $NaBH_4$ to the toluene solutions containing Ag and DDT/DDS, the solutions immediately turned dark brown, indicating the reduction of Ag^+ to Ag. The DDT protected Ag NPs exhibited average diameters of 4.0 ± 1.0 nm, 3.8 ± 0.9 nm, and 2.6 ± 0.5 nm, for the 6Ag1DDT, 3Ag1DDT, and 1Ag1DDT, respectively.

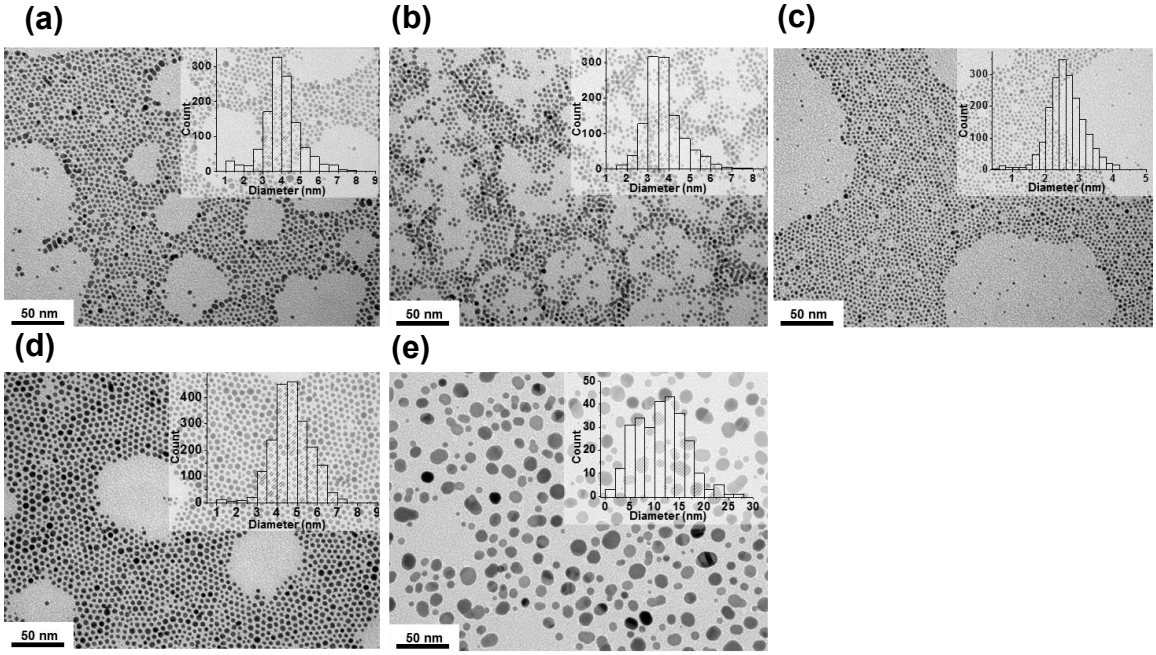

Figure 2.1. TEM images of the DDT- and DDS-Ag NPs. (a) 6Ag1DDT (b) 3Ag1DDT (c) 1Ag1DDT (d) 1Ag3DDS (e) 1Ag1DDS

The purified solutions were examined with UV-vis and showed typical surface plasmon resonance (SPR) peaks of Ag around 425-450 nm (Figure 2.2).[12] It is also noted that the spectra of the unpurified solutions (not shown) contained another absorbance peak around 345 nm which results from Ag^{+}-thiolate[178,179] that is formed between the Ag salt and the DDT. The Ag^{+}-thiolate was removed with purification, as seen by the absence of the peak at 345 nm in the purified samples (Figure 2.2). It was also observed that the SPR peak of the 1Ag1DDT is red-shifted from the 6Ag1DDT SPR peak. This trend is in contrast with the usual blue-shift seen with a decrease in size,[180] which may be due to the greater amount of Ag-S surface bonding in the 1Ag1DDT NPs.[147,181]

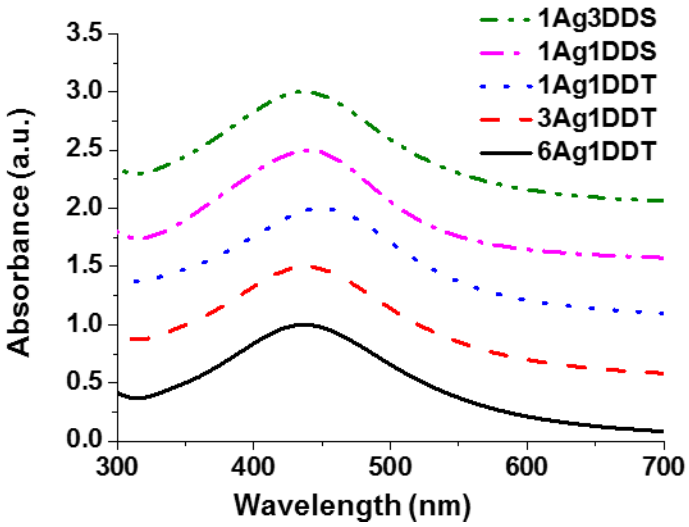

Figure 2.2. UV-vis spectra of DDT- and DDS-Ag NPs.

Since a different bonding mechanism between thiolates to Au NPs and dialkyl sulfides to Au NPs has been demonstrated,[174–176] it was also of interest to explore the effect of using DDS in the synthesis of Ag NPs. The resulting 1Ag1DDS NPs were semi-spherical and had an average diameter of 11.2 ± 4.8 nm (see Figure 2.1), which was much larger and more polydisperse than the size of the DDT-Ag NPs produced with the same ratio (2.6 ± 0.5 nm). We further explored the ligand:metal ratio effect by preparing 1Ag3DDS NPs. The NPs from this synthesis yielded slightly more spherical NPs with an average size of 4.7 ± 0.9 nm (see Figure 2.1), which again, is larger than the Ag NPs prepared with 1Ag1DDT and closer to the Ag NPs prepared with 6Ag1DDT (4.0 ± 1.0 nm). In addition, the DDS-Ag NP SPR peaks also demonstrate a slight blue-shift when adding more ligand (or decreasing in size), which is in contrast to the red-shift observed when adding more DDT. Taken together, the differences of the TEM and UV-vis trends between the DDS-Ag and DDT-Ag NPs likely indicate a different bonding mechanism. In order to explore these differences and more fully characterize the Ag NPs, we used Ag K,

Ag L_3, and S K-edge XAS as presented in the following sections. However, it should be noted that for the following comparisons we omit the 3Ag1DDT and 1Ag1DDS samples, due to the very similar size of the 3Ag1DDT sample to the the 6Ag1DDT sample (3.8 nm vs. 4.0 nm), and the polydispersity of the 1Ag1DDS sample.

2.5.2 Ag K-edge EXAFS

Raw EXAFS data of the 1Ag1DDT, 6Ag1DDT, and 1Ag3DDS samples were converted into *k*-space (Figure 2.3a). It can be seen that the oscillatory patterns of the *k*-space spectra closely resemble the bulk Ag foil *k*-space, which implies that the NPs are metallic. Correspondingly, the *R*-space spectra (Figure 2.3b) demonstrate a notable decrease in the Ag-Ag shell as the Ag NP size decrease.

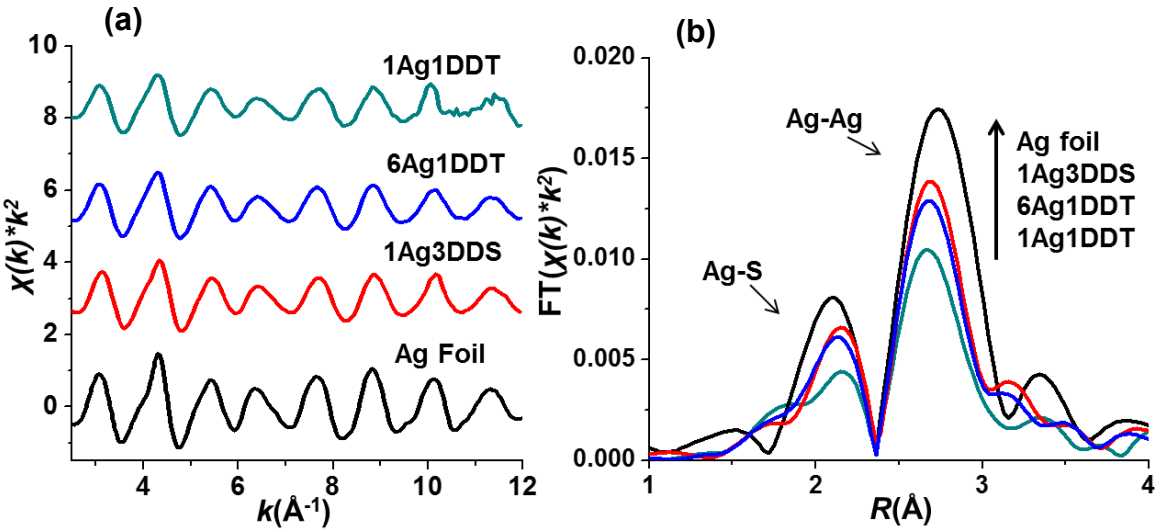

Figure 2.3. Ag K-edge EXAFS of DDT- and DDS-Ag NPs. (a) k^2 weighted Ag K-edge *k*-space spectra of the Ag NPs and (b) Ag K-edge *R*-space spectra of the Ag NPs

To determine quantitative structural information about the bonding and structure of the Ag NPs, the k^2-weighted *R*-space spectra were refined.[182] The resulting overall refinements are presented in Figure 2.4; however, to ensure the reliability of the

refinement results, we compared *R*-space refinements in both k^2- and k^3-weighting (not shown), and the results were consistent. The goodness of fit for each refinement is expressed by the R-factor (Table 2.1), and were all below 0.02, denoting acceptable refinements.[149]

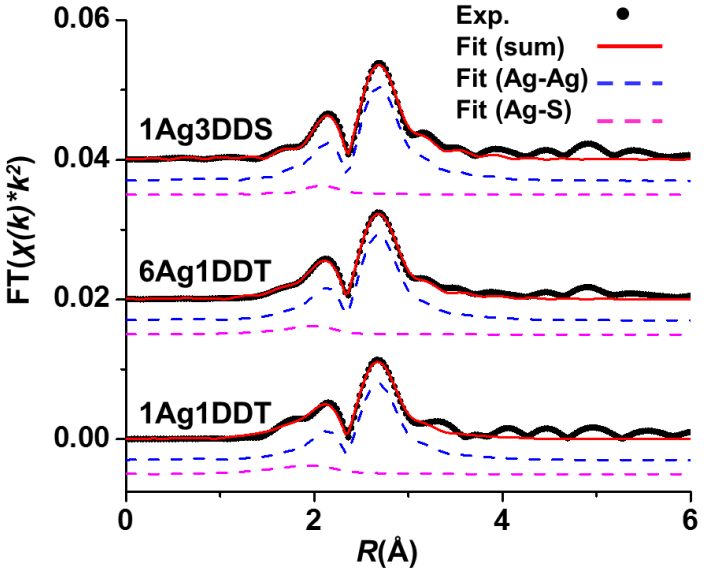

Figure 2.4. Ag K-edge *R*-space spectra of DDT- and DDS-Ag NPs. The spectra were fit with Ag-Ag and Ag-S paths to find experimental coordination numbers and bond lengths.

The metallic character of the samples is further demonstrated by the Ag-Ag bond lengths shown in Table 2.1. The Ag NPs all exhibit Ag-Ag distances of around 2.85 Å, which is comparable to the bulk (~2.87 Å from experimental *R*-space refinement), given that slight lattice contraction is expected for NPs of this size.[155,183] Table 2.1 also shows that the Ag-Ag CNs decrease from around 12 (normal for FCC Ag) to 7.9 in the 1Ag1DDT NPs. The decrease of metal-metal CN is a well-documented phenomenon of metal NPs and is due to the increase of surface atoms which have fewer neighbouring atoms; hence causing the overall CN number to decrease.[158] Indeed, we see that the Ag-

Ag CN follows the decreasing size of the Ag NPs from TEM. However, based on theoretical calculations,[184] the Ag-Ag CN of traditional metallic FCC NPs with sizes of 2.4 nm should exhibit a CN around 9-10; hence the Ag-Ag CNs observed are lower than expected for NPs of this size. From the refinements, the 1Ag1DDT also had the highest Ag-S CN indicating the largest contribution of Ag-S bonds while the 1Ag3DDS had the lowest Ag-S contribution.

Table 2.1. Ag K-edge *R*-space refinement results for DDT- and DDS-Ag NPs. The uncertainties of the refinement values are given by the numbers in parentheses.

Sample	Bond	CN	R(Å)	σ^2 (Å^2)	ΔE_o (eV)	R-factor
1Ag1DDT	Ag-Ag	7.9(9)	2.85(1)	0.011(1)	0.3(5)	0.008
	Ag-S	1.1(4)	2.51(3)	0.019(7)	0.3(5)	
6Ag1DDT	Ag-Ag	9.4(6)	2.85(1)	0.010(1)	0.1(5)	0.004
	Ag-S	0.6(2)	2.51(3)	0.008(7)	0.1(5)	
1Ag3DDS	Ag-Ag	9.8(8)	2.85(1)	0.011(1)	1.2(5)	0.003
	Ag-S	0.3(2)	2.53(4)	0.003(3)	1.2(5)	

The most striking finding from the refinements is the abnormally high Ag-S CN of the 1Ag1DDT sample. For comparison, a recently determined $Au_{25}(SR)_{18}$ cluster[185] (~1 nm) that exhibits the staple motif has a Au-S CN of 1.44. The $Au_{25}SR_{18}$ cluster is made up mostly of surface metal atoms and is much smaller than the 1Ag1DDT NPs. Therefore, we can be certain that the metal-sulfur CN of nominal 2.6 nm Ag NPs with

either a staple-like or metal-thiolate surface structure should be much smaller than 1.44. For the 1Ag1DDT NPs, the average Ag-S CN obtained from EXAFS was 1.1. Based on theoretical models generated in the Crystal Maker program (Figure 2.5),[184] we estimated that there are about 48 % surface atoms in a metal NP around 2.6 nm. By using this model, an average Ag-S CN of 1.1 correlates to a surface structure with 2.3 S per surface Ag, which is larger than that of any known metal-thiolate (Ag-S CN ≈ 1) or staple surface structure (Ag-S CN ≈ 1-2). Therefore, the S in the 1Ag1DDT is likely to be partially incorporated as a sulfide shell, in addition to thiolate-type S on the NP surface which would provide their solubility. In bulk Ag sulfide (Ag_2S), the average Ag-S CN would be somewhere between 2 and 3 given the two types of Ag sites bound to S,[186] which is comparable to the estimated surface Ag-S of 2.3 in the 1Ag1DDT. Furthermore, the lower than expected Ag-Ag CN values for the 1Ag1DDT sample may be attributed to a smaller metallic core within a sulfide shell. Based on the similar synthetic technique used for the 1Ag1DDT and 6Ag1DDT NPs, we would expect to have a similar surface structure between them. By utilizing a similar estimation of 35 % surface atoms (from Figure 2.5), roughly 1.7 S atoms per surface Ag for the 6Ag1DDT NPs is calculated. This is lower than that of the 1Ag1DDT sample, suggesting that the amount of surface sulfide of 6Ag1DDT is lower than the 1Ag1DDT. On the other hand, the 4.7 nm 1Ag3DDS NPs have approximately 31 % surface atoms (Figure 2.5), yielding an estimated 0.9 S atoms per surface Ag. This value is lower than 1 which indicates that there is likely no staple or sulfide present on the surface, and DDS most likely follows a traditional physisorption to the Ag NPs, similar to the bulk metal surface.[174,187,188]

The Ag-S bond lengths of all the Ag NPs are also longer than the typical bond length of a metal-thiolate (*e.g.,* 2.3-2.4 Å of Au-S[189]) and are closer to the Ag-S bond

lengths of Ag_2S (*i.e.,* 2.49-3.07 Å[186]). The 2.51 Å (for 1Ag1DDT and 6Ag1DDT) should therefore be considered as an average of the Ag-S bonds from a sulfide shell and a thiolate-type surface layer (bound to surface Ag in sulfide[190]). However, since it is likely that no sulfide was formed for the DDS, the 2.53 Å bond length may reflect the weaker Ag-S physisorption mechanism at the surface. Further reasoning for this is given in the following section of S K-edge XAS. It is also noted that the Ag-Ag bond lengths from the Ag K-edge *R*-space refinements are similar, which is likely due to the higher contribution of shorter Ag-Ag bonds from the metal core (2.85 Å) versus the longer Ag-Ag bonds in Ag_2S (> 3.0 Å[186]).

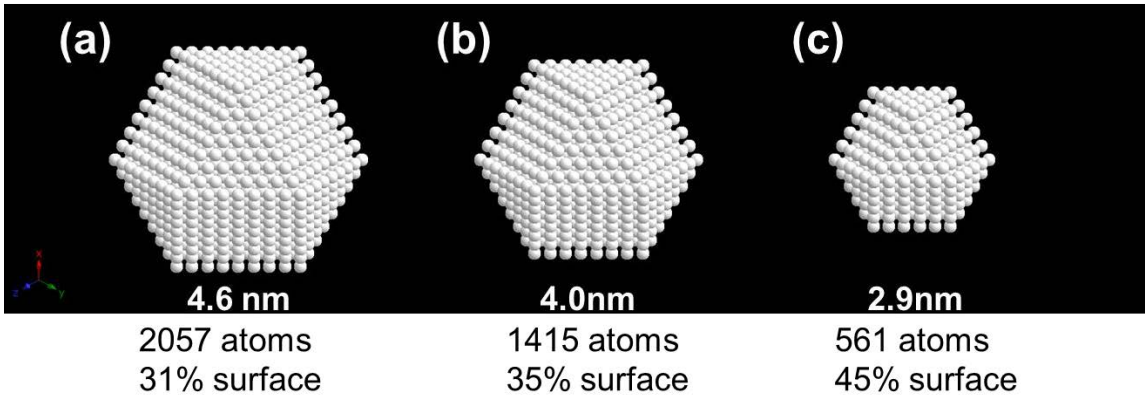

Figure 2.5. Estimation of the number of surface atoms in metal NPs of various sizes.

We can also deduce structural information from the Debye-Waller factor (σ^2) values, which are based on the disorder of the local environment. The 1Ag1DDT has a relatively high σ^2, which is likely a result of a mixture of a more disordered sulfide layer and the thiolate surface layer (bound to Ag in sulfide). In general, when using a single shell to represent multiple shells, a larger σ^2 factor will result; therefore, the mixture of the different types of Ag-S in the sample creates the higher σ^2 in this case.[191] Furthermore, the

smaller σ^2 for the 6Ag1DDT is suggestive of a thinner layer of Ag_2S. The even smaller Ag-S σ^2 for the 1Ag3DDS suggests a more ordered surface structure of DDS on the metal surface.[174,187,188]

Based on the above discussion, we propose that the amount of sulfide was significantly reduced when the size of DDT-Ag NPs was increased from 2.6 nm to 4.0 nm, and that a sulfide layer did not form in the DDS-Ag NPs. These Ag K-edge EXAFS results were consistent with previous findings that there are sulfur-rich, thiolate shells on Ag NPs prepared with DDT.[179,192] However, our results point to a more distinct layer of sulfide on the surface of the 2.6 nm DDT-coated Ag NPs opposed to thiolate shells.[179] In order to get a more detailed picture of the composition and structure of the Ag-S on the DDT- and DDS-Ag NP surfaces, we explored the Ag L_3-edge XANES and S K-edge XAS of the Ag NPs, presented in the following sections.

2.5.3 Ag L_3-edge XANES

The first feature of the Ag L_3-edge XANES spectra in Figure 2.6a is the absorption edge and is generated from electron transitions to metal d-orbitals.[96,155,156] Therefore, a more intense absorption edge corresponds to more unoccupied d-orbitals or fewer d-electrons in Ag. Figure 2.6b demonstrates the slightly higher absorption edge intensities of the 1Ag1DDT and 1Ag3DDS NPs compared to the bulk, which is typically observed for organosulfur-protected NPs.[96] This would also be expected for the 1Ag1DDT NPs, although the more drastic increase in the absorption edge supports the presence of more non-metallic Ag^+, similar to the bulk Ag_2S reference (Figure 2.6c). On the other hand, 1Ag3DDS has the lowest absorption edge intensity which suggests the lack of sulfide and a weaker bonding mechanism overall.

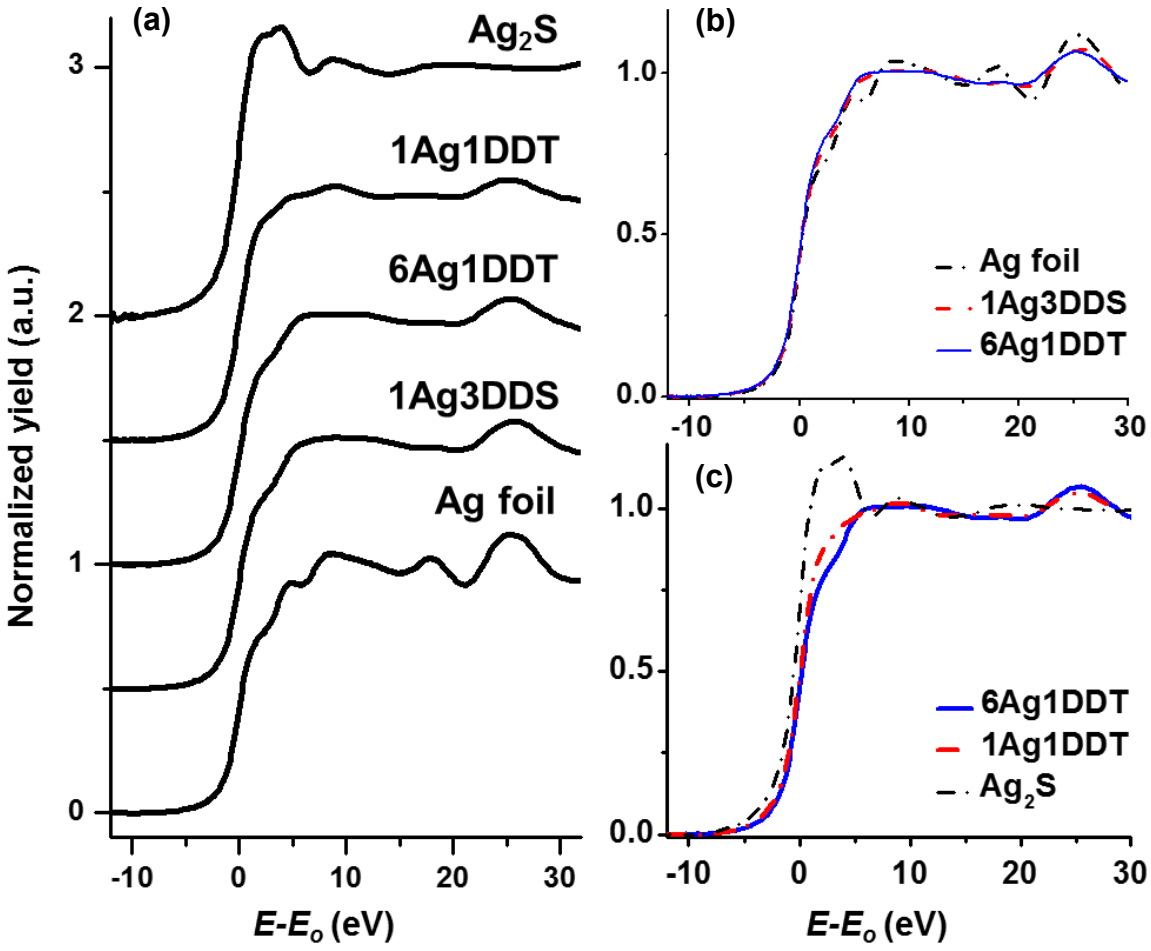

Figure 2.6. Ag L_3-edge XANES of DDT- and DDS-Ag NPs. (a) Ag L_3-edge XANES spectra of Ag NPs and bulk references (b) closer comparison of DDT- and DDS-Ag NPs with Ag foil reference (c) closer comparison of DDT-Ag NPs with bulk Ag_2S

2.5.4 Sulfur K-edge XAS

Sulfur K-edge XANES can also be used to explore the bonding environment at the surface of the NPs from the ligand perspective. Figure 2.7 shows the S K-edge XANES spectra of the three Ag NPs together with reference samples including a thiol reference (tiopronin, RSH), bulk Ag_2S, and DDS. The feature at around -2 eV (E-E_o) can be assigned to thiolate-Ag surface bonding and has been found to increase with particle size

in other NP systems.[154] The RSH reference understandably does not exhibit this feature at -2 eV (E-E_o). However, the 6Ag1DDT Ag NPs exhibit a larger S-Ag feature which indicates that there is Ag-thiolate bonding on the surface of the 6Ag1DDT Ag NPs. In combination with our Ag K-edge EXAFS results, this implies that there most likely exists a mixture of a thin shell of sulfide and metallic Ag-thiolate bonding on the 6Ag1DDT Ag NPs. Furthermore, for the 1Ag1DDT Ag NPs we observe that the S-Ag feature has essentially disappeared, which indicates that thiolate does not directly bind to the Ag metal cores. There is also a change in the intensities of the S-C resonance peaks around 0 eV (E-E_o).[155] Both of the DDT samples show lower S-C feature intensities than the RSH because the formation of Ag-S bond induces a weakening of the S-C bond and results in a lower than normal peak intensity.[187] We can therefore infer that there is less Ag metal core to thiolate bonding in the 1Ag1DDT and hence the higher S-C peak than the 6Ag1DDT. Interestingly, the 1Ag3DDS Ag NPs have a smaller S-Ag and larger S-C feature (Figure 2.7c) than the 6Ag1DDT Ag NPs despite their larger average diameter (4.7 vs 4.0 nm), which further indicates the weaker physisorption mechanism of DDS. Moreover, the overall shape of the 1Ag3DDS S K-edge XANES spectrum is also more similar to the reference DDS than the DDT-Ag NPs are to the RSH reference. This indicates that the ligands were less disturbed after adsorption to the Ag than with DDT and supports the weaker physisorption mechanism as well as supports previous findings that the S-C bond probably does not appreciably cleave upon adsorption to Ag surfaces.[174,187] These results may also help explain why sulfide was not generated on the surface of the DDS-Ag NPs, as the weaker interaction and less available S^{2-} may prevent their sulfidation.

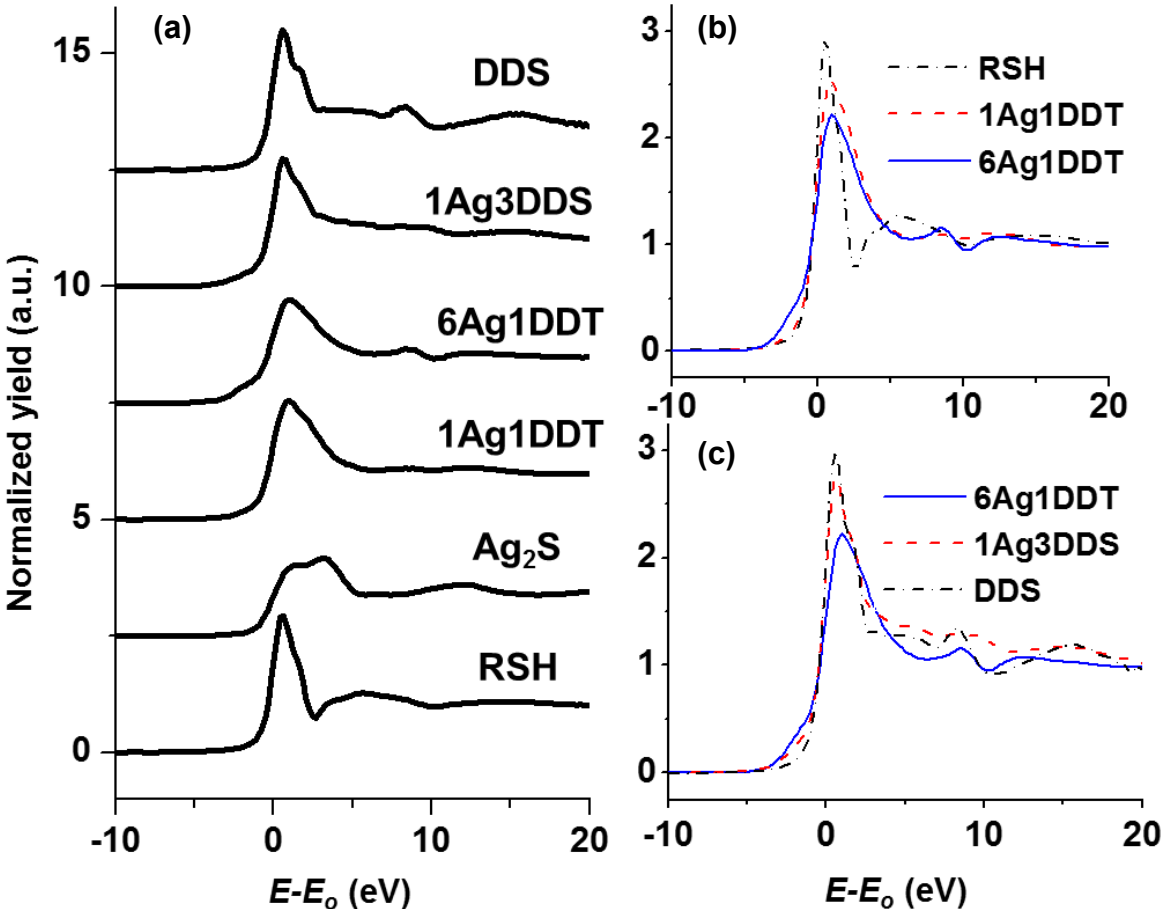

Figure 2.7. S K-edge XANES of DDT- and DDS-Ag NPs. (a) S K-edge XANES spectra of Ag NPs and bulk references (b) closer comparison of DDT-Ag NPs with bulk thiol (RSH) (c) closer comparison of DDT- and DDS-Ag NPs with DDS reference.

Sulfur K-edge EXAFS was also carried out in order to provide a better understanding of the S environment on the surface of the 1Ag1DDT Ag NPs. From Figure 2.8a, the oscillatory patterns of the 1Ag1DDT Ag NPs are almost identical to the reference spectrum of Ag_2S, which supports our previous Ag K-edge EXAFS/L_3-edge XANES findings. From the refinement values (Table 2.2), the S-Ag CN was 2.9 which is lower than that of the bulk Ag_2S (S-Ag ≈ 5) and a metal-thiolate (S-Ag CN ≈ 3), but still larger than that of a staple arrangement (S-Ag CN ≈ 2). We suspect that the lower S-Ag CN than the Ag_2S is likely due to the nanosize effect on the sulfide layer (*i.e.,* reduced

CN from fewer neighbouring atoms). In addition, S-Ag bond lengths in bulk Ag_2S are also between 2.49-3.07 Å,[186] which is most likely why we observed longer bond lengths in our sample than the typical S-Ag bond length of a thiolate on metal NPs (*e.g.,* 2.3-2.4 Å[189]). However, we note that the S K-edge EXAFS S-Ag bond length is shorter than the Ag K-edge EXAFS Ag-S (2.45 vs 2.51 Å) which may be due to the following reasons; first, a relatively short S K-edge *k*-range (k_{max}= 9 $Å^{-1}$) was collected which may produce a slightly higher uncertainty in the value, comparing with a longer Ag K-edge *k*-range (k_{max} = 12 $Å^{-1}$). Second, the S K-edge EXAFS was collected in total electron yield mode which is generally more surface sensitive than transmission mode EXAFS, and may reflect slightly shorter thiolate-type Ag-S on the surface. Third, the S K-edge EXAFS was collected using solid phase (drop-cast) and the Ag K-edge EXAFS was measured in liquid, which may contribute to different bond lengths observed.[191] Each of the three factors could contribute to the difference in the Ag-S bond length obtained from the two EXAFS methods. Finally, a S-C CN of 0.6 was also achieved by the refinement, which demonstrates that S-C bond cleavage occured, similar to previous examinations of alkylthiol adsorption onto bulk Ag and Au.[174,187]

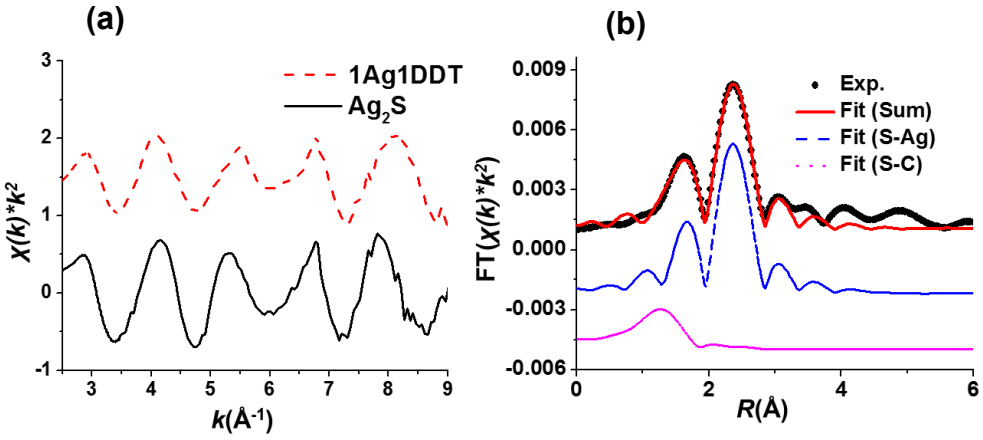

Figure 2.8. S K-edge EXAFS of DDT-Ag NPs (a) k^2-space spectra of 1Ag1DDT and Ag_2S (b) *R*-space refinement with S-C and S-Ag paths.

Table 2.2. S K-edge *R*-space refinement results for DDT-Ag NPs and Ag_2S. The uncertainties of the refinement values are given by the numbers in parentheses.

Sample	Bond	CN	R (Å)	σ^2 (Å^2)	ΔE_o (eV)	R-factor
1Ag1DDT	S-C	0.6(3)	1.78(3)	0.015(9)	-3(1)	0.013
	S-Ag	2.9(2)	2.45(2)	0.006(1)	-3(1)	
Ag_2S	S-Ag	5(1)	2.49(2)	0.007(2)	-1(1)	0.008

The previous results support that S from the DDT has been incorporated as a sulfide into the surface layer of the Ag NPs. Most likely, the Ag^+ is reduced by $NaBH_4$ to Ag atoms, which combine with other Ag atoms to form the Ag NPs, which are then subsequently stabilized by DDT. As the reaction proceeds, the thiolate S-C bonds are cleaved to provide S^{2-} that reacts with the Ag through a sulfidation mechanism. In this way, the S^{2-} is shifted below the surface to expose Ag to propagate further thiol adsorption.[108,193,194] The excess thiol in the solution continues to adsorb to the surface Ag, and the sulfidation proceeds depending on the available thiol, resulting in a sulfide shell around the metal core. Once the metallic surface Ag is covered by sulfide the excess thiols likely coordinate with the surface Ag in the sulfide shell, thereby maintaining their solubility in solution.[190] This type of mechanism has been observed for bulk Ag[187,194] and palladium (Pd),[195,196] and later for Pd NPs.[75,197,198] We believe this phenomenon does not occur for Au NPs prepared with thiols such as DDT because (i) Au sulfides are not thermodynamically stable[108] and (ii) the electronegativity of Au is higher than that of Ag (2.4 vs 1.9) and therefore Au will not readily lose electrons as Ag does (demonstrated by the increase in Ag L_3-edge XANES in Figure 2.6).

2.6 Conclusion

It was found that the preparation of DDT-Ag NPs resulted in metal core/sulfide shell structure. This finding was consistent in Ag K-edge EXAFS, Ag L_3-edge XANES, and S K-edge EXAFS. The presence of sulfide-type shells on the DDT-Ag NPs also explained the increase in the Ag L_3-edge XANES absorption edges and the lower than expected Ag-Ag CNs and higher Ag-S CNs from the Ag K-edge EXAFS. In addition, the S K-edge EXAFS provided evidence to a sulfide layer and supports our other results. Furthermore, we observed a proportional relationship between ligand concentration (and particle size) and the amount of sulfide produced on the Ag NPs; the higher the DDT concentration, the smaller Ag NPs and more sulfide produced. The larger Ag NPs prepared with 6Ag1DDT were more metallic, and the concentration of DDT may not have been enough to produce a significant layer of sulfide on the surface relative to the metallic Ag; hence, the Ag K-edge EXAFS did not show any exaggerated sulfide characteristics. On the other hand, DDS was shown to bond weakly to the Ag NPs and does not likely result in a sulfide-type surface. Overall, a multi-core, multi-element XAS methodology was used to provide a detailed picture of the local structure and bonding of organosulfur-stabilized Ag NPs. Importantly, it was revealed that organosulfur ligand concentration and type can have a dramatic effect on surface structure of Ag NPs.

Chapter 3 - The Impact of Protecting Ligands on the Surface Structure and Antibacterial Activity of Silver Nanoparticles

Sections 3.3-3.6 are reproduced in part with permission from: Padmos, J. D.; Boudreau, R. T. M.; Weaver, D. F.; Zhang, P. Impact of Protecting Ligands on Surface Structure and Antibacterial Activity of Silver Nanoparticles. *Langmuir* **2015**, 31, 3745.

3.1 Contributions

J.D.P. synthesized the NPs, carried out the general characterization, conducted the XAS experiments, and wrote the manuscript. R.M.B. carried out the antibacterial activity assays. D.F.W. supervised R.M.B.. P.Z. supervised J.D.P. and helped revise the manuscript.

3.2 Foreword

The study described in Chapter 2 examined the effect of concentration and type of organosulfur ligands on the surface structure of Ag NPs. A greater understanding of the interaction of thiolates and Ag NPs was given; however, the Ag NPs were prepared in organic solvent, so it was not possible to study of the effect of surface structure on their antibacterial properties. Therefore, the study described in this chapter aims to (i) understand the effect of a thiolate ligand on surface structure of Ag NPs in aqueous solution, and (ii) correlate this surface structure with antibacterial activity.

3.3 Introduction

Metal nanoparticles (NPs) are currently the focus of intensive research because of their unique physicochemical properties.[10,199] Silver (Ag) NPs, in particular, have shown remarkable antibacterial activity relative to bulk Ag, owing largely to their increased surface area. Furthermore, size, morphology, atomic composition, and surface composition and structure are all important Ag NP qualities that can determine antibacterial activity.[19,47,57,200–202]

The antibacterial mechanism of Ag NPs is complex, but thought to be mainly derived from Ag^+ released from their surfaces and/or direct NP surface reactions with bacteria.[37,41,42,45–47,57,61,127] Both Ag and Ag^+ can lead to cell damage either by directly reacting with cellular thiols and amino groups of proteins within cell membranes, or indirectly by generating reactive oxygen species that cause oxidative stress.[41,44,49–54] Complicating the antibacterial mechanism even further is the fact that Ag NP surfaces can readily dissolve in aqueous solution, thereby convoluting the effects of surface Ag and dissolved Ag^+.[33–35] Due to the fact that the Ag NP surface structure plays a significant role in both the Ag^+ dissolution and surface Ag interactions with bacteria, a greater understanding of Ag NP surface structure could provide useful insight to the antibacterial activity of the Ag NPs under study.

The type of protecting ligand used to stabilize Ag NPs plays an obvious role in their surface structure. Although metal NPs have been synthesized with various ligands, by far the most common ligands used to stabilize metal NPs are thiolates (RS-). Thiolates are commonly used to prepare metal NPs because of the resulting stability afforded by strong metal-sulfur interactions. The discovery of a unique surface structure known as a

"staple" (*e.g.,* -SR-Au-SR-) for Au NPs[100] has stimulated surface structure studies of other metal NPs stabilized with thiolates, including Ag NPs.[75,84,103,203] From those particular studies, it was shown that the surface structures of the Ag NPs were composed of highly sulfidized Ag (*e.g.,* Ag_2S, Ag_2S_5), which differ greatly from the surface structures of Au NPs protected by thiolates (*e.g.,*-SR-Au-SR-). Therefore, it is of great interest to examine the effect of other thiolate ligands on the surface structure of Ag NPs.

Unfortunately, elucidating the surface composition and structure of Ag NPs can be difficult with traditional techniques (*e.g.,* UV-vis, TEM, XRD); however, information regarding the NP surface can be reliably achieved with element-specific X-ray absorption spectroscopy (XAS). XAS is especially useful for studying thiolate-protected metal NPs, as they can be studied from both the metal and sulfur (S) perspectives, thus yielding a more comprehensive look at the surface structure. Indeed, this technique has been previously used to successfully examine the surface structures of thiolate-protected Au,[87] Ag,[75] and palladium (Pd) NPs.[197]

As understanding the relationship between the surface and properties of nanomaterials is crucial for both fundamental studies and their applications, we seek to establish that relationship for the type of NPs described herein. We examined the atomic composition and surface structure of Ag NPs stabilized with water-soluble, biocompatible cysteine (Cys) and polyvinylpyrrolidone (PVP) using XAS, as well as other physical chemistry techniques, in order to first compare the ligand effect on the resulting surface structures. This information was then used to rationalize the antibiotic activities of the different Ag NPs against various bacteria.

3.4 Experimental

3.4.1 Synthesis of Ag NPs

Silver nitrate ($AgNO_3$, 99.9+ %) and polyvinylpyrrolidone (PVP, M.W. 8,000) were purchased from Alfa Aesar. Sodium borohydride ($NaBH_4$, 99 %) and L-cysteine (Cys, ≥ 98 %) were purchased from Sigma-Aldrich. Nitric acid (HNO_3(aq), 67-70 % (w/w) was purchased from Caledon Laboratory Chemicals. Hydrochloric acid (HCl(aq), 36.5-38.0 % w/w) and potassium hydroxide (KOH, 85+ %) were purchased from ACP Chemicals. All water used in the syntheses was obtained from a Barnstead NANOpure® DIamondTM UV ultrapure water system (Deionized, 18.2 MΩ·cm). The PVP protected Ag NPs (PVP-Ag NPs) were prepared using a method derived from Zhang et al. with slight modifications.[130] First, 1 mL $AgNO_3$ (0.1 M), 0.4 mL KOH (0.1 M), and 8 grams of PVP were mixed into 93.6 mL of ultrapure water in a sealed round bottom flask. The solution was then allowed to stir for 30 minutes under N_2 gas. After mixing, 5 mL of ice-cold $NaBH_4$ (0.1 M) was added drop-wise to initiate the reaction. After vigorous stirring for 1 hour, the solution was aged for 48 hours (covered, room temperature) to allow for complete $NaBH_4$ decomposition. The Cys protected Ag NPs (Cys-Ag NPs) were prepared using a method derived from Li et al.[204] and Mandal et al.[205] with slight modifications. Briefly, 100 ml of 1 x 10^{-3} M concentrated aqueous solution of $AgNO_3$ was reduced by 0.01 g of $NaBH_4$ under N_2 bubbling to produce Ag NP seeds. After stirring for 10 minutes, the Ag NPs were further reacted with 2 ml aqueous solution of 1 x 10^{-2} M Cys. The solution was then allowed to stir for an additional two hours under N_2 bubbling to ensure the complete reaction, and then aged for 48 hours (covered, room temperature). After initial preparation of both NPs, they were purified to remove any excess

constituents by acetone/water precipitation.[206,207] First, the water was completely removed from each solution by drying under vacuum. A 3:1 mixture of acetone:water was then added to each sample and then centrifuged for 15 minutes (10,000 *g*, 5 °C) in Nalgene tubes to precipitate the NPs from solution. The acetone was removed completely from the tubes and 1 mL of water was added to re-disperse the NPs into solution. Each sample underwent the same purification procedure a total of 3 times, and they were finally re-dispersed into water. The samples were then sealed and stored at 4 °C for subsequent characterization.

3.4.2 General Characterization

NP size and shape were assessed by transmission electron microscopy (TEM) using a Philips Technai-12 TEM (80 kV). A 20 µL aliquot of each diluted sample was dropped on separate formvar-coated TEM grids and allowed to dry (covered, room temperature) before measurements were conducted. TEM images were taken, and their size distribution was measured using ImageJ image processing software.[143] The surface plasmon resonance (SPR) peaks of each NP solution were characterized using a Varian Cary 100 Bio UV−visible spectrophotometer. A 50 µL aliquot of each sample was diluted to 3 mL with water in a quartz cuvette. Spectra were recorded from 300-800 nm and background-corrected with a water reference. Inductively coupled plasma optical emission spectroscopy (ICP-OES) was also carried out to determine the resulting Ag concentration in each NP solution. In preparation for ICP-OES, the samples were first digested in a solution of HNO_3 and HCl. A 20 µL of each sample was diluted to 1 mL with water and then heated to 80 °C in a covered test-tube. To this, 1 mL of HNO_3 was added and allowed to sit for 1 hour at 80 °C. A 2 mL volume of HCl was then added to

form aqua regia, and allowed to sit for an additional hour. Following cooling, the solutions were dispersed into 10 mL of water in a volumetric flask. The ICP-OES measurements were then collected for the Ag NPs using a PerkinElmer Optima8000 at a wavelength of 328.068 nm for Ag.

3.4.3 X-ray Absorption Spectroscopy (XAS)

Ag K-edge XAS was conducted at the Advanced Photon Source (BM-20 beamline) at Argonne National Laboratory, Argonne, IL, USA. Ag L_3-edge and S K-edge XAS was conducted at the Canadian Light Source (SXRMB beamline, Saskatoon, SK, Canada). In preparation for solid phase XAS measurements, the water from the NP solutions was completely removed by freeze-drying the NP solutions into powders. For Ag K-edge XAS, the powders were placed in kapton film pouches and loaded into the sample holder along with Ag foil. The sample holder was then placed into a cryostatic chamber which was then set at a constant temperature of 50 K for all of the measurements. Ag K-edge spectra were collected with a 32-element solid state Ge X-ray fluorescence detector with simultaneous foil reference spectra collected using standard gas-ionization chamber detectors. For Ag L_3-edge and S K-edge XAS, the powdered samples were placed on double-sided carbon tape attached to the sample holder. The sample holder was then placed in the sample chamber and allowed to reach an ultra-high vacuum atmosphere before data collection. The Ag L_3-edge and S K-edge spectra were collected with a 4-element Silicon drift detector. All of the XAS spectra were processed with the WinXAS software program.[162] The x-axes of the spectra were first normalized to their absorption energies (Ag or S) and then the y-axes were normalized to exhibit a difference of one between the pre-edge and post-edge. For the extended X-ray absorption

fine structure spectroscopy (EXAFS) analysis of Ag K-edge, the raw data were k^2-weighted, Fourier-transformed using a Hanning function from k = 3-12 Å^{-1}, and then refined with WinXAS from R = 1.5-3.3 Å.[75] An amplitude reduction factor (S_o^2) of 0.95 was held constant during the refinements, which was based on bulk Ag R-space refinement (spectrum collected at 50 K). *Ab initio* simulations of Ag structural models were obtained from the FEFF 8.2 code in order to refine the experimental data.[164,165] The R-space refinements obtained structural information about the NPs, including coordination numbers (CNs), bond lengths (R), Debye-Waller coefficients (σ^2), and E_o-shifts (ΔE_o). The refinement of the S K-edge EXAFS was carried out in a similar way, albeit the k-space spectra were Fourier-transformed using a Hanning function from k = 2.5-9 Å^{-1}, and refined from R = 1.3-3.0 Å.[75] The S_o^2 value used for the refinement was 0.65, based on bulk Ag_2S R-space refinement. For the Ag L_3-edge and S K-edge XANES data, the normalized spectra were used for qualitative comparison to reference materials.

3.4.4 Antibacterial Activity

The antibacterial activity assays of the Ag NPs were conducted by R. Boudreau (DeNovaMed, Halifax, NS, Canada) and the following section describes the procedure used. The antibacterial activity of each NP solution was tested against *Staphylococcus aureus* (*S. aureus,* ATCC 29213)*, Escherichia coli* (*E. coli,* ATCC 23716)*,* and *Pseudomonas aeruginosa* (*P. aeruginosa,* ATCC 25619) with a serial dilution method in broth based on Clinical and Laboratory Standards Institute (CLSI) standard methodology.[208] Briefly, Mueller-Hinton II Cation-Adjusted (MHIICA) agar plates were first streaked with bacteria and incubated for 24 hours at 37 °C. A single colony of each type of bacteria was then picked from the plates and inoculated into 2 mL of liquid broth.

The resulting bacteria suspensions were then further incubated at 35 °C under orbital shaking (220 rpm) for 24 hours until stationary phase was reached. 200 μL aliquots of liquid broth were then added to all wells of a round-bottom 96-well plate (Becton Dickinson, Canada). Ag NP solutions were added to the first column wells to give approximate Ag concentrations of 1 mM, along with controls (positive (DMSO as vehicle) and negative (broth alone as sterility control)) in separate wells. The subsequent 11 column wells were diluted two-fold followed by the addition of 10 μL aliquots of bacteria suspension (0.2 OD units) to each well. The plate was then left in an incubator for approximately 20 hours at 35 °C. The minimum inhibitory concentration (MIC) was determined to be the lowest concentration at which no visible turbidity was observed.

3.5 Results and Discussion

3.5.1 General Characterization

Transmission electron microscopy (TEM) was used to measure the average diameter of the Ag NPs. Figure 3.1 shows a representative TEM image of each Ag NP sample, along with their size distributions. It should be noted that the measurements for the PVP-Ag NPs were based on four TEM images, thus the larger number of NP counts in its size distribution (Figure 3.1 insets). The mean diameters of the PVP-Ag and Cys-Ag NPs were found to be 7.7 ± 1.5 nm and 7.6 ± 1.6 nm, respectively, indicating their essentially identical average diameters. Furthermore, the arrangement of the NPs on the TEM grids is indicative of the ligands used. For example, the PVP-Ag NPs were found to be more separated from neighbouring NPs, resulting from repulsion between the bulky PVP protecting the individual NPs. On the other hand, Cys-Ag NPs were found to form large agglomerates comprising individual NPs, potentially as a result of electrostatic

interaction between the ligands of the NPs.[209] However, the individual Cys-Ag NPs remained separated and negligible aggregation into larger NPs was observed overall.

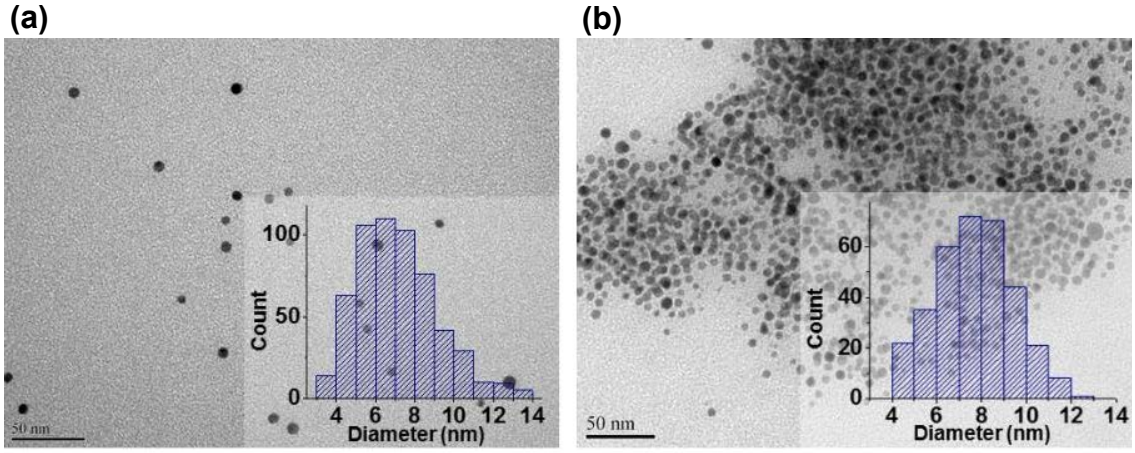

Figure 3.1. TEM images of PVP- and Cys-Ag NPs. (a) PVP-Ag NPs, (b) Cys-Ag NPs. Note that the size distribution of the PVP-Ag NPs was calculated from four TEM images.

UV-visible spectroscopy was conducted to observe the surface plasmon resonance (SPR) of the Ag NPs. Typically, the SPR of Ag NPs occurs in the UV-visible region around 400-450 nm, depending on the surrounding media. Figure 3.2a shows the UV-vis spectra of the Cys-Ag NP and PVP-Ag NP solutions, with significant SPR peaks around 400 nm. In both spectra, the lack of absorbance peaks below 390 nm indicates the absence of impurities, such as unreduced Ag from $AgNO_3$ or Ag^+-Cys thiolates.[49,75,179] Both Ag NPs exhibited similar UV-vis spectra after long-term storage in water (Figure 3.2b) which demonstrates their stability and negligible aggregation, similar to previous studies of other Cys-Ag and PVP-Ag NPs.[33,209] It should also be noted that despite the almost identical size for the Cys-Ag and PVP-Ag NPs, their overall spectra are significantly different. Because SPR peaks are largely dependent on the surface of the NPs, the difference in the spectra alludes to a very different surface structure of the two

types of NPs. In order to fully elucidate the surface structure of the NPs, XAS was carried out and presented in the following sections.

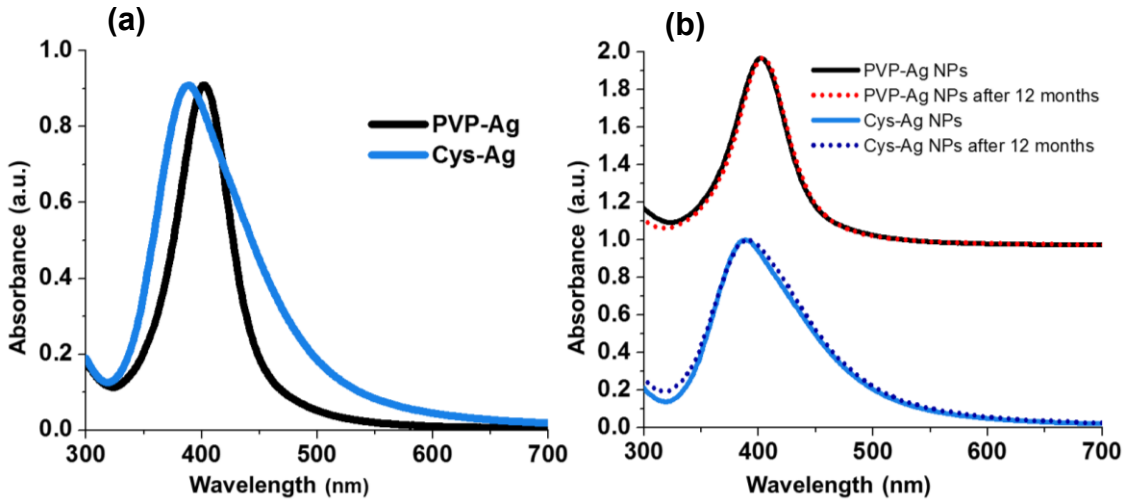

Figure 3.2. UV-vis spectra of PVP- and Cys-Ag NPs. (a) The PVP-Ag NPs show one distinct peak at 403 nm while the Cys-Ag NPs show one major peak at 396 nm with a potential broad peak between 450 and 500 nm. Note that the spectra were normalized to the same absorbance values at their major SPR peaks to enable a closer comparison. (b) The PVP-Ag and Cys-Ag NPs exhibited almost identical SPR features after long-term storage in water indicating their overall stability.

3.5.2 Structural Characterization by XAS

The surface structure of the Cys-Ag and PVP-Ag NPs were first examined by their Ag K-edge EXAFS. The k^2-weighted Ag K-edge spectra of the Cys-Ag and PVP-Ag NPs (Figure 3.3a) show similar spectral oscillations to the Ag reference foil, indicating metallic Ag. The k^2-weighted spectra were then Fourier-transformed to the *R*-space and the resulting spectra are shown in Figure 3.3b. The major doublet peak in the region of 2-3 Å is consistent with first-shell Ag-Ag bonding. The Ag *R*-space spectra reveal a decrease in overall intensity from the PVP-Ag NPs to the Cys-Ag NPs, even though the NPs were observed to have essentially the same average size.

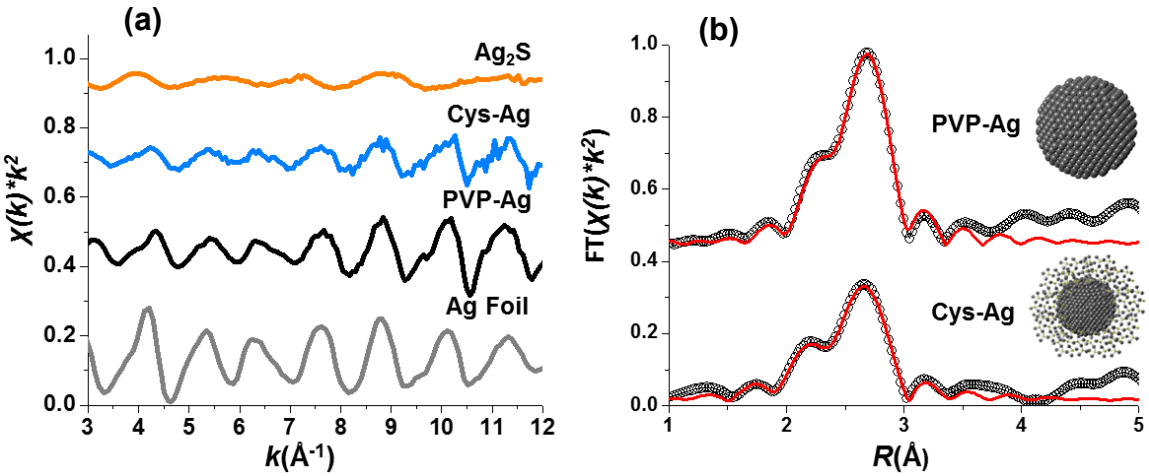

Figure 3.3. Ag K-edge EXAFS of PVP- and Cys-Ag NPs. (a) k^2-weighted EXAFS spectra of the Ag NPs and references, (b) *R*-space spectra of the NPs along with the refinements. The experimental data is represented by black circles while the refinements are the red lines. The proposed surface structures (without ligands) of each NP are schematically illustrated above their corresponding spectra.

The *R*-space spectra were then refined to determine bonding and surface structural information about the Ag NPs. As the oxygen (O) and nitrogen (N) containing functional groups of PVP are responsible for the surface protection of the NPs,[121,122,210] theoretical bonding paths of Ag-O, Ag-N, and Ag-Ag were included the initial *R*-space refinements for the PVP-Ag NP sample. However, the Ag-O, Ag-N, paths led to unphysical results and were not considered further. Although O and/or N are likely responsible for the protection of the PVP-Ag NP surfaces, a reasonable refinement was only achieved with a single Ag-Ag bonding path, given the relatively low percentage of surface atoms coordinated with O or N (Figure 3.3b). For the Cys-Ag NPs, a reasonable refinement was obtained with Ag-Ag and Ag-S bonding paths consistent with previous work[75] (Figure 3.3b). The refinement values for both samples are presented in Table 3.1.

Table 3.1. Ag K-edge *R*-space refinement results for PVP- and Cys-Ag NPs. The uncertainties of the refinement values are given by the numbers in parentheses.

Sample	Bond	CN	R (Å)	σ^2 (Å^2)	ΔE_o (eV)
Cys-Ag NPs	Ag-Ag	7.0(5)	2.87(2)	0.003(1)	-2(1)
	Ag-S	0.9(2)	2.53(2)	0.006(5)	-4(2)
PVP-Ag NPs	Ag-Ag	10.9(8)	2.87(1)	0.004(1)	3(1)

The Ag-Ag bond length results confirm the presence of metallic Ag in both NPs, as the bond length of 2.87 Å was also observed for the Ag reference foil refinement. The Ag-Ag CNs of the PVP-Ag and Cys-Ag NPs are also expectedly lower than bulk Ag (*i.e.,* Ag-Ag CN = 12), due to the increase of lower coordinated surface atoms in the NPs. Therefore, the Ag-Ag CN of 10.9 for the PVP-Ag NPs is consistent for NPs of this size; however, the Cys-Ag NPs exhibit a remarkably lower Ag-Ag CN of 7.0. The much smaller Ag-Ag CN can be explained by the Ag-S component for the Cys-Ag NPs. Given that the percentage of surface atoms for Ag NPs of this size can be estimated to be approximately 25-30 % calculated from model FCC metal NPs,[184] an average Ag-S CN of 0.9 would correlate to around 3.0-3.5 S per surface Ag if S was only on the surface. This CN is unrealistic as it is much larger than those of metal-thiolate (Ag-S CN ≈ 1) or staple (Ag-S CN ≈ 1-2) structures,[99,100] and therefore suggests the S is incorporated into a sulfide-like phase (*e.g.,* Ag_2S Ag-S CN ≈ 3[186]). Moreover, the Ag-S bond length of 2.53 Å is within the bond length distribution of Ag_2S (*i.e.,* 2.49-3.07 Å)[186] versus a typical metal-thiolate bond of Au-S (2.3-2.4 Å).[189] Therefore, the overall structure of the Cys-Ag NP is proposed to be a Ag core encompassed by a sulfide-like shell and surface thiolates (see Figure 3.3b for schematic illustration). On the other hand, the PVP-Ag NPs exhibit a

completely metallic core and surface based on its CN and bond length information (see Figure 3.3b for schematic illustration).

In order to support the proposed structures determined from the Ag K-edge EXAFS, the Ag L_3-edge XANES of the NPs were compared to reference materials. The first feature of the Ag L_3-edge XANES spectra (historically referred to as the "whiteline") is derived from electron transitions into Ag 4d-orbitals, and therefore is indicative of oxidation state.[96,155,156] From Figure 3.4, the PVP-Ag NPs whiteline is slightly less intense than the Ag foil whiteline, which is consistent with other metallic Ag NPs.[158] On the other hand, the whiteline of the Cys-Ag NPs is between the Ag foil and the Ag_2S references indicating Ag^+, which can be attributed to the sulfide in the Cys-Ag NPs.

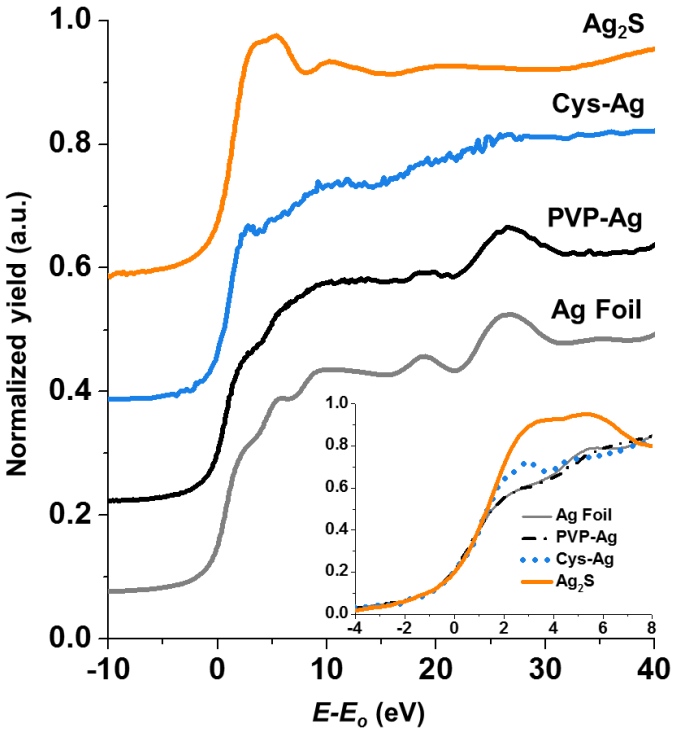

Figure 3.4. Ag L_3-edge XANES of PVP- and Cys-Ag NPs. Spectra of the Ag NPs and bulk references are stacked to show overall oscillation comparison and overlapped (inset) to show relative whiteline position and intensity. For clarity, the dotted line and dashed-dotted line represent the Cys-Ag and PVP-Ag NPs, respectively, in the inset figure.

S K-edge XAS can also provide details regarding the surface of the Cys-Ag NPs from the ligand perspective. First, the k^2-weighted S K-edge EXAFS (Figure 3.5a) show similar oscillations to the Ag_2S reference, indicating a similar local environment for S. The k^2-weighted spectra were then Fourier-transformed to *R*-space and show similar S-Ag bonding profiles (Figure 3.5b).

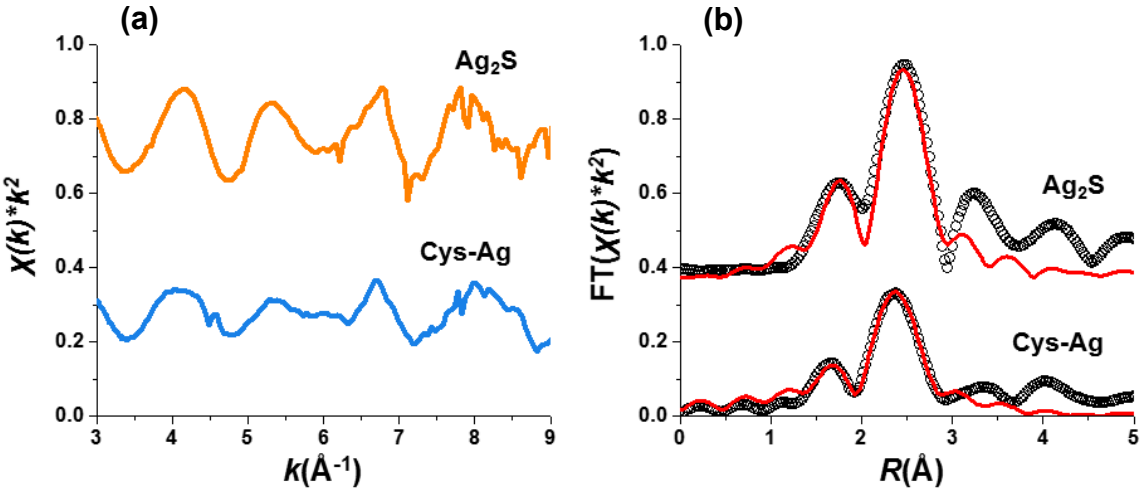

Figure 3.5. S K-edge EXAFS of Cys-Ag NPs. (a) k^2-weighted S K-edge EXAFS spectra of the Cys-Ag NPs compared to bulk Ag_2S (b) S *R*-space spectra with overall refinements for each sample. The experimental data is represented by black circles while the refinements are the red lines.

The S K-edge *R*-space spectra were then refined with S-Ag paths for both the Ag_2S and Cys-Ag NP spectra, along with a second S-C path for the Cys-Ag NPs. The overall refinements are presented in Figure 3.5b with the values given in Table 3.2. First, the S-Ag CN of 2.5 is higher than a staple structure (S-Ag CN = 2),[99,100] and in combination with the Ag K-edge EXAFS results, supports a similar bonding structure to that of Ag_2S (S-Ag CN ≈ 5). In this case the average S-Ag CN is lower than that of bulk sulfide due to a smaller number of neighbouring atoms on the surface of the NPs.

Furthermore, the S-C CN of 0.4 demonstrates S-C bond cleavage in the Cys, which has also been previously observed for thiolate adsorbed to Ag NPs and bulk Ag.[75,187] The S-Ag bond lengths are also indicative of a sulfide; however, it should be noted that there was a slight difference between the Ag-S and S-Ag bond lengths obtained by Ag EXAFS and S EXAFS (*i.e.,* 2.53 vs 2.47 Å). This difference has been previously observed[75] and is thought to originate from the different *k*-range used (*i.e.*, k = 2.5-12 Å^{-1} for Ag and k = 2.5-9 Å^{-1} for S), in addition to the different mode of EXAFS collection (*i.e.,* fluorescence vs. total electron yield).

Table 3.2. S K-edge *R*-space refinement results for Cys-Ag NPs and Ag_2S. The uncertainties of the refinement values are given by the numbers in parentheses.

Sample	Bond	CN	R (Å)	σ^2 (Å^2)	ΔE_o (eV)
CYS-Ag NPs	S-Ag	2.5(4)	2.47(3)	0.009(3)	-2(1)
	S-C	0.4(3)	1.79(3)	0.01(1)	-2(1)
Ag_2S	S-Ag	5(1)	2.50(3)	0.008(3)	-3(2)

S K-edge XANES can also be used to determine surface structural features of the Cys-Ag NPs (Figure 3.6). For the cysteine and Ag_2S reference spectra, the XANES features are caused by S-C and S-Ag resonances,[155] respectively, and have been shown to decrease in intensity and broaden for other thiolate-protected NPs relative to thiol references.[75] Taken in combination with the fact that the water-solubility of the Cys-Ag NPs is given by amine or carboxylic acid groups from the Cys, thiolates are also likely present on the surface of the NPs. At the same time, the Cys-Ag NP spectrum lacks the size-dependent pre-edge feature around -2 eV (E-E_o), which arises from S-metal interactions in thiolate-protected NPs.[75,155] Since the Cys-Ag NPs here are much larger

than other thiolate-protected Ag NPs that exhibit this feature (*i.e.,* 7.7 nm vs. 4.0 nm),[75] the lack of the pre-edge feature (see Figure 1.9b) demonstrates that the sulfide layer on the NPs is thick enough to prevent direct S interaction between the NP metal core and Cys ligands.

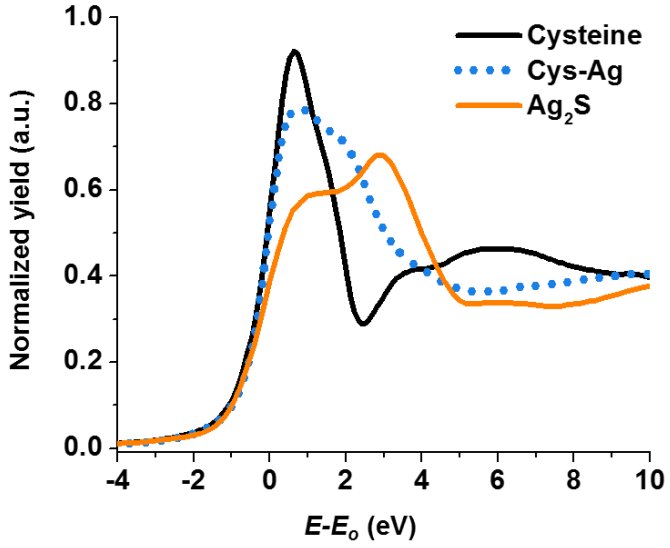

Figure 3.6. S K-edge XANES of Cys-Ag NPs. Spectra of the Cys-Ag NPs with cysteine and Ag_2S reference materials are overlapped

Based on the Ag and S XAS presented, a clear distinction can be made between the surface of the PVP-Ag and Cys-Ag NPs. The PVP-Ag NPs exhibit a metallic core and surface, owing to the relatively weak interactions between O and N functional groups of the PVP.[121,122,211] On the other hand, the Cys-Ag NPs exhibit a sulfide-like shell around a metallic core as a result of sulfidation by the Cys ligands. This type of sulfidation by organosulfur ligands has been previously seen in both dodecanethiol (DDT) protected Ag NPs[75] and DDT and octadecanethiol (ODT) protected palladium NPs prepared in organic solvents.[197] In this context, it is also interesting to note the more recently determined surface structure of thiolate-protected Ag_{44}[84,103] and Ag_{62}[203] nanoclusters (NCs), which

exhibit a similar sulfide-like surface around a metallic core. Although the syntheses used to prepare the Ag_{44}, Ag_{62}, and DDT-Ag NPs were quite different than the synthesis used here, the formation of a similar sulfidized surface in each case presents an interesting trend that may have implications in the synthesis and structural characterization of other thiolate-protected Ag nanomaterials. Moreover, this type of surface structure has practical implications towards Ag NP antibacterial activity, which is demonstrated in the following section.

3.5.3 Antibacterial Activity

MIC assays against both Gram-positive and Gram-negative bacteria were carried out and the results are presented in Figure 3.7. For Gram-positive *S. aureus,* the Cys-Ag NPs exhibited an MIC of 580 μM, which is approximately eight times the MIC of the PVP-Ag NPs at 70 μM. Taking into account that thick peptidoglycan layers may prevent the penetration of whole Ag NPs into Gram-positive bacteria,[37] the antibacterial effect of Ag NPs against Gram-positive bacteria is likely derived from Ag^+, which can still traverse the peptidoglycan layers.[37,212] In the case of the Cys-Ag NPs, their sulfide-like surfaces likely inhibited Ag^+ dissolution,[110] and therefore caused a much higher MIC than the PVP-Ag NPs, as the weakly adsorbed PVP ligands would not inhibit the release of Ag^+.[33,46,110]

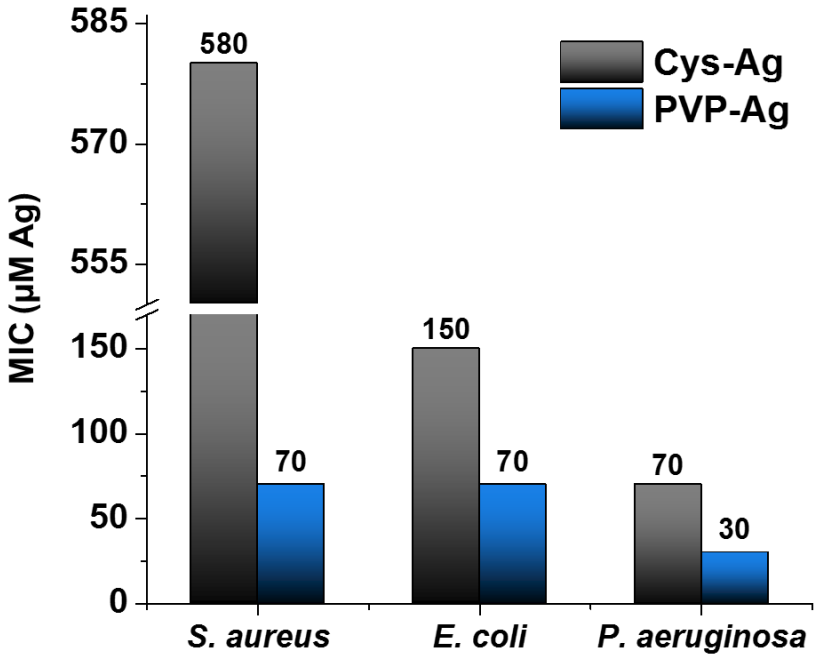

Figure 3.7. MIC values of the Cys-Ag and PVP-Ag NPs after 20 hours.

On the other hand, the MICs of the Cys-Ag and PVP-Ag NPs against both types of Gram-negative bacteria were much closer. For *E. coli*, the Cys-Ag and PVP-Ag NPs exhibited MICs of 150 μM and 70 μM, respectively; while for *P. aeruginosa,* the Cys-Ag and PVP-Ag NPs exhibited MICs of 70 μM and 30 μM, respectively. The more comparable MICs are likely the result of similar penetration of the identically sized PVP-Ag and Cys-Ag NPs and their subsequent surface-related reactions.[37,38,43,213] It is noted that inhibited Ag^+ dissolution in the Cys-Ag NPs could have contributed to a lower activity; however, this effect appears to be less significant to the overall activity for Gram-negative bacteria than for Gram-positive bacteria. In addition, the higher antibacterial activity of both types of Ag NPs against *P. aeruginosa* agrees with other studies of PVP-Ag NPs[47] and Cys-Ag NPs.[52] Overall, the Cys-Ag NPs exhibited consistently lower activity than the PVP-Ag NPs for both Gram-positive and Gram-

negative bacteria, which demonstrates the impact of sulfidized surface structure on Ag NP antibacterial properties.

3.6 Conclusion

In summary, we elucidated the surface structure of Cys-Ag NPs prepared in aqueous solution. The Cys-Ag NPs were found to have metallic cores surrounded by sulfide-shells, based on a multi-element, multi-edge XAS characterization. The type of surface structure observed here was comparable to the surface structures of thiolate-protected Ag NPs[75] and thiolate-protected Ag_{44}[84,103] and Ag_{62}[203] clusters, showing similar local structure of Ag and S. The Cys-Ag NPs were compared to identically-sized PVP-Ag NPs which exhibited a metallic Ag surface protected by weakly coordinated N and O from the PVP. The antibacterial activity of both types of Ag NPs were then examined against Gram-positive and Gram-negative bacteria. From this it was found that the Cys-Ag NPs exhibited lower antibacterial activity for each of the bacteria tested. In particular, the MIC values of the Cys-Ag NPs were eight times higher for *S. aureus*, but only two times higher for *E. coli* and *P. aeruginosa*. These results suggest that the antibacterial activity of the Cys-Ag NPs is inhibited by their sulfide-shell, but that they are still effective towards Gram-negative bacteria. Therefore, both the Cys-Ag NPs and PVP-Ag NPs show promise for their antibacterial activity, but a more thorough examination of cytotoxic activity against cultured mammalian cells must be carried out in order to fully evaluate their therapeutic potential. Overall, this work shows the importance of the surface structure in mediating antibacterial activity and may help guide the application of Ag NPs currently being investigated.

Chapter 4 - The Structure of Tiopronin-protected Nanoclusters in a One-dimensional Assembly and Their Antibacterial Activity

Sections 4.3-4.5 and 4.7 are reproduced in part with permission from: Padmos, J. D.; Boudreau, R. M.; Weaver, D. F.; Zhang, P. Structure of tiopronin-protected nanoclusters in a one-dimensional assembly. *Journal of Physical Chemistry Part C* **2015**, 119, 24627. *Section 4.6 is a follow-up study which has not yet been published.*

4.1 Contributions

J.D.P. synthesized the NPs, carried out the general characterization, conducted the XAS experiments, and wrote the manuscript. R.M.B. carried out the antibacterial activity assays. D.F.W. supervised R.M.B.. P.Z. carried out the wavelet-transform analysis, supervised J.D.P., and helped revise the manuscript.

4.2 Foreword

The studies described in Chapters 2 and 3 examined the surface structure of Ag NPs protected by thiolates in both organic and aqueous phases. Based on the highly sulfidized surface structures that were found in both cases, it is of great interest to examine other thiolate ligands and their effect on surface structure and antibacterial activity. Since a greater understanding of surface structure is enabled by having more surface area to study, we utilized methods to prepare smaller nanoparticles, or nanoclusters, thereby enabling a greater amount of surface area to be examined from the

Ag perspective. Therefore, this chapter describes the effect of tiopronin on the surface structure of the Ag nanoclusters, as well as their antibacterial activity.

4.3 Introduction

Noble metal nanoclusters (NCs), which contain metal atoms on the order of tens or hundreds, have drawn significant interest owing to their unique physicochemical properties that are in between single atoms and larger nanoparticles (NPs, usually > 2 nm).[14,214] The unique properties of NCs have initiated their application in many fields of science such as biological sensing,[1,4] antibacterial applications,[215–217] and catalysis,[1–3] to name a few. Several different types of metal NCs have been synthesized using protecting ligands such as proteins,[93] peptides,[4,218] and dendrimers,[219] although the most well-researched NCs are those prepared with thiols as they provide high stability, small cluster size, and low size distributions as a result of the strong metal-thiolate bonding.[84–87]

Many NC properties are derived from their unique surface structures and the nature of the interaction between surface atoms and the protecting ligands. For example, in the case of Au NCs, thiolates have been shown to induce discrete surface structures with "staple" motifs (-RS-Au-SR-) which have translated to their incredible stability and interesting surface related properties.[87,98,100,220,221] However, some thiolate-protected silver (Ag) NCs have exhibited more sulfidized surface structures. For example, the recently elucidated crystal structures of $Ag_{44}(SR)_{30}$ NCs (Ag_{44} NCs for short, SR = SPhF, $SPhF_2$ or $SPhCF_3$) exhibit both Ag_2S and Ag_2S_5 subunit structures on the surface of metallic Ag, which are suggested to be the reason for their "ultrastability" as well as their unique electronic properties.[84,222] Slightly larger $Ag_{62}S_{13}(SBu^t)_{32}(BF_4)_4$ NCs (Ag_{62} NCs for short) exhibit even more highly sulfidized surfaces with very little metallic Ag in their

cores, and their enhanced luminescence was attributed to this.[104] Furthermore, larger Ag NPs protected by thiolates have also shown high sulfidation at their surfaces,[58,137] and this was suggested to hinder their antibacterial effects in some cases.[58] Hence, sulfidation at the surface of Ag NCs or NPs as a result of thiolate ligands is an emerging trend in both NC and NP synthesis, and has far reaching implications for both understanding the surface structures of Ag NCs/NPs and their application to various fields. Therefore, understanding the effect of other thiols on the surface structure of Ag nanomaterials is an important and ongoing topic of research.

It has been found that the ligands that protect NCs/NPs not only play a significant role in determining their surface structures, but they can also determine their overall assembly into larger superstructures.[207,223–226] The assembly of NCs/NPs is becoming an important concept, as their spatial orientation can potentially provide new properties which can be exploited for different applications.[76] For the most part, assembly of NCs/NPs in colloidal suspensions is driven by weak interactions between ligand molecules, and can differ depending on the type of ligand, ligand side groups, and overall ligand size.[76,207,223,224] Interestingly, a recent study showed that 2-mercaptopropionylglycine (commonly known as tiopronin) induced the formation of one-dimensional (1D) chains of separated Ag NPs.[225] This finding alone could have many different implications for biomedical or plasmonic applications, although it remains to be answered how the surface structure of the individual NCs are affected by the tiopronin and what effect of the arrangement on its practical applications will be. These answers will undoubtedly provide important information that will be useful for their future applications which rely on the surface chemistry and assembly of the NCs.

Therefore, the main objective of this work is to distinguish the surface structure of Ag NCs protected by tiopronin. Typically, X-ray diffraction (XRD) has been the main tool employed to study the surface structure of metal NCs. However, XRD is limited by the difficulty in achieving completely uniform sizes and single crystals of the NCs/NPs required for this technique. As an alternative, X-ray absorption spectroscopy (XAS) can be utilized to provide an element-specific perspective of NC surface structure.[87] Normally for thiolate-protected Ag NCs/NPs, both the metal (Ag) and ligand (S) can potentially be probed by XAS for their local coordination environments, although in the case presented here, the Ag NCs are also mixed with excess Ag^+-thiolates, adding further complexity to the elucidation of surface structure. Therefore, we utilize a recent wavelet-transformed XAS analysis method along with advanced multi-path XAS analysis to distinguish the surface structure of Ag NCs protected by tiopronin. In addition to this comprehensive atomic structure characterization, the antibacterial activity of these NCs was examined to explore the potential scaling effects of the NCs with a higher surface area compared to larger Ag NPs, as well as the effect of their unique assembly.

4.4 Experimental

4.4.1 Synthesis of Ag Nanoclusters (NCs)

Silver nitrate ($AgNO_3$, 99.9+ %) was purchased from Alfa Aesar. Sodium borohydride ($NaBH_4$, 99 %) and 2-mercaptopropionylglycine (tiopronin, 98 %) were purchased from Sigma-Aldrich. Nitric acid (HNO_3(aq), 67−70 % (w/w)) was purchased from Caledon Laboratory Chemicals and Hydrochloric acid (HCl(aq), 36.5−38.0 % (w/w)) was purchased from ACP Chemicals. All water used in these experiments was from a Barnstead NANOpure DIamond UV ultrapure water system (Deionized, 18.2

MΩ·cm). The Ag NCs were synthesized using a similar procedure to Hwang et al. with minor modifications.[227] First, 0.034 grams of $AgNO_3$ (0.2 mmol) was added to 20 mL of ultrapure water and allowed to stir in an ice bath. Tiopronin (0.032 g, 0.2 mmol) was then added to the solution and allowed to mix for 30 minutes. After the mixing time, 0.014 g of $NaBH_4$ (0.4 mmol) was added to initiate the reduction of the Ag under vigorous mixing. The solution was allowed to mix for 2 hours in the ice bath. Laboratory grade methanol (100 mL) was then added to the solution and centrifuged (2000 *g*) to precipitate the NCs. The solution was decanted and the NCs were then washed three times with methanol (3 x 50 mL) and once with laboratory grade acetone (1 x 50 mL). The acetone was completely removed by vacuum and the final product was redispersed into water. The NC solution was then dialysized (Spectra/Por CE, MWCO 14000) over a period of 3 days, refreshing twice per day. In addition to the NCs, a Ag^+-thiolate reference was also prepared with the same amount of $AgNO_3$/tiopronin in 20 mL of ultrapure water and allowed to stir for 30 minutes in an ice-bath. The Ag^+-thiolate reference then underwent the same purification procedure as the NC solution. The purified solutions were then stored as solutions in sample vials, sealed under Argon and refrigerated (4 °C).

4.4.2 General Characterization

Immediately after purification, UV-visible spectroscopy (UV-vis) was carried out on the NCs and Ag^+-thiolate sample using a Varian Cary 100 Bio UV-visible spectrophotometer. A 50 µL aliquot of each solution was diluted into 3 mL with water and placed into quartz cuvettes. Spectra were then recorded from 300 to 800 nm and both sample spectra were corrected for background effects with a water reference. The morphology of the NCs was then examined by transmission electron microscopy (TEM)

using a Philips Technai-12 TEM operating at 80 kV. To prepare the NC sample for TEM, a 20 μL aliquot of a diluted NC solution was dropped onto a Formvar-coated copper TEM grid (Electron Microscopy Sciences) and allowed to dry overnight (covered, room temperature). Images from TEM were then captured at a variety of magnifications while ensuring no morphological changes occurred from the electron beam. Individual NCs were counted from the recorded images and their size distribution was measured using ImageJ image processing software.[143] To measure the concentration of Ag in the NC and Ag^+-thiolate samples, inductively coupled plasma optical emission spectroscopy (ICP-OES) was carried out with a PerkinElmer Optima8000 (at 328.068 nm for Ag) with element standards provided by PerkinElmer. To prepare the samples for ICP-OES, a 20 μL aliquot of each sample was diluted to 1 mL water and heated to 80 °C. Then, 1 mL of HNO_3 was added to each and allowed to sit for 1 h at 80 °C to dissolve the Ag. Two mL of HCl was then added to each (forming aqua regia) and allowed to sit for an additional hour to dissolve any other metal impurities. The solutions were then cooled to room temperature and dispersed into 10 mL solutions for the ICP-OES measurements.

4.4.3 X-ray Absorption Spectroscopy (XAS)

Ag K-edge XAS was conducted at the Advanced Photon Source (BM-20 beamline) at Argonne National Laboratory, Argonne, IL, USA. Ag L_3-edge XAS was conducted at the Canadian Light Source (SXRMB beamline, Saskatoon, SK, Canada). In preparation for solid-phase XAS measurements, the water from the purified solutions was removed by freeze-drying the solutions into powders. For Ag K-edge XAS, the powders were wrapped in kapton and loaded into the sample holder. The sample holder was placed into a cryostatic chamber, which was then set to 50 K. Ag K-edge spectra were collected

with a 32-element solid-state Ge X-ray fluorescence detector with simultaneous Ag foil reference spectra collected with standard gas-ionization chamber detectors. For Ag L_3-edge XAS, the powdered samples were attached to the sample holder with double-sided carbon tape. The sample holder was then placed into the SXRMB sample chamber and allowed to reach an ultrahigh vacuum atmosphere before collecting Ag L_3-edge spectra with a four-element silicon drift detector. All of the XAS spectra were processed with the WinXAS software program.[162] The x-axes of the spectra were first normalized to the absorption energies (Ag or S) and then the y-axes were normalized to exhibit a difference of one between the pre-edge and post-edge. For the Ag L_3-edge X-ray absorption near-edge structure (XANES) data, the normalized spectra were used for qualitative comparisons to references. For extended X-ray absorption fine structure spectroscopy (EXAFS) analysis of Ag K-edge, the raw data were k^2-weighted, Fourier-transformed by using of a Hanning function from $k = 3-12$ Å^{-1}, and then refined with WinXAS from $R = 1.5-3.3$ Å (for two-path refinements) or $R = 1.5$-3.6 Å (for three-path refinements). An amplitude reduction factor (S_o^2) of 0.95 was held constant during the refinements, which was based on bulk Ag R-space refinement collected at 50 K. *Ab initio* simulations of Ag structural models were obtained from the FEFF 8.2 code in order to refine the experimental data.[164,165] The refinements calculated structural information about the NCs, including coordination numbers (CNs), bond lengths (R), Debye-Waller coefficients (σ^2), and E_o shifts (ΔE_o). In addition, the Ag K-edge EXAFS spectra also underwent wavelet-transformation analysis using methods developed by Funke and Chukalina.[166] A Cauchy wavelet of order 400 was used for the wavelet-transformed EXAFS spectra with a k^2-weighting in the range of 2.5-10 Å^{-1}.

4.4.4 Antibacterial Activity

The antibacterial activity assays of the Ag NPs were conducted by R. Boudreau (DeNovaMed, Halifax, NS, Canada) based on a similar procedure described in section 3.4.4. The antibacterial activity of the NCs and Ag^{+}-thiolate were tested against *Staphylococcus aureus* (*S. aureus,* ATCC 29213)*, Escherichia coli* (*E. coli,* ATCC 23716)*,* and *Pseudomonas aeruginosa* (*P. aeruginosa,* ATCC 25619)*.*

4.5 Results and Discussion

4.5.1 General Characterization

The NCs were found to have average diameters of 2.0 ± 0.5 nm (Figure 1a) and were assembled into 1D chain-like arrangements approximately 2-5 μm in length (Figure 4.1b). The NCs can also be seen to form thicker bundles of the chains, although upon further magnification were still found to be slightly separated similar to those shown in Figure 4.1a.

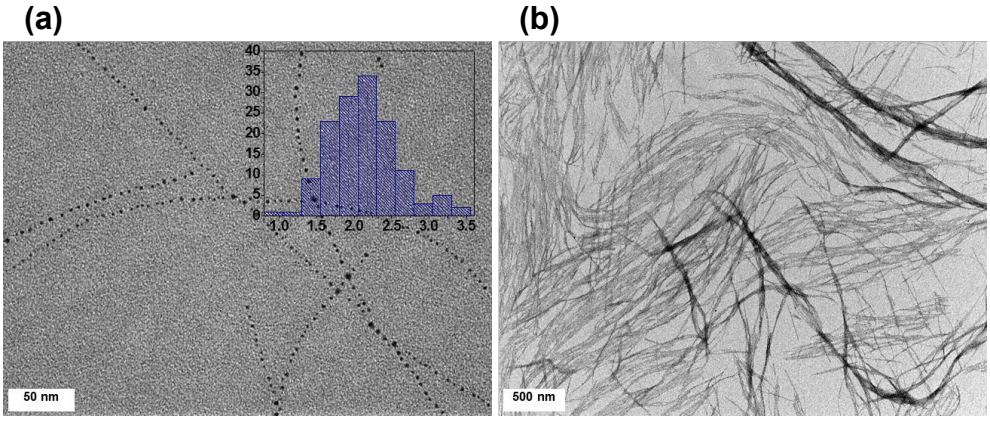

Figure 4.1. TEM images of the tiopronin-protected Ag NCs. (a) the average diameter of the NCs was 2.0 ± 0.5 nm (b) the NCs were arranged into 1D chains approximately 2-5 μm in length.

We propose that Ag^+-thiolate structures were formed during the prolonged mixing of $AgNO_3$/tiopronin, and are responsible for the final arrangement of the NCs. Indeed, Ag^+-thiolate formation was indicated by the observation of a cloudy yellow-white solution and by characteristic absorbance features shown in UV-vis (shown later), which are consistent with chain- and cyclic-type Ag^+-thiolate structures.[178,228,229] The addition of $NaBH_4$ then initiated the reduction of Ag^+ to form the NCs (indicated by a colour change of yellow-white to dark brown) which were subsequently protected by tiopronin. After this, the ligand interactions between the carboxylic acid side groups from the Ag^+-thiolate structures and the tiopronin on the NCs likely directed the observed superstructure assembly. In fact, these chain-like assemblies are similar to what was observed by Shiers et al.,[225] although their technique was reliant on the sonication of pre-synthesized Ag NPs; here the NCs simply assembled into the chained structures during their initial preparation.

It is also noted that the sizes of the NCs here were smaller than tiopronin-protected Ag NPs prepared by Shiers et al. (~ 4 nm)[225] and Huang et al. (~ 4.8 nm)[227] despite the use of the same 1Ag:1tiopronin ratios. We propose that the formation of the Ag^+-thiolate type structures during the prolonged mixing time could also account for the smaller NCs observed. In this way, it has been previously demonstrated that some low molecular weight thiols can form Ag^+-thiolate complexes with more than one Ag^+ atom per S.[230] Therefore, the formation of the Ag^+-thiolates during NC preparation could have modified the stoichiometry of Ag:S during the reduction step and produced a higher effective thiol concentration, thereby leading to the smaller sized NCs than previously observed for this ligand:metal ratio. In addition, the presence of the Ag^+-thiolates may

have inhibited the agglomeration of the reduced Ag by steric hindrance, leading to smaller NCs overall.

The Ag NCs also exhibited a UV-vis absorbance peak centered at 375 nm (Figure 4.2), which is at a shorter wavelength than what is typically observed for surface plasmon resonance (SPR)-related features of Ag NCs of this size. For example, Huang et al. demonstrated that tiopronin-protected Ag NCs/NPs exhibited SPR peaks at 380 nm (1.6 nm NCs), 390 nm (3.0 nm NCs/NPs), and 396 nm (4.8 nm NCs/NPs), and thus demonstrated a correlation of SPR wavelength to NC size.[227] Therefore, based on the 2 nm NCs here, we expected a SPR-related peak somewhere between 380-390 nm. Similar to this observation, Shiers et al. observed an almost identically positioned peak at 374 nm for their 4 nm Ag NCs,[225] which is also lower than the SPR range demonstrated by Huang et al. (*i.e.,* 390-396 nm). In order to determine the origin of this peak, we discuss the following scenarios.

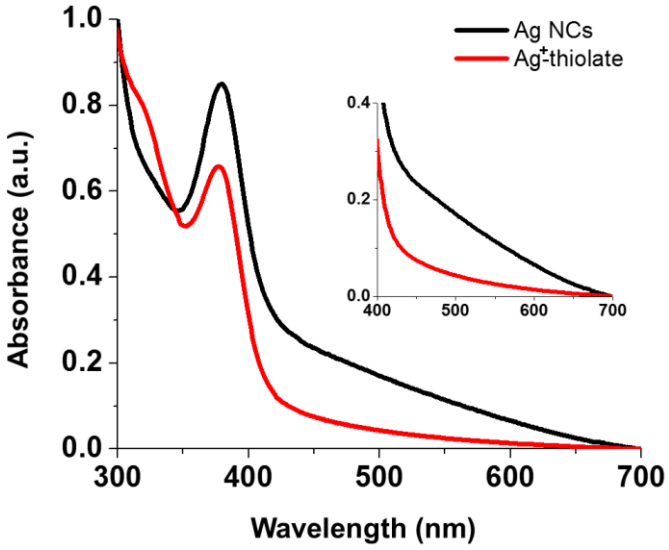

Figure 4.2. UV-vis spectra of Ag NCs and Ag^{+}-thiolate showing the major peak around 375 nm for both. The inset figure shows a zoomed in portion of the spectrum to show a broad feature around 500 nm for the Ag NCs.

First, a shorter than usual SPR wavelength could potentially be caused by the sulfidation of the Ag NCs. In this way, the Ag NCs would have comprised smaller metallic Ag cores than 2 nm, and therefore the potential SPR peak would manifest at a lower wavelength. For example, 0.7-1.1 nm Ag NCs have exhibited an SPR-related peak between 365-380 nm.[231] However, if the Ag NCs here were sulfidized so that the Ag cores were smaller, most likely any potential SPR peak would be dampened, or at least shifted to a higher wavelength as others have observed with larger Ag-core/sulfide shell NPs.[148] Nevertheless, a contribution to the peak at 375 nm from an SPR effect from the small Ag core is possible, but the fact that such an intense peak was observed likely suggests a different mechanism.

Second, we note that Ag_2S has molecular electronic transitions corresponding to wavelengths of 354 and 390 nm[232] and other Ag_2S nanomaterials have exhibited absorbance peaks between 340-370 nm.[233,234] In addition, we also note the presence of a small broad feature around 500 nm in the Ag NC absorbance spectrum (Figure 4.2 inset), which has also been exhibited by Ag-core/sulfide shell and Ag_2S NPs,[104,113,148,235] as well as other thiolate-protected Ag NCs.[215] Therefore, a potential sulfide component could have more directly contributed to the peak at 375 nm (and at ~ 500 nm), however, the peaks in these regions are generally broad, and most likely do not account for the observed intensity of the peak at 375 nm here.

Based on the above considerations, we propose that the peak observed is due to the excess Ag^+-thiolates which induce 1D assembly of the NCs. Ag^+-thiolates can exhibit intense peaks in this region, which are associated with ligand-to-metal charge transfer (LMCT) transitions that are modified by argentophilic interactions between neighbouring Ag^+---Ag^+ atoms, also known as ligand-to-metal-metal charge transfer (LMMCT).[215,236]

For example, sharp absorbance peaks have been observed for similar Ag^+-thiolates prepared with dodecanethiol (~350 nm),[75] cysteine (~360 nm),[237] mercaptoethanol (368 nm),[230] and glutathione (370 nm).[237] To confirm this possibility, we also show the UV-vis spectrum for the Ag^+-thiolate (Figure 4.2), which clearly shows a peak centered around 374 nm, in addition to a peak at 276 nm (shown later in Figure 4.9b), which is also indicative of Ag^+-thiolates.[75,230,237] We note that the peak at 374 nm is slightly less intense than the Ag NCs, which we believe is a result of the other contributing factors in the Ag NC sample (*e.g.,* Ag NCs may also have metallic SPR and sulfide absorbance). Therefore, we believe that the peak around 375 nm for these NCs, as well as the peak at 374 nm for the NCs prepared by Shiers et al., is mostly due to the presence of Ag^+-thiolates. On the other hand, the peaks between 380-396 nm for the NCs described by Huang et al. are likely caused mostly by a SPR-related effect, since there were little to no excess Ag^+-thiolates observed.[227] Overall, we determined that the optical properties of the Ag NCs here are mainly attributed to the Ag^+-thiolates, but likely have some contribution from the other components in the NCs. This gives a preview to the structure of the Ag NCs, but in order to more clearly deduce their atomic structure, we used synchrotron XAS, as described in the next section.

4.5.2 Structural Characterization by XAS

The effect of tiopronin on assembly of NCs is clear from TEM and corroborates previous studies. However, the question remains as to how the surface structure of the individual NCs is affected by the tiopronin ligands. Therefore, Ag K-edge EXAFS measurements were carried out in order to characterize their surface structure. The resulting k^2-weighted spectra of the NCs and bulk Ag_2S, Ag foil, and Ag^+-thiolate are

shown in Figure 4.3a. From their qualitative comparison, the NCs have oscillatory features similar to both metal and Ag_2S, which could signify the presence of both in the NCs. The k^2-weighted spectrum of the NCs was then Fourier-transformed to *R*-space and presented in Figure 4.3b. For comparison, the Ag^+-thiolate *R*-space spectrum is also presented and shows the major bonding feature centered around 2 Å which is derived from Ag-S bonding. The other significant feature in the NC spectrum around 2.7 Å can be ascribed to metallic Ag-Ag, however, it is significantly smaller in the Ag^+-thiolate, thereby denoting little to no metallic Ag in this sample.

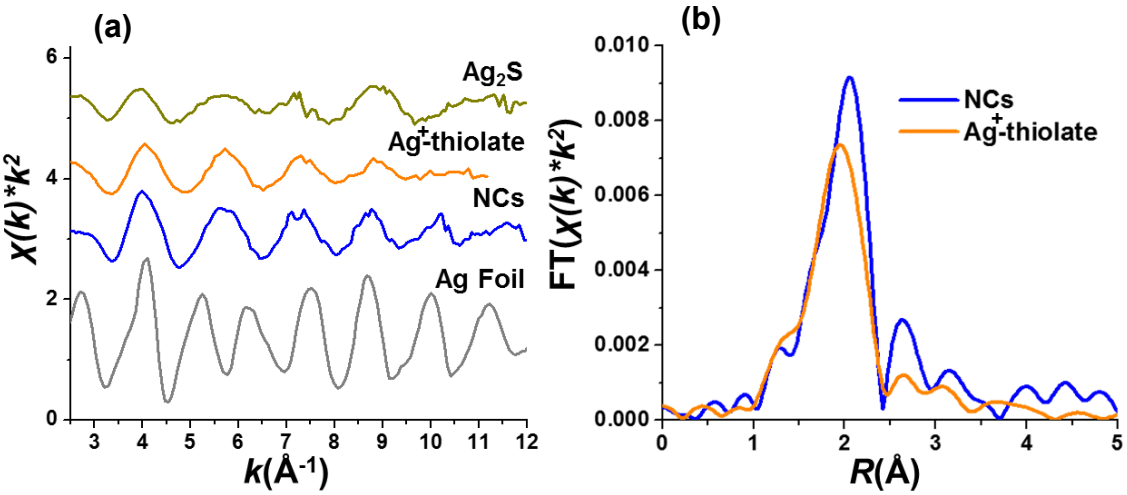

Figure 4.3. Ag K-edge EXAFS of Ag NCs and Ag^+-thiolate. (a) k^2-weighted Ag K-edge EXAFS and (b) *R*-space spectra of the NCs and Ag^+-thiolate samples.

Based on those assignments, a refinement of the *R*-space spectrum was performed with Ag-S and Ag-Ag bonding paths (Figure 4.4, values given in Table 4.1). The presence of metallic Ag in the NCs was confirmed by the Ag-Ag bond length of 2.90 ± 0.02 Å which is within the same range as metallic Ag-Ag. Remarkably, the Ag-Ag CN was far smaller than expected, showing 1.8 ± 0.6 for the NCs where theoretical metallic Ag NCs around 2 nm in diameter would exhibit Ag-Ag CNs on the order of 8-9.[184] The

dramatically lower than expected Ag-Ag CN could potentially be explained by the presence of sulfide-type Ag in the NCs;[58,75] however, even though the Ag-S average bond length is more suggestive of sulfide (Ag-S = 2.522 ± 0.007) than the thiolate type Ag-S bonding (Ag-S = 2.481 ± 0.007 Å), the Ag-S bonding in the NCs also reflects the contribution of the excess Ag^+-thiolate chains in the sample and is not conclusive evidence of a sulfide-type structure. Indeed, the refinements of the Ag^+-thiolate yielded a Ag-S CN of 2.6 ± 0.2 and is essentially the same as the Ag-S CN for the NCs. The observation of the Ag-S CN for the Ag^+-thiolate also demonstrates that a Ag-S complex did indeed form, although we cannot rule out the possibility of either Ag^+-thiolate chains (Ag-S CN = 2) or cyclic structures (Ag-S CN = 3).[178,228,229]

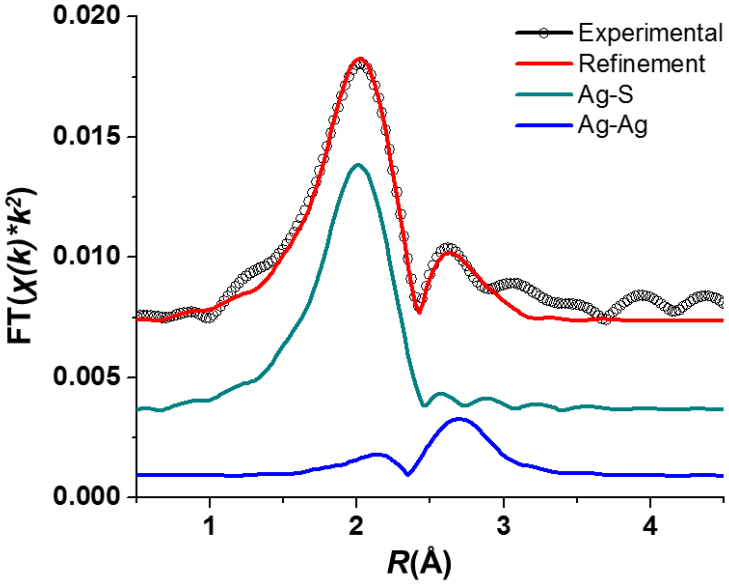

Figure 4.4. Refinement of the k^2-weighted *R*-space spectrum of the Ag NCs with Ag-S and Ag-Ag paths from 1.5-3.3 Å.

Table 4.1. Ag K-edge *R*-space refinement results for the Ag NCs and Ag^+-thiolate. The uncertainties of the refinement values are given by the numbers in parentheses.

Sample	Bond	CN	R (Å)	σ^2 (Å^2)	ΔE_o (eV)
NCs	Ag-S	3.1(3)	2.522(7)	0.006(2)	1(1)
	Ag-Ag	1.8(6)	2.90(2)	0.012(4)	-4(2)
Ag^+-thiolate	Ag-S	2.6(2)	2.481(7)	0.009(2)	0.5(7)

Therefore, in order to further explore the individual NC structure, wavelet-transform EXAFS (WT-EXAFS) analysis of the Ag-K-edge EXAFS was conducted.[166,167] This type of analysis allows for a more visual representation of the EXAFS data and can indicate other binding possibilities which can be overlooked in qualitative *R*-space analysis. Figure 4.5 displays 2D-contour plots of WT-EXAFS magnitudes of the NC and Ag^+-thiolate spectra. In both plots an intense peak centered around $R \sim 2$ Å and $k \sim 7$ Å^{-1} denotes the Ag-S bonding, while the peak around $R \sim 2.6$ Å and $k \sim 8$ Å^{-1} representing metallic Ag-Ag bonding in the NCs is noticeably absent in the Ag^+-thiolate sample. Interestingly, another significant peak around $R \sim 3.3$ Å and $k \sim 8$ Å^{-1} in the NCs can be observed from this analysis. Given that this peak occurs at around the same *k* value as the Ag-Ag, this is most likely also caused by Ag-Ag scattering, and is given the assignment of Ag-Ag_2. Based on the *R* value, as well as the intensity of the peak, we hypothesize that this Ag-Ag_2 bonding is attributed to sulfide-type Ag-Ag. On the other hand, the Ag^+-thiolate exhibits slightly less intense peaks at different *R* values (*i.e.,* 3.1 and 3.7 Å) which may signify the longer argentophilic Ag^+---Ag^+ type bonding of the Ag^+-thiolates.[236]

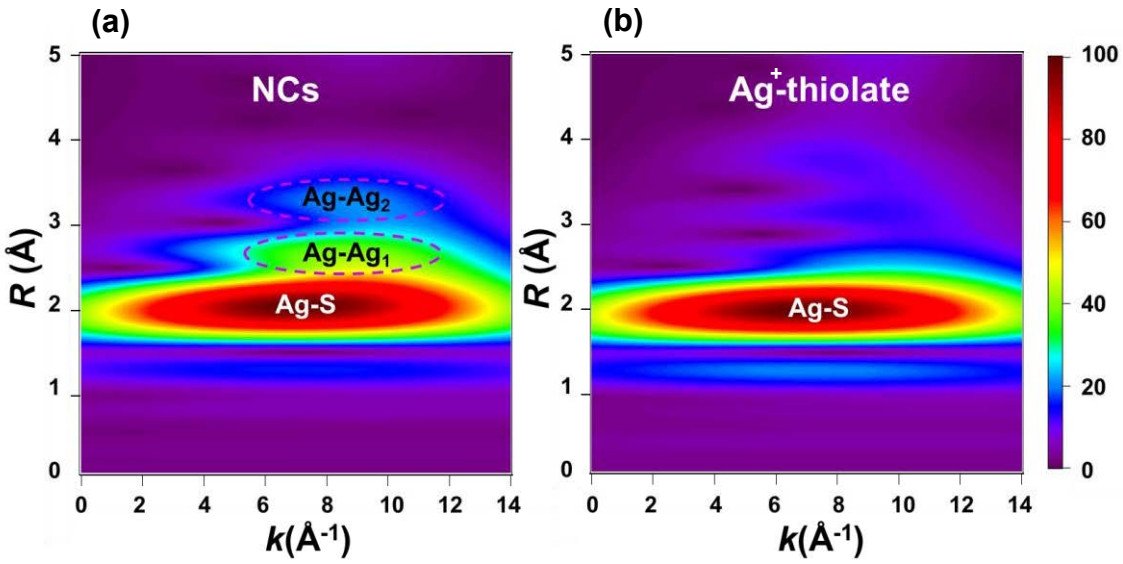

Figure 4.5. WT-EXAFS of Ag NCs and Ag^+-thiolate. (a) Ag NCs and (b) Ag^+-thiolate. The relative wavelet intensity is indicated on the right of the figure. The NCs show metallic Ag-Ag_1 bonding, as well as potential sulfide Ag-Ag_2 bonding, while the Ag^+-thiolate does not exhibit appreciable bonding of either type.

Unfortunately, the presence of excess Ag^+-thiolates in the NC sample convolutes the deduction of sulfide from the S K-edge (or Ag-S bonding from Ag K-edge), as well as convolutes any supporting evidence of S-C cleavage (needed for the generation of S^{2-} to form the sulfide).[58,75,104,112] However, based on the two types of Ag-Ag bonding implied by the WT-EXAFS analysis, we performed a three-path refinement of the *R*-space spectrum, similar to a technique used to study thiolate-protected Au NCs.[238] In this way, the *R*-space spectrum was refined with Ag-S and Ag-Ag paths first, and then the Ag-S path was held constant in the subsequent three-path refinements with Ag-S, Ag-Ag_1 (metal-type) and Ag-Ag_2 (sulfide-type). The resulting refinement is shown in Figure 4.6 with the values shown in Table 4.2.

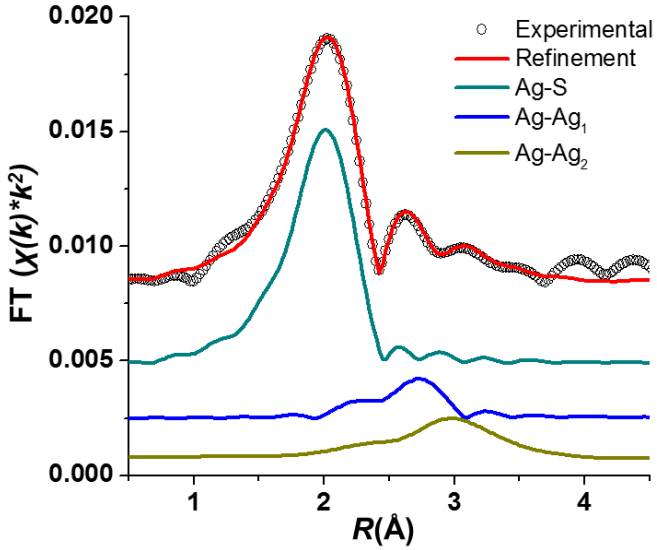

Figure 4.6. Refinement of the k^2-weighted *R*-space spectrum of Ag NCs with Ag-S, Ag-Ag$_1$, and Ag-Ag$_2$ paths from 1.5-3.6 Å.

The refinement of the NC *R*-space spectrum clearly demonstrates a shorter metal-type Ag-Ag bonding around 2.89 Å (Ag-Ag$_1$) and longer sulfide-type Ag-Ag bonding around 3.10 Å (Ag-Ag$_2$). Furthermore, the Debye-Waller factor (σ^2) of the Ag-Ag$_1$ path was 0.004, while the sulfide Ag-Ag$_2$ yielded a larger σ^2 larger value of 0.03, consistent with the more disordered sulfide structure. Interestingly, the distribution of the Ag-Ag$_1$ and Ag-Ag$_2$ CNs imply that the NCs are mostly composed of sulfide-type Ag, which is remarkably different from what has been proposed for previously prepared NCs/NPs protected by tiopronin.[225,227]

Table 4.2. Three-path Ag K-edge *R*-space refinement results for the Ag NCs. The uncertainties of the EXAFS refinement values are given by the numbers in parentheses.

Sample	Bond	CN	R(Å)	σ^2 (Å^2)	ΔE_o (eV)
NCs	Ag-S	3.1(3)	2.522(7)	0.006(2)	1(1)
	Ag-Ag$_1$	0.6(3)	2.894(9)	0.004(3)	2(1)
	Ag-Ag$_2$	5(1)	3.10(3)	0.029(9)	2(1)

Ag L_3-edge XANES was also conducted on the NCs and the Ag^+-thiolate in order to compare their oxidation states to reference materials. The oxidation states can be qualitatively compared by the Ag L_3-absorption edge intensity which describes electronic transitions into Ag 4d-orbitals.[96,155,156] From Figure 4.7, the NCs exhibit an absorption edge (at 0 eV, E-E_o) intensity between the Ag_2S and Ag foil references, consistent with the mixed oxidation states in the NC sample (metal and sulfide). The Ag^+-thiolate also exhibits a similar spectrum to the NCs, although the absorption edge of the NCs is lower in intensity suggesting their slightly more metallic composition.

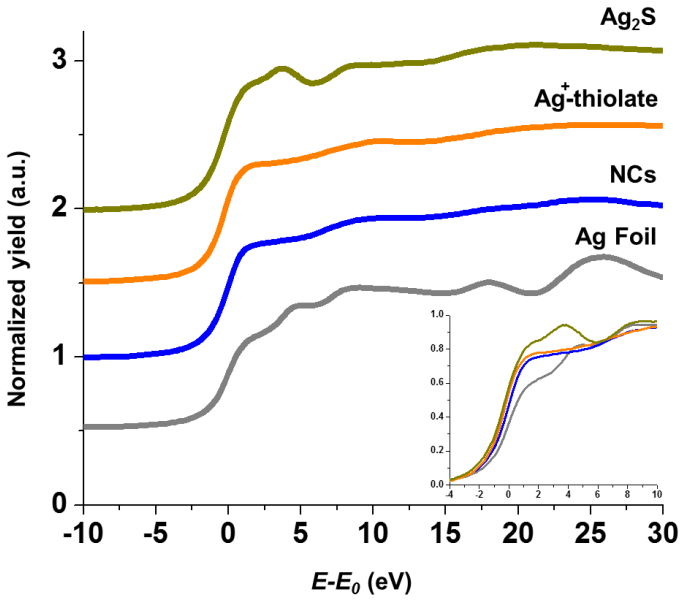

Figure 4.7. Ag L_3-edge XANES spectra to show overall oscillation comparison and overlapped (inset) to show relative whiteline position and intensity.

The presence of both metallic- and sulfide-type Ag is clear from both the Ag K- and L_3-edge XAS analysis, but we also note that the surface coordination environments of the NCs bear a resemblance to recently elucidated Ag_{44} and Ag_{62} NCs with similar sizes (*e.g.,* 1.5-2.5 nm). In this way, both the Ag_{44} and Ag_{62} NCs exhibit similar Ag-S (2.3-3.0 Å), metal type Ag-Ag_1 (2.8-2.9 Å), and sulfide-type Ag-Ag_2 (3.0-3.5 Å) as the NCs here.

Furthermore, the Ag-S, Ag-Ag_1, and Ag-Ag_2 CNs of NCs (3.1 ± 0.3, 0.6 ± 0.3, 5 ± 1, respectively) are remarkably similar to the expected CNs of Ag_{62} NCs (3, 0.4, 4.2, respectively[104]). Therefore, we propose a similar metal-core/sulfide-shell structure for the tiopronin-protected NCs. This is an interesting finding in itself, as the preparation technique used to prepare the Ag_{62} NCs, as well as the thiol, were completely different than those used to prepare the Ag NCs here. This similarity suggests a similar mechanism of surface protection, as well as the potential to have similar physicochemical properties. However, the superstructure of the NCs here are completely different (*i.e.,* 1D chains), which could translate to differences in their properties compared to the Ag_{62} NCs. For these reasons, further studies to examine the similarities and differences relative to Ag_{62} NCs would be worthwhile.

4.5.3 Antibacterial Activity

The antibacterial activity of Ag NCs/NPs has been related to both surface enhanced effects of Ag, as well as Ag^+ released from their surfaces.[37,41,42,45–47,57,61,127,217] Therefore, given that the NCs were mostly composed of sulfide, we expected the antibacterial activity of the Ag NCs to be negligible. On the contrary, MIC assays against *S. aureus*, *E. coli*, and *P. aeruginosa* demonstrated antibacterial activities of 620, 150, and 150 μM Ag, respectively (Figure 4.8). The NCs were also more effective against Gram-negative bacteria than Gram-positive bacteria, which is consistent with MIC values of other Ag NPs that were protected by cysteine (Cys-Ag NPs) described in Chapter 3.[58] The MICs of the NCs were almost identical to the MICs of Cys-Ag NPs against each type of bacteria, despite the fact that the NCs here were composed of more sulfide-type Ag on their surfaces. We expected that the NCs would have had a much lower activity from the

reduced Ag dissolution from their surfaces. In this case, the extra surface area of the NCs (given the smaller size compared to the Cys-Ag NPs) may have increased the dissolution of the metallic Ag, thereby leading to similar MIC results between the NCs and the Cys-Ag NPs. In addition, it is not clear how the Ag^+-thiolate affected the antibacterial mechanism of the NCs here, although, we also found that the Ag^+-thiolate had antibacterial activity towards the bacteria. For the Gram-positive bacteria, the Ag^+-thiolate was much less active demonstrating an MIC of 4000 μM; however, the Ag^+-thiolate had closer MIC values to the NCs, demonstrating MICs of 500 and 250 μM Ag towards *E. coli* and *P. aeruginosa*, respectively. Thus, the Ag^+-thiolate also appears to show preferential activity towards Gram-negative bacteria, which can potentially help indicate the mechanism of the NC's antibacterial activity. However, given the multiple components of the NCs (*i.e.,* metal, sulfide, Ag^+-thiolates), there are likely a combination of factors that cause their observed antibacterial activity. Nonetheless, these results may indicate a potential usefulness for future antibacterial applications against different types of bacteria.

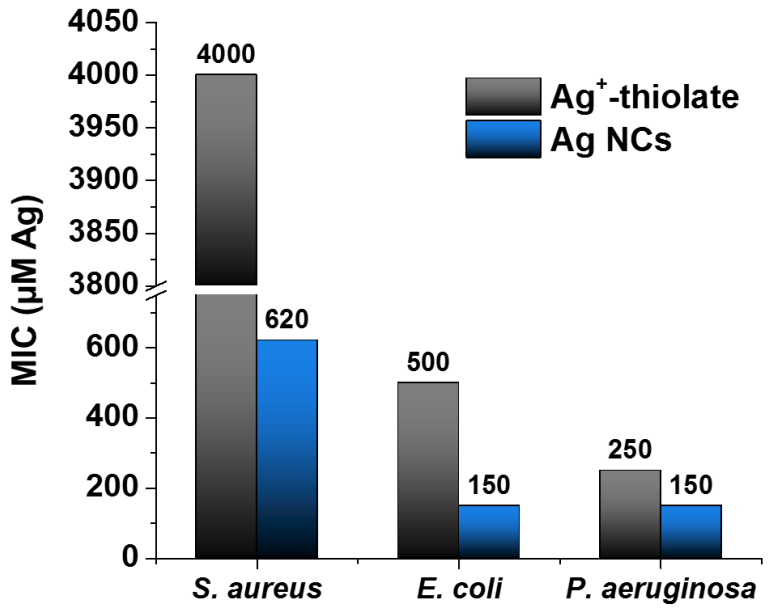

Figure 4.8. MIC assay results of the Ag NCs and Ag^+-thiolate against *S. aureus, E. coli,* and *P. aeruginosa*.

4.6 Ag NCs Prepared Without 1D Assembly

In the previous sections, the tiopronin-protected Ag NCs were shown to have both a highly sulfidized surface structure and to undergo 1D assembly as a result of Ag^+-thiolate formation during preparation of the NCs. As a follow-up to this work, tiopronin-protected NCs without 1D assembly were also studied using a similar methodology. Ag NCs were prepared by immediate addition of all of the reactants (1tiopronin:1$AgNO_3$) which avoided the initial mixing time of the $AgNO_3$ and tiopronin (30 min for the other NCs), thus potentially avoiding the formation of Ag^+-thiolates. After preparation, the NCs were subjected to the same purification procedure as the previous NCs (details given in section 4.4.1). However, it was noted that some of the NC sample precipitated to the bottom of the dialysis tubing during dialysis, although most of the NCs remained in solution and were subsequently collected. The purified NCs exhibited diameters of 2.2 ±

0.6 nm, with no apparent chain-like 1D assembly (Figure 4.9a). A comparison of the UV-vis spectra (Figure 4.9b) of the 1D Ag NCs (herein described as NC-1) and the non-1D NCs (herein described as NC-2), demonstrates the lack of Ag^{+}-thiolate by the absence of the peak at 276 nm. Compared to the NC-1, the peak around 385 nm for NC-2 appears to be consistent with the SPR features observed by Huang et al.[227]

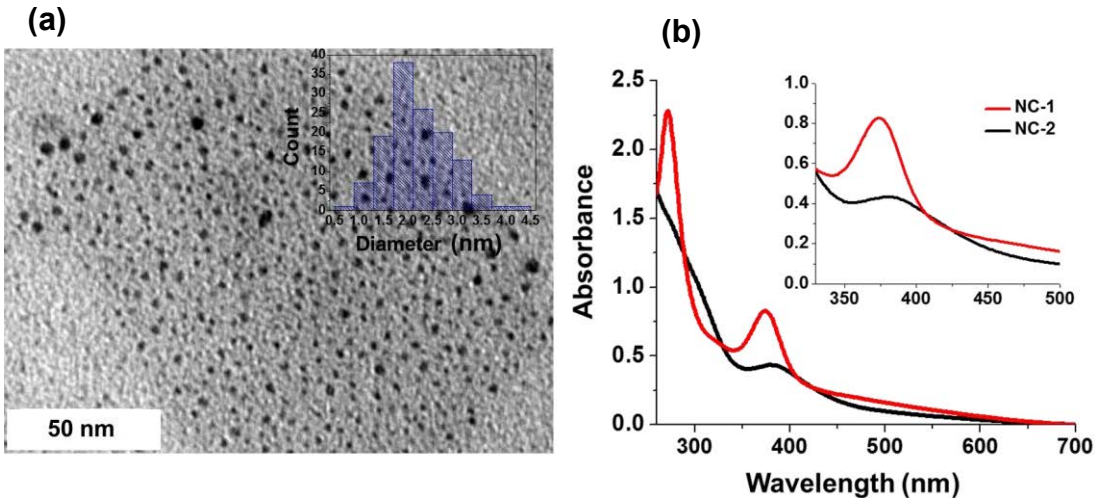

Figure 4.9. TEM and UV-vis of NC-2 (a) TEM image of NC-2 demonstrates no 1D assembly and average diameter of 2.2 ± 0.6 nm. (b) UV-vis spectra of NC-1 and NC-2 demonstrate the difference of the features around 270 nm and 375-385 nm.

The k^2-weighted Ag K-edge EXAFS spectra of the NC-1 and NC-2 samples and Ag foil are shown in Figure 4.10a. The NC-1 and NC-2 spectra are similar, however, the NC-2 appears to also have metallic-like features between 6-8 $Å^{-1}$. The k^2-weighted spectra of the NC samples were then Fourier-transformed and the resulting *R*-space spectra are presented in Figure 4.10b. The NC-2 exhibit similar features around 2 Å (Ag-S) and 2.7 Å (Ag-Ag), however, NC-2 has a much larger contribution of the Ag-Ag feature than the NC-2.

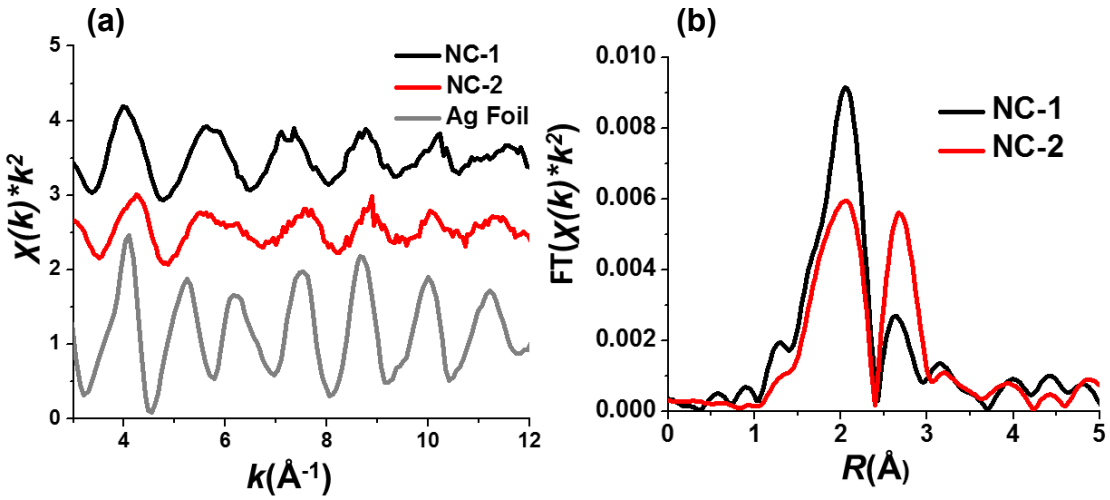

Figure 4.10. Ag K-edge EXAFS of NC-1 and NC-2. (a) k^2-space spectra of the NCs and reference foil (b) *R*-space spectra of the NC-1 and NC-2.

The WT-EXAFS analysis of the NC-2 demonstrates the Ag-S, Ag-Ag_1, and Ag-Ag_2 bonding paths (Figure 4.11a). Notably, the WT_EXAFS of the NC-2 exhibits a much more intense Ag-Ag_1 feature compared to NC-1, which denotes a greater contribution of metallic Ag. Based on the WT-EXAFS, three-path refinements with Ag-S, Ag-Ag_1, and Ag-Ag_2 were conducted. The resulting refinement is shown in Figure 4.11b with the parameters shown in Table 4.3 (NC-1 parameters also shown for comparison). The refinement of NC-2 demonstrates a shorter metal-type Ag-Ag bonding around 2.88 Å (Ag-Ag_1) and longer sulfide-type Ag-Ag bonding around 3.17 Å (Ag-Ag_2). These results imply a similar metal core/sulfide-shell architecture for the NC-2, but the distribution of bonding is different between NC-1 and NC-2. For example, the Ag-Ag_1 and Ag-Ag_2 CNs are higher and lower in the NC-2, respectively, and therefore reveal that the NC-2 has a larger metallic core and potentially a thinner sulfide-shell than the NC-1. Further to this, the Ag-S CN of 1.4 is also much smaller than that of the NC-1, which could indicate a

different type of S-metal bonding structure, although we note that the larger Ag-S CN in the NC-1 could be due to the Ag^{+}-thiolates in the sample as well.

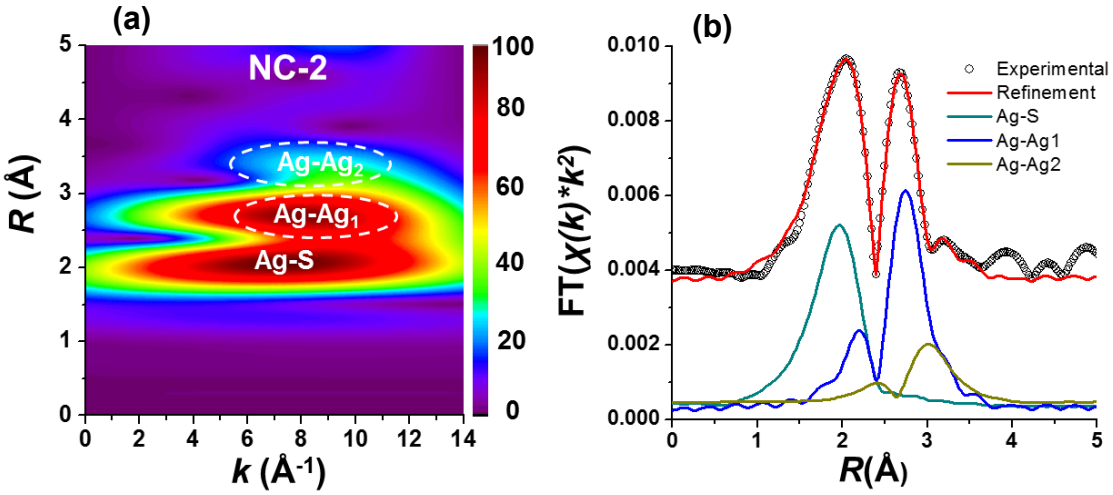

Figure 4.11. Ag K-edge EXAFS analysis. (a) WT-EXAFS (b) three-path refinement of Ag K-edge *R*-space spectrum of NC-2 from 1.5-3.6 Å.

Table 4.3. Three-path *R*-space refinement results for NC-1 and NC-2. The uncertainties of the refinement values are given by the numbers in parentheses.

Sample	Bond	CN	R (Å)	σ^2 (Å^2)	ΔE_o (eV)
NC-1	Ag-S	3.1(3)	2.522(7)	0.006(2)	1(1)
	Ag-Ag$_1$	0.6(3)	2.894(9)	0.004(3)	2(1)
	Ag-Ag$_2$	5(1)	3.10(3)	0.029(9)	2(1)
NC-2	Ag-S	1.4(3)	2.48(1)	0.007(2)	1(1)
	Ag-Ag$_1$	4.8(5)	2.880(7)	0.008(2)	3(1)
	Ag-Ag$_2$	2.2(9)	3.17(2)	0.010(4)	3(1)

It was previously determined that the surface structure of the NC-1 was largely sulfidized and similar to recently prepared Ag_{44} and Ag_{62} NCs, based on Ag-S, Ag-Ag$_1$, and Ag-Ag$_2$ bonding comparisons.[105] Again, based on a similar comparison, we find that

the Ag-S, Ag-Ag_1, and Ag-Ag_2 CNs of NC-2 (1.4 ± 0.3, 4.8 ± 0.3, 2.2 ± 1, respectively) more closely resemble the calculated CNs of the Ag_{44} NCs (1.9, 4.1, 2.2, respectively[104]). Therefore, we propose a Ag_{44} NC-type structure for the NC-2, although we note that the NCs prepared here are likely larger (based on larger Ag-Ag_1 CN), which could contribute to the slight differences in overall structures.

4.7 Conclusion

Overall, this work has presented a detailed picture of the local structure and bonding of tiopronin-stabilized Ag NCs. We found that the formation of Ag^+-thiolates prior to the reduction of Ag^+ had an effect on both the final assembly of the NCs as shown by TEM, as well as the surface structure of the NCs as shown by Ag K-edge EXAFS and Ag L_3-edge XANES analyses. WT-EXAFS analysis demonstrated the potential for a sulfide-shell structure on the surface of the NCs, which initiated the successful multi-path Ag K-edge EXAFS refinements of the NCs with Ag-S, Ag-Ag_1 (metal-type), and Ag-Ag_2 (sulfide-type) paths, and led to the deduction of a metal-core and sulfide-shell type structure. For the NCs arranged in 1D assemblies (NC-1), the distribution of the Ag-Ag_1 and Ag-Ag_2 also demonstrated that the NCs were mostly composed of sulfide. In addition, the antibacterial properties of the NC-1 were found to present similar trends as other Ag-core/sulfide-shell NPs despite their more highly sulfidized surface. Therefore, because the NCs have properties of both metallic and semiconductor materials, they may be useful for a variety of applications. For example, Ag_2S NCs have shown enhanced luminescence,[104,214,215] while metallic Ag NCs have demonstrated antibiotic potential.[215,217] The NC-1, which exhibit both types of structures and potentially related effects, could lead to novel optical probes that could examine the

antibacterial activity of Ag NCs *in situ*. Not only that, but their unique assembly may have further potential implications for their biomedical or plasmonic applications.[76] Finally, further investigations of the synthetic method allowed the preparation of Ag NCs without the 1D assembly (NC-2). Structural evaluations using the same methodology revealed a larger metal core with a thinner sulfide-shell, with coordination and bonding similar to recently prepared Ag_{44} NCs. Further investigations of the antibacterial properties of the NC-2 and structural comparisons to other similar NCs such as Ag_{44} would be worthwhile to carry out.

Chapter 5 - Correlating the Atomic Structure of Bimetallic Silver-Gold Nanoparticles to Their Antibacterial and Cytotoxic Activities

Sections 5.3-5.6 are reproduced in part with permission from: Padmos, J. D.; Langman, M.; MacDonald, K.; Comeau, P.; Yang, Z.; Filiaggi, M.; Zhang, P. Correlating the Atomic Structure of Bimetallic Silver-Gold Nanoparticles to Their Antibacterial and Cytotoxic Activities. *Journal of Physical Chemistry Part C* **2015**, *119*, 7472.

5.1 Contributions

J.D.P. synthesized the NPs, carried out the general characterization, conducted the XAS experiments, carried out the bacteria minimum inhibitory concentration and cytotoxic activity assays, and wrote the manuscript. M.L. supervised J.D.P. in carrying out the minimum inhibitory concentration and cytotoxic activity assays. K.M. carried out the disc-diffusion assays and the statistical analysis for their results. P.C. carried out the inductively coupled plasma analysis and helped with some of the antibacterial activity assays. Z.Y. supervised K.M.. M.F. supervised P.C./M.L. and helped revise the manuscript. P.Z. supervised J.D.P. and helped revise the manuscript.

5.2 Foreword

The previous chapters demonstrated lower antibacterial activity as a result of the sulfidized surface structure of thiolate-protected Ag NPs and higher activity of polymer-protected Ag NPs. Realizing that the cytotoxicity of Ag NPs is a growing concern, it is

proposed that the synthesis of AgAu alloy NPs is a potential strategy to yield antibacterial NPs with low cytotoxicity towards normal cells. In addition, tailoring the structure of AgAu NPs may cause their antibacterial and cytotoxicity properties to drastically change. Despite AgAu bimetallic NPs being somewhat well-studied, a detailed characterization of their atomic composition and its relationship with antibacterial function is lacking. Therefore, this chapter describes XAS studies used to analyze the compositions and surface structures of bimetallic AgAu NPs in order to correlate them with their antibacterial and cytotoxic activities.

5.3 Introduction

Nanomaterials have unique physicochemical properties that have initiated their use in many different fields of science and biomedical technologies.[10,199] Silver nanoparticles (Ag NPs) in particular have attracted much interest due to their remarkable antibacterial properties and relatively low bacterial resistance.[5] As a result, they have become possible therapeutic options and are found in a number of commercial biomedical products such as catheters[28] and wound dressings.[29] Ag NPs and other metal NPs are also beginning to be considered as strategies to reduce infection and improve the longevity of orthopaedic and dental implants.[31,239–242]

Although the effect of Ag NPs on bacteria has been well reported, the mechanism by which Ag NPs exert their antibacterial effects is not fully understood. This is largely debated to be through direct surface reactions with bacteria or from surface Ag^+ ion release and subsequent reaction with bacteria.[37,41,42,45–47,57,61,127] In both cases, Ag or Ag^+ has a high affinity for cellular thiols or amino acids, and thus can disrupt bacteria cell membranes, leading to subsequent cell death. Furthermore, Ag and Ag^+ reactions that

produce reactive oxygen species (ROS) within bacteria have also been shown to play a large role in their antibacterial activity.[61] Realistically, the determination of the exact mode of antibacterial action is complicated by many different factors given the variation in protecting ligand, size, and morphology of Ag NPs tested in previous studies. Nonetheless, the surface composition and structure of the NPs will play a large part in those potential reactions; therefore, control over the surface can potentially provide increased therapeutic efficacy, in addition to providing further understanding of the antibacterial mechanism.

A surprisingly overlooked aspect in the application of Ag NPs is their overall health implications.[61,62] It is feasible that the properties that make Ag NPs effective against bacteria, may also affect healthy human cells. Indeed, some studies have shown that Ag NPs are toxic to certain mammalian cells.[48,61,62,243,244] This toxic effect could also be exacerbated in the body by the potential of NPs to interact with many different organs and types of cells, due to high systemic circulation resulting from their small size. Therefore, engineering Ag NPs with specific compositions and surface structure is a worthy endeavor to balance toxicity to healthy human cells and antibacterial activity in order to achieve the best performance and safety.

One potential strategy explored here is to add a different metal to tailor the atomic structure and physicochemical properties of Ag NPs in order to reduce the cytotoxic effect (*i.e.,* yielding higher biocompatibility), but maintain the antibacterial effect of the Ag. Bulk gold (Au) is generally considered to be more biocompatible than Ag, and Au NPs have also been shown to have relatively low cytotoxic effects on mammalian cells.[61,245] Furthermore, in some cases they have also revealed antibacterial

properties.[246,247] Therefore, the formation of Ag and Au into bimetallic AgAu NPs may be a viable solution for antibacterial applications. However, the type of Ag and Au incorporation (*i.e.,* resulting atomic structure) will no doubt play an important role in bioactivity and must be controlled for maximum Ag efficacy. For example, the structure of some common bimetallic AgAu NP structures including homogenous AgAu alloy, Ag-core/Au-shell, and Au-core/Ag-shell nanostructures can be vastly different, which could feasibly have an impact on the bioactivities of the NPs. Controlling the structure of NPs is predicated on the ability to characterize the NPs but, unfortunately, complete characterization of atomic structure of bimetallic NPs with traditional techniques (*e.g.,* TEM, UV-vis, XRD) can be challenging. X-ray absorption spectroscopy (XAS) is known to be an effective technique to provide explicit details regarding the atomic structure of NPs.[75,248] XAS is also element specific, which allows NPs to be analyzed from the perspective of both metals in order to provide a more comprehensive picture of the overall composition and surface structure.

Therefore, the objectives of this study were characterize the atomic structure of a series of bimetallic AgAu NPs and then assess their activities against *S. aureus* bacteria and fibroblast cells as *in-vitro* models of bioactivity. In this way, both the physicochemical and bioactive properties of the NPs were correlated in order to provide a guiding methodology for the study of Ag NPs and their potential biomedical applications.

5.4 Experimental

5.4.1 Synthesis of Ag and AgAu NPs

Silver nitrate ($AgNO_3$, 99.9+ %), gold tetrachloroaurate trihydrate ($HAuCl_4 \cdot 3H_2O$, 99.9 %), and polyvinylpyrrolidone (PVP, M.W. 8,000) were purchased from Alfa Aesar.

Sodium borohydride ($NaBH_4$, 99 %) was purchased from Sigma-Aldrich. Nitric acid (HNO_3(aq), 67-70 % (w/w) was purchased from Caledon Laboratory Chemicals. Hydrochloric acid (HCl(aq), 36.5-38.0 % w/w) and potassium hydroxide (KOH, 85+ %) were purchased from ACP Chemicals. Water used in these experiments was from a Barnstead NANOpure® DiamondTM UV ultrapure water system (Deionized, 18.2 MΩ·cm). All chemicals were used without further purification. The PVP protected Ag and AgAu NPs were prepared using a method derived from Zhang et al. with slight modifications.[130] First, 1 mL $AgNO_3$ (0.1 M), 0.4 mL KOH (0.1 M), and 8 grams of PVP were vigorously mixed with 93.6 mL of ultrapure water in a sealed round bottom flask. The solution was then allowed to stir vigorously for 30 minutes under N_2 gas. After mixing, 5 mL of fresh, ice-cold $NaBH_4$ (0.1 M) was added drop-wise and then allowed to stir vigorously for 1 hour. The solution was then aged for 48 hours (covered, room temperature) to allow for complete reaction. The as prepared solution was denoted as R0 (describing no replacement reaction with Au) and used to prepare the AgAu NP samples.

Each AgAu NP sample was prepared by refluxing 20 mL of the R0 at 100 °C and then adding 0.44 mL, 0.62 mL, or 1.0 mL of 10 mM $HAuCl_4$ (in water) to prepare the R1, R2, or R3 samples, respectively. The mixtures were refluxed for an additional 10 minutes and then allowed to cool to room temperature under N_2 gas. The samples were allowed to sit for 24 hours before centrifuging at 3,000 *g* to remove any insoluble AgCl precipitates. The supernatants were further purified to remove any excess constituents by acetone precipitation.[206,207,249] A 3x volume of acetone (laboratory grade) was added to each sample and then centrifuged for 15 minutes (10,000 *g* and 5 °C) in Nalgene tubes to precipitate the NPs from solution. The acetone was removed completely from the tubes and a small amount of water was added to re-disperse the NPs into solution. Each sample

underwent the same purification procedure a total of 3 times, and then were finally re-dispersed into water and put into cold storage (4 °C) for later characterization.

5.4.2 General Characterization

To characterize the surface plasmon resonance of each NP solution, Ultraviolet-visible spectroscopy (UV-vis) was carried out using a Varian Cary 100 Bio UV−vis spectrophotometer. A 50 µL aliquot of each purified sample was diluted to 3 mL with water in a quartz cuvette. Spectra were recorded from 300-800 nm and background-corrected with a water reference. NP size and shape were assessed by transmission electron microscopy (TEM) using a Philips Technai-12 TEM operating at 80 kV. Samples were prepared by dropping 20 µL of diluted solutions on formvar-coated TEM grids. The films on the TEM grids were allowed to dry overnight (covered, room temperature) before analysis. From recorded TEM images, individual NPs were counted and their size distribution was measured using ImageJ image processing software. In order to determine the resulting elemental composition of each NP solution, inductively coupled plasma optical emission spectroscopy (ICP-OES) was carried out using a PerkinElmer Optima8000 at wavelengths of 328.068 nm and 267.595 nm for Ag and Au, respectively. All element standards were provided by PerkinElmer. In preparation for analysis, the samples were digested in HNO_3 and HCl to enable the measurements. First, 20 µL of each sample was diluted to 1 mL water and heated to 80 °C in a covered test-tube. To this, 1 mL of HNO_3 was added and allowed to sit for 1 hour at 80 °C to dissolve the Ag. 2 mL of HCl was then added to form aqua regia, and allowed to sit for an additional hour to dissolve the Au. Following cooling, the solutions were dispersed into 10 mL of water in a volumetric flask for the ICP-OES measurements.

5.4.3 X-ray Absorption Spectroscopy (XAS)

Ag K-edge and Au L_3-edge XAS was conducted at the Advanced Photon Source (BM-20 beamline) at Argonne National Laboratory, Argonne, IL, USA. Ag L_3-edge XAS was conducted at the Canadian Light Source (SXRMB beamline, Saskatoon, SK, Canada). In preparation for XAS experiments, the samples were frozen and then lyophilized to enable solid-phase measurements. For Ag K-edge and Au L_3-edge XAS, the lyophilized powders were placed in kapton film pouches and loaded into the sample holder along with Ag and Au foils. The sample holder was then placed into a cryostatic chamber which was then maintained at a constant temperature of 50 K for all of the measurements. Ag K-edge and Au L_3 edge spectra were collected with a 32-element solid state Ge X-ray fluorescence detector with simultaneous foil reference spectra recorded using standard gas-ionization chamber detectors. For Ag L_3-edge XAS, the powdered samples were placed on double-sided carbon tape attached to the sample holder. The sample holder was then placed in the sample chamber and allowed to reach an ultra-high vacuum atmosphere before data collection. The Ag L_3-edge spectra were collected with a 4-element Silicon drift detector. All of the XAS spectra were processed with the WinXAS program.[162] The x-axes of the spectra were normalized to their absorption energies (Ag or Au) and then the y-axes post-edge was normalized to one. For the extended X-ray absorption fine structure spectroscopy (EXAFS) analysis of Ag K-edge and Au L_3-edge, the raw data were k^2- or k^3-weighted and then Fourier-transformed to *R*-space spectra using a Hanning function from k = 2.5-12.5 Å^{-1}. The *R*-space spectra were then refined from R = 1.7-3.3 Å with WinXAS using *ab initio* simulations of AgAu structural models obtained from the FEFF 8.2 code.[164,165] The refinements calculated structural information about the samples, including coordination numbers (CNs), bond lengths (R), Debye-

Waller coefficients (σ^2), and E_o-shifts (ΔE_o). The ratio of free variables and independent points before each refinement was 9 and 12, respectively. However, in order to reduce the ratio to allow for more accurate refinements, certain parameters were constrained. For example, the amplitude reduction factor (S_o^2) was fixed during the Ag K-edge ($S_o^2 = 0.92$) and Au L_3-edge ($S_o^2 = 0.95$) refinements, respectively, based on bulk metal *R*-space refinements at 50 K. The Ag-Au bond length from the Ag K-edge and Au L_3-edge EXAFS was also correlated for each bimetallic sample during the refinements.[250] In addition, the ΔE_o values were correlated for the Au L_3-edge refinement for the R1 sample due to the slightly lower quality spectrum at higher *k*-range, most likely caused by its lower concentration of Au. Therefore, the ratio of free parameters to independent points was at most 8 out of 12, with other constraints in some particular cases lowering the ratio further. For the Ag L_3-edge XAS data, the normalized spectra were used for qualitative comparison to reference materials.[162]

5.4.4 Antibacterial Activity

The antibacterial activity of each NP solution was first tested against Gram positive *Staphylococcus aureus* (*S. aureus*, ATCC 25923) by K. MacDonald and Z. Yang (Crandall University, Moncton, NB, Canada), using a Kirby-Bauer disc diffusion assay,[251] modified from Clinical and Laboratory Standards Institute (CLSI) standards.[208] Bacteria were cultured for 24 hours on Mueller-Hinton agar plates. Three viable colonies were then transferred to 1 mL of Mueller-Hinton broth and the bacterial turbidity was adjusted to a 0.5 McFarland turbidity standard, corresponding to a bacteria concentration around $1x10^8$ CFU/mL. The prepared inoculum was then swabbed on Mueller-Hinton agar plates using sterile cotton swabs. Sterilized No. 1 Whatman filter paper discs

(Becten, Dickson, and Company), with a diameter of 6 mm, were placed on the inoculated agar and impregnated directly by 40 μL of the NP solutions along with the controls. The solutions were allowed to dry for approximately 15 minutes in a Biosafety Cabinet (SterilGARD III Advance, The Baker Company) before incubating at 37 °C for 24 hours. Chloramphenicol discs were used as the positive control while polyvinylpyrrolidone (PVP) was used as the negative control. The average diameters of the inhibition zones were measured with a ruler and recorded in millimeters. The mean and standard deviation for each AgAu NP solution were based on three to five replicates. A two tailed pair sample t-test carried out in Microsoft Excel (2012) was utilized in order to determine the extent and significance of differences between the testing agents and negative control's inhibition of bacterial growth in the disc diffusion assays.

The antibacterial activity of each NP solution was further tested against *S. aureus* (ATCC 6538) with a serial dilution method in broth,[252] modified from CLSI standards.[208] Mueller-Hinton agar plates were inoculated with *S. aureus* and cultivated for 24 hours at 37 °C. A bacteria suspension of 2 x 10^5 CFU/mL was then prepared in Mueller-Hinton broth and added in 100 μL aliquots to each well in a 96-well plate (CoStar, Corning, Canada). NP solutions in 100 μL aliquots (diluted with broth) were added to the wells to give total metal concentrations ranging from 50 to 750 μM and final bacteria concentrations of 1 x 10^5 CFU/mL. Each NP sample was tested in duplicate for each concentration along with duplicate positive (broth and bacteria) and negative (broth) controls. The plate was then left in an incubator for 20 hours at 37 °C. The minimum inhibitory concentration (MIC) was determined to be the lowest concentration at which bacteria growth was inhibited after 20 hours, detected by visual inspection and comparison to the controls.

5.4.5 Cytotoxicity

The cell viability of immortalized rat fibroblasts (NIH-3T3) were tested against the NP solutions using an MTT assay.[253] The fibroblast cells were prepared at a density of 1 x 10^4 cells/mL in Dulbecco's Modified Eagle's Medium (DMEM) with 5 % fetal calf serum (FCS). The cells were then added in 200 µL aliquots to a 96-well plate (CoStar, Corning, Canada) and incubated at 37C (10 % CO_2/90 % air atmosphere) for 24 hours. The cells were then treated with 20 µL aliquots of each NP solution containing total metal concentrations of 95 to 750 µM (in DMEM/FCS media). Dimethyl sulfoxide (DMSO) was used as a negative control, while culture media/fibroblasts and culture media alone were used as positive controls (quadruplicates). The plate was then incubated for 24 h at 37° C (10 % CO_2/90 % air atmosphere). Subsequently, 22 µL of an MTT (M2128, Sigma Aldrich Canada) solution in phosphate-buffered saline (5 mg/mL) was added to each well and the plate incubated for another 3 hours. Following this, the media was removed, and 100 µL of DMSO was added to each well. The plate was gently agitated for 15 minutes while covered by tinfoil. Finally, the absorbance of each well was measured at a wavelength of 570 nm on a microplate reader (Synergy HT, BIO-TEK). Percent cell viability was determined to be the absorbance of the test sample divided by the positive control absorbance. All MIC and MTT assays were conducted under aseptic conditions within Biosafety Cabinets.

5.5 Results and Discussion

5.5.1 General Characterization

Ag and Au NPs have unique optical properties that are often characterized by their absorption spectrum under UV-visible light. Some metal NPs exhibit surface plasmon resonance (SPR), which is attributed to a collective oscillation of conduction band electrons. For Ag and Au NPs, SPR peaks occur in the UV-visible region around 400 nm and 550 nm, respectively, and therefore can be characterized by UV-vis.[11,12,20,21] Figure 5.1 shows the composition dependent UV-vis spectra of the NP solutions, along with their corresponding colour in solution (Figure 5.1 inset). With an increase in Au, the solutions exhibit a red-shift in their SPR peaks, and correspondingly change in colour from yellow to red. The shape of the SPR peak can also indicate NP composition, namely homogeneous alloy, core-shell, or a mixture of monometallic NPs.[11,12,20,21] The presence of multiple SPR peaks excludes the possibility of homogenous alloy, and therefore the bimetallic NPs are potentially core-shell or a mixture of Ag and Au NPs. However, the R0 sample exhibits one clear SPR peak, expected of a pure monometallic NP. Unfortunately, UV-vis can only give indirect evidence of morphology and structure, and so the NPs were explored further by TEM, ICP, and XAS characterization.

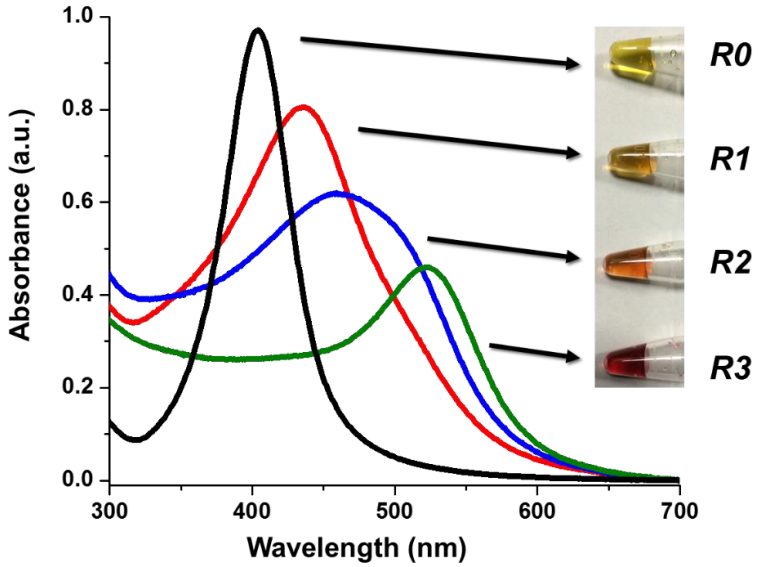

Figure 5.1. UV-vis spectra of bimetallic AgAu NPs. The spectra show the change in SPR peak position with increasing Au additions (R0-R3), along with the corresponding change in solution colour (inset).

Transmission electron microscopy (TEM) was carried out to measure the size distribution of the NPs after addition of the varying amounts of Au. Figure 5.2 shows a representative TEM image of each solution, along with their respective size distributions (Figure 5.2 insets), which were measured from four TEM images of each sample. The mean diameter of the R0, R1, R2, and R3 NPs were found to be 7.7 ± 1.5 nm, 7.2 ± 1.6 nm, 7.1 ± 1.5 nm, 7.0 ± 1.2 nm, indicating similar diameters. The diameters of the NPs were also of a normal distribution, supporting the formation of one type of particle, rather than a bimodal distribution indicative of two separate types of metal particles.

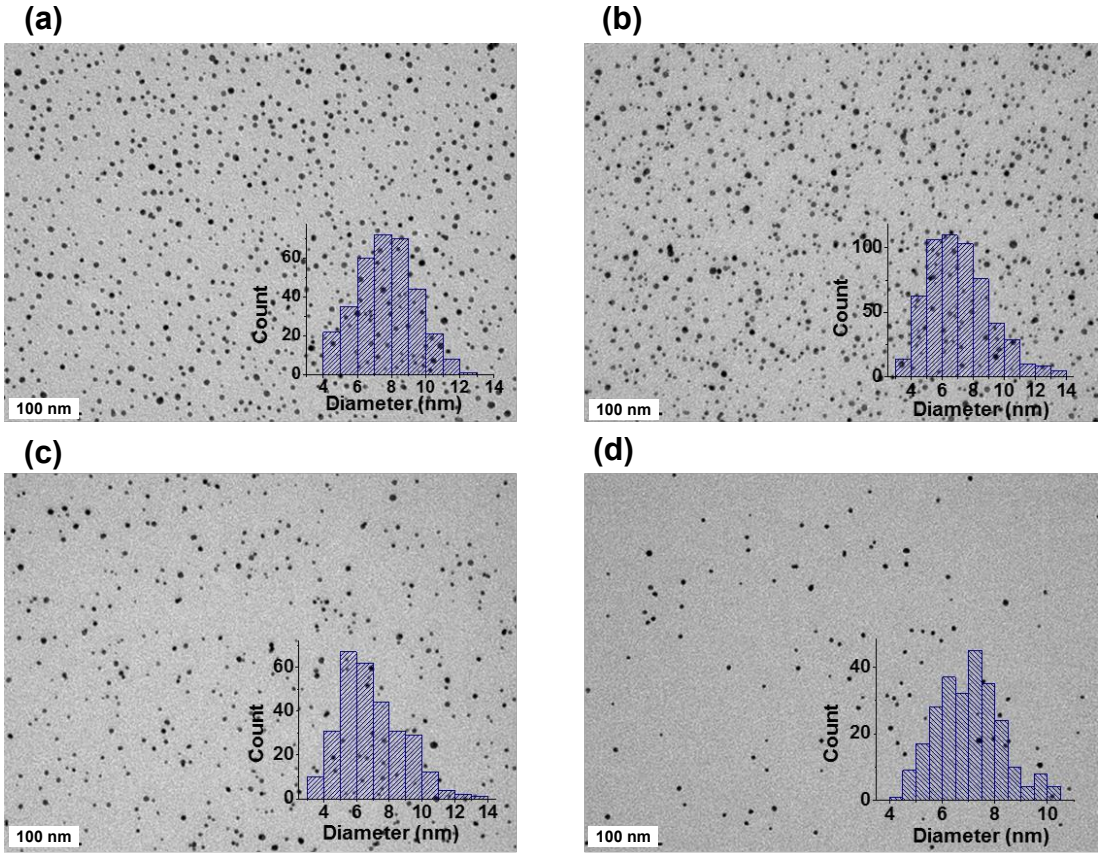

Figure 5.2. TEM images of the AgAu NPs. (a) R0, (b) R1, (c) R2, and (d) R3.

ICP-OES was also conducted in order to provide elemental characterization of the NP solutions, and the results described in Table 5.1. Overall, with increasing Au added to the Ag NPs, more Au was incorporated into the resulting NPs. The concentrations of each metal in the tested solutions were then used to calculate the molar ratios of the metals, also presented in Table 5.1. These molar concentrations were subsequently used to standardize the NP solutions for the MIC and MTT assays.

Table 5.1. ICP-OES results for the AgAu NP samples. The uncertainty of the values for the ICP-OES measurements are 0.02 mg/L for both elements.

Sample	Ag (mg/L)	Au(mg/L)	Ag ratio	Au ratio
R0	390	2	100	0
R1	209.5	202	65	35
R2	125.5	219	50	50
R3	89	390.5	30	70

5.5.2 Structural Characterization by XAS

The bimetallic NPs were studied from both the Ag and Au perspectives using Ag K-edge and Au L_3-edge XAS spectroscopy. Figures 5.3a-b show the k^2-weighted Ag K-edge spectra and k^3-weighted Au L_3-edge spectra. The spectral oscillations of each NP sample were similar to their respective reference foils, indicating the presence of both metallic Ag and Au. The k^2-weighted spectra were then Fourier-transformed into *R*-space and the resulting spectra are shown in Figures 5.3c-d. The major doublet peaks in the region of 2-3 Å are consistent with first-shell metal-metal bonding for each edge. The Ag K-edge *R*-space spectra also reveal a decrease in overall intensity as the amount of Au increases from R0 to R3, consistent with a decrease of Ag in the NPs. Conversely, the intensity of the Au L_3-edge *R*-space spectra appear to increase with the addition of more Au. The ratio of the peaks in the doublets also appear to change with the different metal ratios, which may be due to the different local environment of the Ag and Au. This will be further examined by refining the *R*-space spectra to calculate NP structural information.

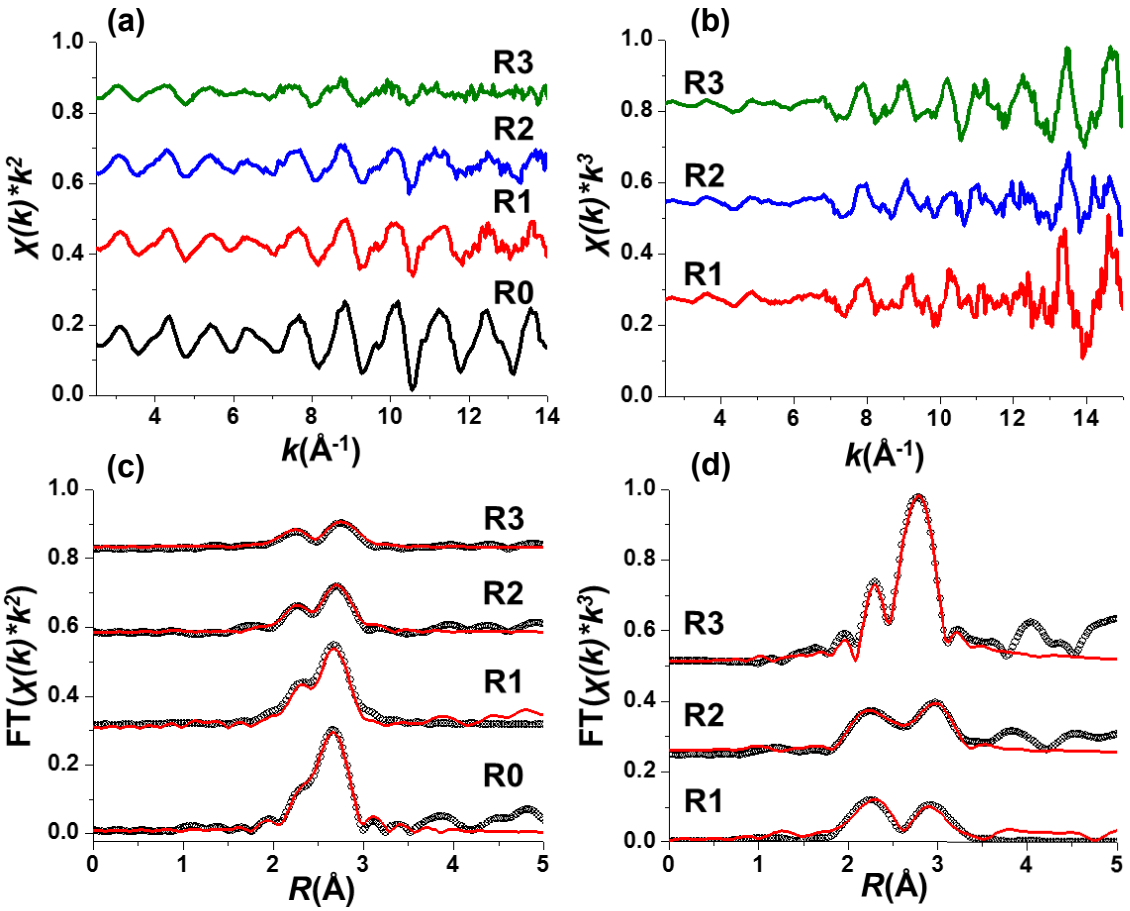

Figure 5.3. Ag K-edge and Au L_3-edge EXAFS results of the AgAu NPs. (a) Ag K-edge k^2-space spectra (b) Au L_3-edge k^3-space spectra (c) Ag K-edge *R*-space refinement spectra (d) Au L_3-edge *R*-space refinement spectra. Note that the refinements were performed with an *R*-window of 1.7-3.3 Å, hence the disagreement outside of those boundaries.

The Ag and Au *R*-space spectra were refined using standard methods.[75,93] As the O- and N-containing functional groups of PVP provide bonding possibilities to the NPs,[121,122,211] theoretical bonding paths of (Ag/Au)-O, (Ag/Au)-N, Ag-Ag, Ag-Au, and Au-Au were first included the *R*-space refinements. However, tentative refinements of (Ag/Au)-O and/or (Ag/Au)-N paths resulted in consistent errors and were not considered further. The lack of observable Ag-O or Ag-N in the *R*-space is thought to be from a combination of low percentage of surface atoms in the NPs (~25 % for 7-8 nm NPs[184]),

less intense *R*-space amplitudes in that range (*e.g.,* ~2 Å), and steric repulsion between ligands leading to less O and N surface bonding.[254] Therefore, even though there were interactions between the PVP ligands and the surface of the NPs, reasonable overall refinements were achieved with only Ag-Ag and Ag-Au bonding paths for the Ag EXAFS, and Au-Au and Au-Ag for the Au EXAFS. Figure 5.3 presents the refinement spectrum of each sample, while the refinement values are presented in Table 5.2. The first observation from the refinements is that the pure Ag NP (R0) exhibited a Ag-Ag CN of 10.9(7), that is consistent with face-centered cubic (FCC) metal NPs of this size (*i.e.,* Ag-Ag CN ≈ 11).[184] This CN is expectedly lower than the FCC coordination of 12, due to the higher ratio of surface atoms with lower coordination. The *R*-space refinements for the bimetallic NPs also provided average CNs corresponding to Ag-Au, Au-Au, and Au-Ag. As the incorporation of Au is increased from R0 to R3, there was a corresponding decrease in the Ag-Ag CNs. Similarly, there was also an increase in the Au-Au CNs with an increase of Au composition. There was no increasing trend in the Ag-Au or Au-Ag alloy CNs; however, the incorporation of Au is also accompanied by the disappearance of Ag, which may make this trend less observable.

Table 5.2. *R*-space refinement results and resulting alloy parameters. The uncertainties of the values are given by the numbers in parentheses.

NP	Edge	Path	CN	R(Å)	σ^2(Å^2)	ΔE_o(eV)	α_{Ag}, α_{Au}	J_{Ag},J_{Au} (%)
R0	Ag	Ag-Ag	10.9(7)	2.879(2)	0.003(1)	2(1)		
R1	Ag	Ag-Ag	7.9(7)	2.884(4)	0.003(1)	1(1)	α_{Ag}=0.45(7)	J_{Ag}=2.9(7) x 10^1
		Ag-Au	1.9(7)	2.859(4)	0.004(2)	-7(3)		
	Au	Au-Au	5(1)	2.875(8)	0.001(1)	1(1)	α_{Au}=0.4(1)	J_{Au}=1.1(1) x 10^2
		Au-Ag	3(1)	2.859(4)	0.002(1)	1(1)		
R2	Ag	Ag-Ag	6(1)	2.880(8)	0.003(1)	2(1)	α_{Ag}=0.3(1)	J_{Ag}=7(1) x 10^1
		Ag-Au	3(1)	2.85(2)	0.003(1)	-7(2)		
	Au	Au-Au	8(1)	2.866(6)	0.002(1)	1(1)	α_{Au}=0.47(5)	J_{Au}=5(1) x 10^1
		Au-Ag	2.9(4)	2.85(2)	0.002(1)	2(1)		
R3	Ag	Ag-Ag	4.0(8)	2.89(2)	0.004(2)	1(1)	α_{Ag}=0.4(1)	J_{Ag}=1.5(1) x 10^2
		Ag-Au	3.1(7)	2.90(2)	0.004(2)	-3(1)		
	Au	Au-Au	10(1)	2.873(4)	0.003(1)	3(1)	α_{Au}=0.44(6)	J_{Au}=2.4(6) x 10^1
		Au-Ag	2.0(7)	2.90(2)	0.005(3)	3(1)		

The CNs of each bonding path also provide crucial information regarding the atomic arrangement of the Ag and Au. For example, the Cowley parameter (α) for short range order can be used to quantitatively measure the segregation tendency of the atoms within bimetallic NPs.[255,256] The Cowley parameters (α_{Ag}, α_{Au}) were calculated by:[255,256]

$$\alpha_{Ag} = 1 - \frac{(CN_{Ag-Au}/CN_{Ag\ total})}{X_{Au}} \quad (5.1)$$

$$\alpha_{Au} = 1 - \frac{(CN_{Au-Ag}/CN_{Au\ total})}{X_{Ag}} \quad (5.2)$$

$CN_{Ag\ total}$ represents (CN_{Ag-Ag} + CN_{Ag-Au}), $CN_{Au\ total}$ represents (CN_{Au-Au} + CN_{Au-Ag}), x_{Ag} or x_{Ag} represent the molar ratios of each metal in the NPs. This parameter can range from ($-1 \leq \alpha \leq 1$), where a positive value demonstrates that atomic segregation has occurred (*e.g.,* heterogeneous alloy), and a negative value demonstrates more alloying interactions (*e.g.,* homogeneous alloy).[256] For each bimetallic NP, α_{Ag} and α_{Au} were found to be positive, thereby indicating that the segregation of Ag and Au atoms occurred within the NPs (Table 5.2).

In order to determine the type of segregation and further predict the atomic arrangement of the Ag and Au in the bimetallic NPs, the XAS structural parameters of J_A (*i.e.,* J_{Ag}) and J_B (*i.e.,* J_{Au}) were calculated by:[257,258]

$$J_A = (P_{observed}/P_{random}) \times 100\ \% \quad (5.3)$$

$$J_B = (R_{observed}/R_{random}) \times 100\ \% \quad (5.4)$$

For each bimetallic NP, $P_{observed}$ was the ratio of CN_{Ag-Au} to $CN_{Ag\ total}$ and $R_{observed}$ was the ratio of CN_{Au-Ag} to $CN_{Au\ total}$. P_{random} was the molar ratio of Ag (0.65, 0.5, 0.3 for R1, R2, R3, respectively) and R_{random} was the molar ratio of Au (0.35, 0.5, 0.7 for R1, R2, R3, respectively) in each bimetallic NP. The J_{Ag} and J_{Au} parameters were calculated for each bimetallic NP and shown in Table 5.2. For the R1 NPs, $J_{Ag} < J_{Au}$, which demonstrates that the NPs are Ag-rich in the core and Au-rich on the surface.[257,258] On the other hand, $J_{Ag} > J_{Au}$ for the R2 and R3 NPs, which reveals that they are Au-rich in the core and Ag-rich on the surface.

From the previously calculated Cowley parameters and the basic comparisons of J_{Ag} and J_{Au}, it can be determined that all the bimetallic NPs exhibit core-shell type structures. However, finer details of these structures can be given by further examination

of J_{Ag} and J_{Au} according to the methods of Hwang et al.[257] In this way, $J_{Ag} < 50$ % and $J_{Au} > 100$ % for the R1 NPs, which suggests that there is not a continuous layer of Au on their surfaces and is more consistent with a Au-rich pseudo-shell around a Ag-rich core. Conversely, the R3 NPs yield $J_{Ag} > 100$ % and $J_{Au} < 50$ %, indicating a Ag-rich pseudo-shell around a Au-rich core. On the other hand, $J_{Ag} < 100$ % and $J_{Au} < 100$ % for the R2 NPs, which describe a homophilic NP structure.[257] The J_{Ag} and J_{Au} of the R2 NPs are also closer to 50 % than 100 %, which is similar to ideal core-shell NPs (*i.e.,* $J_{Ag} < 50$ %, $J_{Au} < 50$ % for ideal core-shell NPs). Therefore, the R2 NPs likely contain homophilic Ag layers at their surfaces, and are more similar to ideal core-shell NPs than the R1 and R3 NPs. It should also be noted that these structures are also supported by the UV-vis results (see Figure 5.1) in which the R2 NPs exhibited two major SPR peaks (indicative of a thicker shell), while the R1 and R3 NPs both exhibited one major SPR peak along with a minor SPR peak (indicative of a thinner shell).

Metal-metal bond lengths for the NPs were also elucidated by the EXAFS refinements. For each type of NP, the Ag-Ag and Ag-Au bond lengths were indistinguishable from those of Ag and Au bulk bond lengths around 2.87-2.90 Å, as observed by low temperature EXAFS.[259] These are typical metal bond lengths for NPs of this size (~ 7-8 nm), as detectable lattice contraction is usually only observed around 5 nm in nanostructures.[183] On the other hand, the R1 and R2 NPs exhibited shorter Ag-Au bond lengths than in $Ag_{50}Au_{50}$ bulk alloy at low temperature (*i.e.,* 2.874(2) Å),[259] while the R3 NPs exhibited a longer Ag-Au bond length. The disparity between the Ag-Au bond lengths seen here is proposed to be a result of the unique local structure exhibited by the NPs.

The alloying interaction between Ag and Au was also examined from Ag L_3-edge and Au L_3-edge XANES. The first feature in the Ag and Au L_3-edge XANES spectra is attributed to the electronic transition from p- to unoccupied d-orbitals.[96,155,156] For metal NPs, this feature is size-dependent and commonly observed to be less intense relative to bulk metals.[96,97,155,157] In addition, the intensity of this feature is inversely proportional to the amount of alloying in the system[156,158] and thus can be useful in resolving the alloy interactions in the NPs, which may be important in resolving the antibacterial or cytotoxic effect. The Ag and Au XANES are presented in Figure 5.4, and show that there is a decrease in both Ag and Au whitelines for R1, R2, and R3. From the Ag L_3-edge spectra, the decrease of the whiteline is proportional to the amount of alloying in the NPs. The R3 NPs show the least intense whiteline, which may imply the most alloying as a result of the higher number of Au neighbouring atoms. However, the R3 Ag whiteline is reduced even further because of the thin layer (*i.e.,* smaller size) of Ag on the surface of the NPs, which may be the reason for the difference in intensity to the other bimetallic NPs. For the Au L_3-edge spectra, the NP whiteline intensities are also lower than the bulk reference, although the bimetallic NPs show very similar intensities to each other.

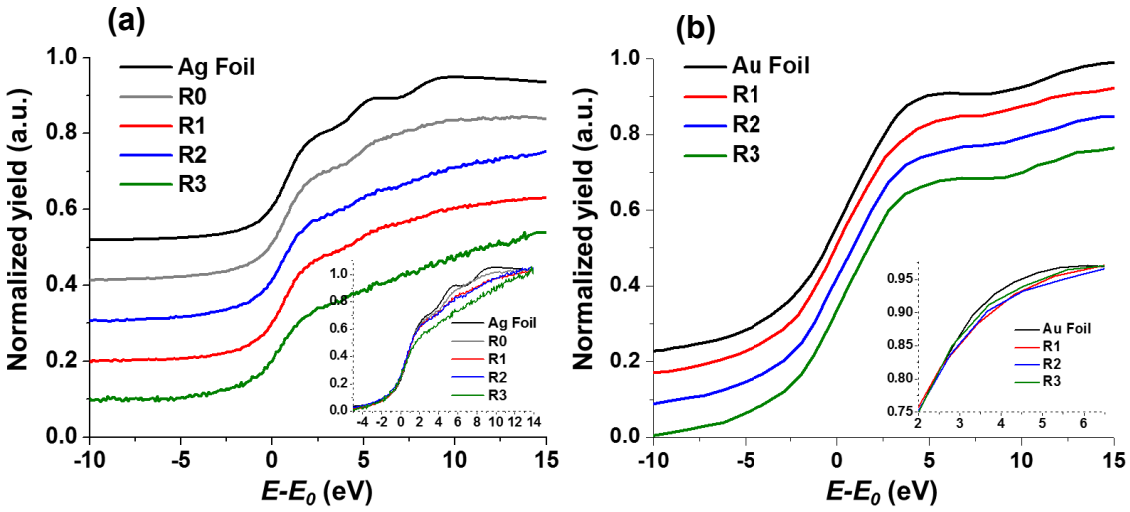

Figure 5.4. Ag L_3-edge and Au L_3-edge XANES of the AgAu NPs. (a) Ag L_3-edge XANES and (b) Au L_3-edge XANES of pure Ag NPs, and bimetallic AgAu NPs. The inset of each edge shows the overlap of the XANES spectra for each sample.

Based on the information provided by EXAFS and XANES analyses, the proposed atomic structures of the NPs are presented in Figure 5.5. It is proposed that Au initially forms at the surface of the Ag NPs and as more Au is added, the Au replaces the Ag in the core as the Ag diffuses to the surface of the NPs. The replacement is thought to occur by the galvanic reaction of:

$$3Ag_{(s)} + AuCl_4^{+}{}_{(aq)} \rightarrow Au_{(s)} + 3\ Ag^{+}_{(aq)} + 4\ Cl^{-}_{(aq)} \qquad (5.5)$$

where 3 Ag atoms are oxidized to reduce 1 Au atom.[130,260] Therefore, the addition of more $HAuCl_4$ will lead to less Ag, hence the observed change in molar ratio. This reaction mechanism would also imply that the NPs would undergo a change in size with the different amounts of Au^{3+} added. Given that the bimetallic NPs had similar average diameters, there was likely an additional reduction taking place during the reactions. In these cases, the PVP ligands could have contributed to the overall mechanism as it has Ag^{+} and Au^{3+} reductive capabilities,[206,261,262] and may account for the similar NP sizes. However, it is noted that PVP has a stronger reducing effect on Ag^{+}, which could imply

the preferential reduction of the newly formed Ag^+ (see Eqn. 5.5) onto the surface of the NPs.[262] The observed structural arrangements were also likely due to Ag and Au interdiffusion, given their similar lattice constants (*i.e.,* ~ 4.08 Å). In these cases, the rate of Ag and Au interdiffusion was also dramatically increased because of the small size the NPs,[263] and the higher temperature used in the synthesis (100 °C)[264]. Furthermore, the predicted Au-Au bond energy (226.2 ± 0.5 kJ/mol[265]) is higher than that of Ag-Ag (162.9 ± 2.9 kJ/mol[265]), which supports the Au core enrichment of the bimetallic NPs. In addition, the surface energy of Ag (78 meV $Å^{-2}$) is lower than that of Au (97 meV $Å^{-2}$), which supports the surface enrichment of Ag.[129]

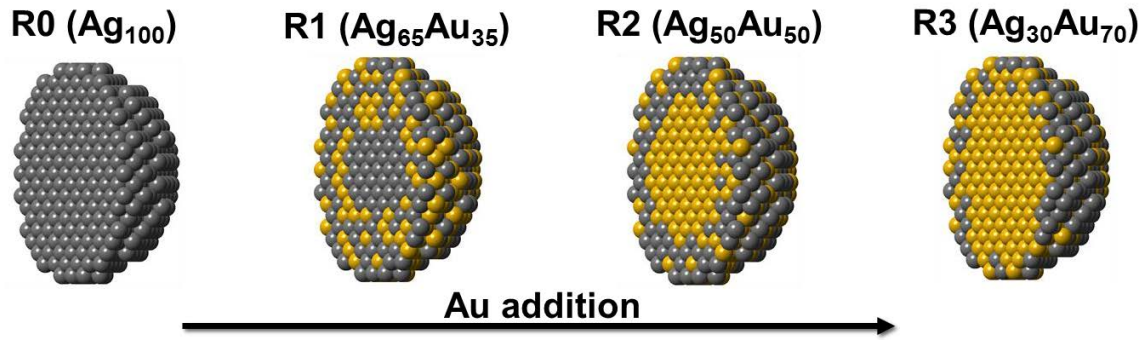

Figure 5.5. Proposed AgAu NP structures based on coordination results. The Au and Ag atoms are shown as yellow and grey spheres, respectively.

5.5.3 Antibacterial Activity

The antibacterial activity of the NPs was first examined using a standard disc diffusion assay with *S. aureus*. Figures 5.6a-c show representative images of the zones of inhibition, and Figure 5.6d shows the overall results based on at least three replicates for each sample. First, the R0 NPs had significantly higher zones of inhibition compared to all of the bimetallic NPs and negative control ($p < 0.05$), despite the lower amount of Ag in the R0 NPs. Second, the R2 NPs ($Ag_{50}Au_{50}$) had a slightly higher inhibition zone than

the R1 NPs ($Ag_{70}Au_{30}$). This result is interesting because the R2 NPs had lower amounts of Ag, yet still exhibited a significantly higher activity against the bacteria ($p < 0.05$). This may be a result of the different NP surface arrangements observed by EXAFS, where the R2 sample presented most of the Ag at the surface of the NP. Unfortunately, the R3 NPs exhibited a large standard deviation in the inhibition zone, which prevented an observable trend overall. However, the main finding from the assay results is that the addition of Au reduces the antibacterial activity significantly, and there may be a correlation between NP surface structure and activity.

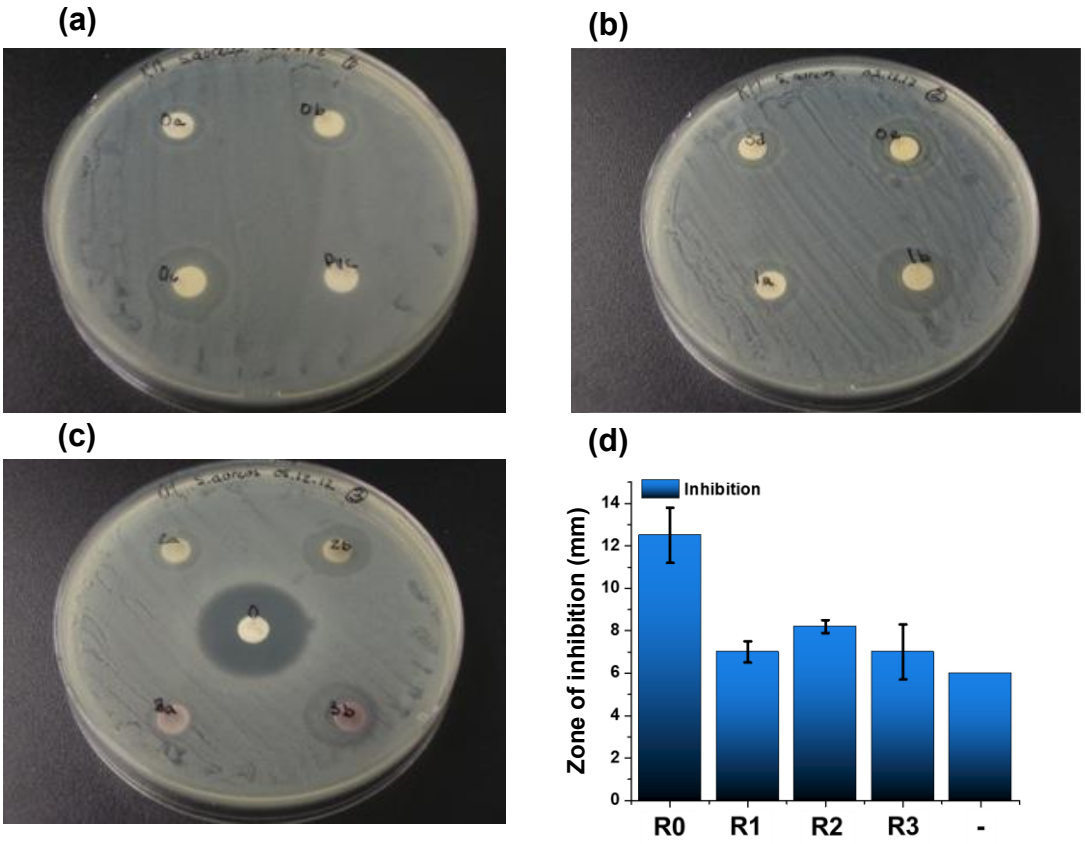

Figure 5.6. Disc diffusion assays of the AgAu NPs. (a-c) Representative disc diffusion assay results against *S. aureus.* The samples are represented by 0a-e for R0, 1a-b for R1, 2a-b for R2, and 3a-b for R3. PVP and chloramphenicol are also represented by PVP in (a) and 0 in (c), respectively. (d) Comparison of the results based on three replicates for each NP along with the negative PVP control.

In order to verify the disc diffusion results and more effectively compare the antibacterial activity of the NPs, an MIC assay with *S. aureus* was also carried out. Figure 5.7 shows the MICs for each solution based on their total metal concentrations, which were then used to retrospectively calculate the Ag and Au concentrations based on the molar ratios determined by ICP-OES. The first observation from a comparison of the MICs was that the R0 sample gave the lowest MIC of 50 μM total metal, indicating the highest antibacterial activity. On the other hand, all bimetallic NPs showed the same MIC values of 460 μM, based on their total metal concentrations. A similar trend in the antibacterial activity of the AgAu NPs against Gram-negative bacteria (*Escherichia coli, E. coli*) was also observed, albeit under slightly different assay conditions. These MIC values against *E. coli* and a brief description of the assay method are presented in Appendix A. For *S. aureus*, the MIC results are similar to the disc diffusion assay results, although the bimetallic NPs demonstrated identical MIC values. Given that there were different amounts of Ag in each bimetallic NP, we initially expected this to lead to different MICs. However, we can rationalize these antibacterial activities given their structural determination by XAS (Figure 5.5). By examining the structure of NPs, the location of the Ag in each NP was determined to be slightly different. For example, the R1 NPs exhibited a mixed surface layer of Ag and Au, the R2 sample had a thinner layer of Ag enriched with Au, and the R3 NPs had a thin layer of mostly Ag. Based on the EXAFS and MIC results, it is proposed that the antibacterial activity of the NPs is largely a result of the location of the Ag and not the overall Ag concentration in the NP. Therefore, the similar amount of Ag located on the immediate surface for all of the bimetallic NPs led to similar antibacterial effects. The slight difference between the MIC and the disc diffusion assay results, (*e.g.,* for R2), may be a result of the different

conditions in the assays. For example, the permeation of the whole NP or Ag^+ from the surface in the different media may have contributed to a difference in observed antibacterial activity. However, both sets of results indicate that the location of the Ag is an important aspect of the antibacterial activity.

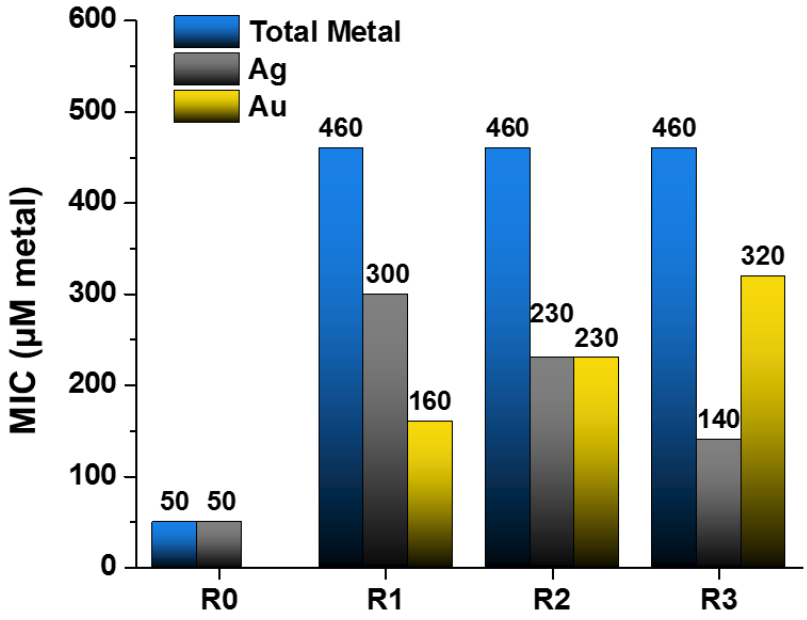

Figure 5.7. Minimum inhibitory concentrations against *S. aureus* for the AgAu NPs compared by total metal, Ag, and Au concentrations.

It should be noted that normalizing the NP solutions by their total metal concentration allowed for the solutions to be compared by the same number of NPs interacting with the bacteria, based on the fact that the NPs were similar in size (from TEM results). This is a different approach than previous studies which examine Ag NP MIC from the perspective of Ag only,[127] which may have skewed the observed MICs here. For example, the Ag NP solution containing 50 μM Ag would have much less surface area than AgAu NP solutions containing 50 μM Ag, if the NPs are the same size. Therefore, it is feasible that the AgAu NPs would be more effective, due to the increased

amount of NP surface area interacting with bacteria. The MIC results show that even with a lower amount of Ag (*i.e.,* R3), there was still an antibacterial effect, because the Ag was located primarily on the surface. Had the NPs been normalized based on Ag concentration only, the R3 NPs may have appeared to be more effective at inhibiting bacteria growth, as they showed the lowest MIC based on Ag concentration. However, only through the comparison of similar NP surface areas and structural determination by XAS was a reliable comparison of MIC values achieved.

Our results clearly show that per mole of NP, and hence per individual NP, the bimetallic NPs were less active against the *S. aureus* bacteria. Nevertheless, since the surface of the bimetallic NPs were composed primarily of Ag atoms (see Figure 5.5), the large difference between the MICs of the bimetallic NPs and the pure NPs was unexpected. Taking into account that the thick peptidoglycan wall likely inhibits the penetration of entire NPs into Gram-positive bacteria,[37] the antibacterial effect observed here is likely dependent on the penetration of Ag^+. Therefore, since the alloying in the NPs implies stronger bonding between Ag and Au (*i.e.,* 202.5 ± 9.6 kJ/mol[265] for Ag-Au; 162.9 ± 2.9 kJ/mol[265] for Ag-Ag) we propose that the large difference in MICs between R0 and the bimetallic NPs was a result of the Au inhibiting the release of the Ag^+. On the other hand, it is also conceivable that the Au component of the NPs could have contributed to the antibacterial activity; however, previous work has shown that Au NP surface reactions were the predominant mechanism of antibacterial effect and not surface released Au^{3+}.[246] Again, since the peptidoglycan wall likely inhibited the penetration of the entire NPs into the bacteria, the surface interactions of the Au would be limited and the antibacterial mechanism of the bimetallic NPs was mostly reliant on the Ag^+ release

as discussed. Nevertheless the role of the Au becomes further defined in the cytotoxicity assessment in the following section.

5.5.4 Cytotoxicity

Despite the lower activity of the bimetallic NPs against bacteria, another important aspect of NPs is their cytotoxicity against normal mammalian cells. Therefore, the cytotoxicity of the NP solutions were tested against NIH-3T3 fibroblasts and the results presented in Figure 5.8. The assay was conducted with NP concentrations standardized by total metal concentration in order to compare to the disc diffusion and MIC assay results. The results show that there was a consistent decreasing trend in the cell viability of the fibroblasts as each NP total metal concentration was increased. Based on a minimum cell viability of 70 %,[252] R0 is considered to be cytotoxic at < 95 μM, which was similar to other PVP protected Ag NPs.[244] On the other hand, the bimetallic NPs showed 70 % viability at 280 μM, 370 μM, and 460 μM, for the R1, R2, and R3 samples respectively. Therefore, the cytotoxicity of the NPs followed R0 > R1 > R2 > R3. As shown in Figure 5.8b, at 70 % viability, the Ag content in each sample at the above concentrations would be <95 μM, 180 μM, 185 μM, 140 μM for R0, R1, R2, and R3, respectively. Correspondingly, the Au concentrations would be 0 μM, 100 μM, 185 μM, and 320 μM. In the case of the R3 NPs, the lower amount of Ag and higher amount of Au likely contributed to the lowest cytotoxicity towards the fibroblasts. As the EXAFS results showed that there was a similar amount of Ag on the immediate surface of the bimetallic NPs; these results suggest that the location of the Ag is less important to their cytotoxicity towards the fibroblasts. As the uptake of NPs into the intracellular matrix of other fibroblast cell lines has been reported,[65] it is feasible that the NPs are engulfed by

the fibroblasts, and the Au and/or Ag is released into the cell. In this case the molar ratio of the metals, and not the location of the Ag, will be the determining factor in the cytotoxicity.

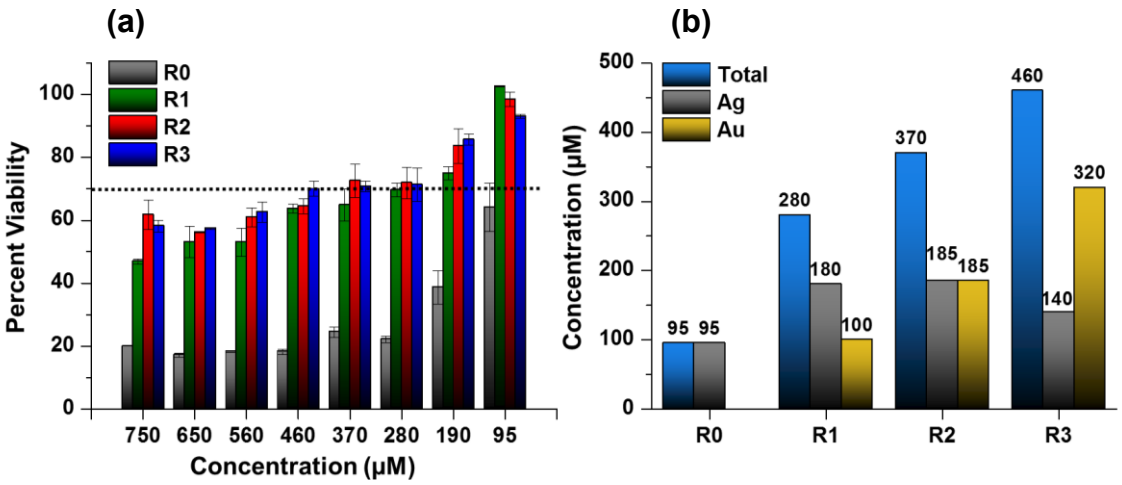

Figure 5.8. Cytotoxicity assays of the AgAu NPs. (a) Cytotoxicity against fibroblasts for the R0, R1, R2, R3 NP solutions of total metal concentrations from 750 to 95 μM. The concentration at which yielded a minimum percent viability of 70 % was taken to be the indicator of cytotoxicity. (b) Concentrations of the NPs at which the 70 % viability was reached, normalized by total metal, Ag, and Au concentrations.

5.6 Conclusion

In summary, we have presented a detailed picture of the correlation between atomic structure and bioactivity of a series of AgAu NPs. It was found that the addition of Au to the Ag NPs drastically changed the atomic structure of the NPs, resulting in the Ag core of the NPs gradually replaced with Au as more Au was added. Such information was then used to correlate to their antibacterial activity towards *S. aureus* and cytotoxicity towards NIH-3T3 fibroblast cells. The pure Ag NPs exhibited a MIC of 50 μM, while all of the bimetallic NPs yielded MICs of 460 μM even though there were differing amounts of Ag in each bimetallic NP. Using the structural information garnered from XAS, we

were able to rationalize the similar MICs for the bimetallic NPs. On the other hand, the cytotoxicity of the pure Ag NPs against fibroblasts was much higher than the bimetallic NPs, which was dependent on the concentration of the Au in the bimetallic NPs. The results show that there is indeed a therapeutic window of these bimetallic AgAu NPs to provide the highest antibacterial activity with the least cytotoxicity towards mammalian cells. Moreover, the correlation of bioactivity to NP atomic structure was demonstrated, which is the first step in providing more architectural control over NP structures for increased benefit.

Chapter 6 - The Surface Structure of Silver-Coated Gold Nanoparticles and Its Influence on Shape Control

Sections 6.3-6.6 are reproduced in part with permission from: Padmos, J. D.; Personick, M. L.; Tang, Q.; Duchesne, P. N.; Jiang, D.; Mirkin, C. A.; Zhang, P. The Surface Structure of Silver-Coated Gold Nanocrystals and Its Influence on Shape Control. *Nature Communications* **2015**, *6*, 7664. Copyright 2015, Nature Publishing Group. *The supporting information for this publication is included in Appendix B.*

6.1 Contributions

J.D.P. conducted the XAS experiments and XANES simulations, analyzed the XAS and DFT results and wrote the manuscript. M.L.P. synthesized the NC samples. Q.T. carried out the DFT experiments and helped with interpretation of the DFT results. P.N.D. helped carry out some of the EXAFS experiments. D.J. supervised Q.T., carried out the DFT experiments and helped with interpretation of the DFT results. C.A.M. supervised M.L.P.. P.Z. supervised J.D.P. and helped revise the manuscript.

6.2 Foreword

The previous chapter described the effect of alloying of Au to Ag NPs on their resulting atomic structure and resulting bioactivities. This chapter also describes alloying effects between Ag and Au but focuses on the surface structure of more distinct Ag monolayers on anisotropic Au NPs with specific surface facets. Instead of correlating this

information to the antibacterial activity of the NPs, it was used to rationalize their surface stabilization and growth mechanism.

6.3 Introduction

Metal nanoparticles (NPs) with well-defined shapes and facet indices are promising nanomaterials for many different applications due to the fascinating properties associated with their unique morphologies and surface structures.[139,266–269] Moreover, recent studies on silver (Ag)-assisted seeded growth with select halides have shown that gold (Au) NPs with unusual morphologies and high-index facets can be deliberately prepared in high yield.[120,139,269] The preparation of such Au NPs has demonstrated the correlation between Ag precursor concentration and Au NP facet index and shape. Most importantly, it has also identified the significance of the underpotential deposition (UPD) of Ag on the resulting rhombic dodecahedra with {110} facets, truncated ditetragonal prisms with {310} facets, and concave cubes with {720} facets. The same method was also used to prepare Au octahedra with {111} facets, but their growth was found to be governed by a more typical thermodynamic formation process.[120] In addition, halide ions, such as the chlorides (Cl^-) used in those syntheses, are an important factor governing the shape evolution of NPs prepared by the UPD method.[139] Briefly, halides have been shown to control the growth of specific facets on Au NP surfaces by (i) modifying the reduction potential and solubility of the Au^+-halide complexes formed in solution and (ii) passivating the Au NP surface thereby changing the amount of Au surface available for the catalyzed reduction of Au^+.[139] Furthermore, in Ag-assisted Au NP syntheses, the resulting halide-Ag UPD layer can control specific facet growth by its stability on the Au NP surface, and the facet type produced is dependent on the type of halide used.[270]

Although the synergistic roles of Ag and halides have been implicated in the formation mechanisms of the aforementioned NPs, their facet-specific surface structure is still largely unknown, despite being critically important to understanding their growth mechanisms and structure-property relationships. In particular, little is known about the halide portion of the structure, as halides are nearly invisible to traditional analytical techniques. Therefore, elucidating the surface structure of multicomponent systems, such as Cl^--adsorbed Ag-coated Au NPs, is a challenging yet worthwhile endeavor due to its impact on controlling NP shape and functionality.

Towards this end, X-ray absorption spectroscopy (XAS) can provide surface structure information regarding oxidation state, electronic structure, and local coordination environment (including metal-metal and metal-adsorbate bonding) from the perspective of a given element.[248] Due to this element specificity, XAS is particularly useful in probing multicomponent surface structures, including AgAu bimetallic NPs.[75,87,198,250,271,272] Although, typically, extracting information regarding surface bonding configurations from XAS is limited to smaller NPs (*i.e.,* < 10 nm), as the signals from the more numerous non-surface atoms in larger NPs outweigh those from the surface atoms. However, in the case of the relatively large NPs described herein (*i.e.,* > 50 nm), their surfaces are covered by a thin layer of Ag that can be isolated using element-specific XAS, thus allowing their surface structures to be determined. In addition, density functional theory (DFT) can be used to model the coordination environments of these NP surfaces, as their large sizes permit their treatment as bulk surfaces. DFT has been previously used to calculate adsorbate interactions with low-index bulk metal surfaces ({111}, {110}, {100}, *etc.*);[273–276] however, higher index surfaces, let alone those on NPs, are less commonly prepared and have not been correspondingly studied with DFT.

In this study, we implement element-specific XAS to reveal the atomic surface structures of Cl^--adsorbed Ag-coated Au NPs with {111}, {110}, {310}, and {720} surface facets. In this way, we identify key differences between non-UPD and UPD NP surface coordination and bonding, as well as characterize the facet-index dependent Ag-Cl bonding between all of the NCs. We then use DFT structural optimization calculations to generate a more complete description of the NP surfaces, in particular the Cl^- adsorbates on the Ag. Moreover, we systematically explore the effect of Cl^- adsorption on each NP surface by XAS simulations, and those results are used in conjunction with experimental XAS to both identify the Ag valence state on the NP surfaces and further confirm the Ag-Cl bonding environment. This combination of experimental/simulated XAS and DFT modelling demonstrates the ability to comprehensively study the surface structure of shape and facet-index controlled bimetallic NPs.

6.4 Experimental

6.4.1 Preparation of Ag-coated Au NPs

The synthesis and characterization methods of the NP samples has been previously published.[120] Briefly, cetyltrimethylammonium chloride (CTAC) stabilized seed Au NPs were mixed with a growth solution containing CTAC, hydrochloric acid (HCl), ascorbic acid, hydrogen tetrachloroaurate ($HAuCl_4$), and differing amounts of silver nitrate ($AgNO_3$). The concentration of $AgNO_3$ has been shown to determine the resulting shape and surface index and samples prepared with 1, 10, 40, and 100 μM $AgNO_3$ produced {111} octahedra, {110} faceted rhombic dodecahedra, {310} faceted truncated ditetragonal prisms, and {720} faceted concave cubes, respectively.

6.4.2 X-ray Absorption Spectroscopy (XAS)

After preparation, the samples were freeze-dried and packed into kapton film pouches in order to conduct XAS experiments at the Advanced Photon Source (BM-20 beamline, Argonne National Laboratory, Argonne, IL, USA) or the Canadian Light Source (SXRMB beamline, Saskatoon, SK, Canada). For Ag K-edge XAS measurements, the samples were placed in a cryostatic sample holder at 50 K while the Ag K-edge XAS measurements were collected using a 32-element Ge fluorescence detector; XAS data for Ag foil was collected simultaneously using standard gas-ionization chamber detectors. This low-temperature fluorescence XAS method was used to compensate for the dilute concentration of Ag in the samples, and to reduce the dynamic thermal disorder.[277] For Ag L_3-edge XAS, the freeze dried samples were affixed to double-sided carbon tape on a sample holder and then placed in the sample chamber and allowed to reach an ultra-high vacuum atmosphere. The Ag L_3-edge XANES spectra were collected with a 4-element Silicon drift detector.

All of the XAS spectra were processed with the WinXAS[162] or IFEFFIT[160,161] software packages. The raw EXAFS data (see Appendix Figure B1) were converted to *k*-space (see Appendix Figure B2) and then Fourier-transformed into *R*-space using a Hanning function with a range of k = 2.5-12.7 $Å^{-1}$, which was chosen by the overall data quality of the samples (see Appendix Figures B3-B6). The *R*-space spectra were then refined with WinXAS[162] using bonding paths from an *ab initio* simulation of Cl^--adsorbed Ag on Au{111} model generated using the FEFF code (version 8.2).[164,165] The refinements calculated structural information such as CN, bond length (R), and Debye-Waller factors (σ^2) along with the energy shift parameter, ΔE_o, which helps account for refinement assumptions. Given the composition of the samples, it was surmised that Ag-

Cl, Ag-O, Ag-N, Ag-Ag, and AgAu were potential bonding paths, as those theoretical phase amplitudes generated by FEFF are contained within the *R*-space region of around 2-3 Å (without phase correction). However, tentative refinements of Ag-N and Ag-O paths produced entirely unphysical results; thus, they were not considered in any further refinements. The smaller peaks under 1.5 Å for the samples are most likely too short to be attributed to nearest neighbour backscattering and may be an artifact of low frequency noise in the fluorescence data (see Appendix Figures B3-B6). Therefore, all of the *R*-space spectra underwent refinements with Ag-Cl, Ag-Ag, and Ag-Au bonding paths within the *R*-space range of 1.7-3.3 Å. In order to reduce the number of free running parameters to number of independent points, the ΔE_o values for all of the paths, and the σ^2 values for the two metal-metal paths were correlated. The ΔE_o values account for the phase differences of the experimental data to the theoretical FEFF input data. These values are often correlated in EXAFS refinements given the assumption that each path will have the same phase differences if the same model was used in the input files. In our case, the same model was used and therefore we can correlate them to reduce the number of variables. In addition, the σ^2 values were correlated because Ag and Au have very similar lattice constants and bonding, therefore the disorder in their bonds should be similar. It should be noted that the {111} spectrum could not be refined with correlated σ^2, which is likely a result of the very different bonding arrangement of the Ag in that sample demonstrated later (*e.g.,* higher degree of alloying). For each refinement, WinXAS calculated the number of free parameters to be 8 (except for {111} with 9 free parameters) and the number of independent points to be 13. The uncertainties reported were calculated from off-diagonal elements of the correlation matrix of each refinement,

weighted by the square root of the reduced chi-squared value, taking into account the experimental noise for each *R*-space spectrum from 15 to 25 Å.[278]

6.4.3 Density Functional Theory (DFT)

The DFT computations were performed with a frozen-core plane-wave pseudopotential approach using the Vienna *ab initio* simulation package (VASP).[279] Since the NPs were relatively large, periodic slab surface models with different indices represented the corresponding facets of the NPs. A 4×4×1, 2×2×1, 2×2×1 and 2×1×1 supercell size was used to simulate the {111}, {110}, {310}, and {720} surfaces, which contained about 80/16, 28/4, 20/4 and 58/10 Au/Ag atoms, respectively. Among these surfaces, {111} surface has a planar shape, while {110}, {310}, and {720} surfaces have step-like shapes. The Au {111}, {110}, {310}, and {720} periodic slab surfaces were modeled with six, seven, ten, and thirteen layers of Au atoms, respectively, and are within a thickness of 1-2 nm, in order to provide qualitatively reasonable predictions on the NP core behavior. The Cl^- anion was modeled by placing Cl atoms on the slab surfaces, letting the electronic density converge and then determining the partial atomic charges on the Cl atoms. The full 1.0 monolayer (ML) Cl^- coverage for each surface was created by the following: for the {111} surface, about ¼ Ag diffuse into the Au layer, and the vacant surface Ag sites were then occupied by Cl, while the remaining ¾ of surface Ag atoms are coordinated to adsorbed Cl^- in the 3:1 ratio. For the {310} and {720} surfaces, full coverage was also created by coordinating Cl^- in a 3:1 ratio, while for the {110} surface, a 4:1 ratio was used. Based on the full coverage model for each surface, other coverage models were constructed (*e.g.,* 25 %, 50 %, 75 %) by taking out either the substituted Cl^- or adsorbed Cl randomly, and then used a low-lying energy model for further structural

analysis. During the computations, pseudopotentials with $5d^{10}6s^1$, $4d^{10}5s^1$ and $3s^23p^5$ valence electron configurations were used for Au, Ag and Cl atoms, respectively and the scalar-relativistic effect was included in the pseudopotential for Au. Since the surfaces contained strong covalent Ag-Cl and Ag-Au bonds, no correction for the long-range aurophilic interactions was implemented. The ion-electron interaction was described with the projector augmented wave (PAW) method.[280] Electron exchange-correlation was represented by the generalized gradient approximation (GGA) functionals from Perdew, Burke and Ernzerhof (PBE).[281] A cutoff energy of 450 eV was used for the plane-wave basis set. The Brillouin zone was sampled using a 4×4×1 Monkhorst-Pack *k*-point mesh. The convergence threshold for structural optimization was set to be 0.02 eV/Å in interatomic force. The thickness of the vacuum layer was set to be 12 Å which is large enough to ensure decoupling between neighbouring slabs, as the further increase of the vacuum thickness leads to a small energy change of less than 0.01eV. During optimization, the top three, two, four, and six layers of the respective {111}, {110}, {310}, and {720} Au surfaces were allowed to relax together with the surface Ag layer and adsorbed Cl atoms, while the bottom layers were kept at their bulk positions. The resulting atomic coordinates from the DFT computations were obtained for each surface and modelled with the Crystal Maker program (version 9.0.2).

6.4.4. XANES Simulations and Linear Combination Fitting

Simulated Ag K-edge XANES spectra were calculated using the FEFF code with atomic coordinates obtained from the DFT-optimized structures. The coordinates for the bulk models were generated from their respective symmetries and space groups. For each simulation, a full multiple scattering (FMS) diameter of 30 Å and a self-consistent field

(SCF) radius of 6 Å was used for each individual Ag site, which equated to approximately 100 and 30 atoms for the FMS and SCF calculations, respectively. An amplitude reduction factor (S_o^2) of 0.95 was used to render the results directly comparable to the experimental data. The linear combination fitting of the Ag K-edge XANES spectra were conducted with Athena, part of the IFEFFIT software package.[160,161] In this way, the experimental XANES of each NP sample was individually fit with the corresponding average of the simulated XANES spectra for each coverage model. The linear combination fits were conducted within a range of -20 to 30 eV of the E_o-normalized spectra. The resulting R-factor, which represent the goodness of fit, was recorded for each coverage model.[149]

6.5 Results and Discussion

The preparation and general characterization of octahedra with {111} facets, rhombic dodecahedra with {110} facets, truncated ditetragonal prisms with {310} facets, and concave cubes with {720} facets have been published elsewhere.[120] Briefly, their specific facets were identified by a combination of electron diffraction and facet-angle measurements using scanning electron microscopy, and were found to have approximate edge lengths between 70-120 nm.[120,282,283] The Ag coverage on each surface was identified by a combination of X-ray photoelectron spectroscopy and inductively coupled plasma spectroscopy and each NP type exhibited slightly lower than full monolayer Ag coverage (60-80 %).[120] In the work presented here, synchrotron Ag K-edge extended X-ray absorption fine structure (EXAFS) experiments were used to elucidate a three-component bonding structure composed of Ag-Cl, Ag-Au, and Ag-Ag for each NP surface (schematically illustrated in Figure 6.1a). The validity of this three-component

structure is supported by the high quality Ag K-edge *R*-space refinements shown in Figure 6.1b (see Appendix Table B1 for refinement results table and Appendix Figures B3-B6 for the refinement components and residuals). The most notable result from the EXAFS bond length analysis (Figure 6.1c) is that the {111} Ag-Cl bond (2.66 ± 0.02 Å) is longer than those of the {110} (2.62 ± 0.01 Å), {310} (2.61 ± 0.01 Å), and {720} (2.58 ± 0.01 Å) surfaces. Likewise, the Ag-Au bond length of the {111} sample (2.99 ± 0.03 Å) is longer than those of the {110} (2.87 ± 0.01 Å), {310} (2.88 ± 0.01 Å), and {720} (2.86 ± 0.01 Å) samples. These two findings indicate the remarkable difference in adsorbate- and alloy-bonding between the non-UPD and UPD NPs (*i.e.,* {111} versus {110}, {310}, and {720}), and illustrate the effectiveness of the UPD mechanism in inducing stronger Ag-Cl and Ag-Au interactions (*i.e.,* shorter bond lengths). Furthermore, Ag-Cl bond lengths in the NPs are shown to be facet-index dependent, suggesting that Ag-Cl bonding is a key component in stabilizing the increasing surface energies of the NPs (*i.e.,* $\gamma_{111} < \gamma_{110} < \gamma_{310} < \gamma_{720}$[140]). On the other hand, there is no discernable trend in the Ag-Au bond length between the UPD samples, and therefore the Ag-Au bonding in these structures is likely more dependent on the UPD mechanism rather than facet-specific bonding. Moreover, the Ag-Ag bond lengths do not demonstrate any clear trend, which may be a result of interplay between facet-specific bonding and the UPD mechanism.

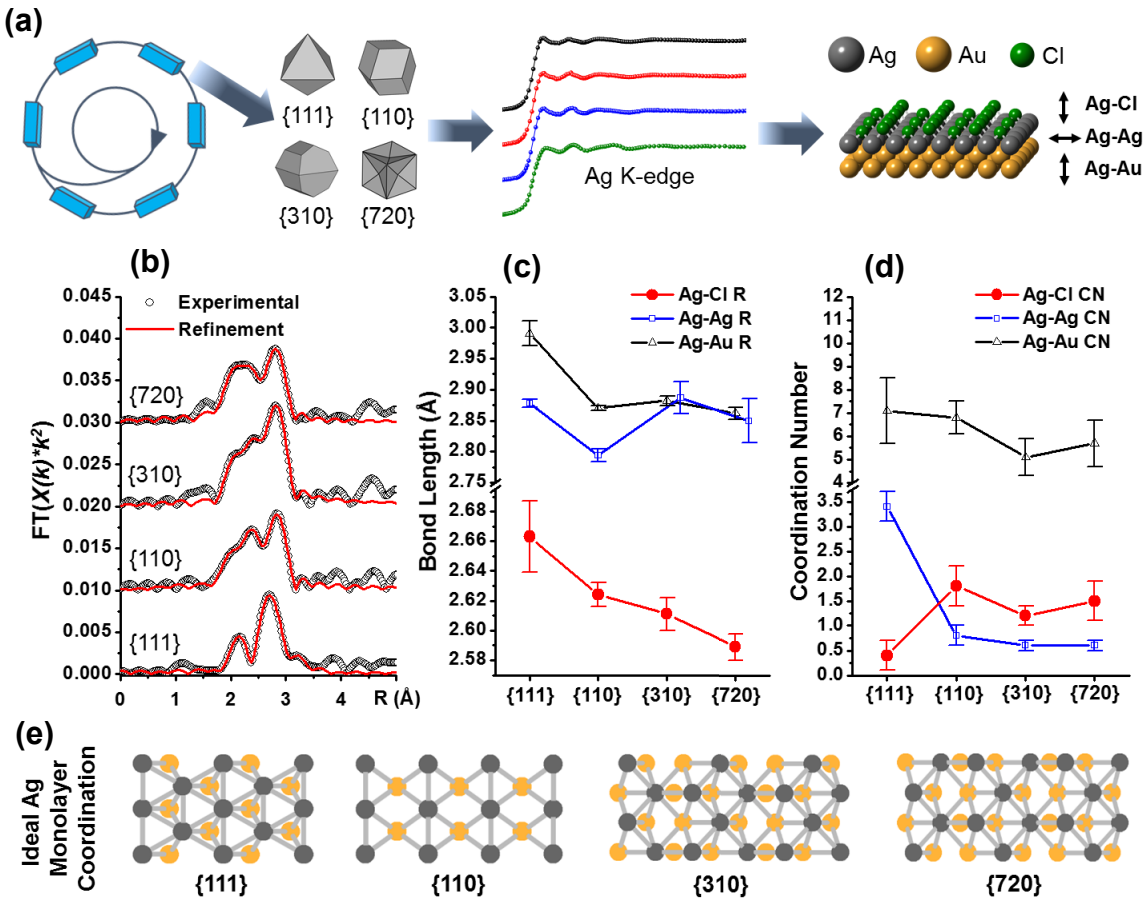

Figure 6.1. Surface structure of Ag-coated Au NPs from Ag K-edge XAS. (a) Schematic illustration of synchrotron X-rays used to obtain Ag K-edge EXAFS spectra from the Ag on the NP surfaces, from which three-layer Ag-Cl, Ag-Ag, and Ag-Au surface structures were determined. (b) *R*-space spectra of the Au NPs were refined based on theoretical bonding paths generated by FEFF. The refinements were conducted over *R*-space ranges of 1.7-3.3 Å, hence the disagreement of the refinements to the experimental data outside of that range. (c) Experimentally determined Ag-Cl, Ag-Au, and Ag-Ag bond lengths and (d) coordination numbers of each NP surface. The error bars in (c) and (d) represent uncertainties in the refinement and details of their calculation can be found in section 6.4.2. (e) Top-down view of ideal monolayer Ag coverage on Au with {111}, {110}, {310}, and {720} facets, giving average Ag-Ag/Ag-Au coordination numbers of 6/3, 2/5, 2/5, 3/4.8, respectively.

The average coordination numbers (CNs) of each NP surface were revealed from the Ag K-edge *R*-space refinements and plotted in Figure 6.1d. To assist in the interpretation of the CNs, ideal monolayer models of Ag on Au (Figure 6.1e) were used

to calculate average Ag-Ag/Ag-Au CNs, yielding 6/3 for {111}, 2/5 for {110}, 2/5 for {310} and 3/4.8 for {720}. In order to compare the experimentally observed CNs to the ideal monolayer CNs, it is first useful to note that NP surfaces are commonly found to have under-coordinated surface sites (edges, corners, defects, *etc*.).[155] In addition, the slightly less than monolayer coverages of Ag on the NPs could contribute to under-coordinated Ag. The under-coordinated Ag on these NP surfaces will greatly influence their Ag-Ag CNs, and could explain why the Ag-Ag CNs are lower than the ideal (*i.e.,* 3.4 ± 0.3 versus 6 for {111}, 0.8 ± 0.1 and 0.6 ± 0.1 versus 2 for {110} and {310}, and 0.6 ± 0.1 versus 3 for {720}). However, the subsurface Au (the main component of the NPs) will be less influenced by Ag under-coordination, and therefore the Ag-Au CN is a more reliable parameter to evaluate the surface structure in these cases. Taking this into account, the Ag-Au CNs of the two high-index surfaces (4.9 ± 0.8 for {310} and 5.7 ± 0.9 for {720}) are consistent with the ideal monolayer models (Ag-Au CN of 5 and 4.8). On the other hand, the {110} shows a slightly higher Ag-Au CN (6.8 ± 0.7) than the ideal Ag-Au CN of 5, indicating that the Ag is perhaps present both in and below the top-most surface layer. However, the {110} Ag-Cl CN of 1.8 ± 0.4 is similar to 1.2 ± 0.2 for {310} and 1.5 ± 0.4 for {720}, indicating that the Ag is mostly on the surface and therefore more consistent with a monolayer model. In contrast to the UPD NPs, the {111} Ag-Au CN of 7.1 ± 1.4 is significantly higher than the ideal CN (*i.e.*, 3). This is consistent with interdiffused Ag on Au-core/Ag-shell NPs,[271] and supports the presence of Ag below the surface of the {111} NPs. In addition, the Ag-Cl CN is significantly lower for the {111} NPs (*i.e.,* 0.4 ± 0.2) compared to that of the three UPD NPs with Ag monolayer type structures. This low Ag-Cl CN further supports the notion that there is a significant amount of Ag below the {111} NP surface. Conversely, the higher Ag-Cl CNs of the

{110}, {310}, and {720} NPs support that the Ag is predominantly on their surfaces, and also demonstrates the increased Cl^- adsorption from the UPD mechanism.[284] Collectively, the Ag-Ag, Ag-Au, and Ag-Cl CN results suggest that the Ag atoms in the {111} NP surface are both in and below the top-most metal layer, whereas the {110}, {310}, and {720} NP surfaces are more distinct Ag monolayer type structures.

In order to confirm the experimental EXAFS coordination trends and provide more detailed information about the Ag-Cl, we carried out DFT structural optimization calculations for the {111}, {110}, {310}, and {720} surfaces (see models in Figure 6.2a). In these structural optimizations, we considered the amount of Cl^- coverage and compared 0, 0.25, 0.50, 0.75, and 1.0 (full) Cl^- monolayer (ML) coverages on each surface type (20 DFT models in total, see Appendix Figures B7-B11). Remarkably, the {111} DFT model (see Figure 6.2a top-left) was in good agreement with an embedded Ag configuration (*i.e.,* Ag below and in top-most layer), while the {110}, {310}, and {720} DFT models showed more distinct Ag monolayer-type structures (Figure 6.2a). These DFT-optimized structures were also in excellent agreement with the EXAFS CN results (see Appendix Table B2 for further comparison). Moreover, the DFT results were used to determine actual Cl^- coverages on the NP surfaces by plotting Ag-Cl CN versus Cl^- coverage for each DFT-optimized surface model (Figure 6.2b). The high-index UPD NPs were found to have similar Cl^- coverages of 0.41 ML for {310} and 0.48 ML for {720}. Interestingly, the higher Cl^- coverage for the {110} UPD NPs (0.73 ML) is consistent with a higher degree of Cl^- interaction to stabilize the surface, as it has the lowest number of surface Ag atoms per unit area of Au.[120] In contrast, the {111} Cl^- adsorption was much lower than the others (0.23 ML), again highlighting its difference from the UPD NPs and affirming the notion that it is stabilized by a different mechanism.

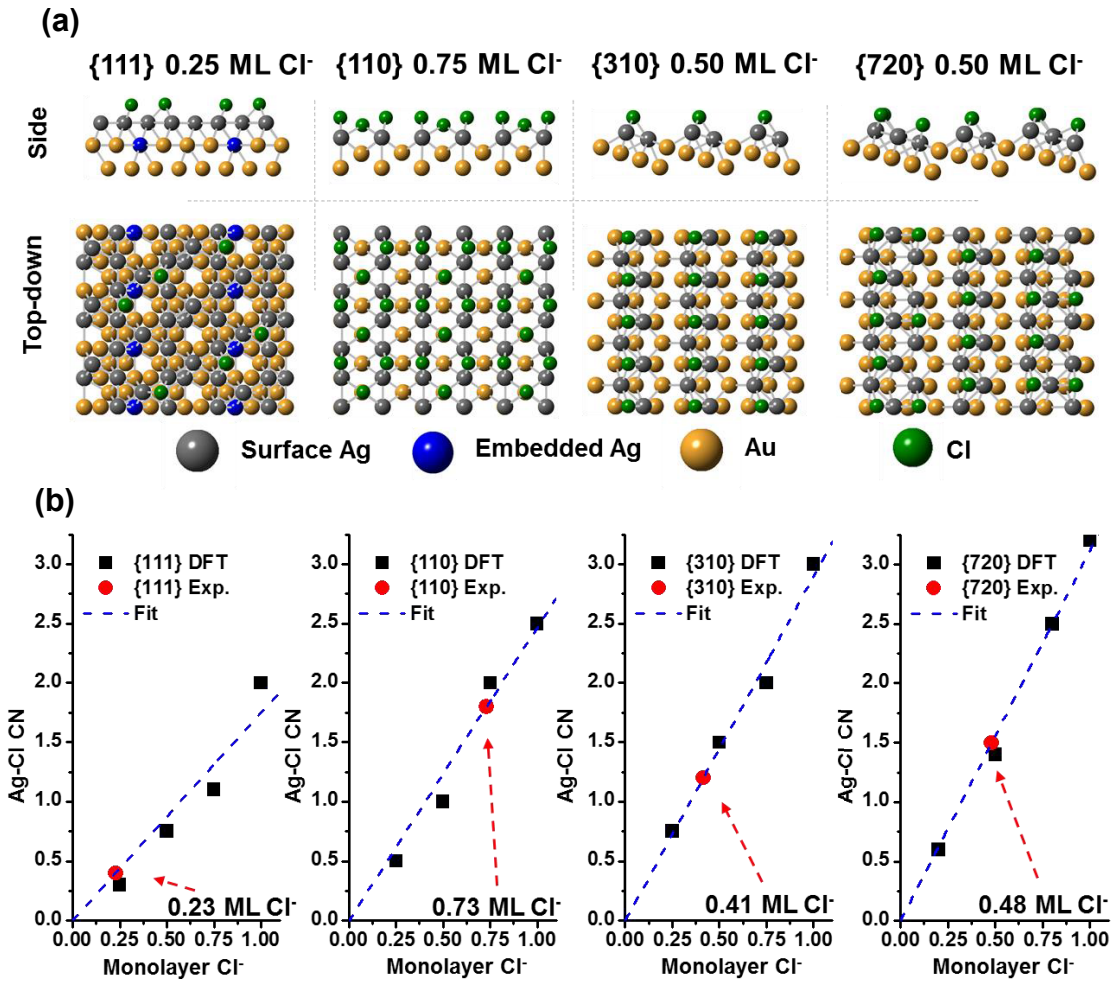

Figure 6.2. DFT model optimization results. (a) Side and top-down views of DFT-optimized structures with Cl^- coverage of 0.25 ML Cl^-, 0.75 ML Cl^-, 0.50 ML Cl^-, and 0.50 ML Cl^- for the {111},{110},{310}, and {720} NP surfaces, respectively. (b) Calibration curves of Cl^- coverage versus Ag-Cl CN for each calculated surface, and the corresponding experimental Cl^- coverage.

In order to verify the surface structure models deduced above, we employed a combined approach using DFT-optimized models (Figure 6.3a), site-specific simulations of X-ray absorption near edge structure (XANES) (Figure 6.3b), and experimental XANES (Figure 6.3c). In this way, site-specific Ag K-edge XANES simulations were carried out with the FEFF code using the coordinates provided by the DFT-optimized models of the proposed Cl^- coverages (see Appendix Figures B12-B15). The site specific simulations of each surface were averaged and overlaid with experimental data (Figure

6.3c) and in each case were found to fit well with the simulations, thus verifying the proposed DFT models (Figure 6.2a). Furthermore, the spectral feature (i) in Figure 6.3c for each surface matches with the reference Ag foil, indicating that the surfaces are of a similar valence state (*i.e.,* zero-valent). The later oscillatory feature (ii) in Figure 6.3c of all of the surfaces also lines up with the reference Ag foil, denoting similar metal-metal interactions, although it is less intense because of the lower backscattering amplitude from fewer Ag neighbours in the NP surfaces. In contrast, the NP spectral features are much different from the AgCl reference, which rules out the presence of ionic Ag and highlights the more extensive halide-metal bonding nature of the NP surfaces. We also carried out Ag L_3-edge XANES experiments on each NP sample to further confirm the oxidation state of the Ag on the NP surfaces (see Appendix Figure B16). The NPs all exhibited similar features to the Ag foil reference and showed the typical reduction in the first peak of the XANES due to nanosize and alloying effects.[123,158] thereby confirming the metallic oxidation state of the Ag on each surface.

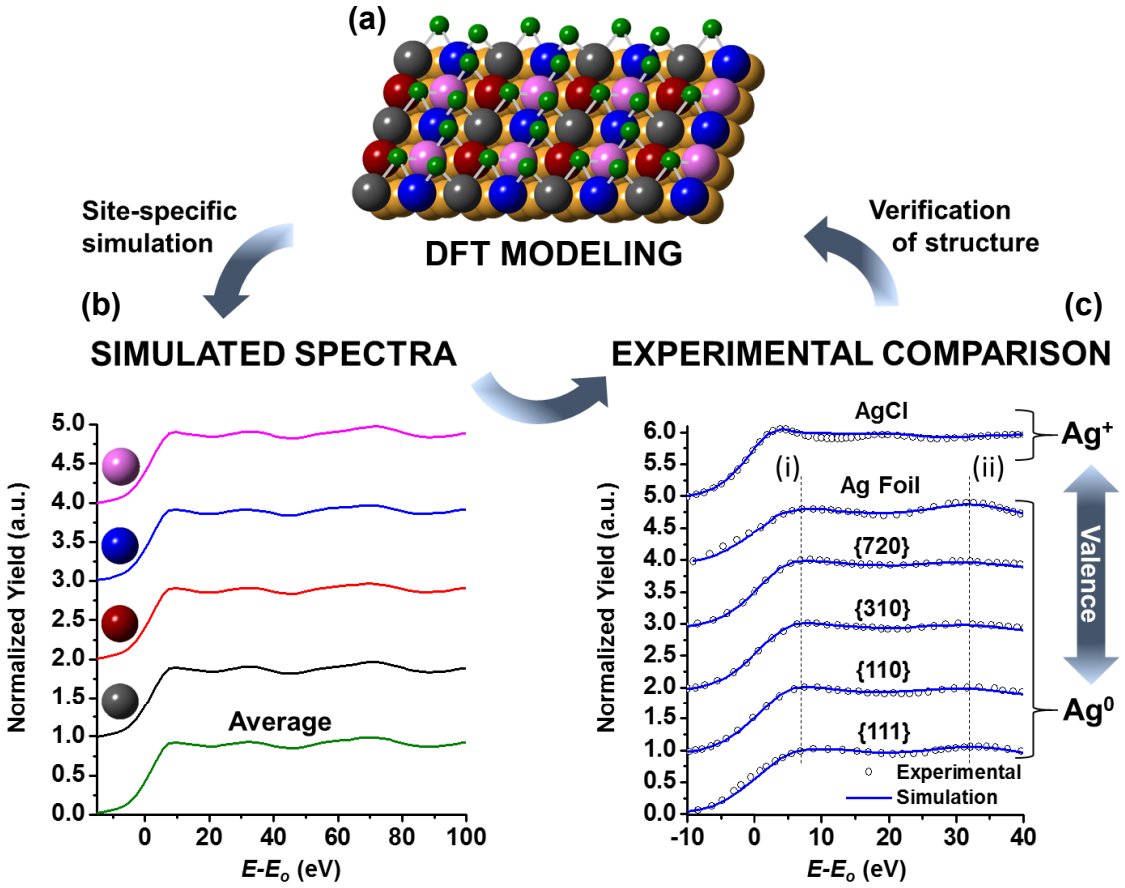

Figure 6.3. Combined approach of three techniques for validation of surface structure and identification of Ag valence state. (a) DFT-optimized model of the {110} NP surface showing the four different Ag sites shown in different colours. (b) Site-specific XANES spectra of the {110} surface were simulated by the FEFF code and then averaged. The simulated XANES spectra for the other surfaces are shown in the Appendix Figures B12-B15 (c) Averaged simulated XANES spectra were compared to experimental XANES spectra in order to verify the DFT models, as well as compared to reference materials to determine valence state of Ag on the NP surfaces.

Since the XANES region of metal K-edges are sensitive to both ligand adsorption and coordination,[153] further Ag K-edge XANES simulations were carried out in order to evaluate the effect of different amounts of Cl^- adsorption on each DFT-modeled surface (see Appendix Figures B17-B20 for the complete set of 131 simulations). The simulations for each surface with the five different Cl^- coverages (Figure 6.4a shows the {110} surface for illustration) were averaged and a significant change in the position and

intensity of the first XANES peak in proportion to the amount of Cl^- adsorbed was observed (Figure 6.4b). The averaged XANES were then used to conduct a linear combination fit of the experimental data of the corresponding NP surface and the best fitting model was identified by the lowest R-factor (Figure 6.4c).[160,161] The Cl^- coverage results from the linear combination fits are in excellent agreement with the findings shown in Figure 6.2 and Figure 6.3, and further support the NP surface structures presented in this work.

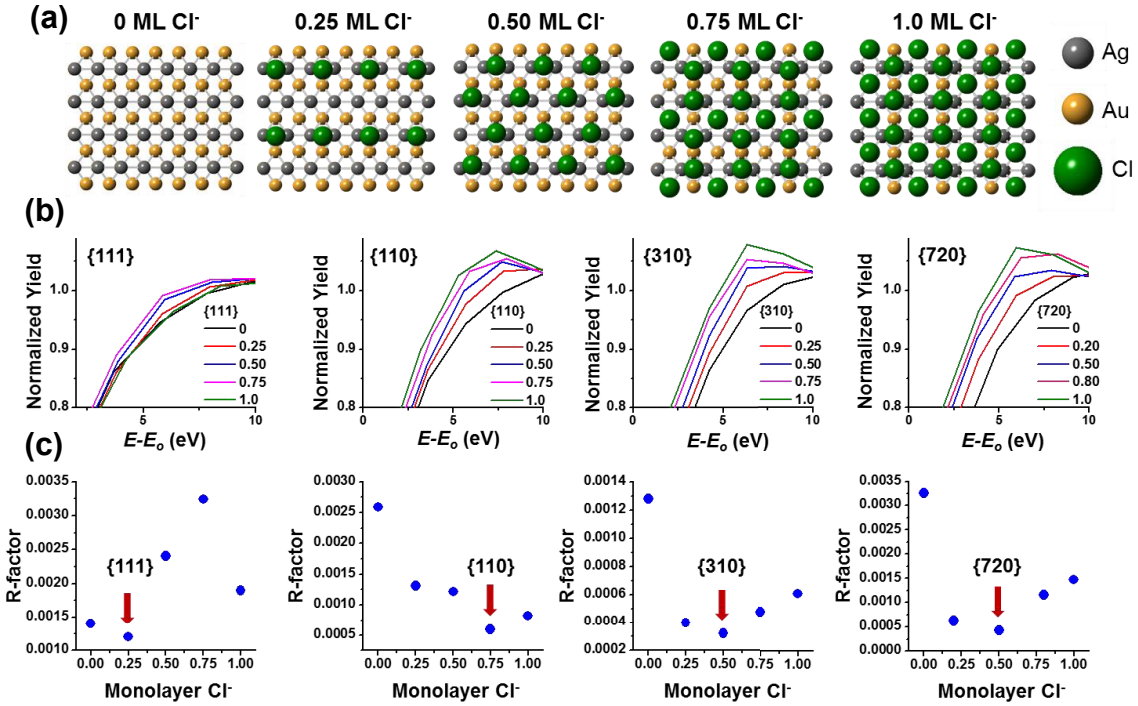

Figure 6.4. Simulated Ag K-edge XANES spectra and linear combination fitting results. (a) Representative illustrations of the {110} DFT-optimized models with different Cl^- coverages. The Cl^- was enlarged to more clearly see the different coverages. (b) Averaged XANES simulation from each DFT-modeled surface with 0, 0.25, 0.50, 0.75, and 1.0 ML Cl^- coverages. The averaged spectra were normalized to their absorption energies and used as individual standards to conduct a linear combination fit of the experimental data. The closeness of the averaged model spectra to the experimental spectra are represented by the R-factors shown in (c). The closest fit is characterized by the lowest R-factor, also indicated by the red arrow for each surface.

6.6 Conclusion

In this work, we uncovered the multicomponent surface structures of Cl^--adsorbed, Ag-coated {111}, {110}, {310}, and {720} Au NPs. These NPs represent excellent systems to elucidate the unique properties of NPs derived from specific synthetic approaches (*e.g.,* UPD vs. non-UPD) and specific surface crystallography (*e.g.,* low vs. high index). Our results can also help to clarify a number of fundamental concepts related to shape-controlled anisotropic NPs. First, the surface structures of the NPs were identified at the atomic scale and shown to be composed of Ag-Cl, Ag-Ag, and Ag-Au bonding. Interestingly, the NP surfaces comprised metallic Ag which demonstrates the ability of these NPs to maintain the metallic nature of the less noble surface metal (*i.e.,* Ag). This finding is in contrast to the typical surface oxidation that occurs at other Ag NP surfaces. Second, the significant differences between non-UPD and UPD NP surface structure were revealed in this work. In particular, the non-UPD NPs ({111}) exhibited Ag atoms embedded within the subsurface Au, whereas the UPD NPs ({110}, {310}, and {720}) showed more distinct Ag monolayer type structures on top of Au. This finding alone may have a substantial impact on the surface engineering of bimetallic NPs, as the UPD method may represent an important strategy to prevent the commonly observed metal-interdiffusion at NP surfaces.[271] In addition, the Ag-Au alloy bond of the non-UPD NPs was significantly longer than those of the UPD NPs, implying that the UPD mechanism produced a stronger alloying interaction (*i.e.,* shorter alloy bonding) at the surface of the NPs. Third, and most importantly, this work sheds light on the still-debated halide-induced formation mechanisms of shape-controlled Au NPs[139] by providing a detailed picture of the surface halide-metal bonding. So far, the special stabilization of Ag

by Cl^- adsorbates has been proposed as an explanation for the formation of a wider variety of Au NP shapes in the presence of Cl^- than in the presence of other halides, such as Br^- and I^-.[285] The four NPs studied in this work exhibited surface-index dependent Ag-Cl bond lengths and coverage, and such remarkable flexibility of the Ag-Cl bonding on the NP surfaces helps to explain this special Cl^- stabilization mechanism and particular NP growth. Finally, our work also demonstrates the usefulness of combining EXAFS, DFT modelling, and experimental/simulated XANES to reliably uncover the surface structure of shape and facet-index controlled bimetallic NPs. The potential of this technique towards more in-depth studies of bimetallic NP formation mechanisms is enormous, given the ability of *in-situ* and liquid/solid phase element-specific XAS measurements.[286]

Chapter 7 - Conclusions and Future Work

7.1 Conclusions

The surface structures of metal NPs are heavily correlated with their physicochemical properties and subsequent applications. Thus, it is important to characterize the surface and atomic structure of metal NPs, and understand ligand and alloy formation effects. Consequently, three specific subject areas have been emphasized in this thesis:

1. The effects of organic and aqueous organosulfur ligands on the surface structure and antibacterial activities of Ag NPs.

2. The effects of Au alloying on the atomic arrangement, antibacterial activity, and cytotoxic activity of bimetallic AgAu NPs.

3. The surface structure of Ag monolayers on anisotropic Au NPs and its influence on shape control.

In Chapter 2, a study of the structure and composition of a series of organosulfur-stabilized Ag NPs was carried out from both metal and ligand perspectives using XAS. It was determined that Ag NPs of varied sizes prepared with dodecanethiol (DDT) exhibited neither the "staple" surface structure nor the traditional metal-thiolate structure (*i.e.,* with thiolates bound at three-fold hollow sites of the metal surface). Instead, a concentration-dependent layer of Ag-sulfide on the surface of the metallic Ag cores was formed.

Moreover, a comparison between the surface structure of DDT-Ag NPs and those protected with didodecyl sulfide (DDS), indicated that the sulfide layer formation was inhibited when DDS was used. These results showed that surface structure and bonding in Ag NPs can be tailored by controlling the Ag/S molar ratio of the precursor materials and type of organosulfur ligand used, and demonstrated that the bonding between Ag and S is generally different from that of Au and S in a similar system.

In Chapter 3, a similar methodology was used to identify the structure and composition of Ag NPs protected with an aqueous thiol (cysteine, Cys) to compare these qualities with those of identically sized Ag NPs protected with polyvinylpyrrolidone (PVP). The PVP-Ag NPs showed a metallic Ag surface, consistent with metal NPs protected by weakly binding protecting ligands. On the other hand, the Cys-Ag NPs exhibited a distinct surface shell of sulfide, which is remarkably different from previously studied Cys-Ag NPs, and more similar to the Ag NPs prepared with DDT (discussed in Chapter 2). The effect of this sulfidized surface structure on the antibacterial activity of the Cys-Ag NPs was also examined. In this way, the minimum inhibitory concentrations (MIC) of both PVP-Ag NPs and Cys-Ag NPs were tested against Gram-positive (*S. aureus)* and Gram-negative (*E. coli* and *P. aeruginosa)* bacteria. It was found that the MICs of the Cys-Ag NPs were significantly higher, and therefore less effective, than the PVP-Ag NPs for each strain of bacteria, implicating a reduced activity from the sulfidized surface structure. Therefore, this work demonstrated the similar effect of thiols on Ag NP surface structure, consistent with that described in Chapter 2, as well as the importance of the surface structure in controlling antibacterial activity.

In Chapter 4, XAS was used to identify the structure and composition of 2 nm tiopronin-protected Ag NCs arranged in 1D chain assemblies. Wavelet-transformed

EXAFS analysis and multi-path *R*-space refinements found that the NCs comprised small metal cores surrounded by sulfide-type shells, further demonstrating that the sulfide shell is a prevalent surface structure among thiolate-protected Ag NCs and Ag NPs. The antibacterial activities of the NCs were also examined, and they were found to be active against both Gram-positive and Gram-negative bacteria in similar capacity to the larger Ag NPs protected by cysteine (discussed in Chapter 3). As a follow-up to this study, Ag NCs were also prepared without 1D assemblies by preventing initial Ag^{+}-thiolate formation; their structure was then studied using a similar XAS methodology and were found to exhibit a larger metallic core with a thinner sulfide shell in comparison to the 1D NC structure. Therefore, this shed more light on the influence of the Ag^{+}-thiolates on both the surface structure and overall assembly of tiopronin-protected Ag NCs.

Chapter 5 built upon the work in Chapter 3 which demonstrated the relatively higher antibacterial activity of PVP-protected Ag NPs than thiolate-protected Ag NPs. Ag NP cytotoxicity towards normal mammalian cells is also a subject of interest, and so the addition of Au to PVP-Ag NPs was carried out to measure its effect on their atomic structures and bioactivities. The addition of Au was found to drastically change the atomic structure of the Ag NPs. In brief, the Ag core of the NPs was gradually replaced with Au, with Ag being subsequently mixed with Au at the surface. As a result, the antibacterial activity of the bimetallic NPs was lower than that of pure Ag NPs, and was overall dependent on the location of Ag within the NPs. On the other hand, the cytotoxicity of the bimetallic NPs was much lower than that of the pure Ag NPs, and was dependent on the overall Au concentration. Using the structural information garnered from XAS, it was possible to rationalize the bioactivities of the NPs based on their atomic

structure, and to provide guiding principles for the design of AuAg NPs with specific antibacterial and cytotoxic activities.

Chapter 6 studied alloy and ligand effects at the surface of anisotropic Au NPs coated by Ag monolayers. These effects are important due to their impact on NP shape and functionality. However, in the case of halide-adsorbed NPs, they are particularly challenging to study due to the difficulty in analyzing interactions between metals and light-halides (*e.g.,* Cl^-). Thus, XAS and DFT modeling were required in order to uncover the surface structures of Cl^--adsorbed, Ag-coated Au NPs with {111}, {110}, {310}, and {720} indexed facets. The Ag-Cl, Ag-Ag, and Ag-Au bonding structures differed markedly between the NP surfaces, and were sensitive to the formation mechanism and facet type of the NP. A unique approach combining DFT and experimental/simulated XAS further verified the surface structure models and identified the previously indistinguishable valence states of Ag atoms at the NP surfaces. Similar to the surface-related reactions of Ag NPs with bacteria, the location and alloying interactions between Ag and Au were related to the shape control of anisotropic NPs, whereby the strong alloying and ligand interactions provide the stabilization mechanisms for the high-index facets and guide subsequent growth.

Finally, the effectiveness of synchrotron XAS techniques in the characterization of nanomaterials was demonstrated throughout all of the studies presented. XAS allowed many of the challenges associated with the characterization of nanomaterials to be overcome and contributed to a greater fundamental understanding of the surface structure of various Ag NPs. In addition, the insight gained from these results allowed for the rationalization of surface-related activities, namely bioactivity and NP growth, which are important applications for Ag NPs in general. The methods and results presented within

this thesis will no doubt find potential application in the rational design of future Ag nanomaterials.

7.2 Future work

7.2.1 Control of Ag NP sulfidation

From the studies of thiolate-protected Ag NPs/NCs, it was proposed that electron displacement from the S-Ag interaction in thiolate-metal bonding results in S-C bond cleavage (as demonstrated by S K-edge XAS in this work), which in turn generates S^{2-} leading to surface sulfidation.[287] Based on this proposition, it would seem likely that the amount of sulfidation would depend on the concentration of the thiol available. Indeed, it was observed in Chapter 2 that the 6Ag1DDT Ag NPs exhibited less sulfide at the surface of the NPs compared to 1Ag1DDT Ag NPs. Based on these results, it was hypothesized that a similar 6Ag:1thiol ratio used to prepare the Cys-Ag NPs in Chapter 3 would result in a similar surface structure. As it turned out, the resulting Cys-Ag NPs had more significantly sulfidized surface structure, which could be related to the type of thiol used. Therefore, one potential area of future exploration for this system is to assess the effect of cysteine concentration on the sulfidation of the Ag NPs, in a manner similar to the methodology employed in Chapter 2. Furthermore, the examination of other thiols in this type of synthesis would provide important insight into thiol dependent sulfidation. In terms of their application, the amount of sulfide at the NP surface could also provide a potential control mechanism for the antibacterial activity and cytotoxicity of the Ag NPs, which could then be explored using similar methods presented in this thesis.

7.2.2 Comparison of Tiopronin-protected Ag NCs to Other Ag NCs

Overall, the preparation of Ag NCs using tiopronin has afforded control over both the surface structure and assembly of the resulting NCs. Further studies of surface bonding interactions between tiopronin and NC-1 (1D assembly) and NC-2 (no 1D assembly) would be worthwhile, for comparison with previously identified structures of Ag_{62} and Ag_{44} NCs.[84,104] This study could be carried out using Ag K-edge XAS to examine the experimental coordination numbers and bond lengths of both Ag_{44} and Ag_{62} NCs, and then comparing these results to those of the NC-1 and NC-2. In addition, the examination of the S K-edge XAS of the NCs may also provide useful insight, although this would be less useful for the NC-1 due to the excess Ag^+-thiolates which make up the 1D assembly. Finally, the antibacterial properties of NC-2 would be interesting to compare to those of NC-1, as the combination of their more metallic nature and potentially less steric hindrance from Ag^+-thiolates may lead to a greater antibacterial effect. The stability of NC-2 in solution should be more closely assessed though, as their potential for aggregation during dialysis was a concern that prevented their assessment of their antibacterial activity.

7.2.3 Antibacterial Mechanism and Cytotoxicity of Ag NPs

Although the antibacterial activity assessments carried out in Chapter 3, 4, and 5 yielded much information regarding the overall effect of the surface structure on antibacterial activity, the mechanism of action was only partially explored through the comparison of activity against Gram-positive and Gram-negative bacteria. Further study of antibacterial action from other perspectives may elucidate useful information relevant to their applications. This should include examining dissolution of Ag^+ ions from the NPs

in the biological solutions used for the antibacterial activity assays as well as measuring the antibacterial activity of the Ag^+ ions themselves and correlating this information to the data collected for the Ag NPs. Furthermore, corresponding studies of the bacteria structure after exposure to Ag NPs would be worthwhile in order to determine any potential membrane-specific effects. This could be carried out by using TEM studies in order to observe the locations of the Ag NPs in and/or around the bacteria. Finally, although the thiolate-protected Ag NPs were found to be less active against bacteria relative to more metallic Ag NPs, their cytotoxicity should also be examined in order to assess their overall therapeutic effectiveness.

7.2.4 Varied Metal Concentrations in AgAu Bimetallic NPs

The bimetallic AgAu NPs described in Chapter 5 demonstrated a rearrangement of the Ag and Au atoms depending on the concentration of the Au added to the Ag seed NPs. The amounts added in the preparation were generally spaced out in order to yield definitive changes in the structures produced, and thus potentially change their bioactivities in a significant way. The amounts of Au added led to Ag:Au ratios of approximately 100:0, 65:35, 50:50, and 30:70 within the NPs. Taking this concept further, it would be interesting to examine the effect of adding both smaller and larger amounts of Au to the Ag seeds, in order to prepare different ratios of Ag:Au in the NPs and study their resulting atomic arrangement and bioactivities.

7.2.5 Delivery Mechanism Exploration

From the results presented in Chapter 5, the application of these bimetallic NPs to biomedical technologies may be of potential use. One aspect not discussed thus far is the potential delivery method for the NPs. One drug delivery application that could be

explored is a polyphosphate (CPP) matrix delivery system for bone graft models.[252,288] CPP consists of long phosphate polymeric chains connected via calcium (Ca^{2+}) ions between chains (Figure 7.1).[289]

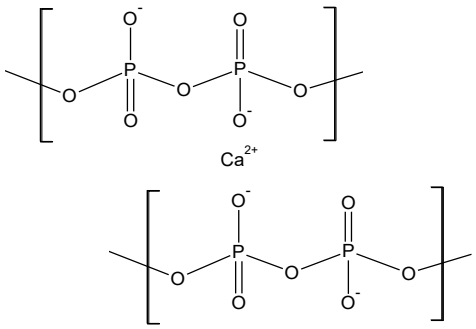

Figure 7.1. Schematic of polymeric unit of calcium polyphosphate chains.

CPP matrices in general have been shown to be good bone biomaterials and feasible drug delivery platforms.[252,288] In this methodology, CPP matrices can be loaded with antibiotics and used to fill bone defects, in order to prevent infection while the bone grows. However, the development of new antibiotic formulations, such as those containing Ag NPs, are of interest due to their ability to overcome bacterial resistance. Therefore, employing a previously used methodology for other antibiotics, the as-prepared AgAu NPs could be formulated into CPP matrices in order to assess their Ag release in an *in vitro* bone defect model as a proof of concept.[252] Preliminary results on this concept demonstrated that Ag and Au were released with approximately the same profile, and exhibited cumulative release that was dependent on the original concentration of the Ag and Au in the NPs. In addition, the Ca and P concentrations in the media deviated negligibly between the NP groups and the blanks. Future work should include XAS characterization of the NPs within the CPP discs which could provide information complementary to the results discussed in Chapter 5. Furthermore, the antibacterial (or

cytotoxic) activity of the NP loaded CPP discs could be conducted using a similar elution apparatus *in situ*, wherein the discs are suspended in bacteria solutions and their activity over time is subsequently measured.

7.2.6 Applications of Ag-coated Au NPs

The surface structure study of Ag-coated Au NPs may yield further insights into the stability mechanisms of other anisotropic NP systems, but also holds interesting implications for both their catalytic and biomedical applications. For example, the alloying of Pt to Au has been shown to increase in the efficiency of oxygen-reduction catalysts.[290] Combined with increased catalytic efficiency from higher-indexed facets,[268,291] the NPs studied herein may have great potential as catalyst materials, and are worth examining in future work. In addition, the precise location of the Ag on the high energy surface facets of the NPs may also affect antibacterial activity. Since the NPs were also composed primarily of Au, their cytotoxicity towards mammalian cells would also be of interest.

Bibliography

(1) Liu, X.; Wang, F.; Niazov-Elkan, A.; Guo, W.; Willner, I. *Nano Lett.* **2013**, *13*, 309.

(2) Lu, Y.; Chen, W. *J. Power Sources* **2012**, *197*, 107.

(3) Tang, D.; Chen, Z.; Hu, J.; Sun, G.; Lu, S.; Hu, C. *Phys. Chem. Chem. Phys.* **2012**, *14*, 12829.

(4) Yuan, X.; Tay, Y.; Dou, X.; Luo, Z.; Leong, D. T.; Xie, J. *Anal. Chem.* **2013**, *85*, 1913.

(5) Rai, M.; Yadav, A.; Gade, A. *Biotechnol. Adv.* **2009**, *27*, 76.

(6) Chernousova, S.; Epple, M. *Angew. Chem. Int. Ed. Engl.* **2013**, *52*, 1636.

(7) Shiao, Y.; Chiu, H.; Wu, P.; Huang, Y. *ACS Appl. Mater. Interfaces* **2014**, *6*, 21832.

(8) Vajda, S.; Pellin, M. J.; Greeley, J. P.; Marshall, C. L.; Curtiss, L. A.; Ballentine, G. A.; Elam, J. W.; Catillon-Mucherie, S.; Redfern, P. C.; Mehmood, F.; Zapol, P. *Nat Mater* **2009**, *8*, 213.

(9) Burda, C.; Chen, X.; Narayanan, R.; El-Sayed, M. A. *Chem. Rev.* **2005**, *105*, 1025.

(10) Daniel, M. C.; Astruc, D. *Chem. Rev.* **2004**, *104*, 293.

(11) Eustis, S.; El-Sayed, M. *Chem. Soc. Rev.* **2006**, *35*, 209.

(12) Liz-Marzán, L. M. *Langmuir* **2006**, *22*, 32.

(13) Qian, H.; Zhu, M.; Wu, Z.; Jin, R. *Acc. Chem. Res.* **2012**, *45*, 1470.

(14) Jin, R. *Nanoscale* **2010**, *2*, 343.

(15) Murphy, C. J.; Sau, T. K.; Gole, A. M.; Orendorff, C. J.; Gao, J.; Gou, L.; Hunyadi, S. E.; Li, T. *J. Phys. Chem. B* **2005**, *109*, 13857.

(16) Xia, Y.; Xiong, Y.; Lim, B.; Skrabalak, S. E. *Angew. Chemie Int. Ed.* **2009**, *48*, 60.

(17) Nikoobakht, B.; El-Sayed, M. A. *Chem. Mater.* **2003**, *15*, 1957.

(18) Yin, A.-X.; Min, X.-Q.; Zhang, Y.-W.; Yan, C.-H. *J. Am. Chem. Soc.* **2011**, *133*, 3816.

(19) Pal, S.; Tak, Y. K.; Song, J. M. *Appl. Environ. Microbiol.* **2007**, *73*, 1712.

(20) Liu, S.; Chen, G.; Prasad, P. N.; Swihart, M. T. *Chem. Mater.* **2011**, 4098.

(21) Link, S.; Wang, Z. L.; El-Sayed, M. A. *J. Phys. Chem. B* **1999**, *103*, 3529.

(22) Barber, D. J.; Freestone, I. C. *Archaeometry* **1990**, *1*, 33.

(23) Alexander, J. W. *Surg. Infect. (Larchmt).* **2009**, *10*, 289.

(24) Sims, J. M. *Int. Urogynecol. J.* **1998**, *9*, 236.

(25) Klasen, H. J. *Burns* **2000**, *26*, 117.

(26) Klasen, H. J. *Burns* **2000**, *26*, 131.

(27) Zhang, F.; Wu, X.; Chen, Y.; Lin, H. *Fibers Polym.* **2009**, *10*, 496.

(28) Samuel, U.; Guggenbichler, J. P. *Int. J. Antimicrob. Agents* **2004**, *23 Suppl 1*, S75.

(29) Burd, A.; Kwok, C. H.; Hung, S. C.; Chan, H. S.; Gu, H.; Lam, W. K.; Huang, L. *Wound Repair Regen.* **2007**, *15*, 94.

(30) Eby, D. M.; Luckarift, H. R.; Johnson, G. R. *ACS Appl. Mater. Interfaces* **2009**, *1*, 1553.

(31) Prokopovich, P.; Leech, R.; Carmalt, C. J.; Parkin, I. P.; Perni, S. *Int. J. Nanomedicine* **2013**, *8*, 2227.

(32) Brennan, S. A.; Ni Fhoghlu, C.; Devitt, B. M.; O'Mahony, F. J.; Brabazon, D.; Walsh, A. *Bone Joint J.* **2015**, *97-B*, 582.

(33) Loza, K.; Diendorf, J.; Sengstock, C.; Ruiz-Gonzalez, L.; Gonzalez-Calbet, J. M.; Vallet-Regi, M.; Köller, M.; Epple, M. *J. Mater. Chem. B* **2014**, *2*, 1634.

(34) Peretyazhko, T. S.; Zhang, Q.; Colvin, V. L. *Environ. Sci. Technol.* **2014**, *48*, 11954.

(35) Levard, C.; Mitra, S.; Yang, T.; Jew, A. D.; Badireddy, A. R.; Lowry, G. V.; Brown, G. E. *Environ. Sci. Technol.* **2013**, *47*, 5738.

(36) Silhavy, T. J.; Kahne, D.; Walker, S. *Cold Spring Harb. Perspect. Biol.* **2010**, *2*, a000414.

(37) Taglietti, A.; Diaz Fernandez, Y. A.; Amato, E.; Cucca, L.; Dacarro, G.; Grisoli, P.; Necchi, V.; Pallavicini, P.; Pasotti, L.; Patrini, M. *Langmuir* **2012**, *28*, 8140.

(38) Boopathi, S.; Gopinath, S.; Boopathi, T.; Balamurugan, V.; Rajeshkumar, R.; Sundararaman, M. *Ind. Eng. Chem. Res.* **2012**, *51*, 5976.

(39) Shrivastava, S.; Bera, T.; Roy, A.; Singh, G.; Ramachandrarao, P.; Dash, D. *Nanotechnology* **2007**, *18*, 225103.

(40) Morones, J.; Elechiguerra, J.; Camacho, A. *Nanotechnology* **2005**, *16*, 2346.

(41) Li, W.-R.; Xie, X.-B.; Shi, Q.-S.; Zeng, H.-Y.; OU-Yang, Y.-S.; Chen, Y.-B. *Appl. Microbiol. Biotechnol.* **2009**, *85*, 1115.

(42) Li, W.-R.; Xie, X.-B.; Shi, Q.-S.; Duan, S.-S.; Ouyang, Y.-S.; Chen, Y.-B. *Biometals* **2011**, *24*, 135.

(43) Amato, E.; Diaz-Fernandez, Y. A.; Taglietti, A.; Pallavicini, P.; Pasotti, L.; Cucca, L.; Milanese, C.; Grisoli, P.; Dacarro, C.; Fernandez-Hechavarria, J. M.; Necchi, V. *Langmuir* **2011**, *27*, 9165.

(44) Holt, K. B.; Bard, A. J. *Biochemistry* **2005**, *44*, 13214.

(45) Xiu, Z.; Zhang, Q.; Puppala, H. L.; Colvin, V. L.; Alvarez, P. J. J. *Nano Lett.* **2012**, *12*, 4271.

(46) Kittler, S.; Greulich, C.; Diendorf, J.; Köller, M.; Epple, M. *Chem. Mater.* **2010**, *22*, 4548.

(47) Bondarenko, O.; Ivask, A.; Käkinen, A.; Kurvet, I.; Kahru, A. *PLoS One* **2013**, *8*, e64060.

(48) AshaRani, P. V; Low Kah Mun, G.; Hande, M. P.; Valiyaveettil, S. *ACS Nano* **2009**, *3*, 279.

(49) Kim, J. Y.; Lee, C.; Cho, M.; Yoon, J. *Water Res.* **2008**, *42*, 356.

(50) Gordon, O.; Vig Slenters, T.; Brunetto, P. S.; Villaruz, A. E.; Sturdevant, D. E.; Otto, M.; Landmann, R.; Fromm, K. M. *Antimicrob. Agents Chemother.* **2010**, *54*, 4208.

(51) Bovenkamp, G. L.; Zanzen, U.; Krishna, K. S.; Hormes, J.; Prange, A. *Appl. Environ. Microbiol.* **2013**, *79*, 6385.

(52) Priester, J. H.; Singhal, A.; Wu, B.; Stucky, G. D.; Holden, P. A. *Analyst* **2014**, *139*, 954.

(53) Schrand, A. M.; Rahman, M. F.; Hussain, S. M.; Schlager, J. J.; Smith, D. A.; Syed, A. F. *Wiley Interdiscip. Rev. Nanomed. Nanobiotechnol.* **2010**, *2*, 544.

(54) Choi, O.; Hu, Z. *Environ. Sci. Technol.* **2008**, *42*, 4583.

(55) Martínez-Castañón, G. A.; Niño-Martínez, N.; Martínez-Gutierrez, F.; Martínez-Mendoza, J. R.; Ruiz, F. *J. Nanoparticle Res.* **2008**, *10*, 1343.

(56) Padmos, J. D.; Langman, M.; MacDonald, K.; Comeau, P.; Yang, Z.; Filiaggi, M.; Zhang, P. *J. Phys. Chem. C* **2015**, *119*, 7472.

(57) Liu, J.; Sonshine, D. A.; Shervani, S.; Hurt, R. H. *ACS Nano* **2010**, *4*, 6903.

(58) Padmos, J. D.; Boudreau, R. T. M.; Weaver, D. F.; Zhang, P. *Langmuir* **2015**, *31*, 3745.

(59) Pariser, R. J. *Arch. Dermatol.* **1978**, *114*, 373.

(60) Lankveld, D. P. K.; Oomen, A. G.; Krystek, P.; Neigh, A.; Troost-de Jong, A.; Noorlander, C. W.; Van Eijkeren, J. C. H.; Geertsma, R. E.; De Jong, W. H. *Biomaterials* **2010**, *31*, 8350.

(61) Johnston, H. J.; Hutchison, G.; Christensen, F. M.; Peters, S.; Hankin, S.; Stone, V. *Crit. Rev. Toxicol.* **2010**, *40*, 328.

(62) de Lima, R.; Seabra, A. B.; Durán, N. *J. Appl. Toxicol.* **2012**, *32*, 867.

(63) Greulich, C.; Diendorf, J.; Simon, T.; Eggeler, G.; Epple, M.; Köller, M. *Acta Biomater.* **2011**, *7*, 347.

(64) Caballero-Díaz, E.; Pfeiffer, C.; Kastl, L.; Rivera-Gil, P.; Simonet, B.; Valcárcel, M.; Jiménez-Lamana, J.; Laborda, F.; Parak, W. J. *Part. Part. Syst. Charact.* **2013**, *30*, 1079.

(65) Peng, H.; Zhang, X.; Wei, Y.; Liu, W.; Li, S.; Yu, G.; Fu, X.; Cao, T.; Deng, X. *J. Nanomater.* **2012**, *2012*, 1.

(66) Jiang, G. B.; Liu, W.; Wu, Y. a; Wang, C.; Li, H. C.; Wang, T.; Liao, C. Y.; Cui, L.; Zhou, Q. F.; Yan, B. *Nanotoxicology* **2010**, *4*, 319.

(67) Faraday, M. *Philos. Trans. R. Soc. London* **1857**, *147*, 145.

(68) Turkevich, J.; Stevenson, P. C.; Hillier, J. *Discuss. Faraday Soc.* **1951**, *11*, 55.

(69) Frens, G. *Kolloid-Zeitschrift Zeitschrift Polym.* **1972**, *250*, 736.

(70) Dong, X.; Ji, X.; Wu, H.; Zhao, L.; Li, J.; Yang, W. *J. Phys. Chem. C* **2009**, *113*, 6573.

(71) Brust, M.; Walker, M.; Bethell, D.; Schiffrin, D. J.; Whyman, R. *J. Chem. Soc. Chem. Commun.* **1994**, *1994*, 801.

(72) Brust, M.; Kiely, C. J. *Colloids Surfaces A Physicochem. Eng. Asp.* **2002**, *202*, 175.

(73) Goulet, P. J. G.; Lennox, R. B. *J. Am. Chem. Soc.* **2010**, *132*, 9582.

(74) Li, Y.; Zaluzhna, O.; Xu, B.; Gao, Y.; Modest, J. M.; Tong, Y. J. *J. Am. Chem. Soc.* **2011**, *133*, 2092.

(75) Padmos, J. D.; Zhang, P. *J. Phys. Chem. C* **2012**, *116*, 23094.

(76) Jones, M. R.; Osberg, K. D.; Macfarlane, R. J.; Langille, M. R.; Mirkin, C. A. *Chem. Rev.* **2011**, *111*, 3736.

(77) Krämer, S.; Fuierer, R. R.; Gorman, C. B. *Chem. Rev.* **2003**, *103*, 4367.

(78) Haynes, C. L.; Van Duyne, R. P. *J. Phys. Chem. B* **2001**, *105*, 5599.

(79) Khayati, G. R.; Janghorban, K. *Adv. Powder Technol.* **2012**, *23*, 393.

(80) Das, B.; Subramaniam, S.; Melloch, M. R. *Semicond. Sci. Technol.* **1993**, *8*, 1347.

(81) Vieu, C.; Carcenac, F.; Pépin, A.; Chen, Y.; Mejias, M.; Lebib, A.; Manin-Ferlazzo, L.; Couraud, L.; Launois, H. *Appl. Surf. Sci.* **2000**, *164*, 111.

(82) Wuithschick, M.; Paul, B.; Bienert, R.; Sarfraz, A.; Vainio, U.; Sztucki, M.; Kraehnert, R.; Strasser, P.; Rademann, K.; Emmerling, F.; Polte, J. *Chem. Mater.* **2013**, *25*, 4679.

(83) Polte, J.; Tuaev, X.; Wuithschick, M.; Fischer, A.; Thuenemann, A. F.; Rademann, K.; Kraehnert, R.; Emmerling, F. *ACS Nano* **2012**, *6*, 5791.

(84) Desireddy, A.; Conn, B. E.; Guo, J.; Yoon, B.; Barnett, R. N.; Monahan, B. M.; Kirschbaum, K.; Griffith, W. P.; Whetten, R. L.; Landman, U.; Bigioni, T. P. *Nature* **2013**, *501*, 399.

(85) Wu, Z.; Lanni, E.; Chen, W.; Bier, M. E.; Ly, D.; Jin, R. *J. Am. Chem. Soc.* **2009**, *131*, 16672.

(86) Udayabhaskararao, T.; Pradeep, T. *J. Phys. Chem. Lett.* **2013**, *4*, 1553.

(87) Zhang, P. *J. Phys. Chem. C* **2014**, *118*, 25291.

(88) Love, J. C.; Estroff, L. a; Kriebel, J. K.; Nuzzo, R. G.; Whitesides, G. M. *Chem. Rev.* **2005**, *105*, 1103.

(89) Ulman, A. *Chem. Rev.* **1996**, *96*, 1533.

(90) Ansar, S. M.; Perera, G. S.; Gomez, P.; Salomon, G.; Vasquez, E. S.; Chu, I. W.; Zou, S.; Pittman, C. U.; Walters, K. B.; Zhang, D. *J. Phys. Chem. C* **2013**, *117*, 27146.

(91) Wangoo, N.; Bhasin, K. K.; Mehta, S. K.; Suri, C. R. *J. Colloid Interface Sci.* **2008**, *323*, 247.

(92) Burt, J. L.; Gutiérrez-Wing, C.; Miki-Yoshida, M.; José-Yacamán, M. *Langmuir* **2004**, *20*, 11778.

(93) Simms, G. A.; Padmos, J. D.; Zhang, P. *J. Chem. Phys.* **2009**, *131*, 214703.

(94) Shimmin, R. G.; Schoch, A. B.; Braun, P. V. *Langmuir* **2004**, *20*, 5613.

(95) Shelley, E. J.; Ryan, D.; Johnson, S. R.; Couillard, M.; Fitzmaurice, D.; Nellist, P. D.; Chen, Y.; Palmer, R. E.; Preece, J. A. *Langmuir* **2002**, *18*, 1791.

(96) López-Cartes, C.; Rojas, T. C.; Litrán, R.; Martínez-Martínez, D.; de la Fuente, J. M.; Penadés, S.; Fernández, A. *J. Phys. Chem. B* **2005**, *109*, 8761.

(97) Zhang, P.; Sham, T. K. *Appl. Phys. Lett.* **2002**, *81*, 736.

(98) Jiang, D. E.; Tiago, M. L.; Luo, W.; Dai, S. *J. Am. Chem. Soc.* **2008**, *130*, 2777.

(99) Häkkinen, H. *Nat. Chem.* **2012**, *4*, 443.

(100) Jadzinsky, P. D.; Calero, G.; Ackerson, C. J.; Bushnell, D. A.; Kornberg, R. D. *Science* **2007**, *318*, 430.

(101) Alloway, D. M.; Graham, A. L.; Yang, X.; Mudalige, A.; Colorado, R.; Wysocki, V. H.; Pemberton, J. E.; Lee, T. R.; Wysocki, R. J.; Armstrong, N. R. *J. Phys. Chem. C* **2009**, *113*, 20328.

(102) Vericat, C.; Vela, M. E.; Corthey, G.; Pensa, E.; Cortés, E.; Fonticelli, M. H.; Ibañez, F.; Benitez, G. E.; Carro, P.; Salvarezza, R. C. *RSC Adv.* **2014**, *4*, 27730.

(103) Yang, H.; Wang, Y.; Huang, H.; Gell, L.; Lehtovaara, L.; Malola, S.; Häkkinen, H.; Zheng, N. *Nat. Commun.* **2013**, *4*, 2422.

(104) Li, G.; Lei, Z.; Wang, Q. M. *J. Am. Chem. Soc.* **2010**, *132*, 17678.

(105) Padmos, J. D.; Boudreau, R. T. M.; Weaver, D. F.; Zhang, P. *J. Phys. Chem. C* **2015**, *119*, 24627.

(106) Battocchio, C.; Meneghini, C.; Fratoddi, I.; Venditti, I.; Russo, M. V.; Aquilanti, G.; Maurizio, C.; Bondino, F.; Matassa, R.; Rossi, M.; Mobilio, S.; Polzonetti, G. *J. Phys. Chem. C* **2012**, *116*, 19571.

(107) Liu, M.; Guyot-Sionnest, P. *J. Mater. Chem.* **2006**, *16*, 3942.

(108) Schmidbaur, H.; Cronje, S.; Djordjevic, B.; Schuster, O. *Chem. Phys.* **2005**, *311*, 151.

(109) Reinsch, B. C.; Levard, C.; Li, Z.; Ma, R.; Wise, A.; Gregory, K. B.; Brown, G. E.; Lowry, G. V. *Environ. Sci. Technol.* **2012**, *46*, 6992.

(110) Levard, C.; Reinsch, B. C.; Michel, F. M.; Oumahi, C.; Lowry, G. V; Brown, G. E. *Environ. Sci. Technol.* **2011**, *45*, 5260.

(111) Levard, C.; Hotze, E. M.; Colman, B. P.; Dale, A. L.; Truong, L.; Yang, X. Y.; Bone, A. J.; Brown, G. E.; Tanguay, R. L.; Di Giulio, R. T.; Bernhardt, E. S.; Meyer, J. N.; Wiesner, M. R.; Lowry, G. V. *Environ. Sci. Technol.* **2013**, *47*, 13440.

(112) Chen, H.-Q.; He, X.; Guo, H.; Fu, N.-Y.; Zhao, L. *Dalt. Trans.* **2015**, *44*, 3963.

(113) León-Velázquez, M. S.; Irizarry, R.; Castro-Rosario, M. E. *J. Phys. Chem. C* **2010**, *114*, 5839.

(114) Luque, N.; Santos, E. *Langmuir* **2012**, *28*, 11472.

(115) Park, J. W.; Shumaker-Parry, J. S. *J. Am. Chem. Soc.* **2014**, *136*, 1907.

(116) Wuithschick, M.; Birnbaum, A.; Witte, S.; Sztucki, M.; Vainio, U.; Pinna, N.; Rademann, K.; Emmerling, F.; Kraehnert, R.; Polte, J. *ACS Nano* **2015**, *9*, 7052.

(117) Jana, N. R.; Gearheart, L.; Murphy, C. J. *Langmuir* **2001**, *17*, 6782.

(118) John, V. T.; Simmons, B.; McPherson, G. L.; Bose, A. *Curr. Opin. Colloid Interface Sci.* **2002**, *7*, 288.

(119) Sui, Z. M.; Chen, X.; Wang, L. Y.; Xu, L. M.; Zhuang, W. C.; Chai, Y. C.; Yang, C. J. *Phys. E Low-dimensional Syst. Nanostructures* **2006**, *33*, 308.

(120) Personick, M. L.; Langille, M. R.; Zhang, J.; Mirkin, C. A. *Nano Lett.* **2011**, *11*, 3394.

(121) Zhang, Z. *J. Solid State Chem.* **1996**, *121*, 105.

(122) Wang, H.; Qiao, X.; Chen, J.; Wang, X.; Ding, S. *Mater. Chem. Phys.* **2005**, *94*, 449.

(123) Padmos, J. D.; Langman, M.; MacDonald, K.; Comeau, P.; Yang, Z.; Filiaggi, M.; Zhang, P. *J. Phys. Chem. C* **2015**, *119*, 7472.

(124) Wiley, B.; Sun, Y.; Mayers, B.; Xia, Y. *Chemistry* **2005**, *11*, 454.

(125) Sun, Y. *Science* **2002**, *298*, 2176.

(126) Haldar, K. K.; Kundu, S.; Patra, A. *ACS Appl. Mater. Interfaces* **2014**, *6*, 21946.

(127) Banerjee, M.; Sharma, S.; Chattopadhyay, A.; Ghosh, S. S. *Nanoscale* **2011**, *3*, 5120.

(128) Toshima, N.; Yonezawa, T. *New J. Chem.* **1998**, *22*, 1179.

(129) Ferrando, R.; Jellinek, J.; Johnston, R. L. *Chem. Rev.* **2008**, *108*, 846.

(130) Zhang, Q.; Lee, J. Y.; Yang, J.; Boothroyd, C.; Zhang, J. *Nanotechnology* **2007**, *18*, 245605.

(131) Shahjamali, M. M.; Bosman, M.; Cao, S.; Huang, X.; Saadat, S.; Martinsson, E.; Aili, D.; Tay, Y. Y.; Liedberg, B.; Loo, S. C. J.; Zhang, H.; Boey, F.; Xue, C. *Adv. Funct. Mater.* **2012**, *22*, 849.

(132) Yang, Y.; Shi, J.; Kawamura, G.; Nogami, M. *Scr. Mater.* **2008**, *58*, 862.

(133) Erwin, W. R.; Coppola, A.; Zarick, H. F.; Arora, P.; Miller, K. J.; Bardhan, R. *Nanoscale* **2014**, *6*, 12626.

(134) Herrero, E.; Buller, L. J.; Abruña, H. D. *Chem. Rev.* **2001**, *101*, 1897.

(135) Szabó, S. *Int. Rev. Phys. Chem.* **1991**, *10*, 207.

(136) Oviedo, O. A.; Vélez, P.; Macagno, V. A.; Leiva, E. P. M. *Surf. Sci.* **2015**, *631*, 23.

(137) Padmos, J. D.; Personick, M. L.; Tang, Q.; Duchesne, P. N.; Jiang, D.; Mirkin, C. A.; Zhang, P. *Nat. Commun.* **2015**, *6*, 7664.

(138) Barnard, A. S. *Cryst. Growth Des.* **2013**, *13*, 5433.

(139) Lohse, S. E.; Burrows, N. D.; Scarabelli, L.; Liz-Marzán, L. M.; Murphy, C. J. *Chem. Mater.* **2014**, *26*, 34.

(140) Wang, Z. L. *J. Phys. Chem. B* **2000**, *104*, 1153.

(141) Shi, D.; Guo, Z.; Bedford, N. In *Nanomaterials and Devices*; Elsevier, **2015**;25–47.

(142) Rasmus Schröder and Martin Müller. In *Encyclopedia of Chemical Physics and Physical Chemistry*; Moore, J.H.; Spencer, N., Eds.;Taylor & Francis, **2001**; 1622–1654.

(143) Abràmoff, M. D.; Magalhães, P. J.; Ram, S. J. *Biophotonics Int.* **2004**, *11*, 36.

(144) Kelly, K. L.; Coronado, E.; Zhao, L. L.; Schatz, G. C. *J. Phys. Chem. B* **2003**, *107*, 668.

(145) Henglein, A. *J. Phys. Chem.* **1993**, *97*, 5457.

(146) Linnert, T.; Mulvaney, P.; Henglein, A. *J. Phys. Chem.* **1993**, *97*, 679.

(147) Peng, S.; McMahon, J. M.; Schatz, G. C.; Gray, S. K.; Sun, Y. *Proc. Natl. Acad. Sci.* **2010**, *107*, 14530.

(148) Djoković, V.; Krsmanović, R.; Božanić, D. K.; McPherson, M.; Van Tendeloo, G.; Nair, P. S.; Georges, M. K.; Radhakrishnan, T. *Colloids Surfaces B Biointerfaces* **2009**, *73*, 30.

(149) Koningsberger, D. C.; Mojet, B. L.; Dorssen, G. E. Van; Ramaker, D. E. *Top. Catal.* **2000**, *10*, 143.

(150) Newville, M. *Rev. Mineral. Geochemistry* **2014**, *78*, 33.

(151) Durham, P. J. *X-Ray Absorption: Principles, Applications, Techniques of EXAFS, SEXAFS and XANES*, 1st ed.; Koningsberger, D. C., Prins, R., Eds.; Wiley-Interscience, **1988**.

(152) Bunker, G. *Introduction to XAFS*; Cambridge University Press: Cambridge, **2010**.

(153) Sarangi, R. *Coord. Chem. Rev.* **2013**, *257*, 459.

(154) MacDonald, M. A.; Zhang, P.; Qian, H.; Jin, R. *J. Phys. Chem. Lett.* **2010**, *1*, 1821.

(155) Zhang, P.; Sham, T. *Phys. Rev. Lett.* **2003**, *90*, 3.

(156) Bzowski, A.; Sham, T. K.; Yiu, Y. M. *Phys. Rev. B* **1994**, *49*, 13776.

(157) Teng, X.; Ji, X. In *Nanowires - Recent Advances*; InTech, **2012**; 325–340.

(158) Liu, F.; Wechsler, D.; Zhang, P. *Chem. Phys. Lett.* **2008**, *461*, 254.

(159) Norman, D. *J. Phys. C Solid State Phys.* **2000**, *19*, 3273.

(160) Newville, M. *J. Synchrotron Radiat.* **2001**, *8*, 322.

(161) Ravel, B.; Newville, M. *J. Synchrotron Radiat.* **2005**, *12*, 537.

(162) Ressler, T.; WinXAS, version 3.1; **2005**.

(163) Kelly, S. D.; Ravel, B. *AIP Conf. Proc.* **2007**, *882*, 132.

(164) Rehr, J. J. *Rev. Mod. Phys.* **2000**, *72*, 621.

(165) Rehr, J. J.; Kas, J. J.; Prange, M. P.; Sorini, A. P.; Takimoto, Y.; Vila, F. *C.R. Phys.* **2009**, *10*, 548.

(166) Funke, H.; Scheinost, A. C.; Chukalina, M. *Phys. Rev. B* **2005**, *71*, 094110.

(167) Filez, M.; Redekop, E. A.; Poelman, H.; Galvita, V. V.; Marin, G. B. *Anal. Chem.* **2015**, *87*, 3520.

(168) Attwood, D. *Soft X-Rays and Extreme Ultraviolet Radiation*; Cambridge University Press: Cambridge, **1999**.

(169) Hu, Y. Soft X-Ray Microcharacterization (SXRMB / 06B1-1) bending-magnet beamline http://www.lightsource.ca/beamlines/sxrmb.php.

(170) Chen, N. Hard X-ray Micro Analysis (HXMA/06ID-1) wiggler beamline http://www.lightsource.ca/beamlines/hxma.php.

(171) Frinfrock, Z. Pacific-Northwest Consortium/X-ray Science Division (PNC/XSD/Sector 20) bending-magnet beamline http://s20.xray.aps.anl.gov/.

(172) Pickering, I. J.; Prince, R. C.; Divers, T.; George, G. N. *FEBS Lett.* **1998**, *441*, 11.

(173) Pedersen, D. B.; Duncan, S. *J. Phys. Chem. A* **2005**, *109*, 11172.

(174) Jung, C.; Dannenberger, O.; Xu, Y.; Buck, M. *Langmuir* **1998**, *7463*, 1103.

(175) Troughton, E. B.; Bain, C. D.; Whitesides, G. M.; Nuzzo, R. G.; Allara, D. L.; Porter, M. D. *Langmuir* **1988**, No. 10, 365.

(176) Lavrich, D.; Wetterer, S.; Bernasek, S. *J. Phys. Chem. B* **1998**, *102*, 3456.

(177) Taleb, A.; Petit, C.; Pileni, M. P. *Chem. Mater.* **1997**, *9*, 950.

(178) Dance, I. G.; Fisher, K. J.; Banda, R. M. H.; Scudder, M. L. *Inorg. Chem.* **1991**, *30*, 183.

(179) Mari, A.; Imperatori, P.; Marchegiani, G.; Pilloni, L.; Mezzi, A.; Kaciulis, S.; Cannas, C.; Meneghini, C.; Mobilio, S.; Suber, L. *Langmuir* **2010**, *26*, 15561.

(180) Link, S.; El-Sayed, M. *Int. Rev. Phys. Chem.* **2000**, *19*, 409.

(181) Keum, C. D.; Ishii, N.; Michioka, K.; Wulandari, P.; Tamada, K.; Furusawa, M.; Fukushima, H. *J. Nonlinear Opt. Phys. Mater.* **2008**, *17*, 131.

(182) Dash, P.; Bond, T.; Fowler, C.; Hou, W.; Coombs, N.; Scott, R. W. J. *J. Phys. Chem. C* **2009**, *113*, 12719.

(183) Huang, Z.; Thomson, P.; Di, S. *J. Phys. Chem. Solids* **2007**, *68*, 530.

(184) Liu, F.; Zhang, P. *Appl. Phys. Lett.* **2010**, *96*, 043105.

(185) Heaven, M. W.; Dass, A.; White, P. S.; Holt, K. M.; Murray, R. W. *J. Am. Chem. Soc.* **2008**, *130*, 3754.

(186) Frueh, A. J. *Zeitschrift für Krist.* **1958**, *110*, 136.

(187) Lim, J. K.; Kim, I.-H.; Kim, K.-H.; Shin, K. S.; Kang, W.; Choo, J.; Joo, S.-W. *Chem. Phys.* **2006**, *330*, 245.

(188) Beulen, M. W. J.; Huisman, B. H.; van der Heijden, P. A.; Veggel, F. C. J. M. Van; Simons, M. G.; Biemond, E. M. E. F.; de Lange, P. J.; Reinhoudt, D. N. *Langmuir* **1996**, *68*, 6170.

(189) Menard, L. D.; Xu, H.; Gao, S. P.; Twesten, R. D.; Harper, A. S.; Song, Y.; Wang, G.; Douglas, A. D.; Yang, J. C.; Frenkel, A. I.; Murray, R. W.; Nuzzo, R. G. *J. Phys. Chem. B* **2006**, *110*, 14564.

(190) Corrigan, J. F.; Fuhr, O.; Fenske, D. *Adv. Mater.* **2009**, *21*, 1867.

(191) MacDonald, M. A.; Zhang, P.; Chen, N.; Qian, H.; Jin, R. *J. Phys. Chem. C* **2011**, *115*, 65.

(192) Goikolea, E.; Garitaonandia, J. S.; Insausti, M.; Gil de Muro, I.; Suzuki, M.; Uruga, T.; Tanida, H.; Suzuki, K.; Ortega, D.; Plazaola, F.; Rojo, T. *J. Appl. Phys.* **2010**, *107*, 09E317.

(193) Sandroff, C. J.; Herschbach, D. R. *J. Phys. Chem.* **1982**, *86*, 3277.

(194) Laibinis, P. E.; Whitesides, G. M.; Allara, D. L.; Tao, Y. T.; Parikh, A. N.; Nuzzo, R. G. *J. Am. Chem. Soc.* **1991**, *113*, 7152.

(195) Love, J. C.; Wolfe, D. B.; Haasch, R.; Chabinyc, M. L.; Paul, K. E.; Whitesides, G. M.; Nuzzo, R. G. *J. Am. Chem. Soc.* **2003**, *125*, 2597.

(196) John, N. S.; Thomas, P. J.; Kulkarni, G. U. *J. Phys. Chem. B* **2003**, *107*, 11376.

(197) Sun, Y.; Frenkel, A. I.; Isseroff, R.; Shonbrun, C.; Forman, M.; Shin, K.; Koga, T.; White, H.; Zhang, L.; Zhu, Y.; Rafailovich, M. H.; Sokolov, J. C. *Langmuir* **2006**, *22*, 807.

(198) Murayama, H.; Ichikuni, N.; Negishi, Y.; Nagata, T.; Tsukuda, T. *Chem. Phys. Lett.* **2003**, *376*, 26.

(199) Roduner, E. *Chem. Soc. Rev.* **2006**, *35*, 583.

(200) Ivask, A.; Elbadawy, A.; Kaweeteerawat, C.; Boren, D.; Fischer, H.; Ji, Z.; Chang, C. H.; Liu, R.; Tolaymat, T.; Telesca, D.; Zink, J. I.; Cohen, Y.; Holden, P. A.; Godwin, H. A. *ACS Nano* **2014**, *8*, 374.

(201) Carlson, C.; Hussain, S. M.; Schrand, A. M.; Braydich-Stolle, L. K.; Hess, K. L.; Jones, R. L.; Schlager, J. J. *J. Phys. Chem. B* **2008**, *112*, 13608.

(202) Ciceo Lucacel, R.; Radu, T.; Tătar, A. S.; Lupan, I.; Ponta, O.; Simon, V. *J. Non. Cryst. Solids* **2014**, *404*, 98.

(203) Jin, S.; Wang, S.; Song, Y.; Zhou, M.; Zhong, J.; Zhang, J.; Xia, A.; Pei, Y.; Chen, M.; Li, P.; Zhu, M. *J. Am. Chem. Soc.* **2014**, *136*, 15559.

(204) Li, H.; Bian, Y. *Nanotechnology* **2009**, *20*, 145502.

(205) Mandal, S.; Gole, A.; Lala, N.; Gonnade, R.; Ganvir, V.; Sastry, M. *Langmuir* **2001**, *17*, 6262.

(206) Hoppe, C. E.; Lazzari, M.; Pardiñas-Blanco, I.; López-Quintela, M. A. *Langmuir* **2006**, *22*, 7027.

(207) Bauer, C. A.; Stellacci, F.; Perry, J. W. *Top. Catal.* **2008**, *47*, 32.

(208) *Clinical and Laboratory Standards Institute (CLSI) Standard M07-A10: Methods for Dilution Antimicrobial Susceptibility Tests for Bacteria That Grow Aerobically; Approved Standard-Tenth Edition*; Wayne, Pennsylvania, USA, **2014**.

(209) Bayram, S.; Zahr, O. K.; Blum, A. S. *RSC Adv.* **2015**, *5*, 6553.

(210) Behera, M.; Ram, S. *Int. Nano Lett.* **2013**, *3*, 17.

(211) Okumura, M.; Kitagawa, Y.; Kawakami, T.; Haruta, M. *Chem. Phys. Lett.* **2008**, *459*, 133.

(212) Jung, W. K.; Koo, H. C.; Kim, K. W.; Shin, S.; Kim, S. H.; Park, Y. H. *Appl. Environ. Microbiol.* **2008**, *74*, 2171.

(213) Lok, C.-N.; Ho, C.-M.; Chen, R.; He, Q.-Y.; Yu, W.-Y.; Sun, H.; Tam, P. K.-H.; Chiu, J.-F.; Che, C.-M. *J. Proteome Res.* **2006**, *5*, 916.

(214) Díez, I.; Ras, R. H. A. *Nanoscale* **2011**, *3*, 1963.

(215) Yuan, X.; Setyawati, M. I.; Tan, A. S.; Ong, C. N.; Leong, D. T.; Xie, J. *NPG Asia Mater.* **2013**, *5*, e39.

(216) Liu, Y.; Wang, L.; Bu, C.; Wang, G.; Zhang, Y.; Fang, S.; Shi, W. *J. Nanomater.* **2015**, *2015*, 1.

(217) Yuan, X.; Setyawati, M. I.; Leong, D. T.; Xie, J. *Nano Res.* **2014**, *7*, 301.

(218) Slocik, J. M.; Wright, D. W. *Biomacromolecules* **2003**, *4*, 1135.

(219) Zhao, M.; Sun, L.; Crooks, R. M. *J. Am. Chem. Soc.* **1998**, *120*, 4877.

(220) Qian, H.; Eckenhoff, W. T.; Zhu, Y.; Pintauer, T.; Jin, R. *J. Am. Chem. Soc.* **2010**, *132*, 8280.

(221) Zhu, M.; Aikens, C. M.; Hollander, F. J.; Schatz, G. C.; Jin, R. *J. Am. Chem. Soc.* **2008**, *130*, 5883.

(222) AbdulHalim, L. G.; Ashraf, S.; Katsiev, K.; Kirmani, A. R.; Kothalawala, N.; Anjum, D. H.; Abbas, S.; Amassian, A.; Stellacci, F.; Dass, A.; Hussain, I.; Bakr, O. M. *J. Mater. Chem. A* **2013**, *1*, 10148.

(223) Motte, L.; Pileni, M. P. *Appl. Surf. Sci.* **2000**, *164*, 60.

(224) Gao, F.; Lu, Q.; Zhao, D. *Nano Lett.* **2003**, *3*, 85.

(225) Shiers, M. J.; Leech, R.; Carmalt, C. J.; Parkin, I. P.; Kenyon, A. J. *Adv. Mater.* **2012**, *24*, 5227.

(226) Li, M.; Johnson, S.; Guo, H.; Dujardin, E.; Mann, S. *Adv. Funct. Mater.* **2011**, *21*, 851.

(227) Huang, T.; Murray, R. W. *J. Phys. Chem. B* **2003**, *107*, 7434.

(228) Fijolek, H. G.; González-Duarte, P.; Park, S. H. S. H.; Suib, S. L. S. L.; Natan, M. J. M. J. *Inorg. Chem.* **1997**, *36*, 5299.

(229) Bensebaa, F.; Ellis, T. H.; Kruus, E.; Voicu, R.; Zhou, Y. *Langmuir* **1998**, *14*, 6579.

(230) Andersson, L.-O. *J. Polym. Sci. Part A* **1972**, *10*, 1963.

(231) Zaarour, M.; El Roz, M.; Dong, B.; Retoux, R.; Aad, R.; Cardin, J.; Dufour, C.; Gourbilleau, F.; Gilson, J. P.; Mintova, S. *Langmuir* **2014**, *30*, 6250.

(232) Leiggener, C.; Bruhwiler, D.; Calzaferri, G. *J. Mater. Chem.* **2003**, *13*, 1969.

(233) Qian, X. *Mater. Chem. Phys.* **2001**, *68*, 95.

(234) Yan, S.; Zhang, Y.; Zhang, Y.; Xiao, Z. *Inorg. Mater.* **2009**, *45*, 193.

(235) Tang, A.; Wang, Y.; Ye, H.; Zhou, C.; Yang, C.; Li, X.; Peng, H.; Zhang, F.; Hou, Y.; Teng, F. *Nanotechnology* **2013**, *24*, 355602.

(236) Schmidbaur, H.; Schier, A. *Angew. Chemie Int. Ed.* **2015**, *54*, 746.

(237) Shen, J. S.; Li, D. H.; Zhang, M. B.; Zhou, J.; Zhang, H.; Jiang, Y. B. *Langmuir* **2011**, *27*, 481.

(238) Chevrier, D. M.; Chatt, A.; Zhang, P.; Zeng, C.; Jin, R. *J. Phys. Chem. Lett.* **2013**, *4*, 3186.

(239) Liao, J.; Anchun, M.; Zhu, Z.; Quan, Y. *Int. J. Nanomedicine* **2010**, *5*, 337.

(240) Juan, L.; Zhimin, Z.; Anchun, M. M.; Lei, L.; Jingchao, Z. *Int. J. Nanomedicine* **2010**, *5*, 261.

(241) Padmos, J. D.; Duchesne, P.; Dunbar, M.; Zhang, P. *J. Biomed. Mater. Res. A* **2010**, *95*, 146.

(242) Pauksch, L.; Hartmann, S.; Rohnke, M.; Szalay, G.; Alt, V.; Schnettler, R.; Lips, K. S. *Acta Biomater.* **2014**, *10*, 439.

(243) Piao, M. J.; Kang, K. A.; Lee, I. K.; Kim, H. S.; Kim, S.; Choi, J. Y.; Choi, J.; Hyun, J. W. *Toxicol. Lett.* **2011**, *201*, 92.

(244) Kittler, S.; Greulich, C.; Koeller, M.; Epple, M.; Köller, M. *Mater. Werkst* **2009**, *40*, 258.

(245) Alkilany, A. M.; Murphy, C. J. *J. Nanopart. Res.* **2010**, *12*, 2313.

(246) Badwaik, V. D.; Vangala, L. M.; Pender, D. S.; Willis, C. B.; Aguilar, Z. P.; Gonzalez, M. S.; Paripelly, R.; Dakshinamurthy, R. *Nanoscale Res. Lett.* **2012**, *7*, 623.

(247) Bindhu, M. R.; Umadevi, M. *Mater. Lett.* **2014**, *120*, 122.

(248) Frenkel, A. I.; Yevick, A.; Cooper, C.; Vasic, R. *Annu. Rev. Anal. Chem.* **2011**, *4*, 23.

(249) Chou, K.-S.; Lai, Y.-S. *Mater. Chem. Phys.* **2004**, *83*, 82.

(250) Frenkel, A. I. *Chem. Soc. Rev.* **2012**, *41*, 8163.

(251) Bauer, A. W.; Kirby, W. M.; Sherris, J. C.; Turck, M. *Am. J. Clin. Pathol.* **1966**, *45*, 493.

(252) Dion, A.; Langman, M.; Hall, G.; Filiaggi, M. *Biomaterials* **2005**, *26*, 7276.

(253) Kehoe, S.; Langman, M.; Werner-Zwanziger, U.; Abraham, R. J.; Boyd, D. *J. Biomater. Appl.* **2013**, *28*, 416.

(254) Nishigaki, J.; Tsunoyama, R.; Tsunoyama, H.; Ichikuni, N.; Yamazoe, S.; Negishi, Y.; Ito, M.; Matsuo, T.; Tamao, K.; Tsukuda, T. *J. Am. Chem. Soc.* **2012**, *134*, 14295.

(255) Cowley, J. *Phys. Rev.* **1965**, *138*, A1384.

(256) Frenkel, A. I.; Wang, Q.; Sanchez, S. I.; Small, M. W.; Nuzzo, R. G. *J. Chem. Phys.* **2013**, *138*, 064202.

(257) Hwang, B. J.; Sarma, L. S.; Chen, J. M.; Chen, C. H.; Shin, S. C.; Wang, Q. R.; Liu, D. G.; Lee, J. F.; Tang, M. T. *J. Am. Chem. Soc.* **2005**, *127*, 11140.

(258) Deng, L.; Hu, W.; Deng, H.; Xiao, S.; Tang, J. *J. Phys. Chem. C* **2011**, *115*, 11355.

(259) Frenkel, A.; Machavariani, V.; Rubshtein, A.; Rosenberg, Y.; Voronel, A.; Stern, E. *Phys. Rev. B* **2000**, *62*, 9364.

(260) Sun, Y.; Xia, Y. *J. Am. Chem. Soc.* **2004**, *126*, 3892.

(261) Washio, I.; Xiong, Y.; Yin, Y.; Xia, Y. *Adv. Mater.* **2006**, *18*, 1745.

(262) Kan, C.; Wang, C.; Zhu, J.; Li, H. *J. Solid State Chem.* **2010**, *183*, 858.

(263) Ouyang, G.; Tan, X.; Wang, C. X.; Yang, G. W. *Chem. Phys. Lett.* **2006**, *420*, 65.

(264) Wonnell, S. K.; Delaye, J. M.; Bibolé, M.; Limoge, Y. *J. Appl. Phys.* **1992**, *72*, 5195.

(265) Luo, Y.-R. In *Comprehensive Handbook of Chemical Bond Energies*; CRC Press, **2007**;1027–1040.

(266) Jin, R.; Cao, Y. C.; Hao, E.; Métraux, G. S.; Schatz, G. C.; Mirkin, C. A. *Nature* **2003**, *425*, 487.

(267) Habas, S. E.; Lee, H.; Radmilovic, V.; Somorjai, G. A.; Yang, P. *Nat. Mater.* **2007**, *6*, 692.

(268) Tian, N.; Zhou, Z.-Y.; Sun, S.-G.; Ding, Y.; Wang, Z. L. *Science* **2007**, *316*, 732.

(269) Langille, M. R.; Zhang, J.; Personick, M. L.; Li, S.; Mirkin, C. A. *Science* **2012**, *337*, 954.

(270) Personick, M. L.; Mirkin, C. A. *J. Am. Chem. Soc.* **2013**, *135*, 18238.

(271) Shibata, T.; Bunker, B. A.; Zhang, Z.; Meisel, D.; Vardeman, C. F.; Gezelter, J. D. *J. Am. Chem. Soc.* **2002**, *124*, 11989.

(272) Chen, G.; Zhao, Y.; Fu, G.; Duchesne, P. N.; Gu, L.; Zheng, Y.; Weng, X.; Chen, M.; Zhang, P.; Pao, C.-W.; Lee, J.-F.; Zheng, N. *Science* **2014**, *344*, 495.

(273) Lamble, G.; Brooks, R.; Ferrer, S.; King, D.; Norman, D. *Phys. Rev. B. Condens. Matter* **1986**, *34*, 2975.

(274) de Leeuw, N.; Nelson, C.; Catlow, C.; Sautet, P.; Dong, W. *Phys. Rev. B* **2004**, *69*, 045419.

(275) Migani, A.; Illas, F. *J. Phys. Chem. B* **2006**, *110*, 11894.

(276) Shen, B.; Fang, Z.; Fan, K.; Deng, J. *Surf. Sci.* **2000**, *459*, 206.

(277) Dalba, G.; Fornasini, P. *J. Synchrotron Radiat.* **1997**, *4*, 243.

(278) Newville, M.; Boyanov, B. I.; Sayers, D. E. *J. Synchrotron Radiat.* **1999**, *6*, 264.

(279) Kresse, G.; Furthmüller, J. *Phys. Rev. B. Condens. Matter* **1996**, *54*, 11169.

(280) Blöchl, P. *Phys. Rev. B* **1994**, *50*, 17953.

(281) Perdew, J.; Burke, K.; Ernzerhof, M. *Phys. Rev. Lett.* **1996**, *77*, 3865.

(282) Personick, M. L.; Langille, M. R.; Zhang, J.; Harris, N.; Schatz, G. C.; Mirkin, C. A. *J. Am. Chem. Soc.* **2011**, *133*, 6170.

(283) Zhang, J.; Langille, M. R.; Personick, M. L.; Zhang, K.; Li, S.; Mirkin, C. A. *J. Am. Chem. Soc.* **2010**, *132*, 14012.

(284) Iski, E. V.; El-Kouedi, M.; Calderon, C.; Wang, F.; Bellisario, D. O.; Ye, T.; Sykes, E. C. H. *Electrochim. Acta* **2011**, *56*, 1652.

(285) Langille, M. R.; Personick, M. L.; Zhang, J.; Mirkin, C. A. *J. Am. Chem. Soc.* **2012**, *134*, 14542.

(286) Bordiga, S.; Groppo, E.; Agostini, G.; Van Bokhoven, J. A.; Lamberti, C. *Chem. Rev.* **2013**, *113*, 1736.

(287) Druker, S. H.; Curtis, M. D. *J. Am. Chem. Soc.* **1995**, *117*, 6366.

(288) Petrone, C.; Hall, G.; Langman, M.; Filiaggi, M. J. *Acta Biomater.* **2008**, *4*, 403.

(289) Wang, K.; Chen, F. P.; Liu, C. S.; Russel, C. *Mater. Sci. Eng. C-Biomimetic Supramol. Syst.* **2008**, *28*, 1572.

(290) Zhang, J.; Sasaki, K.; Sutter, E.; Adzic, R. R. *Science* **2007**, *315*, 220.

(291) Wu, B.; Zheng, N. *Nano Today* **2013**, *8*, 168.

Appendix A - Supporting Information for Chapter 5

The antibacterial activity of the AgAu NPs described in Chapter 5 were also tested against *Escherichia coli* (*E. coli,* ATCC 23716) by R. Boudreau (DeNovaMed, Halifax, NS, Canada) with a serial dilution method in broth using a previously established protocol,[58] based on Clinical and Laboratory Standards Institute (CLSI) standard methodology.[208] Using this protocol, the minimum inhibitory concentrations (MICs) of the samples required to prevent any visible growth of bacteria within a 20 hour period were recorded. The main differences between this protocol and that which was used in Chapter 5 was the concentration of bacteria (*i.e.,* 1 x 10^{-5} CFU/mL in Chapter 5 and approximately 1 x 10^{-8} CFU here) and the strain of *E. coli* (*i.e.,* ATCC 6538 in Chapter 5 and ATCC 23716 here). Figure A1 illustrates the MIC values of the AgAu NPs against *E. coli* over a 20 hour period. The MIC values demonstrate that the bimetallic NPs had similar antibacterial activities and were lower than that of the pure Ag NPs.

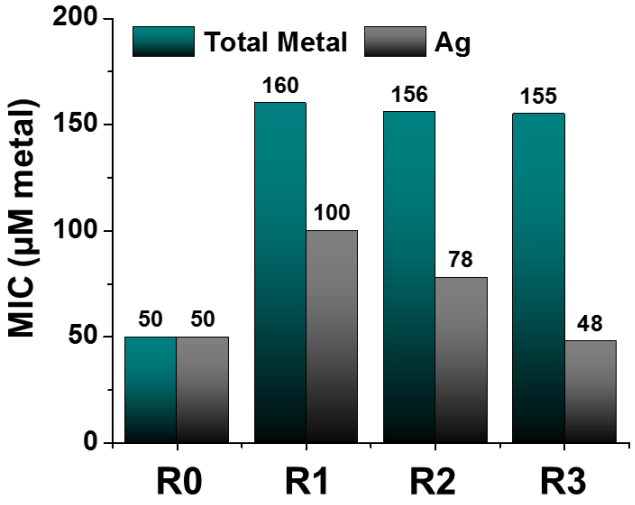

Figure A1. MIC values of the bimetallic AgAu NPs against *E. coli* after 20 hours.

Appendix B - Supporting Information for Chapter 6

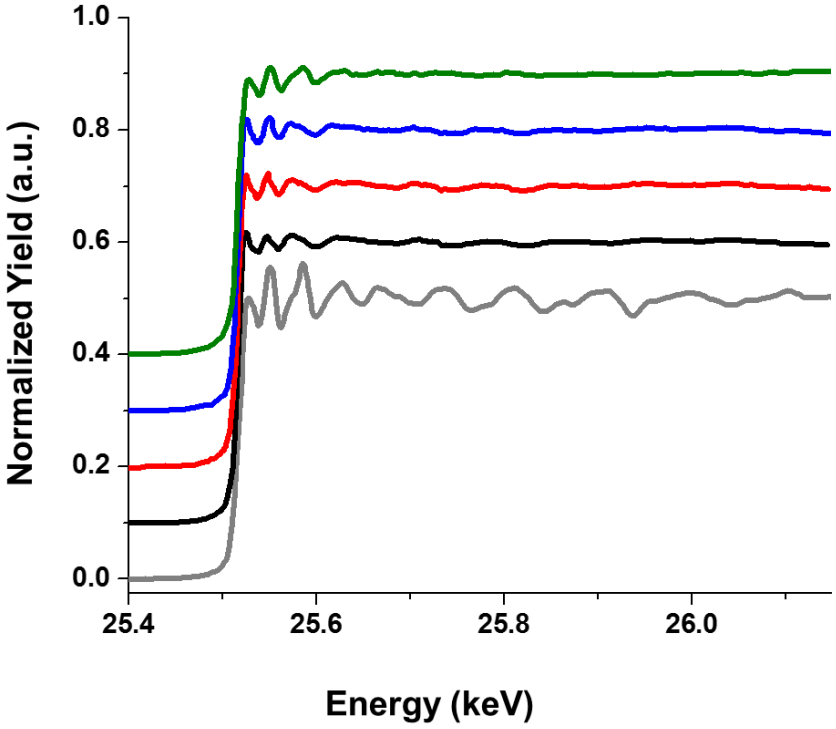

Figure B1. Ag K-edge EXAFS. The Ag K-edge EXAFS for each NP surface and Ag foil was collected by X-ray fluorescence detection at a temperature of 50 K. The spectra were background normalized and shown stacked for a qualitative comparison of oscillatory features.

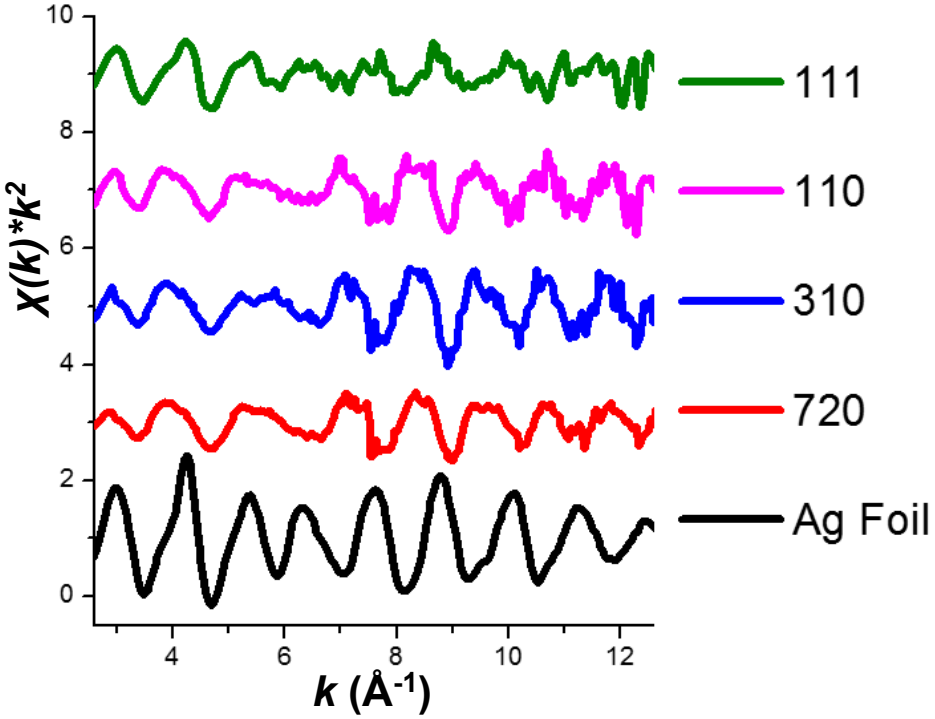

Figure B2. Ag K-edge *k*-space spectra. The EXAFS spectra presented in Figure 6.1 were each fit with a spline curve to obtain *k*-space spectra presented here. The *k*-space spectra are indicative of FCC metal as seen from the oscillations similar to Ag foil. It should be noted that the Ag foil spectrum intensity was divided by a factor of 10 in order to provide a more useful comparison to the NP surfaces.

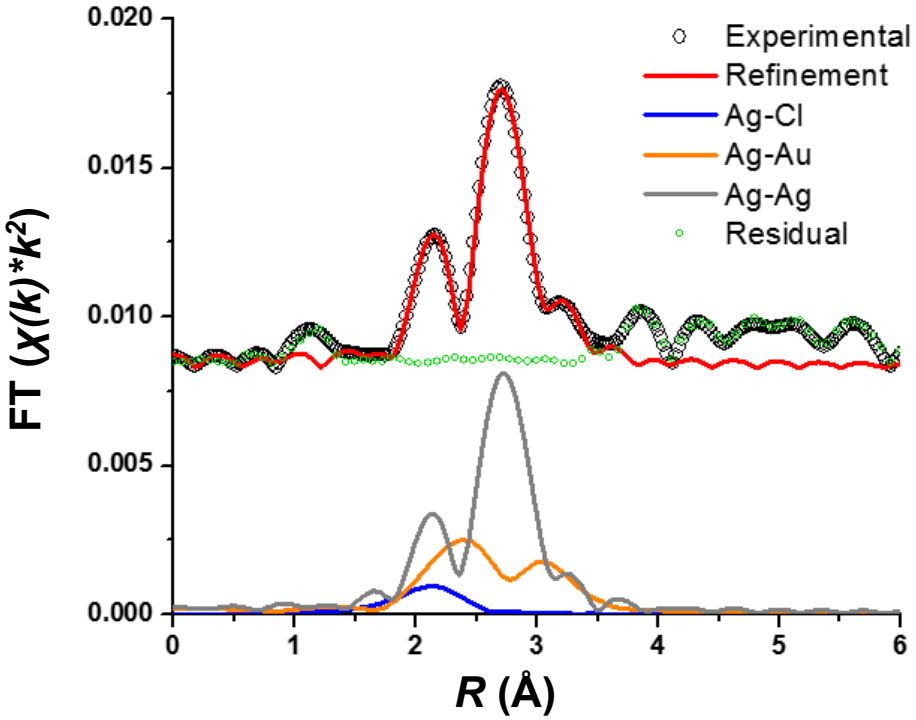

Figure B3. *R*-space refinement for the {111} NPs. The *R*-space spectra were refined with Ag-Cl, Ag-Au, and Ag-Ag paths (shown individually for clarity) and contribute to the overall refinement (red) of the experimental data (black circles). The refinement residual is also given which shows the good agreement between the refinement range of 1.7-3.3 Å.

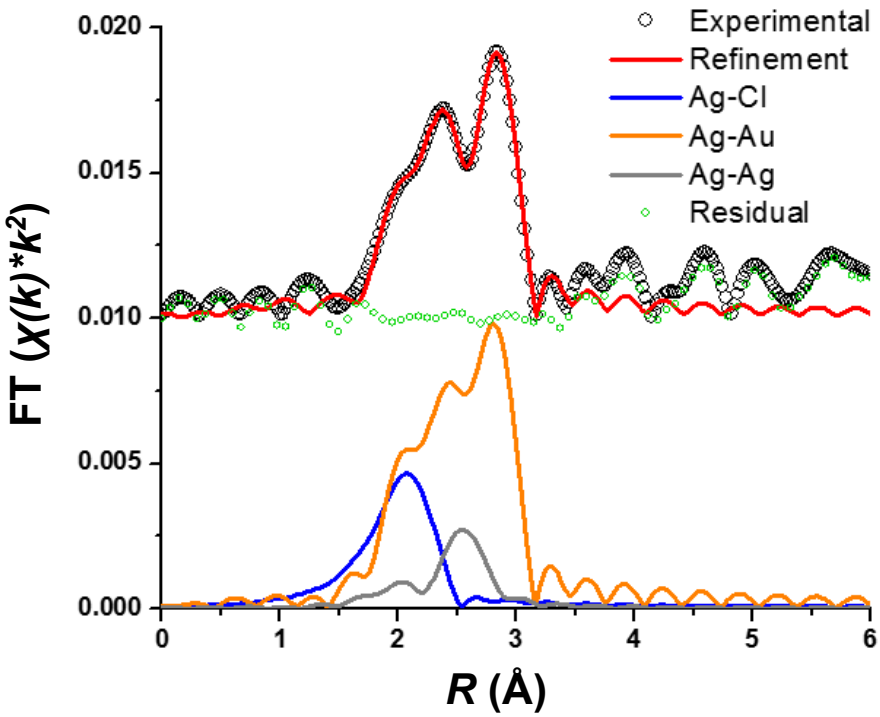

Figure B4. *R*-space refinement for the {110} NPs. The *R*-space spectra were refined with Ag-Cl, Ag-Au, and Ag-Ag paths (shown individually for clarity) and contribute to the overall refinement (red) of the experimental data (black circles). The refinement residual is also given which shows the good agreement between the refinement range of 1.7-3.3 Å.

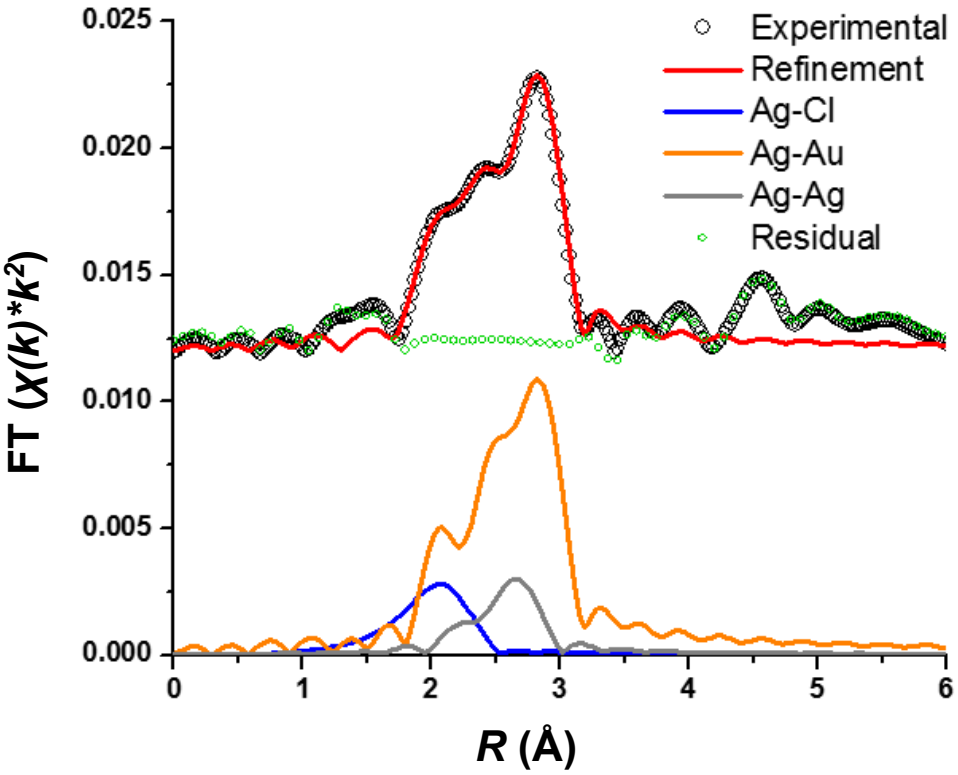

Figure B5. *R*-space refinement for the {310} NPs. The *R*-space spectra were refined with Ag-Cl, Ag-Au, and Ag-Ag paths (shown individually for clarity) and contribute to the overall refinement (red) of the experimental data (black circles). The refinement residual is also given which shows the good agreement between the refinement range of 1.7-3.3 Å.

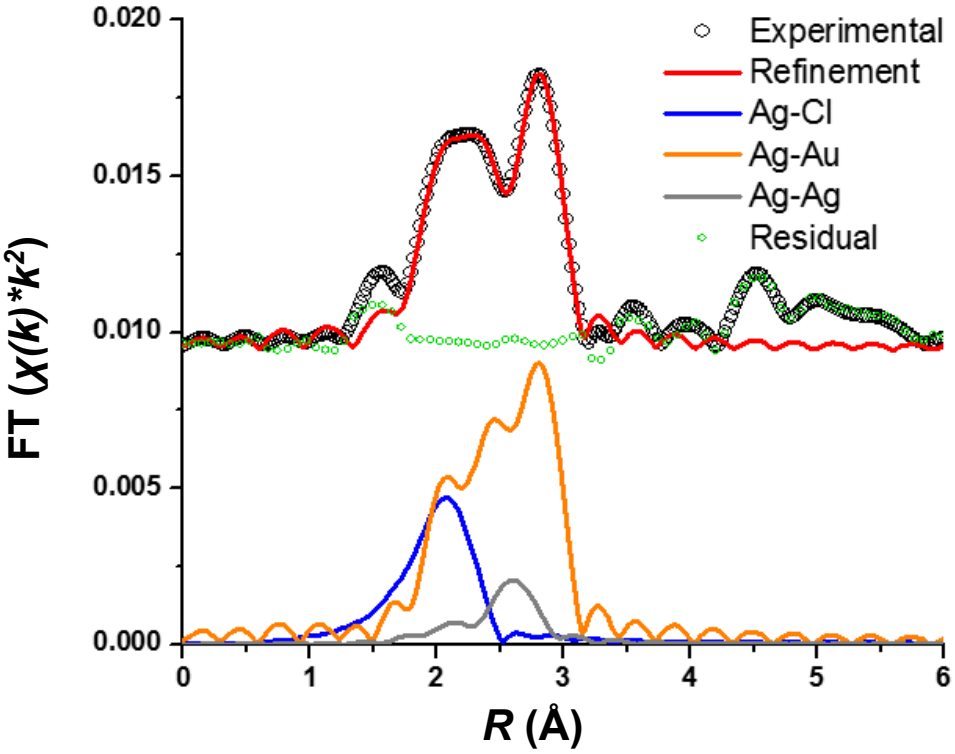

Figure B6. *R*-space refinement for the {720} NPs. The *R*-space spectra were refined with Ag-Cl, Ag-Au, and Ag-Ag paths (shown individually for clarity) and contribute to the overall refinement (red) of the experimental data (black circles). The refinement residual is also given which shows the good agreement between the refinement range of 1.7-3.3 Å.

Table B1. Ag K-edge EXAFS refinement results. The uncertainties of the refinement values are given by the numbers in parentheses.

Sample	Bond	CN	R (Å)	σ^2 (Å²)	ΔE_o (eV)
	Ag-Cl	0.4(2)	2.663(24)	0.011(9)	-1(1)
{111}	Ag-Au	7.1(14)	2.991(30)	0.021(9)	-1(1)
	Ag-Ag	3.4(3)	2.878(6)	0.009(1)	-1(1)
	Ag-Cl	1.8(4)	2.624(8)	0.009(3)	-7(1)
{110}	Ag-Au	6.8(7)	2.870(4)	0.007(1)	-7(1)
	Ag-Ag	0.8(1)	2.790(10)	0.007(1)	-7(1)
	Ag-Cl	1.2(2)	2.611(9)	0.006(2)	-6(1)
{310}	Ag-Au	4.9(8)	2.880(8)	0.004(1)	-6(1)
	Ag-Ag	0.6(1)	2.887(30)	0.004(1)	-6(1)
	Ag-Cl	1.5(4)	2.587(10)	0.007(3)	-6(1)
{720}	Ag-Au	5.7(9)	2.863(10)	0.006(1)	-6(1)
	Ag-Ag	0.6(1)	2.842(50)	0.006(1)	-6(1)

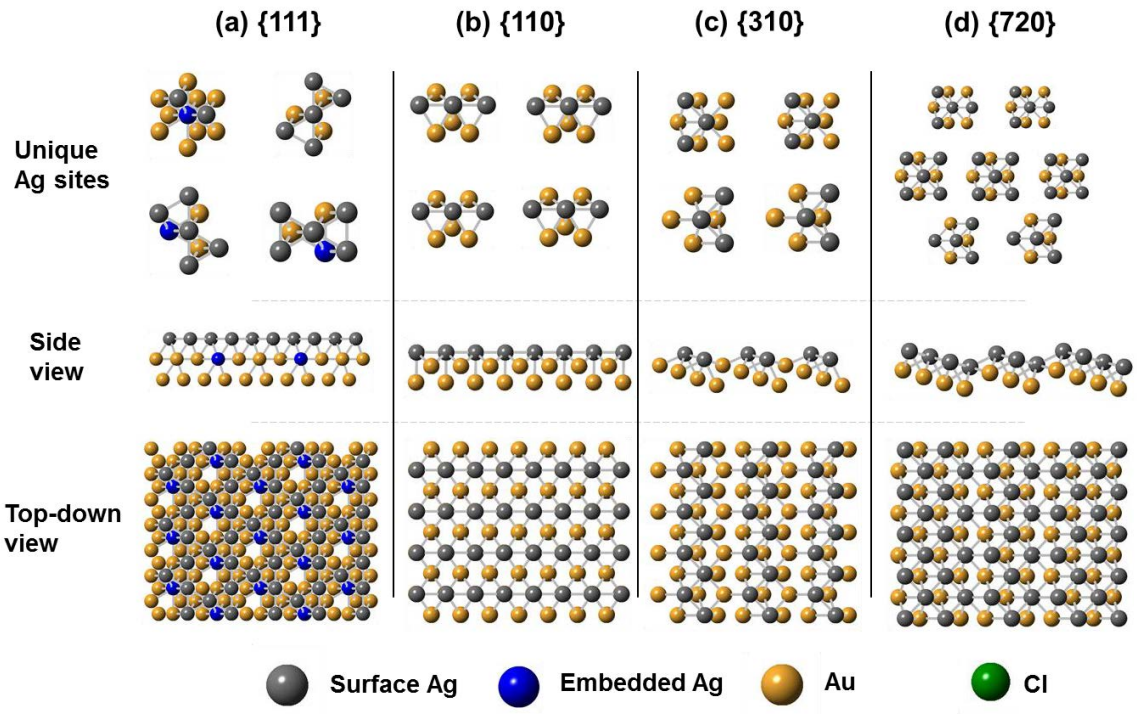

Figure B7. 0 ML Cl^- DFT models. The DFT optimized atomic coordinates of the (a) {111}, (b) {110}, (c) {310}, (d) {720} NP surfaces as modelled by Crystal Maker. The unique Ag sites help show their individual coordination while the side and top-down views of each NP surface show overall perspective.

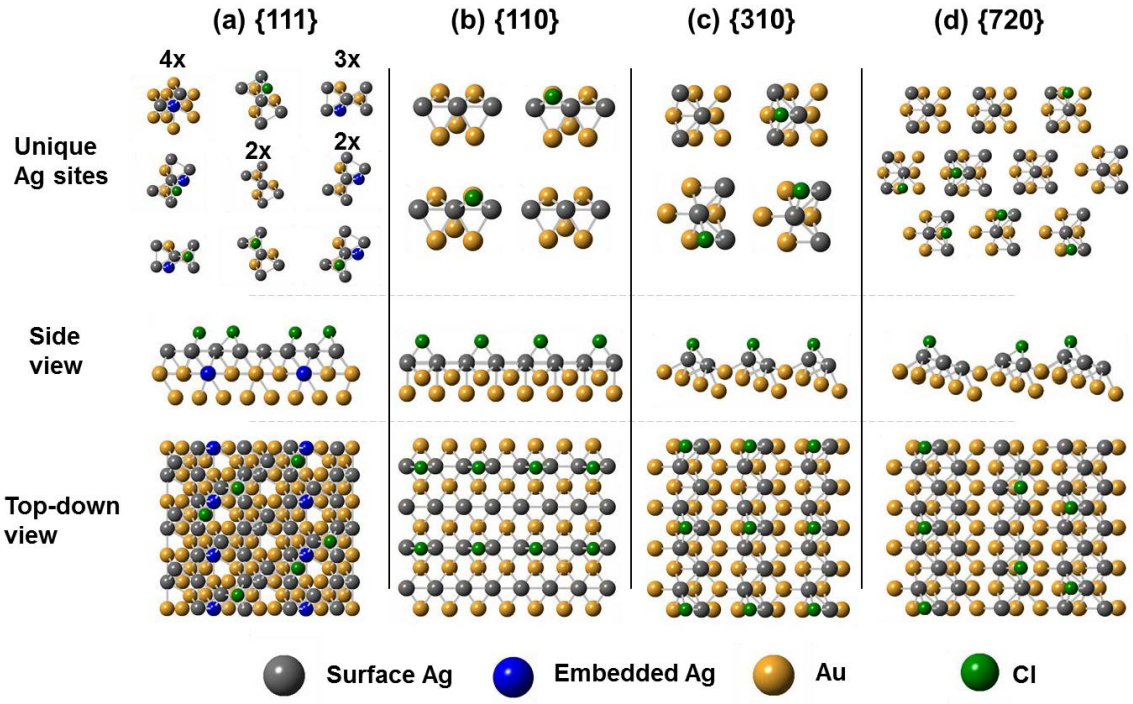

Figure B8. 0.25 ML Cl^- DFT models. The DFT optimized atomic coordinates of the (a) {111}, (b) {110}, (c) {310}, (d) {720} (0.20 ML) NP surfaces as modelled by Crystal Maker. The unique Ag sites help show their individual coordination while the side and top-down views of each NP surface show overall perspective.

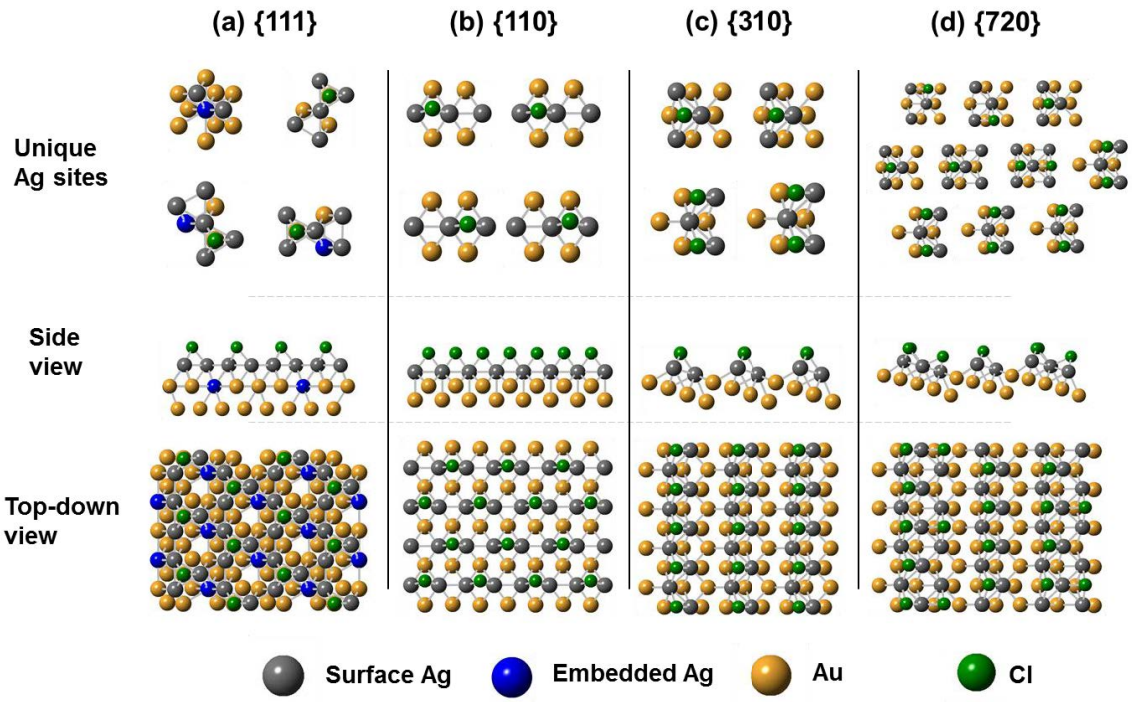

Figure B9. 0.50 ML Cl^- DFT models. The DFT optimized atomic coordinates of the (a) {111}, (b) {110}, (c) {310}, (d) {720} NP surfaces as modelled by Crystal Maker. The unique Ag sites help show their individual coordination while the side and top-down views of each NP surface show overall perspective.

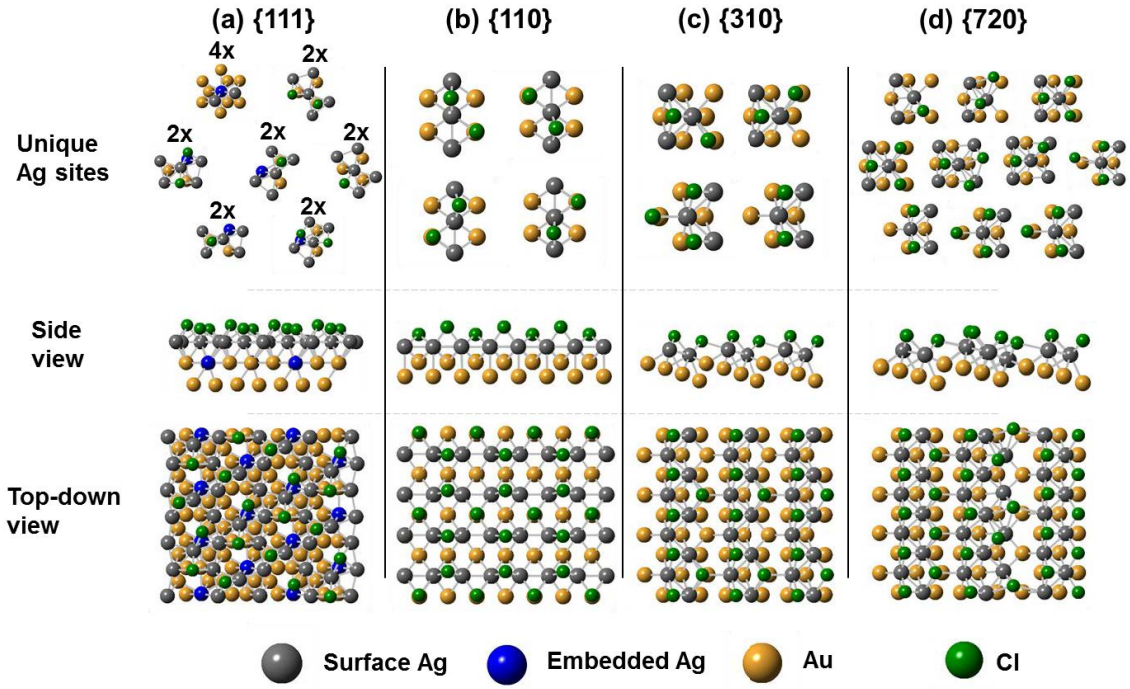

Figure B10. 0.75 ML Cl^- DFT models. The DFT optimized atomic coordinates of the (a) {111}, (b) {110}, (c) {310}, (d) {720} (0.80 ML) NP surfaces as modelled by Crystal Maker. The unique Ag sites help show their individual coordination while the side and top-down views of each NP surface show overall perspective.

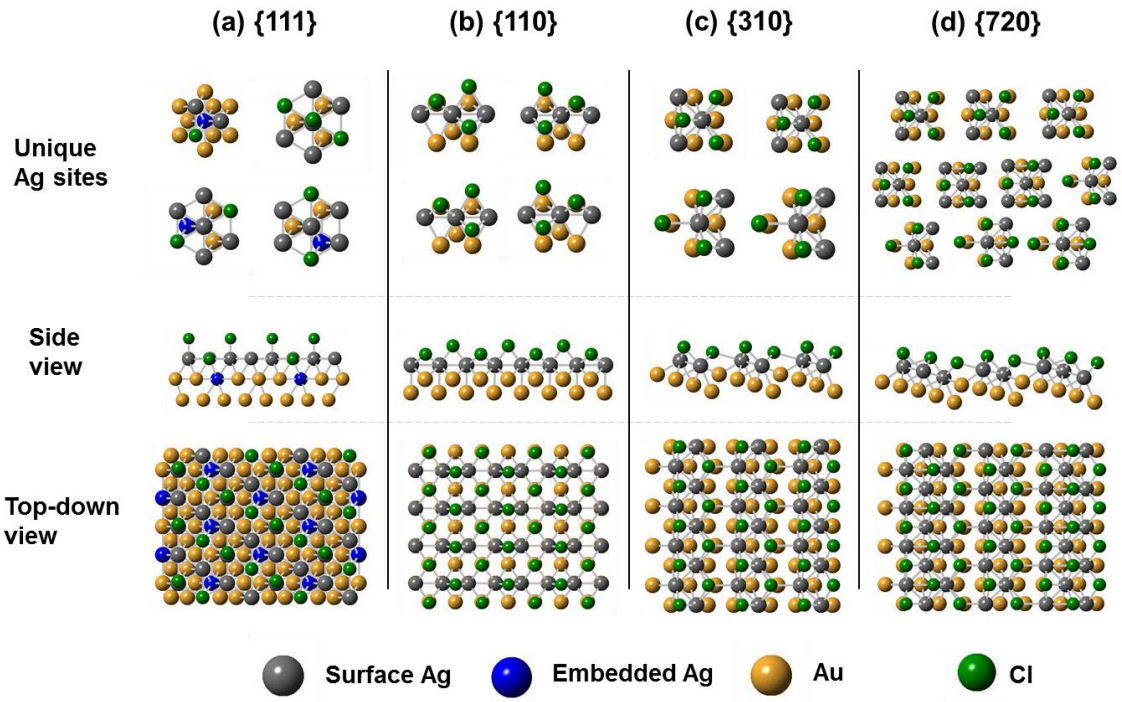

Figure B11. 1.0 ML Cl^- DFT models. The DFT optimized atomic coordinates of the (a) {111}, (b) {110}, (c) {310}, (d) {720} (0.20 ML) NP surfaces as modelled by Crystal Maker. The unique Ag sites help show their individual coordination while the side and top-down views of each NP surface show overall perspective.

Table B2. DFT versus EXAFS CN results. The DFT CNs for each coverage are shown (background darkened to distinguish DFT results), while the proposed surface models based on the experimental results are highlighted in red. The uncertainties of the refinement values are given by the numbers in parentheses.

Surface	Bond	EXAFS CN	0 ML	0.25 ML	0.5 ML	0.75 ML	1.0 ML
{111}	Ag-Cl	0.4(2)	-	0.3	0.75	1.1	2
Non-UPD	Ag-Au	7.1(14)	4	4	4	4	4
	Ag-Ag	3.4(3)	3.25	3.6	4	4	4
{110}	Ag-Cl	1.8(4)	-	0.5	1	2	2.5
UPD	Ag-Au	6.8(7)	5	5	5	5	5
	Ag-Ag	0.8(1)	2	2	2	2	2
{310}	Ag-Cl	1.2(2)	-	0.75	1.5	2	3
UPD	Ag-Au	4.9(8)	5	5	5	5	5
	Ag-Ag	0.6(1)	2	2	2	2	2
{720}	Ag-Cl	1.5(4)	-	0.6	1.4	2.5	3.2
UPD	Ag-Au	5.7(9)	4.8	4.8	4.8	4.8	4.8
	Ag-Ag	0.6(1)	3.0	2.2	2.2	2.2	2.2

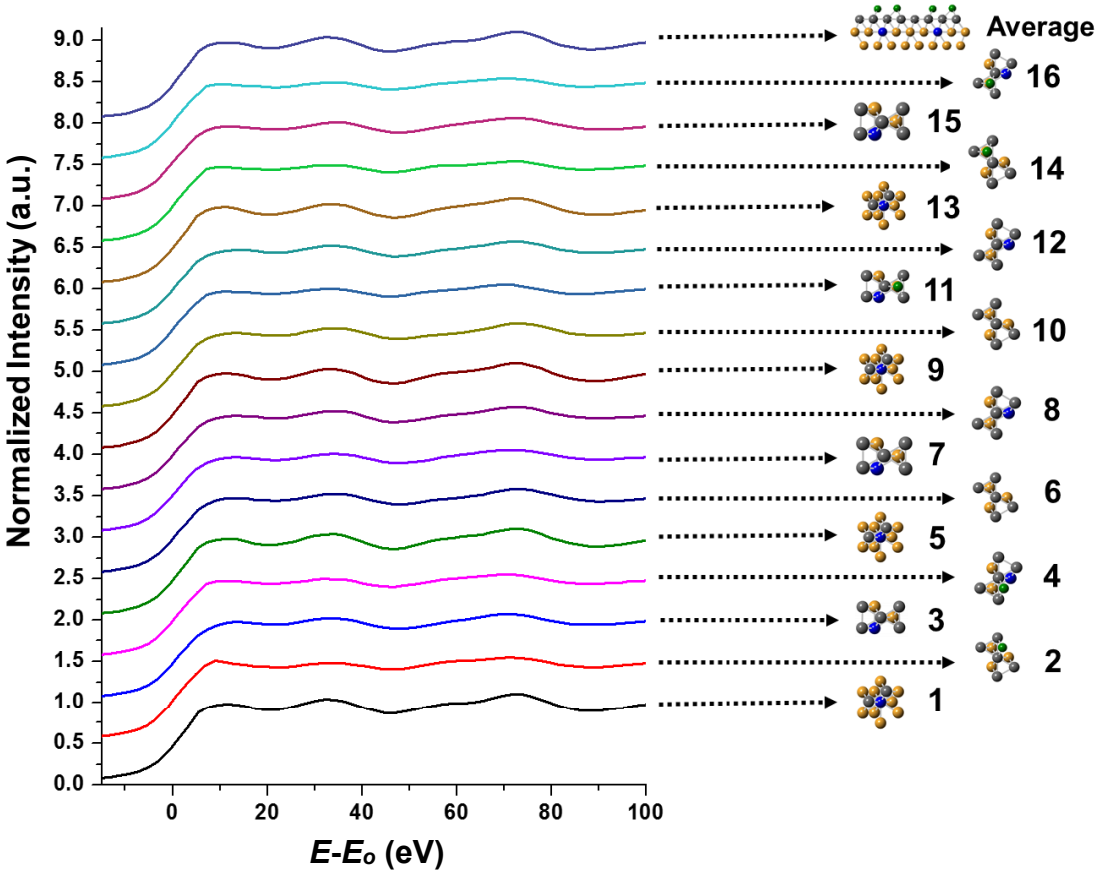

Figure B12. FEFF simulated Ag K-edge XANES spectra for {111}. The XANES spectrum for each unique Ag site in the 0.25 ML Cl^- {111} surface was simulated. The average of all of the spectra was presented in the main text.

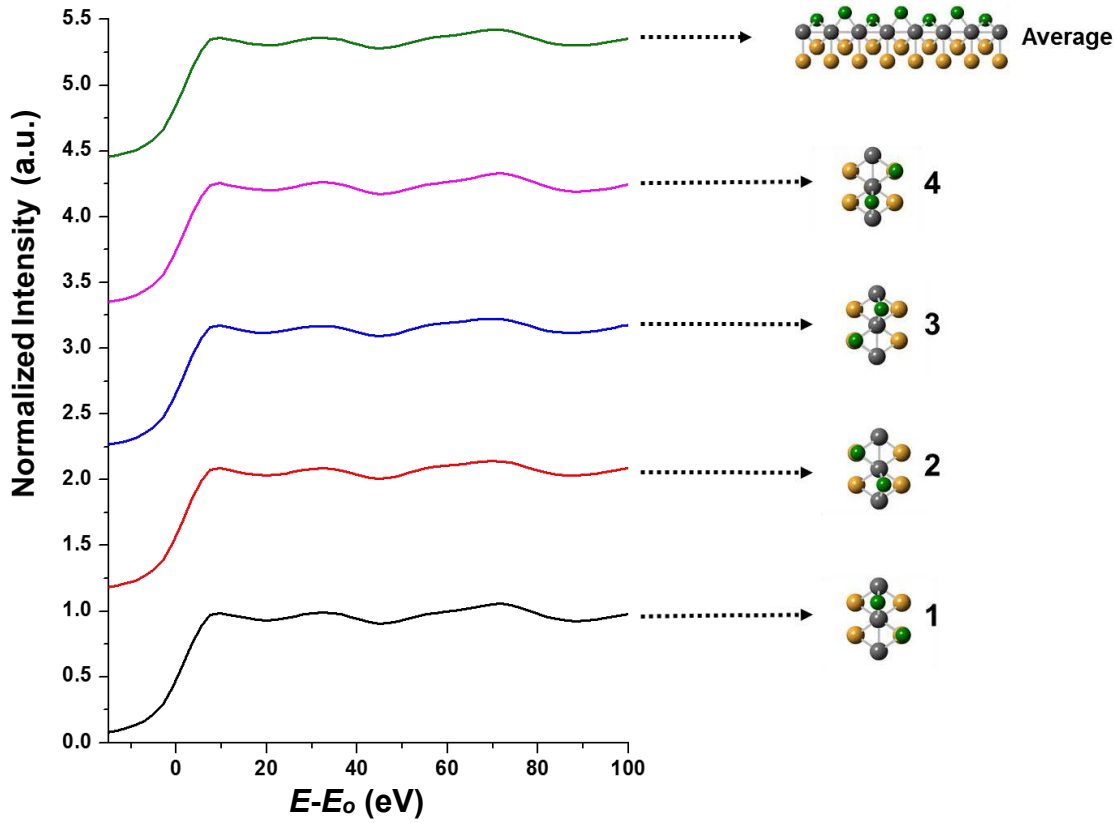

Figure B13. FEFF simulated Ag K-edge XANES spectra for {110}. The XANES spectrum for each unique Ag site in the 0.75 ML Cl^- {110} sample was simulated. The average of all of the spectra was presented in the main text.

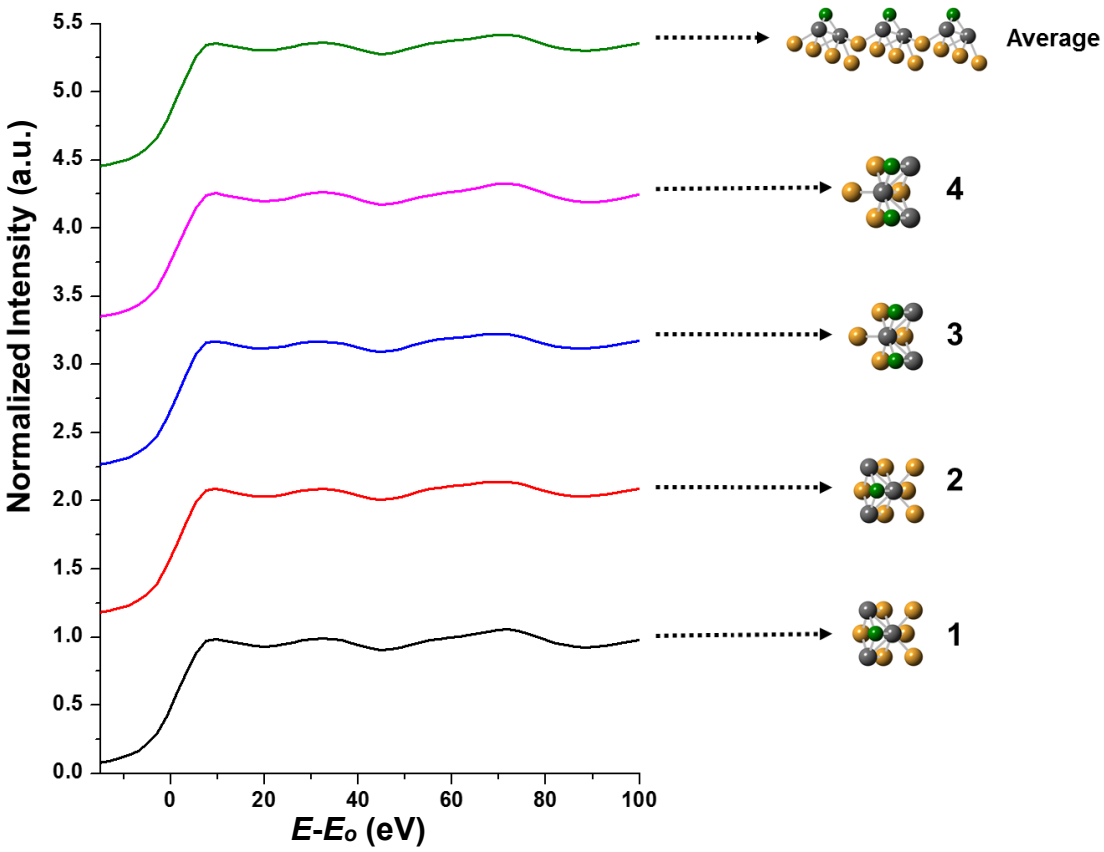

Figure B14. FEFF simulated Ag K-edge XANES spectra for {310}. The XANES spectrum for each unique Ag site in the 0.50 ML Cl^- {310} sample was simulated. The average of all of the spectra was presented in the main text.

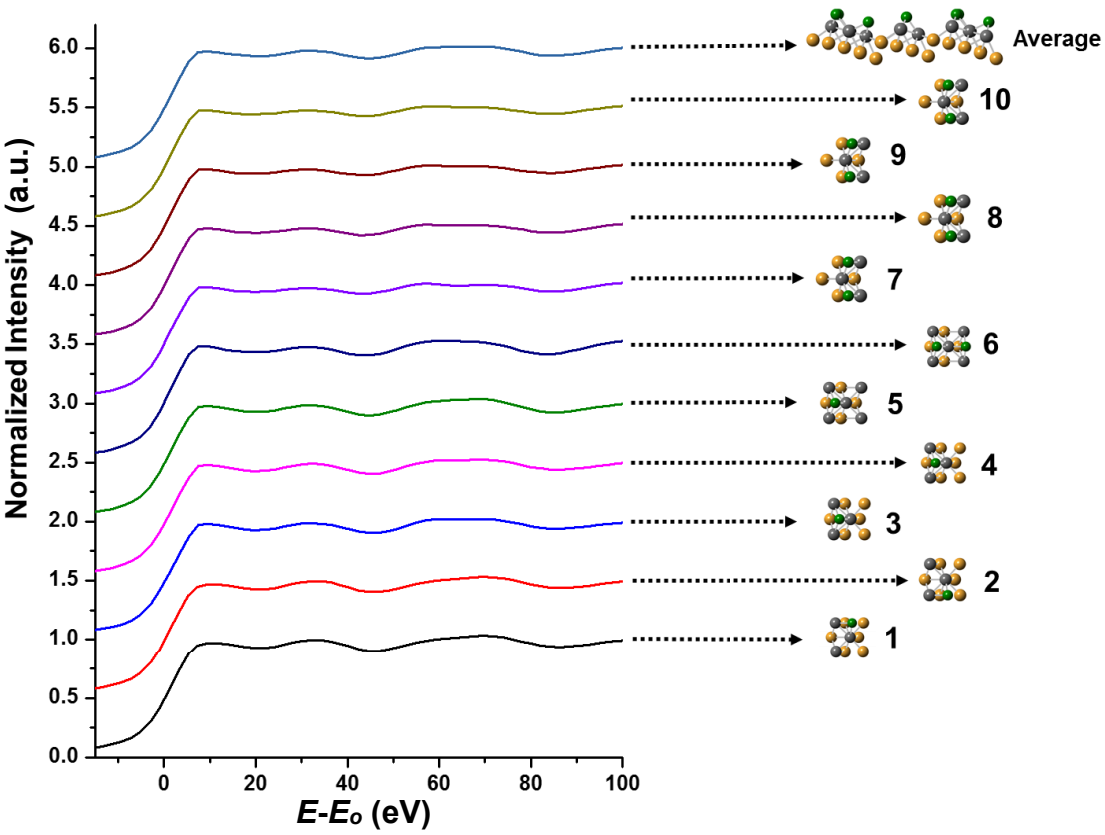

Figure B15. FEFF simulated Ag K-edge XANES spectra for {720}. The XANES spectrum for each unique Ag site in the 0.50 ML Cl^- {720} sample was simulated. The average of all of the spectra was presented in the main text.

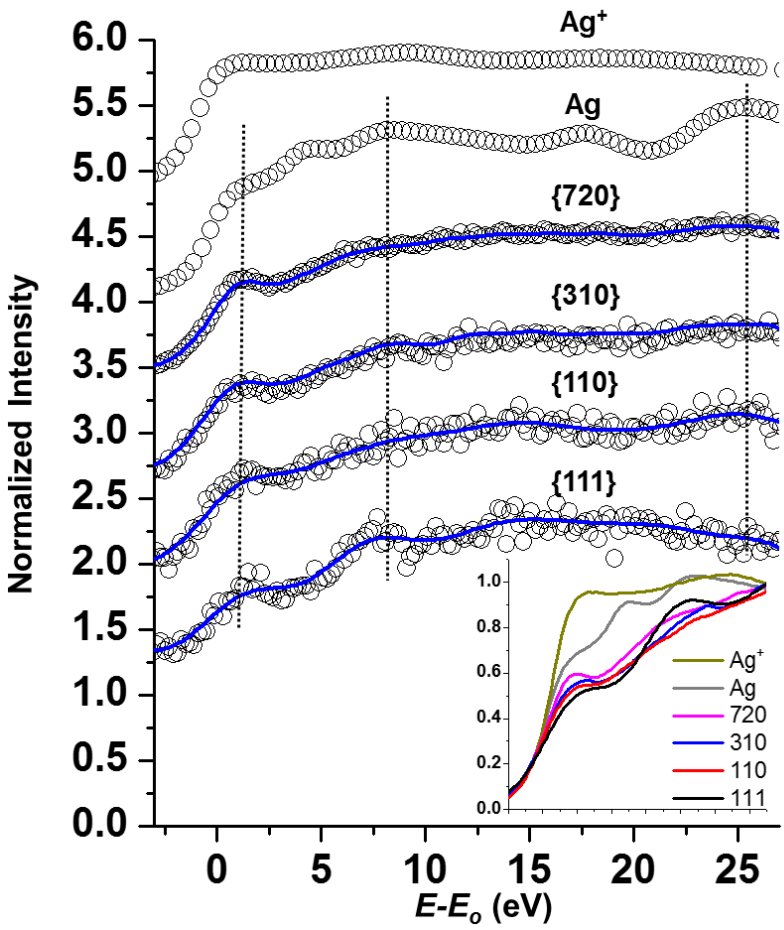

Figure B16. Experimental Ag L_3-edge XANES. The experimental XANES of the NPs (black circles) were fit with a smooth line (in blue) in order to show overall feature similarities (black dashed lines). The large difference between the Ag foil and Ag^+ can be seen by the overlaid spectra in the inset figure. The NPs exhibit a slightly lower intensity of the first feature which as expected for nanosized and alloyed materials. Overall, their similarity to the Ag foil features and their peak intensities confirm their metallic state.

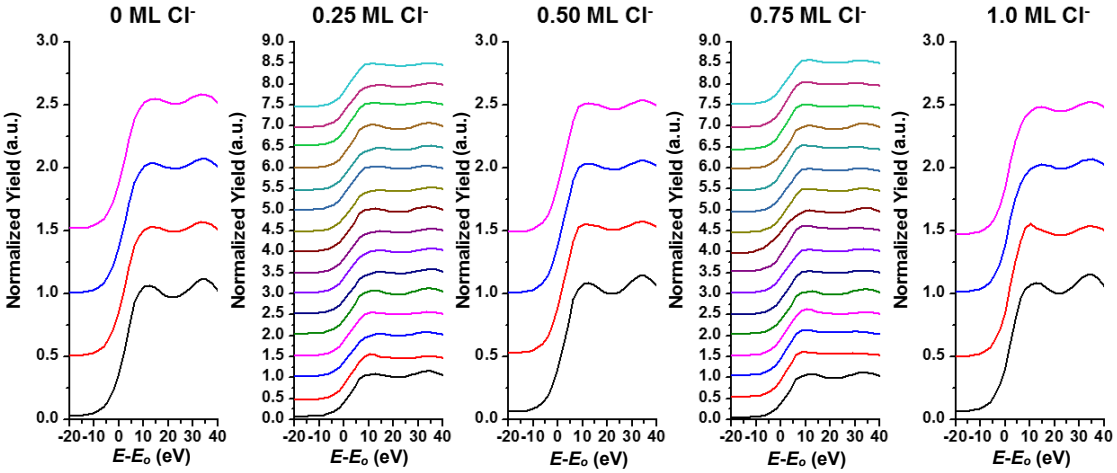

Figure B17. Simulated {111} Ag K-edge XANES spectra for all Cl^- coverages. The XANES spectrum for each unique Ag site (represented by different colours) in each coverage model (0, 0.25, 0.50, 0.75, and 1.0 ML Cl^-) was simulated by FEFF using the atomic coordinates obtained by DFT.

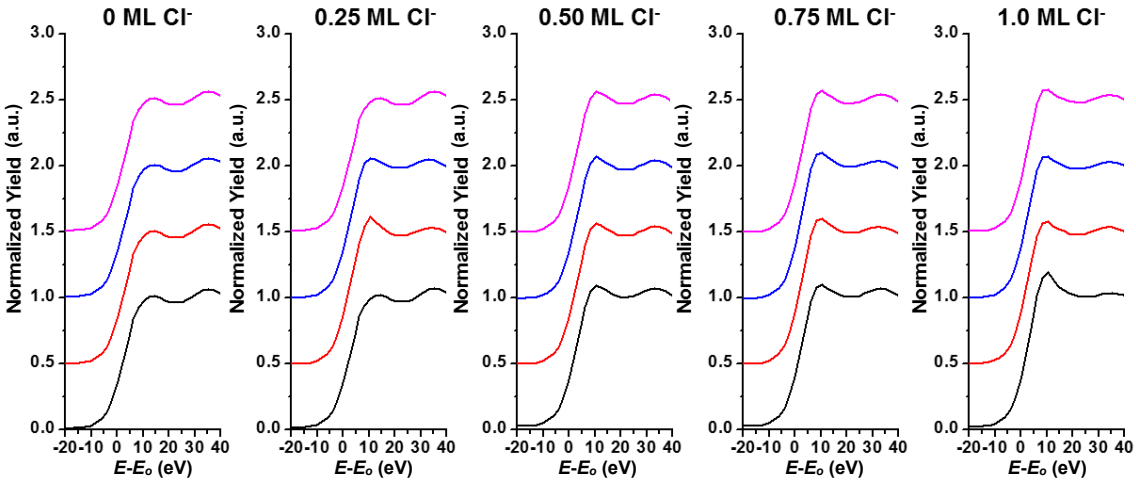

Figure B18. Simulated {110} Ag K-edge XANES spectra for all Cl^- coverages. The XANES spectrum for each unique Ag site (represented by different colours) in each coverage model (0, 0.25, 0.50, 0.75, and 1.0 ML Cl^-) was simulated by FEFF using the atomic coordinates obtained by DFT.

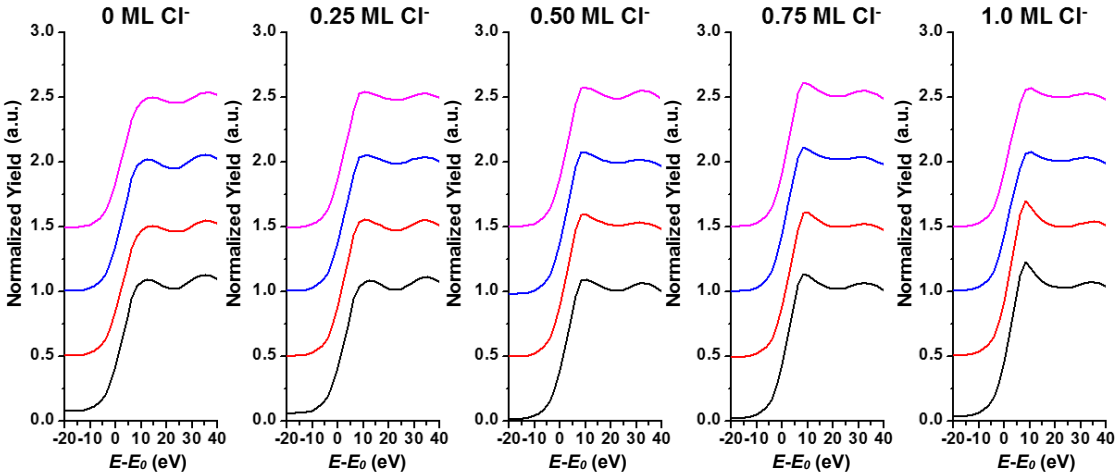

Figure B19. Simulated {310} Ag K-edge XANES spectra for all Cl^- coverages.The XANES spectrum for each unique Ag site (represented by different colours) in each coverage model (0, 0.25, 0.50, 0.75, and 1.0 ML Cl^-) was simulated by FEFF using the atomic coordinates obtained by DFT.

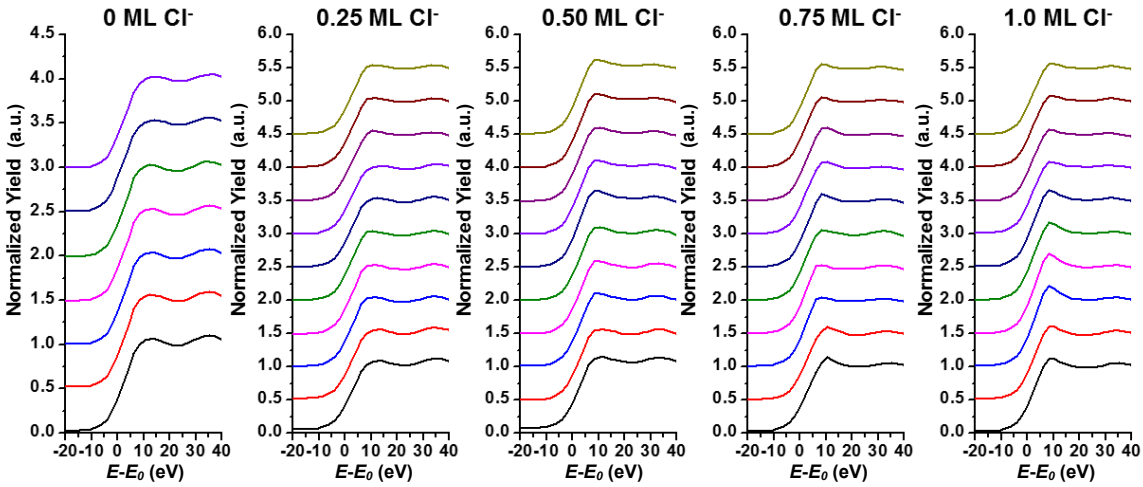

Figure B20. Simulated {720} Ag K-edge XANES spectra for all Cl^- coverages. The XANES spectrum for each unique Ag site (represented by different colours) in each coverage model (0, 0.25, 0.50, 0.75, and 1.0 ML Cl^-) was simulated by FEFF using the atomic coordinates obtained by DFT.

Appendix C - Copyright Agreement for Chapter 2

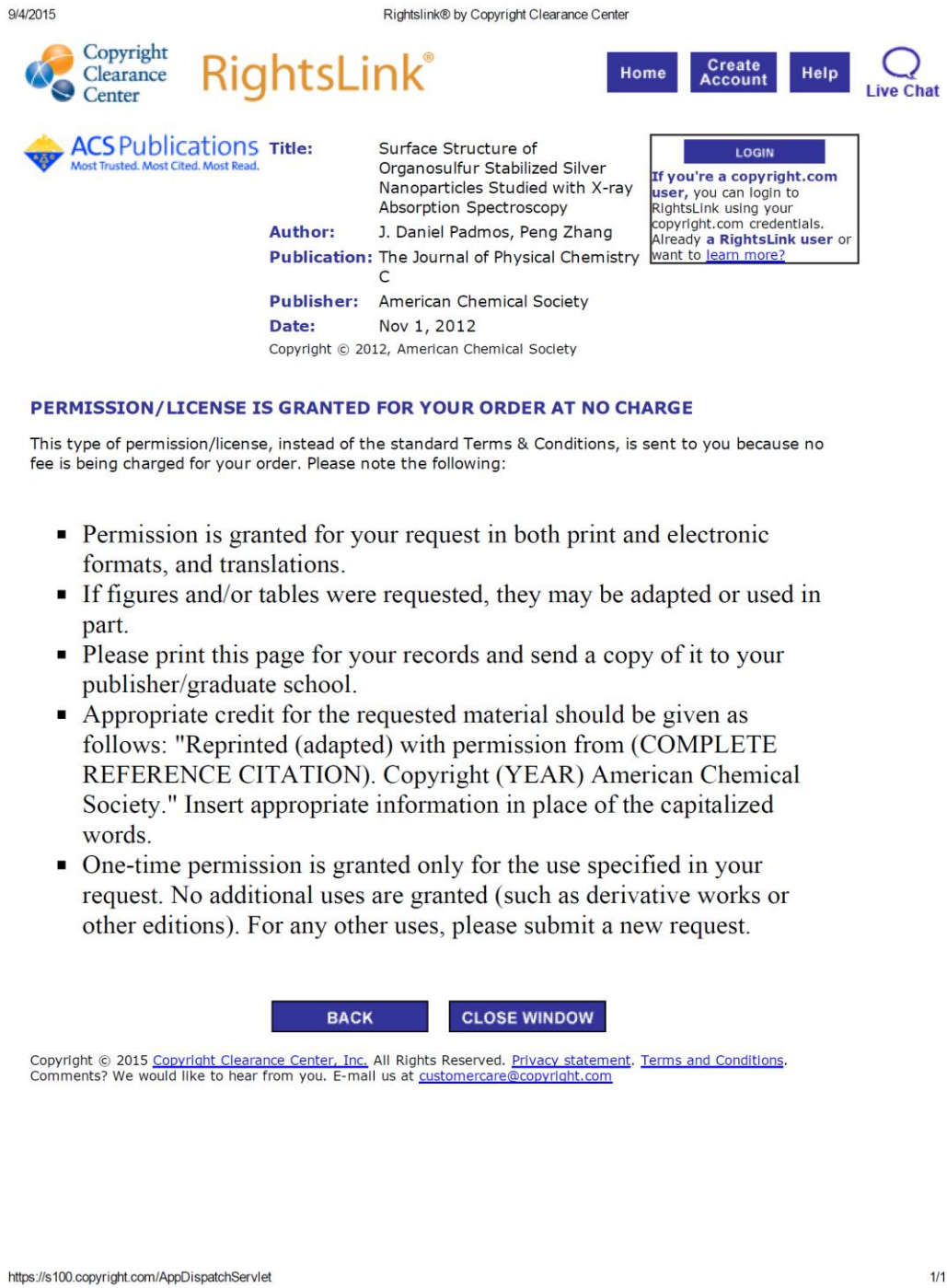

9/4/2015 Rightslink® by Copyright Clearance Center

Copyright Clearance Center RightsLink®

Home | Create Account | Help | Live Chat

ACS Publications Most Trusted. Most Cited. Most Read.

Title: Surface Structure of Organosulfur Stabilized Silver Nanoparticles Studied with X-ray Absorption Spectroscopy

Author: J. Daniel Padmos, Peng Zhang

Publication: The Journal of Physical Chemistry C

Publisher: American Chemical Society

Date: Nov 1, 2012

Copyright © 2012, American Chemical Society

LOGIN

If you're a copyright.com user, you can login to RightsLink using your copyright.com credentials. Already **a RightsLink user** or want to learn more?

PERMISSION/LICENSE IS GRANTED FOR YOUR ORDER AT NO CHARGE

This type of permission/license, instead of the standard Terms & Conditions, is sent to you because no fee is being charged for your order. Please note the following:

- Permission is granted for your request in both print and electronic formats, and translations.
- If figures and/or tables were requested, they may be adapted or used in part.
- Please print this page for your records and send a copy of it to your publisher/graduate school.
- Appropriate credit for the requested material should be given as follows: "Reprinted (adapted) with permission from (COMPLETE REFERENCE CITATION). Copyright (YEAR) American Chemical Society." Insert appropriate information in place of the capitalized words.
- One-time permission is granted only for the use specified in your request. No additional uses are granted (such as derivative works or other editions). For any other uses, please submit a new request.

BACK CLOSE WINDOW

Copyright © 2015 Copyright Clearance Center, Inc. All Rights Reserved. Privacy statement. Terms and Conditions.
Comments? We would like to hear from you. E-mail us at customercare@copyright.com

https://s100.copyright.com/AppDispatchServlet 1/1

Appendix D - Copyright Agreement for Chapter 3

RightsLink®

Home | Create Account | Help | Live Chat

Title: Impact of Protecting Ligands on Surface Structure and Antibacterial Activity of Silver Nanoparticles

Author: J. Daniel Padmos, Robert T. M. Boudreau, Donald F. Weaver, et al

Publication: Langmuir

Publisher: American Chemical Society

Date: Mar 1, 2015

LOGIN

If you're a copyright.com user, you can login to RightsLink using your copyright.com credentials. Already **a RightsLink user** or want to learn more?

PERMISSION/LICENSE IS GRANTED FOR YOUR ORDER AT NO CHARGE

This type of permission/license, instead of the standard Terms & Conditions, is sent to you because no fee is being charged for your order. Please note the following:

- Permission is granted for your request in both print and electronic formats, and translations.
- If figures and/or tables were requested, they may be adapted or used in part.
- Please print this page for your records and send a copy of it to your publisher/graduate school.
- Appropriate credit for the requested material should be given as follows: "Reprinted (adapted) with permission from (COMPLETE REFERENCE CITATION). Copyright (YEAR) American Chemical Society." Insert appropriate information in place of the capitalized words.
- One-time permission is granted only for the use specified in your request. No additional uses are granted (such as derivative works or other editions). For any other uses, please submit a new request.

BACK | CLOSE WINDOW

Appendix E - Copyright Agreement for Chapter 4

Appendix F - Copyright Agreement for Chapter 5

RightsLink®

Home | Create Account | Help | Live Chat

Title: Correlating the Atomic Structure of Bimetallic Silver–Gold Nanoparticles to Their Antibacterial and Cytotoxic Activities

Author: J. Daniel Padmos, Maxine Langman, Katelyn MacDonald, et al

Publication: The Journal of Physical Chemistry C

Publisher: American Chemical Society

Date: Apr 1, 2015

LOGIN

If you're a copyright.com user, you can login to RightsLink using your copyright.com credentials. Already **a RightsLink user** or want to learn more?

PERMISSION/LICENSE IS GRANTED FOR YOUR ORDER AT NO CHARGE

This type of permission/license, instead of the standard Terms & Conditions, is sent to you because no fee is being charged for your order. Please note the following:

- Permission is granted for your request in both print and electronic formats, and translations.
- If figures and/or tables were requested, they may be adapted or used in part.
- Please print this page for your records and send a copy of it to your publisher/graduate school.
- Appropriate credit for the requested material should be given as follows: "Reprinted (adapted) with permission from (COMPLETE REFERENCE CITATION). Copyright (YEAR) American Chemical Society." Insert appropriate information in place of the capitalized words.
- One-time permission is granted only for the use specified in your request. No additional uses are granted (such as derivative works or other editions). For any other uses, please submit a new request.

BACK | CLOSE WINDOW

Appendix G - Copyright Agreement for Chapter 6

RightsLink®

Home | Create Account | Help | Live Chat

Title: The surface structure of silver-coated gold nanocrystals and its influence on shape control

Author: J. Daniel Padmos, Michelle L. Personick, Qing Tang, Paul N. Duchesne, De-en Jiang, Chad A. Mirkin

Publication: Nature Communications

Publisher: Nature Publishing Group

Date: Jul 8, 2015

LOGIN

If you're a copyright.com user, you can login to RightsLink using your copyright.com credentials. Already **a RightsLink user** or want to learn more?

Creative Commons

The article for which you have requested permission has been distributed under a Creative Commons CC-BY license (please see the article itself for the license version number). You may reuse this material without obtaining permission from Nature Publishing Group, providing that the author and the original source of publication are fully acknowledged, as per the terms of the license.
For license terms, please see http://creativecommons.org/

CLOSE WINDOW

Are you the author of this NPG article?

For commercial reprints of this content, please select the Order Commercial Reprints link located beside the Rights and Permissions link on the Nature Publishing Group Web site.